

Using the Profile Likelihood method to
search for dark matter using the
DEAP-3600 detector.

Using the Profile Likelihood method to search for dark matter using the DEAP-3600 detector.



A thesis submitted to Royal Holloway, University of London for the degree of
Doctor of Philosophy

by

Ashlea Kemp

July 2020

"Science can flourish only in an atmosphere of free speech."

–Albert Einstein

Contents

| | |
|--|------------|
| Declaration | vii |
| Acknowledgements | ix |
| Abstract | xi |
| 1 Introduction | 1 |
| 1.1 Evidence for Dark Matter | 2 |
| 1.1.1 On the Galactic Scale | 2 |
| 1.1.2 On the Cosmological Scale | 7 |
| 1.2 Candidates for Dark Matter | 13 |
| 1.2.1 Motivated to Solve Problems in the Standard Model. | 13 |
| 1.2.2 Motivated by Dark Matter Observations | 17 |
| 1.3 Experimental Channels for Dark Matter Detection. | 19 |
| 1.3.1 Nuclear Scattering | 20 |
| 1.4 Statistical Approaches to Limit Setting | 28 |
| 1.4.1 Poisson Method. | 28 |
| 1.4.2 Maximum Gap/Patch Method | 29 |
| 1.4.3 Profile Likelihood Ratio | 31 |

| | | |
|----------|--|------------|
| 2 | The DEAP-3600 Experiment | 37 |
| 2.1 | Liquid Noble Gases as Targets | 38 |
| 2.1.1 | General Properties | 38 |
| 2.1.2 | Scintillation in Liquid Argon | 40 |
| 2.2 | Detector Design | 47 |
| 2.2.1 | Radioactivity Background Budget | 48 |
| 2.2.2 | Inner Detector Components | 53 |
| 2.2.3 | Outer Detector Components | 58 |
| 2.2.4 | Cryogenic System | 60 |
| 2.3 | Detector Electronics | 61 |
| 2.3.1 | Front End System | 62 |
| 2.3.2 | Digitiser and Trigger Module | 64 |
| 2.3.3 | Data Acquisition System | 66 |
| 2.4 | Calibration Systems | 67 |
| 3 | Detector Simulation and Event Reconstruction | 71 |
| 3.1 | Detector Simulation | 72 |
| 3.1.1 | Optical Model | 74 |
| 3.2 | Event Reconstruction | 76 |
| 3.2.1 | Charge Estimation | 77 |
| 3.2.2 | Pulse-Shape Discrimination | 83 |
| 3.2.3 | Event Position | 97 |
| 4 | Review of Backgrounds in DEAP-3600 | 107 |
| 4.1 | Electromagnetic Recoils | 108 |
| 4.1.1 | ^{39}Ar Decay | 108 |
| 4.1.2 | Internal & External β/γ -ray Interactions | 117 |
| 4.1.3 | ^{85}Kr Decay | 121 |

| | | |
|----------|--|------------|
| 4.2 | Nuclear and Nuclear-Like Recoils | 134 |
| 4.2.1 | Radiogenic Neutrons | 134 |
| 4.2.2 | α -decays from the Acrylic Vessel. | 136 |
| 4.2.3 | α -decays from the Acrylic Neck Flow Guides | 139 |
| 4.2.4 | α -decays from Dust Particulates. | 145 |
| 4.2.5 | Data - MC Validation | 150 |
| 5 | Development of the Profile Likelihood Ratio Software | 155 |
| 5.1 | Cut Selection and Region-of-Interest | 156 |
| 5.2 | Likelihood Function | 162 |
| 5.3 | Signal and Background Model Construction | 166 |
| 5.3.1 | WIMPs and ^{39}Ar | 166 |
| 5.3.2 | Neck α -decays. | 179 |
| 5.3.3 | Surface α -decays | 191 |
| 5.3.4 | Dust α -decays. | 198 |
| 5.3.5 | Radiogenic Neutrons | 202 |
| 5.3.6 | Background Expectation and Model Summary | 206 |
| 6 | Limit Setting with the Profile Likelihood Ratio | 211 |
| 6.1 | Calculating an Upper Limit | 212 |
| 6.2 | Systematic Uncertainties | 214 |
| 6.2.1 | Propagation of Systematic Uncertainties in PLR | 217 |
| 6.3 | Software Validation. | 223 |
| 6.4 | Projected Sensitivity | 230 |
| 6.5 | Final Results | 232 |
| 6.6 | Summary and Outlook | 239 |
| | Bibliography | 243 |

Declaration

THIS thesis features a combination of studies performed by the author, the DEAP-3600 collaboration and from individuals within the DEAP-3600 collaboration. A summary of the main contributions from the author are described in the following paragraphs.

In Chapter 3, a procedure to measure the trigger efficiency of the DEAP-3600 detector using periodically-triggered data is developed. This is compared to the measured trigger efficiency as obtained using an independent method developed by fellow DEAP-3600 collaborator, Tina Pollmann [1].

Chapter 4 presents the results of three separate studies performed by the author. These include an in-situ measurement of the Krypton-85 (^{85}Kr) radioactivity inside the liquid argon target of the DEAP-3600 detector, the development of an analytical model that is used to fit the Argon-39 (^{39}Ar) β -decay energy (charge) spectrum measured by the DEAP-3600 detector in order to determine the detector energy response, and a measurement of the background trigger rate in the DEAP-3600 detector from α -decays originating from dust contaminants circulating inside the liquid argon target.

The development of the Profile Likelihood Ratio software performed by the author in Chapter 5 continues on from the existing framework initially developed by Alistair Butcher [2], Navin Seeburn [3] and Shawn Westerdale. Of note, the author

has improved the pre-existing WIMP signal and ^{39}Ar background models and has developed the neck α -decay and dust α -decay background models in their entirety. The author has also implemented an additional dimension into the analysis and has introduced a new technique in order to incorporate several new systematic uncertainties into the analysis. The remaining background models have been developed by fellow DEAP-3600 collaborator, Joe McLaughlin.

The analysis and results presented in Chapter 6 are performed by the author in their entirety. Contributions from other sources, notably the DEAP-3600 collaboration, are explicitly referenced in the text where relevant. In addition to this declaration, the author confirms that this thesis has not been submitted, in whole or in part, to any previous degree application.

–Ashlea Kemp

22nd July 2020

Acknowledgements

UNDOUBTEDLY, the first person I would like to thank is my MSci supervisor, Stewart Boogert, for always pushing me to the best I can be, even as an annoying second year student! Thank you for your continued support and friendship.

Next, I would like to thank all of my past and present friends and colleagues at Royal Holloway and in the Dark Matter and Neutrino group. In particular, I'd like to thank Andrey Abramov and Joe Bayley, who have been there with me since the beginning back in 2012. To Joe Walding, for your mentorship. To Asher Kaboth, for your statistics wisdom. To Nasim Fatemighomi and Alistair Butcher, for helping to fix my code whenever it was (inevitably) broken. To Mark Ward, for your random YouTube videos. To Franco La Zia, for being one of the gentlest souls I've had the pleasure of meeting. To Jordan Palmer, for your friendship and for letting me steal your desk when I came back from Canada. To everyone, for making the department such an insightful and fun place to work; I am proud to have been able to call Royal Holloway my home institution for 8 years.

I feel so fortunate to have been able to spend two years of my PhD abroad in Canada, a place I consider to be a second home in most part due to the friends and memories I made there. I'd like to thank Rob Stainforth and Sarah Lahey, for making me feel so welcome when I first arrived in Ottawa. To Shawn Westerdale, for making me a better physicist. To Damian Goeldi, Matt Dunford, Andrew Er-

landson, Bjoern Lehnert and Waqar Muhammad, for being excellent colleagues and great friends. To Pietro Giampa, for your guidance when I first arrived at SNOLAB and your continued support during my time at TRIUMF. To Tony Flower, for taking me under your wing and making delicious deep dish pizzas. To Mark Boulay, Chris Jillings and Fabrice Retiere, for hosting me at your respective institutions. A special thank you has to go Joe McLaughlin, my right-hand man. Thank you for supporting me both professionally and personally, and for always being willing to queue for Ramen Danbo with me.

Thank you to my dad, Neil, for your love and support, and for always keeping my fridge stocked up.

Thank you to my sister, Georgia, for your love and pride of me as your cool older sister, apparently.

Thank you to my parents, Tracie and Andy. I am eternally grateful to you both, for your unconditional love and support and for always believing in me. Dad, thank you for all the delicious roast dinners. Mum, thank you for always managing to talk some sense into me, for always picking me up when I've been down, and for being the best mum and best friend I could ask for. Also for the gin.

Thank you to Tommaso, my partner-in crime. Thank you for your enduring love, support and faith in me. Me leaving for Canada for two years was hard for us both, but I know I can always count on you and I am truly so grateful to have you.

Lastly, I owe an unmeasurable amount of thanks to my supervisor, Jocelyn Monroe. When you showed me around the dark matter lab after my undergraduate interview at 17 years old I remember thinking, "wow, this stuff is awesome, I'd love to work on this", and now I am. Thank you for giving me this amazing opportunity, for always striving to get the very best from me, and for providing me with the skills, knowledge and confidence to become the physicist that I am today.

Abstract

THE DEAP-3600 detector, based in Sudbury, Ontario, Canada, is a single-phase liquid argon direct detection experiment built specifically to search for dark matter candidates called Weakly-Interacting Massive Particles (WIMPs). In this thesis, a multi-dimensional Profile Likelihood Ratio analysis is applied to data acquired by the DEAP-3600 detector in order to set an exclusion limit on the WIMP-nucleon spin-independent cross section as a function of WIMP mass. A comprehensive background model has been developed for the Profile Likelihood Ratio analysis, based on three main event reconstruction variables: the total event charge, the particle identification parameter and the reconstructed event position. This thesis presents the implementation and validation of the Profile Likelihood Ratio software, explores the projected WIMP sensitivity and reports a 90% confidence level upper limit on the WIMP-nucleon cross section for WIMP masses between $50 \text{ GeV}/c^2$ and $1000 \text{ GeV}/c^2$, based on 231 days of live data acquired by the DEAP-3600 detector. For a $100 \text{ GeV}/c^2$ WIMP, the Profile Likelihood Ratio analysis calculates an upper limit of $3.13 \times 10^{-45} \text{ cm}^2$, a limit 20% more sensitive than the upper limit calculated by the DEAP-3600 collaboration using the cut-and-count method on the same dataset presented in [4].

Chapter 1

Introduction

“How wonderful that we have met with a paradox.

Now we have some hope of making progress.”

–Niels Bohr

THE mystery of dark matter is one that has perplexed physicists for many years. The existence of additional, non-visible matter was proposed back in 1933 by Fritz Zwicky [5] who, by applying the virial theorem to eight galaxies in the Coma cluster, measured the mass-to-light ratio of the system to be ~ 60 , where this number has been rescaled to reflect the current value of the Hubble constant [6]. Since then, there has been an avalanche of evidence pointing towards the existence of dark matter, on smaller (galactic) scales and on larger (cosmological) scales. Key pieces of evidence include observations of galactic rotational curves and galaxy clusters, the Cosmic Microwave Background, Big Bang Nucleosynthesis and large-scale structure,

all discussed in this chapter. Advances in cosmology have also allowed us to quantify the amount of dark matter present in our universe, currently estimated to be $\sim 25\%$ [7]. However, we are yet to answer the fundamental question: what is dark matter made of? There exist a wealth of theories which could give rise to dark matter, some of which include extensions of the Standard Model, a theory which describes the four fundamental forces, all of the elementary particles and all of the gauge bosons which mediate their interactions which have been discovered thus far, and some of which involve entirely new physics. Consequently, there remains a vast amount of parameter space to search.

The structure of this chapter is as follows. Section 1.1 first provides a summary of the most compelling arguments for dark matter. Section 1.2 outlines various popular candidates for dark matter, motivated either by the discrepancies in the Standard Model or simply by our observations of dark matter itself. Section 1.3 details the direct detection experimental channel used in dark matter experiments to search for one of the leading dark matter candidates, Weakly-Interacting Massive Particles, and reviews the current experimental constraints on this candidate. Section 1.4 discusses the evolution of different statistical methods used by dark matter experiments to set exclusion limits on dark matter.

1.1 Evidence for Dark Matter

1.1.1 On the Galactic Scale

Virial Theorem

THE virial theorem states that for a stable, gravitationally bound system of N objects,

$$\bar{T} = -\frac{1}{2}\bar{U}, \quad (1.1)$$

where \bar{T} is the time-averaged kinetic energy of the system and \bar{U} is the time-averaged gravitational potential energy of the system. In 1933, Fritz Zwicky applied the virial theorem to $N = 8$ galaxies in the Coma cluster. For a system of N galaxies orbiting at varying distances $r_{i,i+1,\dots,N}$ from the centre of a spherical and symmetric mass distribution $M(r)$, the total gravitational potential energy of the cluster is given by,

$$U = -4\pi G \int_0^R M(r) \rho(r) r dr, \quad (1.2)$$

assuming an average cluster density of $\rho(r)$. Here, R is the radius of the cluster and G is the gravitational constant. If the total mass enclosed inside radius r is given by $M(r) = (4/3)\pi r^3 \rho(r)$, the total time averaged gravitational potential energy of the cluster can be written as,

$$U = -\frac{3}{5} \frac{GM^2}{R}. \quad (1.3)$$

Using the virial theorem, the total mass of the cluster M can be deduced from the result from Equation 1.3 and the total kinetic energy of the cluster, given by the sum of kinetic energies of the individual galaxies, $\bar{T} = (1/2) \sum m_i \bar{v}_i^2$. The total mass of a galaxy cluster M can be mathematically expressed as,

$$M = \frac{5\bar{v}^2 R}{3G}, \quad (1.4)$$

where \bar{v}^2 is the averaged velocity across the galaxies. By inserting values for the Coma cluster into Equation 1.4, Zwicky calculated that the total cluster mass is approximately ~ 60 times larger than the mass that can be attributed to luminous matter, such as stars and gas. He referred to this discrepancy as “missing” matter, to account for the fact that galaxies in the cluster were moving too fast to be explained solely by luminous matter.

Rotational Velocity Curves

THE phenomenon of galaxy rotation was first discovered in 1914 by Max Wolf and Vesto Slipher, who deduced from measuring the spectrum of an unknown “system” (which later turned out to be the Andromeda M31 galaxy) that it was rotating [8]. In the 1970’s, Vera Rubin and Kent Ford used an image tube spectrograph to perform spectroscopic observations of M31, out to 110 arcminutes from the centre of the galaxy [8]. Kent and Rubin observed a flat rotation curve for M31, deviating from the predicted rotation curve only considering contributions from the visible matter in the galaxy. This implies the presence of additional, non-luminous mass.

Newtonian physics says that the circular velocity of an object in a galaxy, such as a star, residing outside of a bulk region of mass $M(r)$, is inversely proportional to the square of the distance from the galactic centre,

$$v(r) = \sqrt{\frac{GM(r)}{r}}, \quad (1.5)$$

where G is the universal gravitational constant. $M(r)$ is obtained from the mass density profile of the galaxy, which assuming spherical symmetry, is obtained from mass density profile $\rho(r)$, $M(r) \equiv 4\pi \int \rho(r)r^2 dr$. This relationship states that the circular velocity for stars located outside of the luminous disk and at a distance r from the galactic centre should decrease proportionally with \sqrt{r} . This alone can not describe the observed data; the example flat rotation curve shown in Figure 1.1 is well-modelled by including a non-luminous halo of dark matter of $M(r) \propto r$ and $\rho(r) \propto 1/r^2$ [9]. The argument for dark matter is more compelling given the fact that flat rotation curves have been consistently measured for multiple other galaxies, including the isolated dwarf spiral galaxy NGC 6503 located at a distance of 5.2 Mpc [10] as shown in Figure 1.1. Rotation curves indicate that for spiral

galaxies, the dark matter component dominates the luminous component,

$$M_{\text{DM}} = a_0 \cdot M_{\text{L}}, \quad (1.6)$$

where M_{DM} is the dark matter halo mass, M_{L} is the luminous mass comprised of stars and gas, and a_0 ranges between 3 - 10 [11].

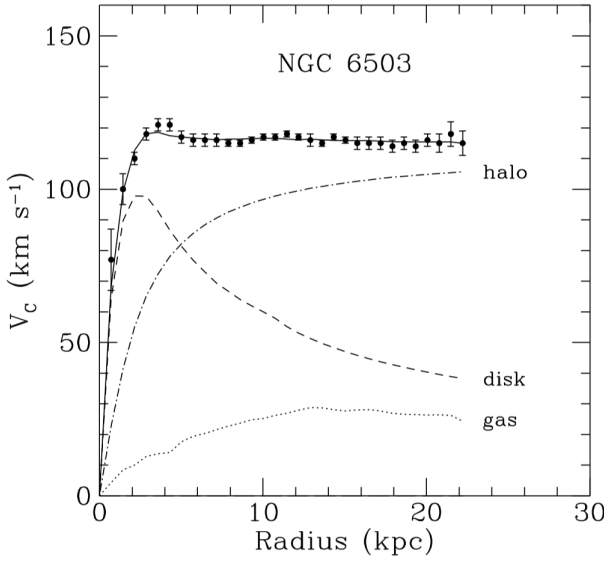


Figure 1.1: Circular velocity [kms^{-1}] of stars in the isolated dwarf galaxy NGC 6503 as a function of radial distance from the centre of the galaxy [kpc], indicated by the data points. The dashed, dotted and dash-dotted lines draw the expected rotation curves from considering the luminous disk, the gas and dark matter halo contributions only [9].

The Bullet Cluster

OBSERVATIONS of the Bullet Cluster provide strong evidence for dark matter, and can be used to deduce an upper limit on the dark matter self-interaction cross section. The Bullet Cluster consists of two merging galaxy clusters, whose cores collided approximately 100 Myr ago [12]. Figure 1.2 shows a composite image of the cluster from optical data, from the Giant Magellan Telescope and the Hubble

space telescope, and X-ray data from the Chandra X-ray observatory. Superimposed on the image is the reconstructed mass map from gravitational lensing results. The two pink regions in the image correspond to the hot gaseous regions of each cluster, containing the majority of the baryonic matter in the two colliding clusters. The rightmost pink region, shaped like a bullet, is the hot gas from the galaxy cluster which traversed through the hot gas of the other cluster. X-rays emitted from the hot gaseous regions in an energy (wavelength) range of 0.08 keV - 10 keV (15 nm - 0.12 nm) are detected by Chandra [13]. During the collision, the two gas regions electromagnetically interacted with one another, resulting in a “drag” force that slowed the two regions. Since dark matter does not interact electromagnetically with baryonic matter or with itself, it was unaffected by the collision. The dark matter regions in each cluster therefore separated from the baryonic matter, moving ahead of the gas regions.

The mass distribution of the two colliding clusters was determined from the effect of weak gravitational lensing of the Bullet Cluster on background galaxies by the Hubble telescope. This estimate is done by modelling the distortion of light from distant galaxies as it bends around the masses of the Bullet Cluster galaxies. The two blue regions in the image correspond to where the majority of the mass from the two clusters is located. The blue regions corresponding to the majority of the mass are clearly isolated from the pink regions corresponding to the hot gas, implying that during the collision, the majority of the mass from the clusters passed right through each other without interacting, dissimilar to the hot gas. This observation can be interpreted as an upper limit on the dark matter self-interaction cross section, currently constrained to $\sigma/m < 0.47 \text{ cm}^2\text{g}^{-1}$ at 95% confidence level [14], and is compelling evidence for non-baryonic dark matter, or very weakly-interacting baryonic dark matter.



Figure 1.2: Composite image of the Bullet Cluster. The pink regions depict the two regions of hot gas that interacted during the collision and subsequently slowed. The blue regions depict where the majority of the mass is located, inferred by weak gravitational lensing observations on background galaxies from the Hubble space telescope. The separation between the pink and blue regions demonstrates that the majority of the mass is both dark and non-baryonic in nature. Credit: X-ray: NASA/CXC/CfA/M.Markevitch et al.; Optical: NASA/STScI; Magellan/U.Arizona/D.Clowe et al.; Lensing Map: NASA/STScI; ESO WFI; Magellan/U.Arizona/D.Clowe et al.

1.1.2 On the Cosmological Scale

Cosmic Microwave Background

THE best constraints on the total amount of dark matter in the universe come from measurements of the Cosmic Microwave Background (CMB). CMB radiation was produced at the time of the Big Bang and decoupled from matter approximately 380,000 years after, at which time the universe was cool enough for simple neutral hydrogen atoms to form. Relic photons from the decoupling epoch have since been propagating through space, decreasing in energy over time due to the increase in their wavelength from the expansion of the universe. The temperature of these photons today is approximately 2.73 K; this was discovered by Penzias and Wilson in 1965 [15]. The cosmological principle states that, when observed on large enough scales, the universe should be both spatially homogenous and isotropic [16];

this has been measured to describe the CMB to the level of 1 part in 10^5 , as a result of data collected from the Planck mission [17]. Figure 1.3 shows the observed temperature anisotropies of the CMB as mapped by the Planck mission in 2018 [18]. These small anisotropies can be used to deduce the content of matter and energy in the universe.

The observed temperature anisotropies in the CMB can be written as an expansion of spherical harmonics $Y_{lm}(\theta, \phi)$ [9],

$$\frac{\delta T}{T}(\theta, \phi) = \sum_{l=2}^{+\infty} \sum_{m=-l}^{+l} a_{lm} Y_{lm}(\theta, \phi), \quad (1.7)$$

where a_{lm} are the expansion coefficients. The variance C_l of the expansion coefficients is defined as [9],

$$C_l = \frac{1}{2l+1} \sum_{m=-l}^l |a_{lm}|^2, \quad (1.8)$$

Typically, the quantity $l(l+1)C_l/2\pi$ is plotted as a function of the multipole moment l [9]. This yields the CMB angular power spectrum, which describes how correlated the temperature anisotropies in different directions are as a function of angular separation. Since the multipole moment l is inversely proportional to the separation angle θ between two points in the sky, larger values of l correspond to smaller angular scales. The Planck anisotropy measurement, reported in these variables, is shown in Figure 1.4.

Measurements of the CMB can be well described with the minimal Λ CDM cosmological model, which parameterises the expansion rate of a spatially flat universe (zero curvature) comprised of four species: baryonic matter, dark matter, radiation (photons, relativistic neutrinos) and dark energy. The minimal Λ CDM model is a function of various cosmological parameters, the values of which can be determined from fitting the power spectrum with the prediction from the Λ CDM model. These

include:

- H_0 : the value of the Hubble constant, which describes the rate of the expansion of the universe, measured at the present day and
- Ω_i : the density parameter for each of the four species. The dimensionless density parameter for the species i is the ratio of the species density to the critical density ρ_{crit} , where ρ_{crit} is the present day value of the density which gives a spatially flat universe. The total density has been measured to be extremely close to ρ_{crit} . The baryon density, dark matter density, radiation density and dark energy density are denoted by Ω_b , Ω_c , Ω_{rad} and Ω_Λ respectively.

Figure 1.4 shows the power spectrum fit with the Λ CDM model as reported by Planck in 2018 [19]. These most recent results find the density contribution of baryonic matter to be $\Omega_b h^2 = 0.022383$ and the density contribution of dark matter to be $\Omega_c h^2 = 0.12011$. Cosmological parameters are often defined in terms of the dimensionless Hubble parameter, h , defined by the relationship $H_0 = 100 h \text{ kms}^{-1} \text{Mpc}^{-1}$, where H_0 is the present day value of the Hubble constant [20].

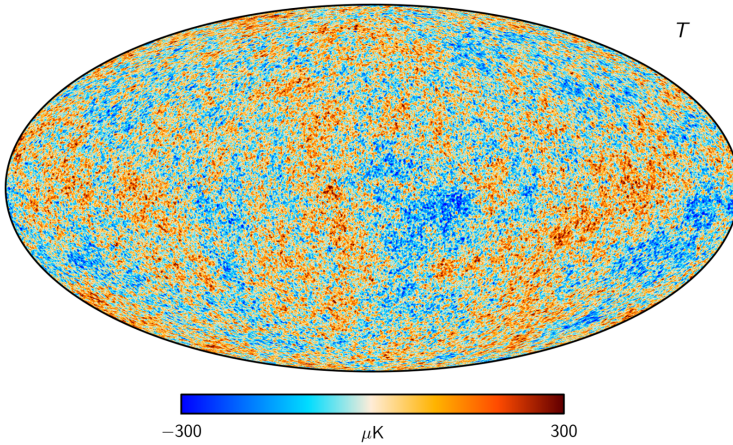


Figure 1.3: CMB radiation temperature map as observed by the Planck mission in 2018, which shows isotropy to the 10^{-5} level [18].

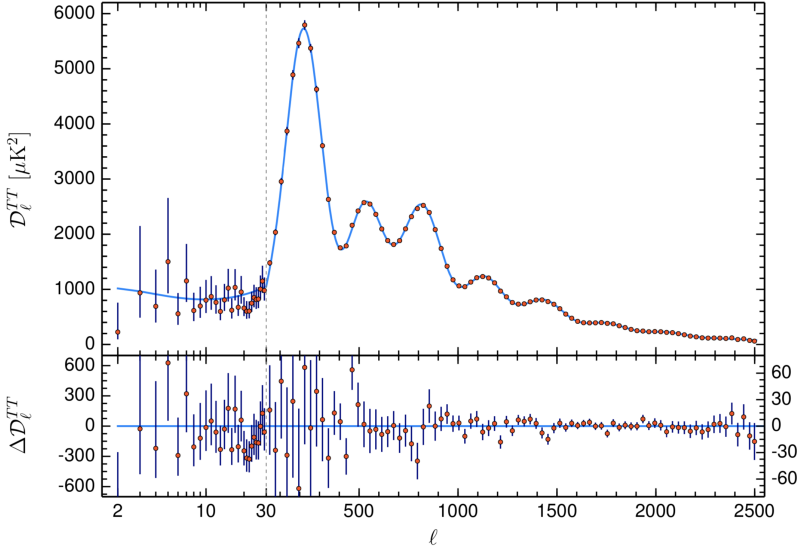


Figure 1.4: Planck 2018 temperature power spectrum, fit with the ΛCDM cosmological model in order to extract the relative baryon matter and dark matter densities [19].

Big Bang Nucleosynthesis

BIG Bang Nucleosynthesis (BBN) offers strong evidence that dark matter is mostly non-baryonic and can provide an additional constraint on the value of Ω_b . BBN occurred in a time window of $t \sim 0.1 - 10^4$ s with respect to the Big Bang [21], when the universe was cool enough for primordial, light elements (heavier than Hydrogen-1, ^1H) to form. At times prior to this, photons had energies that exceeded the nuclear binding energy of deuterium (^2H or D), destroying any ^2H that was momentarily formed. BBN came to an end when the universe expanded enough for the rate of production to fall below the expansion rate; at this “freeze-out” time, the primordial abundances of light elements in the universe such as ^2H , Helium-3 (^3He), Helium-4 (^4He) and Lithium-7 (^7Li) were approximately constant.

The ratio of the number density of baryons in the universe to the number density of photons, $n_b/n_\gamma \equiv \eta_b$, determines the primordial abundances once BBN ends. Thus, estimates of these primordial abundances can be used to constrain the value

of η_b . A constraint on η_b can be directly translated to a constraint on Ω_b . Figure 1.5 shows the primordial abundances as a function of η_b and $\Omega_b h^2$ [22]. The solid vertical band (green) shows the 2σ constraint from the 2015 Planck results [23] and the red boxes show the 2σ observational limits on $Y_p \equiv {}^4\text{He}/\text{H}$ and ${}^7\text{Li}/\text{H}$ and the 4σ limit on D/H , where PPL16 is from [24] and ITG14 is from [25]. Figure 1.5 shows that the estimated value of $\Omega_b h^2$ from primordial abundance estimates are in agreement with the CMB measurements of $\Omega_b h^2$, implying that nearly all baryons in the universe are visible, and thus do not make up the majority of the dark matter component.

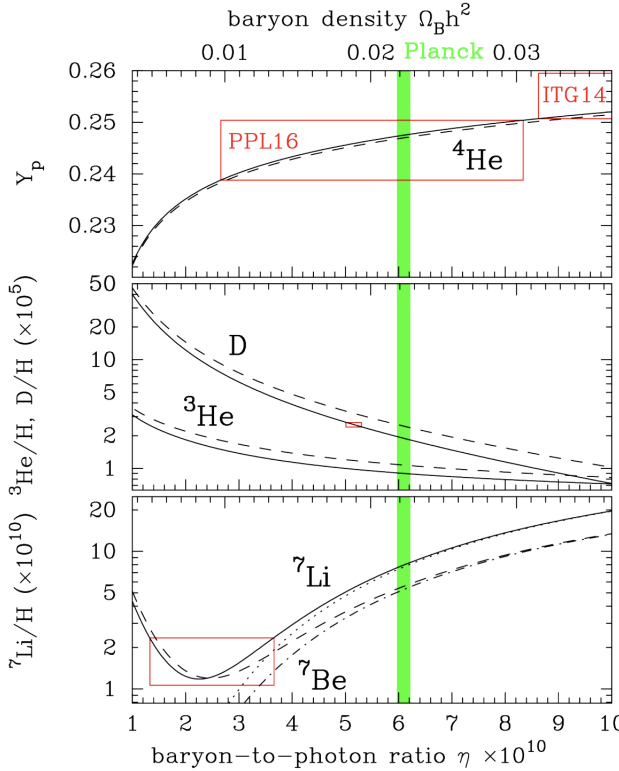


Figure 1.5: Primordial abundances as a function of $\eta_b/\Omega_b h^2$ [22]. The solid vertical band (green) shows the 2σ constraint from the 2015 Planck results [23]. Red boxes show the 2σ observational limits on $Y_p \equiv {}^4\text{He}/\text{H}$ and ${}^7\text{Li}/\text{H}$ and the 4σ limit on D/H ; PPL16 is from [24] and ITG14 is from [25].

Large-Scale Structure

PRIMORDIAL density fluctuations, first produced through quantum perturbations, seed the evolution of large-scale structures. Cold (non-relativistic) dark matter predicts that the large-scale structure we observe today, such as galaxies and galaxy clusters, developed from the expansion of the universe over which time gravitational interactions produced hierarchical evolution [26]. Different dark matter models, such as hot (relativistic) dark matter, predict a different evolution; relativistic hot dark matter predicts that the largest structures (such as superclusters) were formed first, followed by the formation of smaller structures from fragmentation. Comparison of data to large-scale structure simulations can therefore provide constraints on the values of Ω_b and Ω_c , as well as the self-interaction cross section of dark matter particles.

Large redshift surveys, such as the Century Survey [27] and Sloan Digital Sky Survey [28] have confirmed that on large cosmological scales, $\mathcal{O}(10 - 100 \text{ Mpc})$, the distribution of galaxies is not homogenous. This irregular structure can be seen in Figure 1.6, which shows the distribution of galaxies with a recession velocity $\leq 45000 \text{ km s}^{-1}$ measured by Century Survey, for a given slice in the sky [27]. Without a dark matter component in the cosmological model, simulations are not able to reproduce this structure; the small perturbations in the early universe would have been washed out during inflation and substructures, such as galaxies, would not have been formed. Simulations with variations on the dark matter component have been compared with the data collected by the large redshift surveys, and currently show that cold, weakly-interacting dark matter is favoured for structure formation. The power spectrum measured by the Sloan Digital Sky Survey for luminous red galaxies in [28] is well-described with the Λ CDM model, with a goodness-of-fit of $\chi^2/\text{NDF} = 39.6/40$ and a prediction for $\Omega_m h^2 = (\Omega_c + \Omega_b) h^2 = 0.141_{-0.012}^{+0.010}$, consistent with the CMB measurements quoted above.

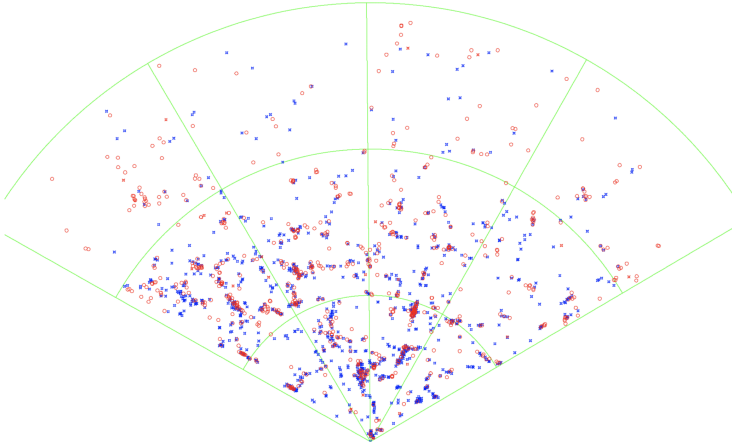


Figure 1.6: Distribution of galaxies with a recession velocity $\leq 45000 \text{ km s}^{-1}$ as observed by the Century Survey. The right ascension ranges between 8.5 h and 16.5 h. The green, radial lines correspond to 2 hour intervals, or equivalently, recession velocity intervals of 15000 km s^{-1} . The blue and red points correspond to spiral galaxies and early-type galaxies respectively, comprised mainly of old stellar populations [27].

1.2 Candidates for Dark Matter

THERE are an abundance of theories that predict potential dark matter candidates simultaneously able to satisfy the observational constraints from astronomy and cosmology, described in Section 1.1, and the constraints from particle physics searches. This section focuses on the candidates motivated to solve problems in the Standard Model of particle physics [29], as well as candidates motivated by observations of dark matter itself.

1.2.1 Motivated to Solve Problems in the Standard Model

HISTORICALLY, favoured dark matter candidates are ones which arise naturally through attempts to mitigate discrepancies in the Standard Model. Two examples of these are Axions and Weakly-Interacting Massive Particles (WIMPs).

Axions

AXIONS were first hypothesised to solve the strong CP problem observed in the Standard Model. CP symmetry is the product of the charge-conjugation (C) and parity (P) symmetries: if a particle is swapped with its antiparticle (C) and its spatial coordinates are mirrored (P), the laws of physics should be invariant. If the laws of physics are not invariant under the combined CP operation, CP symmetry is violated. This phenomenon has been observed experimentally for various decays in the electroweak theory with $>5\sigma$ significance [30], but not in the Quantum Chromodynamics (QCD) sector for strong interactions. The QCD-only Lagrangian density is defined as [31],

$$\mathcal{L}_{QCD} = \frac{g_s^2 \theta}{32\pi^2} G_{\mu\nu}^a \tilde{G}^{a\mu\nu}. \quad (1.9)$$

where g_s is the strong coupling constant, $G_{\mu\nu}^a$ is the gluon field strength tensor and θ is the QCD vacuum angle. When the strong theory is integrated into the Standard Model, the inclusion of electroweak interactions and non-zero quark masses results in chiral transformations that modify the θ vacuum, $\theta \rightarrow \theta + \text{Argdet}(\mathcal{M}_q) = \bar{\theta}$, where \mathcal{M}_q is the quark mass matrix [32]. If CP violation does take place in QCD, the neutron's electric dipole moment, d_n , is predicted to be related to the effective parameter $\bar{\theta}$ by [33],

$$|d_n| \sim 10^{-16} \bar{\theta} \, e \, \text{cm}, \quad (1.10)$$

where e is the electric charge. Experimentally, the neutron electric dipole moment has been measured to be extremely small [33],

$$|d_n| < 6.3 \times 10^{-26} e \, \text{cm}, \quad (1.11)$$

which constrains the effective parameter to be $|\theta| < 10^{-9}$. The smallness of θ is known as the strong CP problem, which states that it is unnaturally fine-tuned for the effective parameter to be close to but non-zero. This can be explained with the introduction of a new global $U(1)$ symmetry into the Standard Model, first postulated by Peccei and Quinn. If the global $U(1)_{PQ}$ symmetry is spontaneously broken by a complex scalar field at energy scale f_a , this can give rise to a pseudo-Nambu-Goldstone boson called the axion, which has a very small mass dependent on the energy scale f_a by [33],

$$m_{a_{\text{QCD}}} \simeq 6 \times 10^{-6} \text{ eV} \left(\frac{10^{12} \text{ GeV}}{f_a} \right). \quad (1.12)$$

Whilst the axion has a small mass, it has been proposed as a non-relativistic, dark matter candidate; a cold population of axion dark matter could be produced out of equilibrium [33].

WIMPs

WIMPs were highly motivated as dark matter candidates, historically, due to the “WIMP miracle”. Following the inflation epoch, the universe was hot and dense enough for Standard Model and dark matter species to be in thermal equilibrium with one another, whereby Standard Model particles annihilated to produce dark matter particles and vice versa,

$$\chi + \chi \iff \text{SM} + \text{SM}. \quad (1.13)$$

At very early times, the temperature of the universe T was high enough for dark matter particles to be relativistic, $T \gg m_\chi$. During this period, the dark matter number density $n_\chi(T) \propto T^3$ [34]. If the universe were static, these reactions would remain in equilibrium, however in an expanding (and cooling) universe, equilibrium

can only be maintained if the annihilation rate exceeds the expansion rate [35],

$$n_\chi \langle \sigma_{\text{ann}} v \rangle > H(t), \quad (1.14)$$

where σ_{ann} is the annihilation cross section, v is the relative velocity between the two annihilating dark matter or Standard Model particles, and $H(t)$ is the Hubble parameter that governs the expansion rate. Once the temperature of the universe drops below the mass of the dark matter particle, $T < m_\chi$, dark matter particles become non-relativistic and $n_\chi(T) \propto e^{-m_\chi/T}$ [35], where this exponential factor suppresses the dark matter production. Consequently, the expansion rate eventually supersedes the annihilation rate and the two particle species fall out of thermal equilibrium. The time of “WIMP freeze-out” is the point where the dark matter number density per co-moving volume becomes so low that the probability for two dark matter particles to interact approaches zero. At the time of WIMP freeze-out, the total number of dark matter particles in the universe becomes constant. The relative dark matter abundance at the time of freeze-out is therefore related to the annihilation rate by [35],

$$\Omega_\chi h^2 \propto \frac{1}{\langle \sigma_{\text{ann}} v \rangle}, \quad (1.15)$$

where Ω_χ is the relative dark matter abundance. Substituting $\Omega_\chi h^2 = 0.1198 \pm 0.0012$ [19] into Equation 1.15 implies the existence of a dark matter particle of electroweak scale mass and weak-scale cross section. A dark matter particle of 100 GeV/c² also aligns well with the predictions of Supersymmetry (SUSY) theories that address the hierarchy problem [36]; this is what is dubbed the WIMP miracle.

Supersymmetry (SUSY) was proposed to solve a number of discrepancies in the Standard Model, including the strong CP problem and the mystery of the Higgs boson mass. SUSY predicts a heavier “super” partner for each particle in the Standard

Model differing in spin by $1/2$ from the original particle, the presence of which could provide an explanation for the lightness of the Higgs boson. In the Minimal Supersymmetric Standard Model (MSSM), the lightest supersymmetric particle (LSP) is the neutralino: the leading WIMP candidate. The neutralino is a particle of mass in the GeV-range that is stable if the discrete symmetry R -parity is conserved [37]; SUSY particles have $R = -1$, where $R = (-1)^{2S+3B+L}$ and S , B and L are the spin, baryon number and lepton number respectively. R -parity conservation means that SUSY particles must be produced in pairs and cannot decay into only Standard Model particles, and thus the LSP must be stable.

1.2.2 Motivated by Dark Matter Observations

Bosonic Super-WIMPs

BOSONIC super-WIMPs are one class of dark matter candidates which do not resolve issues in the Standard Model, but are motivated simply by the observational evidence for dark matter. Two candidates of this kind are pseudoscalar particles, known as axion-like particles (ALPs), and vector particles, such as hidden photons (HPs). A cold population of ALPs and/or HPs could reproduce the correct relic abundance if they are produced non-thermally in the early universe. A proposed mechanism for this is misalignment, summarised here following [38].

After inflation, the initial state of a particle field can be parameterised by a single value, ϕ_i . The equation of motion for this field in an expanding universe is given by [38],

$$\ddot{\phi} + 3H(t)\dot{\phi} + m_\phi^2(t)\phi = 0, \quad (1.16)$$

where $m_\phi(t)$ is the temperature-dependent mass of the field ϕ . At high enough temperatures, the mass term is approximated as zero, $m_\phi(t) \sim 0$. There are two

solutions to Equation 1.16, characterised by two different epochs. The first occurs when the Hubble parameter is much greater than the mass of the field $3H(t) \gg m_\phi$; in this case, the field behaves like an overdamped oscillator resulting in no oscillation motion, $\dot{\phi} = 0$. The second occurs at a later time t_1 when the Hubble parameter is on the order of the field mass $3H(t_1) = m_\phi(t_1) = m_1$. The field behaves like an underdamped oscillator and is able to roll towards and oscillate about its minimum. The solution of Equation 1.16 during this second epoch can be obtained using the WKB approximation [38],

$$\phi \simeq \phi_1 \left(\frac{m_1 a_1^3}{m_\phi a^3} \right) \cos \left(\int_{t_1}^t m_\phi dt \right), \quad (1.17)$$

where a_i is the value of the scale factor at time t_i and $\phi_1 \sim \phi_i$ since the field is frozen before t_1 . The scale factor is a dimensionless parameter which characterises the relative expansion of the universe; it is constructed such that at the present day, $a(t_0) = 1$. The solution in Equation 1.17 can be interpreted as fast oscillations with a slow amplitude decay, and shows that the energy density of dark matter is expected to scale with the expansion of the universe as $\rho \propto a^{-3}$. The consequence of this solution is that the field oscillations can act like a cold dark matter fluid that can survive as a cold dark matter population comprised of ALPs and/or HPs observed today. The energy density of this population today can be written as [38],

$$\rho_\phi(t_0) \simeq \frac{1}{2} m_0 m_1 \phi_1^2 \left(\frac{a_1}{a_0} \right), \quad (1.18)$$

where variables with a subscript of 0 correspond to present day values. Comparing the experimentally measured dark matter energy density value, $\rho_{\text{CDM}} = 1.17(6) \text{ keVcm}^{-3}$, with Equation 1.18 shows that for this population to constitute all of the dark matter component, either a very large value of ϕ_1 is required or a combination of a smaller ϕ_1 value and a small $m_1 (<< m_0)$ is required.

1.3 Experimental Channels for Dark Matter Detection

DARK matter searches employ three different interaction methods: direct detection, indirect detection and pair production. Direct detection probes the scattering of a dark matter particle off of a Standard Model particle in a detector. Whilst the dark matter particle invisibly escapes the detector, the properties of the recoiling particle can be used to deduce the nature of the incoming dark matter particle. Indirect detection probes the annihilation of two dark matter particles in the galaxy, which could produce Standard Model particles such as cosmic rays or photons. Gamma-ray radiation produced from the annihilation itself or by the decay of cosmic rays can be measured using gamma-ray telescopes and used to probe the nature of the annihilating dark matter particles. Pair production at colliders probes the production of dark matter particles from high-energy collisions of Standard Model particles. By studying the jets and/or leptons that may also be emitted in the collision, together with the missing energy attributed to dark matter, collider searches can infer the presence of dark matter. Collider searches are complimentary to indirect and direct detection however, as the missing energy cannot be conclusively attributed to dark matter. Since all three interactions are variants of the same Feynman diagram, these can be eloquently summarised by a single diagram, illustrated by Figure 1.7.

This thesis focuses on the scattering of a WIMP particle off of an atomic nucleus. The expected WIMP interaction rates in a detector are discussed in the next section, followed by a summary of the current experimental constraints placed on the WIMP-nucleon cross section as a function of WIMP mass.

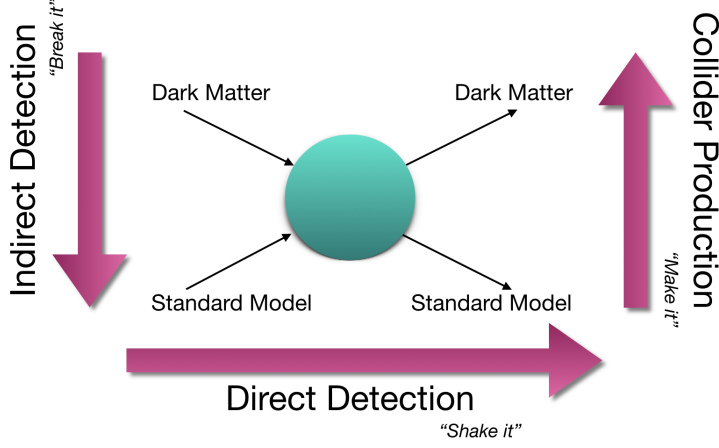


Figure 1.7: Feynman diagram demonstrating all three interaction channels used in experimental dark matter searches: collider production, indirect detection and direct detection. This thesis focuses on the direct detection channel.

1.3.1 Nuclear Scattering

Interaction Rate

ADOPTING the formalism used in [39], the general expression for the differential nuclear recoil rate from WIMP-nucleus scattering can be written as [39],

$$\frac{dR}{dE_R} = N_T \frac{\rho_\chi}{M_\chi} \int_{v_{\min}}^{\infty} v f_{\oplus}(\vec{v}, \vec{v}_e) \frac{d\sigma}{dE_R} d^3v, \quad (1.19)$$

where E_R is the nucleus recoil kinetic energy, N_T is the number of target nuclei, M_χ is the WIMP mass, v is the magnitude of the vector \vec{v} and $f_{\oplus}(\vec{v}, \vec{v}_e)$ is the local dark matter velocity distribution as observed in the detector, or Earth frame. The local dark matter density, ρ_χ , is typically assigned a value of $\rho_\chi = 0.3 \text{ GeV}/\text{cm}^3$ by all direct detection experiments to allow for direct comparisons of dark matter exclusion limits; since $dR/dE_R \propto \rho_\chi$, differences in ρ_χ have a direct effect on the recoil rate and consequently, any excluded cross sections. Currently, there remains significant uncertainty on ρ_χ . As described in [39], two separate studies using different tech-

niques obtained values for ρ_χ of $\rho_\chi = 0.3 \pm 0.1 \text{ GeV/cm}^3$ [40] and $\rho_\chi = 0.43 \pm 0.15 \text{ GeV/cm}^3$ [41].

The velocity distribution is integrated between the minimum velocity the WIMP must have in order to cause a nucleus to recoil with energy E_R and infinity. This minimum velocity, v_{\min} , is defined as [39],

$$\frac{v_{\min}}{c} = \sqrt{\frac{1}{2M_N E_R} \left(\frac{M_N E_R}{\mu_N} + \delta \right)}, \quad (1.20)$$

where M_N is the mass of the nucleus, and μ_N is the WIMP-nucleus reduced mass. The δ term allows for inelastic scattering, by accounting for the mass difference between the incoming and outgoing WIMP. For coherent spin-independent interactions, the WIMP-nucleus differential cross section is given by [39],

$$\frac{d\sigma}{dE_R} = \frac{1}{2v^2} \frac{M_N \sigma_n}{\mu_{ne}^2} \frac{(f_p Z + f_n (A - Z))^2}{f_n^2} F^2(E_R), \quad (1.21)$$

where A and Z are the mass and proton numbers of the target species σ_n is the WIMP-neutron cross section at zero momentum transfer ($q^2 = 0$) and μ_{ne} is the WIMP-nucleon reduced mass. Coherent scattering occurs when the condition,

$$\lambda_{\text{DB}} \propto \frac{1}{p} \geq R_N, \quad (1.22)$$

is satisfied, where λ_{DB} and p are the De Broglie wavelength and momentum of the dark matter particle respectively, and R_N is the radius of the nucleus. As pointed out in [42], direct detection experiments give the strongest constraints on spin-independent interactions, as coherent scattering provides an enhancement that is proportional to the nucleus mass squared.

The parameters f_n and f_p characterise the coupling strength of WIMPs to neutrons and protons respectively. Generally, the assumption is made that $f_n = f_p$, however there exist some isospin-violating models for which $f_n \neq f_p$. In such models

there are small regions of parameter space in which argon targets currently provide the most stringent limits on the WIMP-nucleon cross section over xenon targets, as discussed in [43]. For the purposes of this thesis however, the standard assumption of $f_n = f_p$ is made.

Finally, $F(E_R)$ is the nuclear form factor, which modifies the probability amplitude for a scatter off a point-like target to account for the mass and charge densities of the target nucleus. The form factor describes the suppression of coherence as the momentum transfer squared in the collision increases. $F(E_R)$ can be described by the Helm form factor [44],

$$F^2(E_R) = \left(\frac{3j_1(qR)}{qR} \right)^2 e^{-q^2 s^2}, \quad (1.23)$$

where $j_1(qR)$ is the first order spherical Bessel function, $q = \sqrt{2M_N E_R}$ is the momentum transfer and $R = \sqrt{c^2 + \frac{7}{3}\pi^2 a^2 - 5s^2}$ is the radius of the nucleus. The parameters c, a, s are calculated as $c = 1.23A^{1/3} - 0.6$ fm, $s = 0.9$ fm, $a = 0.52$ fm.

The Standard Halo Model (SHM) is the simplest description of the dark matter distribution, which assumes that dark matter is isotropically distributed within an isothermal sphere with density profile $\rho(r) \propto 1/r^2$. Whilst only the SHM is considered in this thesis, it is important to note that astrophysical data actually favours a more nuanced dark matter distribution than the SHM [45]. In the galactic frame, the dark matter velocity distribution can be modelled with a Maxwell-Boltzmann distribution truncated for velocities greater than the escape velocity [39],

$$f(\vec{v}) = \begin{cases} (1/N)(e^{-v^2/v_0^2} - e^{-v_{\text{esc}}^2/v_0^2}), & v < v_{\text{esc}} \\ 0, & v > v_{\text{esc}}. \end{cases} \quad (1.24)$$

where N is a normalisation parameter and v_0 is the circular speed of the Sun about the galactic centre. The escape velocity has been constrained to $498 \text{ km/s} < v_{\text{esc}} <$

608 km/s by the RAVE survey [46], which quotes the median escape velocity as $v_{\text{esc,med}} = 544$ km/s. As with ρ_χ , the median value is typically used by all experiments for direct comparison of dark matter exclusion limits.

To obtain the dark matter velocity distribution in the Earth frame, as required by Equation 1.19, the dark matter velocity distribution in the galactic frame $f(\vec{v})$ needs to be boosted by the Earth's velocity in the galactic frame \vec{v}_e [39],

$$f_{\oplus}(\vec{v}, \vec{v}_e) = f(\vec{v} + \vec{v}_e), \quad (1.25)$$

where $\vec{v}_e = \vec{v}_0 + \vec{v}_{\otimes} + \vec{v}_{\oplus}$. Here, $\vec{v}_0 = (0, 220, 0)$ km/s is the Sun's circular velocity with respect to the galactic centre, $\vec{v}_{\otimes} = (10.0, 5.25, 7.17)$ km/s is the Sun's peculiar velocity with respect to \vec{v}_0 and \vec{v}_{\oplus} is the Earth's velocity with respect to the rest frame of the Sun.

Combining these factors yields another expression for the recoil rate given in Equation 1.19,

$$\frac{dR}{dE_R} = N_T \frac{\rho_\chi}{M_\chi} \frac{1}{2} \frac{M_N \sigma_n}{\mu_{ne}^2} A^2 F^2(E_R) \zeta(E_R), \quad (1.26)$$

where,

$$\zeta(E_R) = \int_{v_{\min}}^{\infty} \frac{d^3v}{v} f(\vec{v} + \vec{v}_e). \quad (1.27)$$

An analytical expression for $\zeta(E_R)$ can be found in Appendix B of [39]. Equation 1.26, which gives the recoil rate per second, can also be expressed to give the recoil rate per second per kilogram of target mass, by swapping the number of target nuclei N_T with the number density $\eta_T = N_A / (A \cdot 0.001)$ where N_A is Avogadro's number and the factor of 0.001 converts the units of η_T from grams^{-1} to kilograms^{-1} .

Equation 1.26 shows that the recoil rate is proportional to the atomic mass number squared, $dR/dE_R \propto A^2$. Figure 1.8 shows the recoil rate as a function of

recoil energy for four atomic species typically used as targets for direct detection: Silicon (^{28}Si), Argon (^{40}Ar), Germanium (^{72}Ge) and Xenon (^{131}Xe). Since the recoil rate is an exponential distribution, experiments tend to search for WIMPs in lower energy regions before the rate quickly drops off. Energy threshold is therefore one of the key factors in defining an experiment's sensitivity to WIMPs.

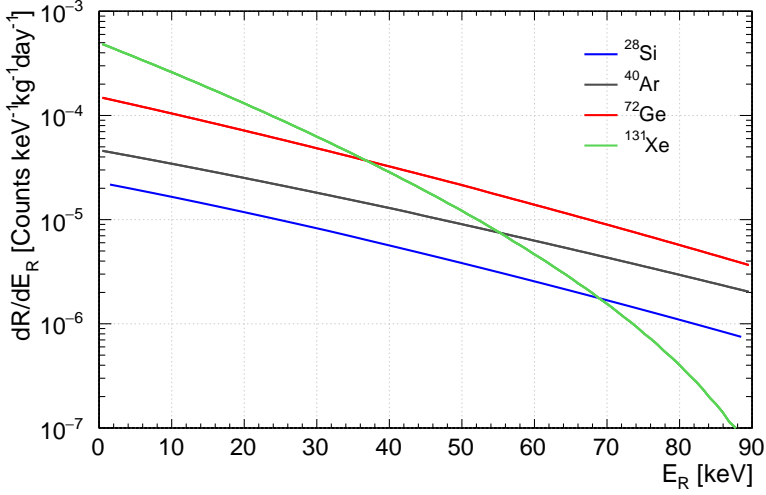


Figure 1.8: Differential nuclear recoil rate as a function of recoil energy for four atomic species: ^{28}Si (blue), ^{40}Ar (grey), ^{72}Ge (red) and ^{131}Xe (green). All four atomic species are commonly used as targets in direct detection experiments. A dark matter mass and cross section of 100 GeV and 10^{-44} cm^2 are assumed.

One of the greatest challenges faced by dark matter experiments is the presence of background particle interactions, due to the low signal rates expected by dark matter interactions. Depending on the experimental signature of the dark matter interaction, some backgrounds can be more detrimental to the search than others. These backgrounds can be split into two categories: ones which induce electronic recoils (ERs), such as γ -rays and β -particles, and ones which induce nuclear recoils (NRs), such as neutrons, or nuclear-like recoils, such as from α -particles emitted in an α -decay. These background sources will be discussed in more detail throughout this thesis.

Experimental Constraints

DIRECT detection searches measure the energy deposited in the detector by the struck target atom in three ways: charge, scintillation and phonons (heat). Depending on the detector design, experiments may use just one or a combination of two of these techniques. The choice of which technique(s) to use is based on the compromise between having the lowest possible energy threshold, the largest exposure and the most powerful background discrimination. Figure 1.9 shows the current experimental constraints placed on the spin-independent WIMP-nucleon cross section as a function of WIMP mass from six different experiments, which use either one or two of these techniques as well as different atomic species as the target medium.

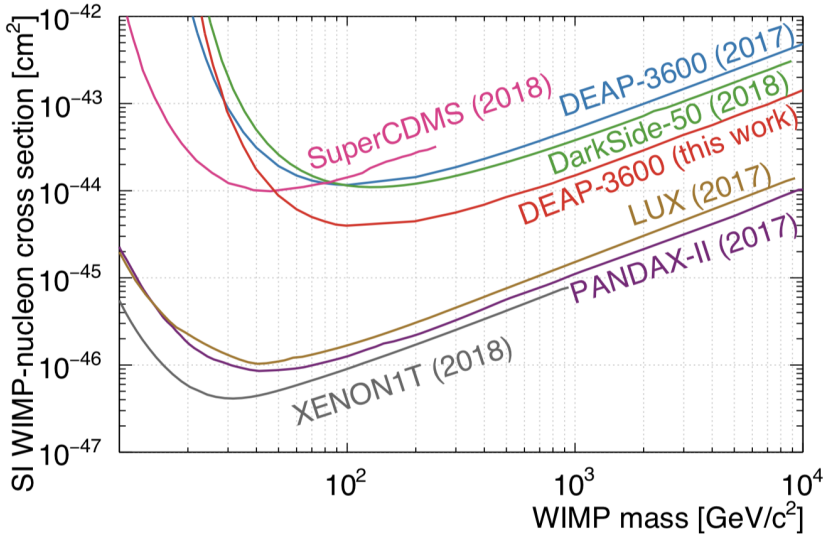


Figure 1.9: Current experimental constraints on the spin-independent WIMP-nucleon cross section [cm^2] as a function of WIMP mass [GeV], taken from the most recent publication from the DEAP-3600 collaboration [4]. Seven recent exclusion limits are shown for six different direct detection experiments. Limits shown are at 90% confidence level.

The pink exclusion curve in Figure 1.9 comes from the SuperCDMS Soudan experiment [47]. The SuperCDMS Soudan detector consists of cylindrical cryogenic

^{72}Ge crystal detectors which measure the phonons and ionisation produced from particle interactions. Each crystal face is composed of grounded phonon sensors interlaced with ionisation electrodes at +2 V and -2 V for the top and bottom faces respectively. This configuration creates a unique electric field that can be used to mitigate backgrounds originating from the detector surfaces. The main discrimination power between ERs and NRs comes from energy partitioning into ionisation versus heat. Currently, the results from the SuperCDMS Soudan experiment from a 1.7 tonne-days exposure dataset sets the strongest limits at 90% confidence level on WIMP-Ge nucleus interactions for WIMP masses $> 12 \text{ GeV}/c^2$ [47]. The next generation of SuperCDMS plans to use larger crystals comprised of both ^{72}Ge and ^{28}Si and two complimentary detector technologies (phonon-only readout, phonon + charge readout), for improved sensitivity to low mass WIMPs [48].

The yellow, purple and grey exclusion curves correspond to the LUX, PandaX-II and Xenon1T experiments respectively, all liquid xenon (LXe) dual-phase time projection chambers (TPCs). Currently, the strongest limit on the spin-independent WIMP-nucleon cross section for WIMPs above $6 \text{ GeV}/c^2$ comes from the Xenon1T 2018 result [49], based on an exposure of 363 tonne-days. The detector consists of a cylinder housing 3.2 tonnes of LXe (2 tonnes of active LXe target) and a gaseous phase (GXe) pocket at the top. Two arrays of photomultiplier tubes (PMTs) reside at the bottom and top of the cylinder in the LXe and GXe phases respectively. Electric fields parallel to the cylindrical axis are applied across the LXe and GXe phases. In this configuration, particle interactions in the active LXe target produce two signals: a prompt scintillation signal (S1) and an ionisation signal (S2) where $t_{S2} > t_{S1}$. The S2 signal originates from ionisation electrons which escape recombination in the LXe, which in the presence of an electric field drift up towards the GXe phase where a scintillation signal proportional to the number of ionisation electrons is produced.

The Xenon1T experiment uses a combination of the S1 and S2 signals to obtain the recoil energy and the ratio $S2/S1$ to discriminate between ERs and NRs. ERs produce more free, ionised electrons than NRs and thus have a larger S2 signal compared to NRs. This can be used to distinguish between interactions with equal S1 signals. Additionally, the anti-correlation between the S1 and S2 signals due to the recombination process, described in Section 2.1.2, can be exploited by searching in S1 vs S2 parameter space. Since free electrons all drift at the same velocity, the time difference between S1 and S2 combined with the pattern of the S2 signal on the top PMT array can be used for three-dimensional position reconstruction; a powerful tool for rejecting backgrounds near the edge of the detector. Dual-phase LXe TPCs continue to be a popular choice for next generation experiments, such as the LZ experiment currently in the construction phase. For a 5600 tonne-day (5.6 fiducial mass tonnes, 1000 live days) exposure, the LZ detector is projected to exclude a spin-independent WIMP-nucleon cross section of $1.4 \times 10^{-48} \text{ cm}^2$ for a 40 GeV/c² WIMP [50].

The remaining three exclusion curves on Figure 1.9 come from two different experiments which both use liquid argon (LAr) as their target medium. The DarkSide-50 experiment is a LAr dual-phase TPC, which operates analogously to the LXe experiments discussed above. The DEAP-3600 experiment is a single-phase LAr detector, which measures only the scintillation light produced in the target LAr from a recoiling particle. Since there is no secondary signal, the DEAP-3600 experiment relies solely on the scintillation properties of LAr for ER/NR discrimination; this technique will be explained in more detail in Section 3.2.2. The DEAP-3600 experiment currently provides the most stringent limits on the spin-independent WIMP-nucleon cross section on an argon target, excluding a spin-independent cross section of $1.3 \times 10^{-45} \text{ cm}^2$ at 100 GeV/c² with a 758 tonne-day exposure dataset [4] indicated by the red exclusion curve. A full description of the DEAP-3600 detector

is given in Chapter 2.

1.4 Statistical Approaches to Limit Setting

THE topic of this thesis is developing a new statistical tool to search for dark matter signals in the DEAP-3600 experiment. To motivate the Profile Likelihood Ratio (PLR) analysis developed in this thesis, this section introduces statistical approaches to limit setting traditionally employed in dark matter searches.

As pointed out in [51], experiments have much to gain from optimising the statistical techniques they use to interpret their experimental data as either an upper limit or a discovery significance. Over the years, as more and more parameter space is excluded, experiments have strived to develop new statistical methods which can enhance dark matter sensitivity whilst competing against issues associated with building larger detectors, such as increasing backgrounds.

1.4.1 Poisson Method

THE Poisson method is the simplest way to set an upper limit on a parameter of interest. Suppose the signal hypothesis is described by a one-dimensional theoretical recoil energy spectrum dN/dE , dependent on some parameter of interest such as the WIMP-nucleon spin-independent cross section, denoted σ . In this context, an “event” in a dataset is defined as a single measurement of the recoil energy. For a given dataset, if all observed events are presumed to be dark matter, the signal hypothesis can be excluded to some desired confidence level (C.L) by adjusting the value of σ to yield the expected number of events μ that satisfies,

$$\alpha = e^{-\mu} \sum_{m=0}^N \frac{\mu^m}{m!}, \quad (1.28)$$

where N is the total number of observed events in the dataset, and μ is calculated by integrating dN/dE over all recoil energies of interest. The C.L is then given by $(1 - \alpha)$. One consequence of using the Poisson method is that in assuming all observed events are signal, the presence of even a small number of background events significantly weakens the upper limit calculated with Equation 1.28. In response, experiments may apply harsher cuts that reduce the signal acceptance to their data to exclude residual events. Either way, the Poisson method can lead to overly conservative upper limits.

1.4.2 Maximum Gap/Patch Method

IF a dataset is contaminated with an unknown source of background, the “Maximum Gap” method as proposed in [52] can be employed to derive a more rigorous upper limit than the Poisson method. For a set of N data points, there exists a vector \vec{x} of dimension $(N - 1)$ containing the "gaps" between the data points, where the gap between two data points E_i and E_{i+1} for a given value of the parameter of interest σ is calculated by integrating over the theoretical spectrum,

$$x_i = \int_{E_i}^{E_{i+1}} \frac{dN}{dE}(\sigma) dE. \quad (1.29)$$

The largest value of x_i corresponds to the largest gap and is called the "maximum gap". For a given value of σ , if there is an excess of predicted events in the maximum gap between two neighbouring events, σ should be rejected as too large a value to be consistent with the observed event distribution in the dataset. If the value of σ were correct, as explained in [52], a random experiment would, on average, always give fewer expected events in its maximum gap. The probability C_0 of the maximum gap size being less than some value of x is described by the cumulative density function (CDF) of the maximum gap [52],

$$C_0(x, \mu) = \sum_{k=0}^m \frac{(kx - \mu)^k e^{-kx}}{k!} \left(1 + \frac{k}{\mu - kx}\right), \quad (1.30)$$

where μ is the total number of events and $m \leq \mu/x$ is the greatest integer. In order to obtain an upper limit on σ at 90% C.L, the value of σ is tuned until the values of μ and x yield $C_0 = 0.9$. Equation 1.30 shows that C_0 is only dependent on μ and x and not the shape of the event distribution, thus the maximum gap explicitly assumes no knowledge of the background distributions. This is a large advantage of using the Maximum Gap method, as one can derive a conservative upper limit that is not badly degraded by the presence of an unknown background, since events in background-populated regions will be too close together for the maximum gap to be found there.

The Maximum Gap technique can also be extended to two dimensions by use of the analogous "Maximum Patch" method [51]. Consider a set of N measurements of recoil energy E and recoil angle ψ (an important parameter for directional dark matter experiments). For N data points, a "patch" in two-dimensional parameter space can be calculated as [51],

$$y_{ijk} = \int_{\cos(\psi)_k}^{\cos(\psi)_j} \int_{E_i}^{E_{i+1}} \frac{d^2 N}{d(\cos(\psi))dE}(\sigma) dE d(\cos(\psi)), \quad (1.31)$$

where i goes from 0 to N and j, k independently go from 1 to N . Further requirements include $\cos(\psi)_j > \cos(\psi)_k$, $E_i < E_j < E_{i+1}$ and $E_i < E_k < E_{i+1}$. Physically, Equation 1.31 represents the two-dimensional areas defined by the boundaries $[E_i, E_{i+1}]$ and $[\cos(\psi)_k, \cos(\psi)_j]$; there is also one additional patch for every i not described by Equation 1.31 that should be included, that has lower and upper angular limits of $[\cos(\psi)_0, \cos(\psi)_{N+1}]$. In this example, ψ is the variable of choice, however this can be any variable. The maximum patch is the largest value of y_{ijk} for the permitted values of i, j and k . A detailed recipe on how exactly to calculate

the maximum patch for a set of two-dimensional measurements can be found in Appendix II of [51]. In order to obtain an upper limit, just like the Maximum Gap method, the probability of the maximum patch size being smaller than some value must be known; this can be obtained by evaluating the CDF of the maximum patch, which can be calculated via the Monte Carlo method as described in [51]. An upper limit at 90% C.L can be placed on σ by adjusting σ until the CDF of the maximum patch is equal to 0.9.

1.4.3 Profile Likelihood Ratio

FOR an experiment where the background distribution is well known, the Profile Likelihood Ratio (PLR) approach is a technique typically favoured as a direct result of Neyman-Pearson's lemma. The lemma states that the most powerful test statistic when performing a test between two hypotheses H_0 , H_1 (null, alternate respectively) on some observed data x which can reject H_1 comes from the ratio of the likelihoods of the alternate hypothesis to the likelihood of the null hypothesis,

$$\lambda = \frac{\mathcal{L}(H_1|x)}{\mathcal{L}(H_0|x)}. \quad (1.32)$$

where λ is known as the likelihood ratio. Similarly to the Maximum Gap method, the upper limit obtained using a PLR approach is not hurt by the presence of background events in the search region so long as the prediction from the background model is consistent with the number of observed events. An experiment can therefore afford to loosen their cuts and enlarge their search region in order to increase signal acceptance, thus improving dark matter sensitivity.

A further advantage of the PLR approach is the ability to include correlations of nuisance parameters in a straightforward manner. Suppose there exists some data, dependent on both a parameter of interest σ and some set of nuisance parameters. One uses the PLR to test how compatible the data are with a hypothesised value

of σ . The nuisance parameters, denoted $\{\theta\}$, typically represent a given set of systematic uncertainties, the values of which are of no real interest. The more sources of systematic uncertainties there are, the weaker the upper limit on σ an experiment can place; thus, it is imperative for experiments to eliminate or reduce as many sources of systematic uncertainty, and hence nuisance parameters, as possible.

The PLR approach involves defining a likelihood function, generally comprised as a product of multiple probability density functions dependent on either both σ and $\{\theta\}$, or just $\{\theta\}$,

$$\mathcal{L}(\sigma, \{\theta\}|x) = f(x|\sigma, \{\theta\}), \quad (1.33)$$

where x denotes an independent, observed dataset. The likelihood function, $\mathcal{L}(\sigma, \{\theta\})$, can be defined as a function of $\{1, 2, \dots, N\}$ dimensions; this gives the PLR approach an advantage over the Maximum Patch method in the case where there are N measurements of > 2 variables. $\mathcal{L}(\sigma, \{\theta\})$, can be maximised in two ways:

- Conditionally, by maximising $\mathcal{L}(\sigma, \{\theta\})$ for a fixed σ value, or,
- Unconditionally, by maximising $\mathcal{L}(\sigma, \{\theta\})$ for a free σ value.

This provides two maximum likelihood estimators (MLEs) of $\mathcal{L}(\sigma, \{\theta\})$. The PLR, denoted λ , is defined as the ratio of the conditional MLE to the unconditional MLE,

$$\lambda = \frac{\mathcal{L}(\sigma, \{\hat{\hat{\theta}}\})}{\mathcal{L}(\hat{\sigma}, \{\hat{\theta}\})}, \quad (1.34)$$

where the double hat notation of $\{\theta\}$ denotes that the values of the nuisance parameters are the MLEs when σ is fixed at the test value, and the single hat notation of $\sigma, \{\theta\}$ denotes that the values of the nuisance parameters are the MLEs when σ is free and allowed to converge at its MLE $\hat{\sigma}$. The ratio λ spans the range $0 \leq \lambda \leq 1$, where values closer to 1 correspond to very good agreement between the data and

the test hypothesis, σ . Since one aims to present a result that depends only on the parameter of interest, σ , it is necessary to exclude the nuisance parameters. In Profile Likelihood analyses, this is referred to as “profiling-out” the systematic uncertainties, and is accounted for in the above definition of λ .

This technique can be used to either produce a sensitivity limit in rejection of a signal hypothesis (exclusion), or to calculate a significance for discovery in rejection of a background-only hypothesis (discovery); the definition of the test statistic thus depends on whether an exclusion or a discovery is being calculated. For an exclusion curve (upper limit), only cases where the MLE of σ , $\hat{\sigma}$, is smaller than the test σ are considered. The definition of the test statistic, q , is as follows:

$$q = \begin{cases} -2 \ln(\lambda), & \hat{\sigma} \leq \sigma \\ 0, & \hat{\sigma} > \sigma \end{cases} \quad (1.35)$$

By definition, $q \geq 0$; this is a direct consequence of the definition of λ . A q value of 0 corresponds to an outcome most compatible with the signal hypothesis, where the MLE of σ is equal to the test σ ($\hat{\sigma} = \sigma$). As q increases, $\hat{\sigma}$ and σ begin to diverge; this corresponds to the data becoming less and less compatible with the signal hypothesis. Testing the observed data under the signal hypothesis H_σ yields the observed q -value, q_{obs} . This is used to construct the signal p -value p_s ,

$$p_s = \int_{q_{\text{obs}}}^{\infty} f(q|H_\sigma) dq, \quad (1.36)$$

where $f(q|H_\sigma)$ is the probability distribution of the test statistic q under the signal hypothesis H_σ ; p_s yields the probability that the q -value of a random experiment will be larger than q_{obs} under the signal hypothesis H_σ . If $p_s \leq 10\%$, H_σ is rejected at 90% C.L.

In the case of a discovery, the test statistic q_0 is instead defined as,

$$q_0 = \begin{cases} -2 \ln(\lambda(0)), & \hat{\sigma} \geq 0 \\ 0, & \hat{\sigma} < 0 \end{cases} \quad (1.37)$$

where $\lambda(0) = \mathcal{L}(\sigma = 0, \{\hat{\theta}\})/\mathcal{L}(\hat{\sigma}, \{\hat{\theta}\})$. Larger values of the test statistic q_0 correspond to less compatibility between the data and the background-only hypothesis, H_0 . The discovery p -value p_0 is calculated as,

$$p_0 = \int_{q_{\text{obs},0}}^{\infty} f(q_0|H_0) dq_0, \quad (1.38)$$

where $f(q_0|H_0)$ is the probability distribution of the discovery test statistic q_0 under the background-only hypothesis H_0 . As discussed in [53], Wilks' theorem states that q_0 follows a chi-square distribution under H_0 , and the discovery significance ($Z\sigma$) is given by $Z = \sqrt{q_{\text{obs},0}}$.

Figure 1.10 shows a comparison of the exclusion curves (excluded median cross section σ_{med} as a function of WIMP mass) produced by the three different statistical methods (Poisson, Maximum Gap and PLR) on a fake dataset consisting of 1 expected one signal (WIMP) event and 10 expected background events in a simulated directional dark matter detector [54]. The variables considered are the recoil energy and recoil angle, (E, ψ) . The detector is assumed to have full three-dimensional event position reconstruction, including perfect angular resolution. In total there are 9 curves; 1 curve per method, assuming 3 different detector energy thresholds. Figure 1.10 shows that for all 3 thresholds, the PLR method yields the most sensitive limit across the full mass range considered $\sim 10 - 10^3 \text{ GeV}/c^2$ whilst the Poisson limit yields the weakest limit across the full mass range. The PLR method is applied to data from the DEAP-3600 detector in Chapter 6.

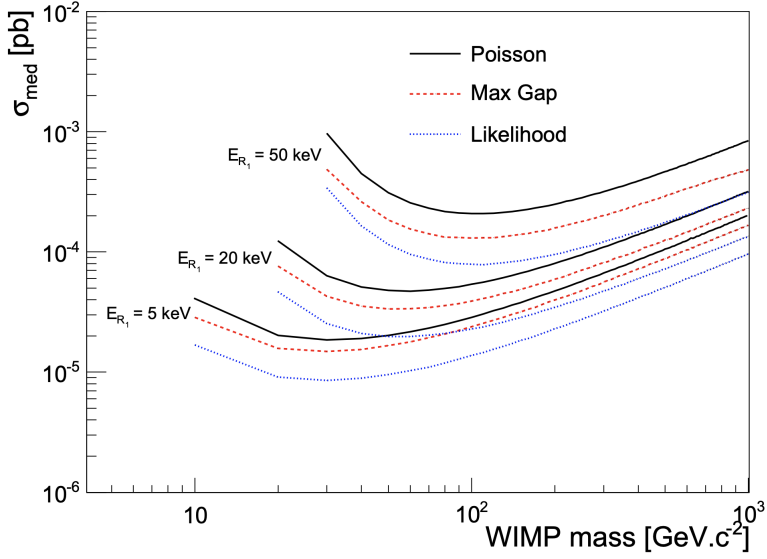


Figure 1.10: Comparison of the excluded median cross section (σ_{med}) as a function of WIMP mass produced by the three methods (Poisson, Maximum Gap and Profile Likelihood Ratio) for a simulated directional dark matter detector, on a fake dataset consisting of 1 expected signal (WIMP) event and 10 expected background events [54]. The variables considered are the recoil energy and recoil angle, (E, ψ) . The detector is assumed to have full three-dimensional event position reconstruction, including perfect angular resolution. An exclusion curve calculated from each of the 3 methods is drawn for 3 different detector energy thresholds.

Chapter 2

The DEAP-3600 Experiment

*“An experiment is a question which science poses to Nature and
a measurement is the recording of Nature’s answer.”*

–Max Planck

THE DEAP-3600 experiment is located 2 km underground in the SNOLAB laboratory in Sudbury, Ontario, Canada. DEAP-3600 is a single-phase liquid argon dark matter direct detection experiment built to observe WIMP-induced argon nuclei recoils and is the focus of this chapter. Section 2.1 begins with a general introduction to liquid noble gases as target materials for dark matter direct detection followed by a discussion on liquid argon scintillation physics. The remaining sections together provide a comprehensive overview of the DEAP-3600 detector, focusing on the detector components, the radioactive backgrounds associated with these components, and the detector read out and slow control systems.

2.1 Liquid Noble Gases as Targets

2.1.1 General Properties

LIQUID noble gases possess many properties that make them desirable target materials for dark matter direct detection. A summary of these properties for three different liquid noble gases typically used experimentally from [55] is displayed in Table 2.1.

Table 2.1: A summary of relevant properties of three liquid noble gases (Xenon, Argon and Neon) typically used as target materials in dark matter direct detection experiments. W_{ph} and $W_{\text{e-ion}}$ are the mean energies required to create a scintillation photon and an electron-ion pair respectively. Information is provided from [55].

| Element | ¹³¹ Xe | ⁴⁰ Ar | ²⁰ Ne |
|--|-------------------|------------------|------------------|
| Boiling Point, T_b [K] | 165.0 | 87.3 | 27.1 |
| Liquid Density at T_b [g/cm ³] | 2.94 | 1.40 | 1.21 |
| Fraction in Earth's atmosphere [ppm] | 0.09 | 9340 | 18.2 |
| Scintillation? | Yes | Yes | Yes |
| W_{ph} (α/β) [eV] | 17.9/21.6 | 27.1/24.4 | - |
| Scintillation Wavelength, λ [nm] | 178 | 128 | 78 |
| Ionization? | Yes | Yes | - |
| $W_{\text{e-ion}}$ [eV] | 15.6 | 23.6 | - |

Energy threshold, exposure, and background discrimination are the three key factors that drive an experiment's sensitivity. Since sensitivity scales proportionally with exposure, next generation experiments always strive to build larger detectors that can be operated for longer durations. One of the most important advantages with using liquid noble gases in larger detectors is their high scintillation yield; especially useful for rare, low energy signal searches. Liquid xenon (LXe) and liquid argon (LAr) are popular targets for dark matter direct detection since they also have sensitivity to the ionisation signal induced by incident particles, which can be used in conjunction with the scintillation signal for improved background discrimination. This is explained in Section 1.3.1.

Another advantage of liquid noble gases is that they have low boiling points,

ranging from 27.1 K (Ne) to 165 K (Xe) from Table 2.1. This makes building and operating multi-tonne liquid noble gas detectors more feasible than Germanium cryogenic detectors, which typically need to be operated at temperatures in the mK range. Low boiling points also allow for relatively easy purification with respect to removing radioactive species dissolved in the target.

The combination of its large atomic mass number A and high light yield makes LXe a common choice for dark matter searches. LXe targets are especially popular for WIMP searches due to the fact that the recoil rate is proportional to A^2 as described by Equation 1.26; this translates to ~ 6 times more expected WIMP recoils in Xe than in Ar for a given WIMP mass, cross section and exposure, integrating over the recoil energy spectrum. LXe is extremely radiopure, however there are still backgrounds present in LXe; the main isotopically similar background found dissolved in LXe targets, due to the similarity of the boiling points, is Krypton. For optimum performance, LXe should be used in dual-phase technology over single-phase, as powerful electronic recoil (ER)/ nuclear recoil (NR) discrimination cannot be easily achieved using only the properties of LXe scintillation; the physics of liquid noble gas scintillation is described in detail in Section 2.1.2.

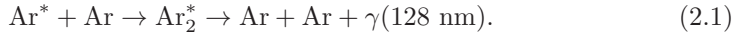
LAr is one of the least costly liquid noble gases given its vast natural abundance, given in Table 2.1. Financially, this makes LAr detectors more scalable. One unfortunate drawback of LAr as a target medium is the presence of a trace amount of ^{39}Ar , a long-lived isotope with half-life $t_{1/2} = 268$ years [56], produced by atmospheric cosmic-ray neutron interactions. ^{39}Ar decays via β^- emission at a specific activity of 1.00 ± 0.02 (stat) ± 0.08 (syst) Bq/kg [57]. This corresponds to a rate of ~ 3300 ER events per second in DEAP-3600, 4% of which populate the WIMP dark matter energy region-of-interest. Fortunately, the majority of this background source can be easily mitigated using LAr scintillation properties. For dark matter searches that produce an ER signal however, this background source becomes much

more problematic.

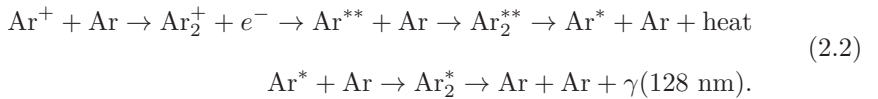
2.1.2 Scintillation in Liquid Argon

Photon Production

WHEN a particle recoils through LAr, it loses energy by exciting and/or ionising argon atoms, creating excitons Ar^* and/or ions Ar^+ respectively. These can interact with nearby argon atoms to form excited argon molecules called excimers, Ar_2^* . Excimers can be created through two different channels, direct excitation or recombination, depending on whether an exciton Ar^* or an ion Ar^+ initiated the scintillation process; both channels are illustrated in Figure 2.1. Excitons interact with the neighbouring argon atoms to directly produce excimers, which emit scintillation photons as they radiatively decay,



Ions, on the other hand, interact with neighbouring argon atoms to first produce ionised molecules, Ar_2^+ , which recombine with free ionised electrons to produce highly excited argon atoms Ar^{**} . Highly excited argon atoms and neutral argon atoms can combine to produce highly excited molecules Ar_2^{**} , which de-excite to an exciton and an argon atom by emitting heat,



Free excitons then interact with argon atoms to form excimers that radiatively decay to produce scintillation light; the same process as described in Equation 2.1.

Scintillation photons are produced in the vacuum ultra-violet (VUV) region of the electromagnetic spectrum, peaked at a wavelength of 128 nm. LAr is transparent

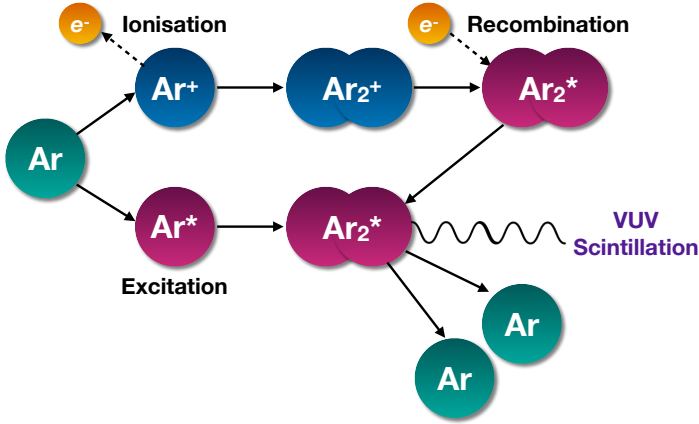


Figure 2.1: Diagram of the LAr scintillation mechanism. Scintillation light can be produced either through direct excitation (bottom) or recombination (top).

to its own scintillation light; a photon wavelength of 128 nm corresponds to an energy less than the energy transition between the ground state and first excited state of atomic argon ($E_T \sim 12$ eV [58]), thus scintillation photons can traverse LAr without being absorbed. Near-infrared scintillation photons can also be produced in LAr, with an intensity ratio of $\sim 10\%$ of VUV scintillation photons.

Excimers can either be formed in one of two low excited singlet (total spin = 1) states, $^1\Sigma_+^u$ and $^1\Sigma_-^u$, or a low excited triplet (total spin = 0) state, $^3\Sigma_+^u$, before decaying to their ground state. The Σ notation used here to represent these atomic quantum states represents the summation of the quantum numbers from the individual electrons. Light is only produced when the $^1\Sigma_+^u$ singlet and $^3\Sigma_+^u$ triplet states transition to their ground states. In LAr, the lifetimes of the $^1\Sigma_+^u$ singlet and $^3\Sigma_+^u$ states are extremely well separated, by approximately 3 orders of magnitude. Since the direct transition $^1\Sigma_+^u \rightarrow ^1\Sigma_+^g$ for the singlet state is allowed,

the lifetime of the singlet state is short, $\tau_s = 7.0 \pm 1.0$ ns [59]. The direct transition $^3\Sigma_+^u \rightarrow ^3\Sigma_+^g$ for the triplet state is forbidden by the selection rules which dictate electronic energy transitions; the decay is only made possible through the mixing of $^3\Sigma_+^u$ and $^1\Pi^u$ states via spin-orbit coupling [60]. This process makes the lifetime of the triplet state significantly longer than τ_s , measured to be $\tau_t = 1.6 \pm 0.1$ μ s [59].

The relative abundances of singlet and triplet states produced in a particle interaction are determined by the linear energy transfer (LET), analogous to the energy loss per unit distance, dE/dx . LET characterises the energy loss per unit distance that a particle locally deposits in the material it is traversing, and is generally less than dE/dx as some energy can be transferred away by high energy particles and/or photons [61]. Neutron-induced NRs and α -particles for example, have a much higher LET than ERs (such as from β/γ particles), producing a greater ionisation track density; as such, higher LET particle tracks have a larger recombination probability than lower LET tracks. The singlet state abundance, enhanced by the recombination process described by Equation 2.2, is therefore larger in NRs compared to ERs.

Since τ_s is very short, the scintillation time profile describing the number of scintillation photons produced as a function of time along the recoil track, is dominated by the fast component for NRs. The scintillation time profile for ERs on the other hand, comprised mainly of triplet states, is dominated by the slow component; this is illustrated later by Figure 3.4. By measuring the fraction of promptly arriving photons (originating from the singlet state) to the total number of scintillation photons and using the well separated lifetimes of the singlet and triplet states, ER and NR events can be easily distinguished. This is a technique called Pulse-Shape Discrimination (PSD), and is used in DEAP-3600 for effective ER background removal. The implementation of PSD in DEAP-3600 is described in Section 3.2.2.

Nuclear Quenching

NUCLEAR recoils are subject to a phenomena known as nuclear quenching; for particle interactions of the same total energy, interactions with a higher LET produce less photons than interactions with a lower LET. Nuclear quenching suppresses the excimer production rate, and thus NRs exhibit a reduced light yield compared to ERs. Nuclear quenching is well described by the Lindhard theory [62], which calculates the relative fractions of energy deposited in the form of ionisations and excitations, which produce scintillation, and atomic motion, which produce heat. The energy-dependent NR quenching factor $q_n(E_{\text{nr}})$, otherwise known as the NR scintillation efficiency, relates the NR energy E_{nr} to the electron-equivalent recoil energy E_{ee} by,

$$E_{\text{ee}} [\text{keV}_{\text{ee}}] = q_n(E_{\text{nr}}) \times E_{\text{nr}} [\text{keV}_{\text{nr}}]. \quad (2.3)$$

The mean value of $q_n(E_{\text{nr}})$ in DEAP-3600, translated from measurements from the SCENE detector [63], is shown as a function of E_{nr} in Figure 2.2, drawn with the $\pm 1\sigma$ error bands. SCENE determines the quenching factor by considering the recombination loss from ERs from a Krypton-83 (^{83}Kr) calibration source, and measuring the ratio of the light yield measured by a fixed energy NR peak to the light yield measured by ^{83}Kr . The uncertainty bands are driven by potential differences in the recombination loss for NRs relative to ERs between DEAP-3600 and SCENE, due to factors such as LAr purity and/or temperature. The uncertainty on $q_n(E_{\text{nr}})$ is a large systematic on the WIMP search; an increase of 1σ in $q_n(E_{\text{nr}})$ in an electron-equivalent energy range of $15 < E_{\text{ee}} [\text{keV}_{\text{ee}}] < 30$, used as the nominal WIMP energy search region in DEAP-3600 (described in Section 2.2.1), increases the predicted WIMP-induced recoil rate in this energy range by $\sim 15\%$.

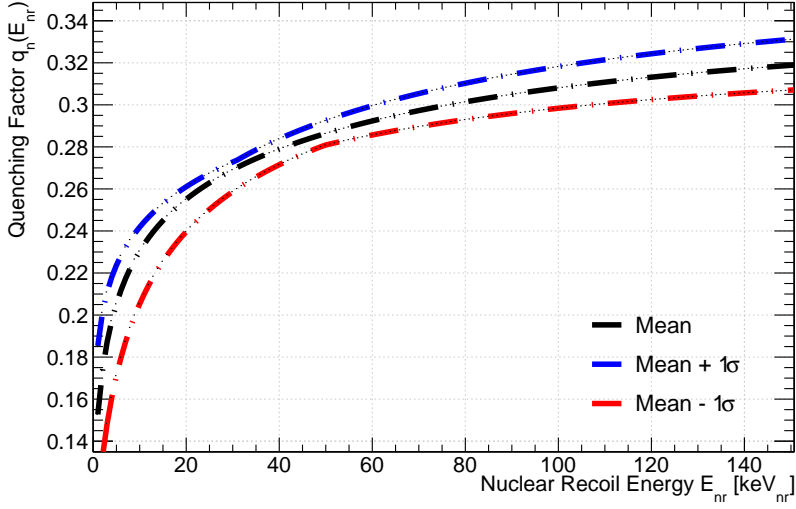


Figure 2.2: Mean NR quenching factor $q_n(E_{nr})$ in DEAP-3600 as a function of NR energy E_{nr} , together with the $\pm 1\sigma$ error bands. The ratio of the light yield measured by a fixed energy NR peak to the light yield measured by a ^{83}Kr ER calibration source is measured by the SCENE detector [63] and interpreted into DEAP-3600 detector data in order to derive these curves.

Light Yield Energy-Dependence

LIGHT yield is defined as the number of photons produced per unit of deposited energy, E . In order to calculate the light yield in LAr, the average energy required to produce one photon W_{ph} is required. This is determined by,

$$W_{ph} = \frac{W_{e-ion}}{1 + N_{ex}/N_{e-ion}}, \quad (2.4)$$

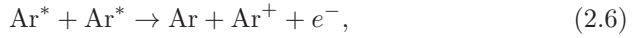
where N_{ex}/N_{e-ion} is the ratio of excitations to ionisations, measured to be $N_{ex}/N_{e-ion} \simeq 0.21$ for ERs [64] and 0.19 for NRs assuming a NR quenching factor of 0.25 [65]. As discussed in [66], the LAr scintillation response is non-linear in the presence of an electric field; an important effect in dual-phase time projection chambers discussed in Section 1.3.1. The ratio N_{ex}/N_{e-ion} is also highly dependent on the incident particle energy. Using $N_{ex}/N_{e-ion} = 0.21$ and the average energy to create an

electron-hole pair from Table 2.1 as $W_{\text{e-ion}} = 23.6$ eV, W_{ph} is calculated to be,

$$W_{\text{ph}} = 19.5 \text{ eV.} \quad (2.5)$$

Theoretically, this corresponds to a light yield of ~ 51 photons/keV of deposited energy in LAr. Experimentally however, there are a number of processes that lead to a reduced photon yield. These include:

- *Biexcitonic quenching*: this takes place in the high LET regime, where the probability of two excitons colliding is high. Biexcitonic quenching occurs via,



where the outgoing ion and electron recombine. This results in the emission of only one photon rather than two.

- *Electron escape*: this takes place in the low LET regime. When an ionised electron becomes thermalised past some critical radius r_c , it will not recombine with its parent ion; the Onsager model describes the probability for an electron to avoid recombination given its distance r from the ion as $\phi(r) = \exp(-r_c/r)$ [67]. As such, no photon is produced from the recombination process.
- *Impurity effects*: if there are impurities present, it is possible for an excimer to collide with an impurity, transferring its excitation energy as kinetic energy in the process and preventing it from radiatively decaying to produce a photon. Impurities have the most severe effect on the triplet state scintillation component; the presence of nitrogen at the ~ 1 ppm level can result in a 20% reduction of the photon yield in LAr [68]. Impurities can also lead to charge carrier trapping, whereby an ionised electron attaches to an electronegative impurity, such as oxygen. This prevents the recombination of the electron

with an argon ion.

Photon Transport

THE dominant optical process that governs photon propagation through LAr is Rayleigh scattering, in which photons elastically scatter off particles that are smaller than the photon wavelength λ inside a medium [69]. For solids and liquids, the Rayleigh scattering process can be described by the following equation,

$$l^{-1} = \frac{16\pi^3}{6\lambda^4} \left[kT\kappa_T \left(\frac{(n^2(\lambda) - 1)(n^2(\lambda) + 2)}{3} \right)^2 \right], \quad (2.7)$$

where l is the Rayleigh scattering length, $n(\lambda)$ is the wavelength-dependent refractive index of the medium, T is the temperature of the medium and κ_T is the isothermal compressibility, dependent on both the temperature and pressure of the medium [69]. Equation 2.7 illustrates that the length a photon travels before undergoing Rayleigh scattering is strongly dependent on the photon wavelength ($\propto \lambda^4$).

The refractive index $n(\lambda)$ is related to the wavelength λ using the Sellmeier dispersion equation, which can be written as [69],

$$n^2(\lambda) = a_0 + \sum_i \frac{a_i \lambda^2}{\lambda^2 - \lambda_i^2}, \quad (2.8)$$

where a_0 , a_i are Sellmeier coefficients. Each term in the sum corresponds to a separate absorption resonance, occurring at wavelength λ_i . The wavelength for VUV scintillation in LAr, $\lambda = 128$ nm, resides between the UV and IR (infrared) resonances, and thus Equation 2.8 can be modified to determine the value of $n(\lambda)$ for VUV scintillation,

$$n^2(\lambda) = a_0 + \frac{a_{\text{UV}} \lambda^2}{\lambda^2 - \lambda_{\text{UV}}^2} + \frac{a_{\text{IR}} \lambda^2}{\lambda^2 - \lambda_{\text{IR}}^2}, \quad (2.9)$$

where λ_{UV} , λ_{IR} are the wavelengths of the closest (if not first) UV/ IR resonances

respectively [69]. This equation is fit to measurements of the refractive index in LAr as a function of wavelength obtained by Sinnock and Smith [70] and the DUNE collaboration [71] in order to determine the values of the Sellmeier coefficients and the corresponding covariance matrix between the Sellmeier coefficients.

Another important optical parameter in describing photon propagation is the photon group velocity in LAr, v_g , dependent on both the wavelength λ and refractive index $n(\lambda)$ via the following relationship [72],

$$v_g = \frac{c}{n(\lambda) - \lambda_0 \frac{dn(\lambda)}{d\lambda_0}}, \quad (2.10)$$

where c is the speed of light, λ_0 is the vacuum wavelength and $dn(\lambda)/d\lambda_0$ is differential refractive index. The covariance between the Sellmeier coefficients defined in Equation 2.8 introduces a correlation between the refractive index, group velocity and Rayleigh scattering length, since the group velocity and Rayleigh length are both dependent on the refractive index. From the covariance matrix, the uncertainties on the three separate optical parameters can be determined. The nominal refractive index is determined directly from the measurement at 128 nm performed by the DUNE collaboration [71] at the temperature of LAr (87 K), $n(\lambda) = 1.369$. Using the Sellmeier coefficients, the group velocity and Rayleigh scattering length at $\lambda = 128$ nm at the temperature of LAr (87 K) are calculated to be $v_g = 13.31$ cm/ns and $l = 0.9357$ m.

2.2 Detector Design

A cross-sectional schematic of the DEAP-3600 detector is shown in Figure 2.3. At the heart of the detector is 3279 kg of LAr volume contained in a spherical acrylic vessel of radius 85 cm. On the inner surface resides a thin layer of Tetraphenyl Butadiene wavelength shifter (TPB), used to shift VUV scintillation light produced

in the LAr to the visible part of the electromagnetic spectrum. Visible light can be detected by any of the 255 inward facing photomultiplier tubes (PMTs) surrounding the LAr volume, each optically coupled to a 45 cm long acrylic light guide attached to the acrylic vessel. Interspersed between the light guides are filler blocks. The inner detector is enclosed inside a steel shell and immersed in a large water tank. Attached to the steel shell are 48 outward facing PMTs, used with the water tank as a muon veto.

This section opens with a discussion on the radioactive background model goals for the DEAP-3600 detector design in Section 2.2.1. Descriptions of the inner and outer detector components are given in Sections 2.2.2 and 2.2.3 respectively. In Section 2.2.4, the cryogenic system is described. This is followed by a discussion on the detector electronics in Section 2.3, and the calibration systems in Section 2.4.

2.2.1 Radioactivity Background Budget

EXTREME care was taken during the design, production and construction of the DEAP-3600 detector to minimise all background sources detrimental to the WIMP search. These include, in order of most concern:

- Neutrons (radiogenic and cosmogenic),
- α -decays, and
- β -particles/ γ -rays.

Table 2.2 provides a summary of the targeted goals of this background model, assuming a 3 year duration, 1000 kg fiducial volume and a nominal WIMP energy “region-of-interest” (ROI) of $15 < E_{ee} [\text{keV}_{ee}] < 30$ in electron-equivalent recoil energy. The fiducial volume is defined as an inner volume of LAr target, constructed specifically to exclude backgrounds originating from the surface of the detector; assuming spherical geometry, a fiducial volume of 1000 kg in DEAP-3600 corresponds

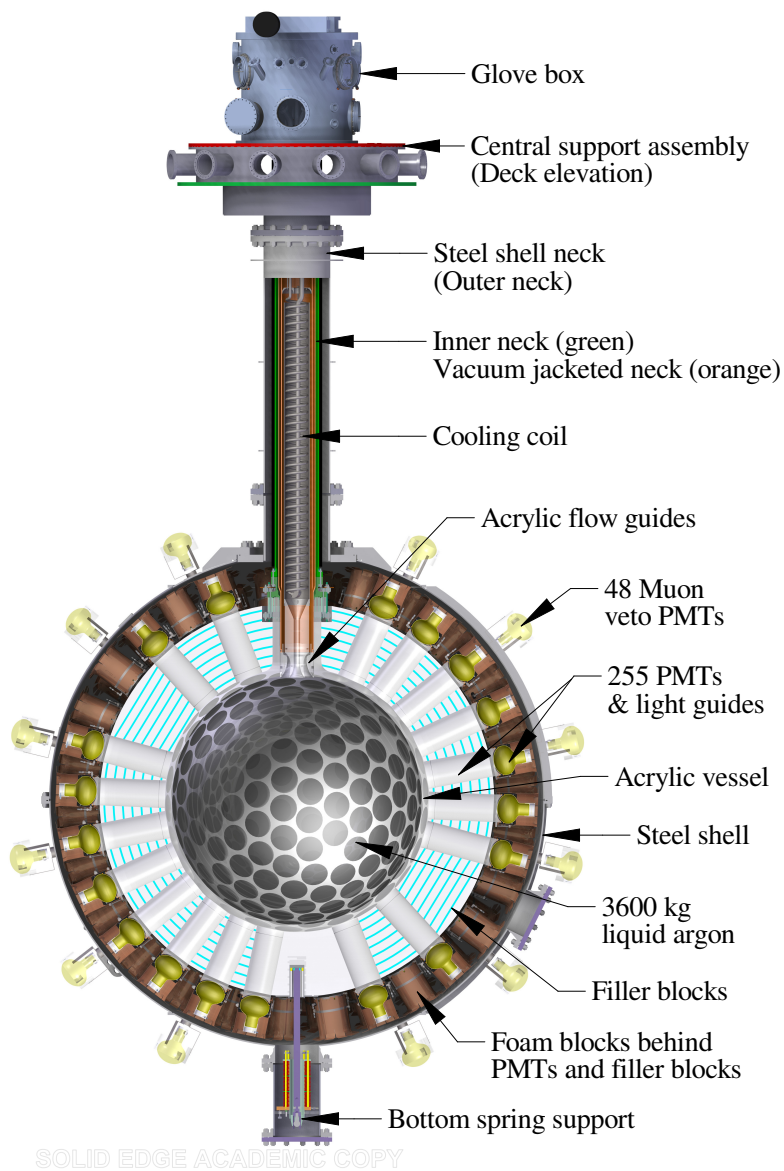


Figure 2.3: Cross-sectional schematic of the DEAP-3600 detector, with various inner and outer detector components labelled. The muon veto water tank in which the inner detector sits is not shown in this diagram.

to a radial cut of < 55 cm. The bounds of the energy ROI are defined by the ability of PSD to discriminate against the ER background dominated by ^{39}Ar β -decay.

Table 2.2: Number of target background events in an energy ROI of $15 < E_{ee} [\text{keV}_{ee}] < 30$ for a 3 tonne-year fiducial exposure. Taken from [73].

| Background | Evts in Energy ROI | Fiducial Evts in Energy ROI |
|------------------------------------|--------------------|-----------------------------|
| Neutrons | 30 | < 0.2 |
| α -decays (Surface) | 150 | < 0.2 |
| β -particles/ γ -rays | 16×10^9 | < 0.2 |
| Summed Total | | < 0.6 |

A brief overview of these background sources and the steps taken to mitigate them through design, production, construction and analysis efforts are discussed below; a more comprehensive overview of the current DEAP-3600 background model is given in Chapter 4.

Neutrons

NEUTRONS are a particularly problematic source of background since their signal can mimic a WIMP event. Neutrons are large and electrically neutral particles that can elastically scatter off of nuclei; the cross section for neutron neutral current elastic scattering, producing a nuclear recoil in the relevant recoil energy range for the WIMP dark matter search, is $\sim 1 \times 10^{-24} \text{ cm}^2$.

Radiogenic neutrons can be produced internally in the detector materials via (α, n) reactions or spontaneous fission from naturally-occurring Uranium-238 (^{238}U) and Thorium-232 (^{232}Th) contamination. The largest neutron source comes from the borosilicate PMT glass from the ^{238}U chain. However, PMT neutrons are effectively blocked by the high-density polyethylene filler blocks and acrylic light guides. Neutrons from other detector materials, such as the acrylic vessel and TPB, are mitigated by design in choosing extremely radiopure materials.

Cosmogenic neutrons are produced from cosmic ray interactions and are most effectively moderated by the location of the detector, 2 km underground. Earth's

rock provides an excellent shield to cosmic rays, reducing the cosmic ray muon flux from approximately 15×10^6 muons $\text{m}^{-2}\text{day}^{-1}$ at sea level to 0.27 muons $\text{m}^{-2}\text{day}^{-1}$ [73]. Surviving cosmic ray muons (and the cosmogenic neutrons they produce) are moderated with the water tank and veto PMTs, described in Section 2.2.3.

α -decays

RADON contamination and its decay progeny in the acrylic vessel and TPB are the leading sources of α -decay backgrounds considered in this background model. Radon gas emerges through the ^{238}U and ^{232}Th decay chains, in the form of Radon-222 (^{222}Rn) and Radon-220 (^{220}Rn) respectively. This means radon is not only present in the air, and able to settle on materials exposed to air, but it can also emanate from materials contaminated with ^{238}U or ^{232}Th . Since ^{222}Rn and ^{220}Rn decay by high-energy α -emission, there are three potential locations of α -decay background: from within the bulk of the detector materials, from the surfaces of materials and from the internal LAr target. Further details on these various sources of origin are provided in Section 4.2.2.

For internal LAr α -backgrounds arising from radon emanation, a dedicated argon purification system explained in Section 2.2.4 was built. Bulk α -backgrounds are mitigated by choosing radiopure detector materials. Exposure to air was strictly controlled during both production and construction in the lab in an effort to minimise surface α -backgrounds from radon deposition. Additionally, a (500 ± 50) μm [73] layer of acrylic from the inside of the acrylic vessel was sanded off with a resurfacer robot. Prior to resurfacing, the calculated radon progeny buildup from the total radon exposure of the acrylic vessel, considering the exposure history and concentration measurements at each of the construction and annealing phases, would have led to a Lead-210 (^{210}Pb) surface background activity of 14 mBq/kg in the acrylic vessel surface [73]. After sanding, the surface background activity is reduced

to $\sim 4\%$ of this activity, consistent with the assay upper limit of 0.62 mBq/kg [73].

Surface α -backgrounds can also be rejected in software using position reconstruction algorithms. Fiducialisation is extremely efficient for acrylic vessel surface α -backgrounds, which all reconstruct very close to or at the acrylic vessel surface; from Monte Carlo simulations, it is estimated that only $\sim 10^{-4}\%$ of surface backgrounds survive a reconstructed radial cut of < 55 cm. Fiducialisation is unfortunately not an effective tool for removing α -backgrounds from the surfaces of the flow guides in the neck, from here on referred to as neck α -decay backgrounds.

Located at the top of the acrylic vessel are four, 2-inch PMTs; events where any of these PMTs detect light are removed in an attempt to exclude background events from inside the neck. However, neck α -decay backgrounds are not always removed by the neck veto PMTs and thus become more problematic as they are not easily removed by fiducialisation. This is because the DEAP-3600 position reconstruction algorithms are developed assuming perfectly spherical geometry, and thus neck α -decay backgrounds can still reconstruct inside the fiducial volume. Understanding the topology of neck α -decay backgrounds was one of the largest challenges faced by the DEAP-3600 experiment, and will be discussed in detail in Chapter 4.

β/γ particles

IN DEAP-3600, the most numerous background comes from intrinsic ^{39}Ar β -decay from within the target LAr volume, introduced earlier in Section 2.1. Over the course of the projected 3 tonne-year exposure of the experiment, ^{39}Ar β -decays produce in total $\sim 1.25 \times 10^{11}$ ER events, approximately 3.75×10^9 of which fall into the WIMP energy ROI ($15 < E_{\text{ee}} [\text{keV}_{\text{ee}}] < 30$). Fortunately, the majority of ^{39}Ar β -decays can be removed with the use of PSD, a technique that has been shown to be very powerful in LAr; the initial projected discrimination power of PSD was found to be $\sim 10^{-10}$ in DEAP-3600 [74],[75]. This corresponds to only 0.4 ER

events from ^{39}Ar residing in the ROI after applying the PSD technique.

Additional radioactivity in the LAr target and external detector components can also induce ER signals through both β -particle and γ -ray interactions. The dominant contribution comes from neutron-capture (n,γ) reactions, where radiogenic neutrons created through (α,n) reactions in the borosilicate PMT glass are captured in the neighbouring detector materials, emitting γ -rays in the process. Since a great amount of care was taken to mitigate neutron backgrounds, the contribution from γ -rays is incidentally reduced. Additionally, the majority of external γ -rays will not make it into the LAr, thus are unlikely to produce a signal. High-energy γ -rays that do reach the LAr, like ^{39}Ar β -decays, can produce an ER signal, which can once again be effectively mitigated using PSD. Further details on the different sources of β -particle and γ -ray backgrounds in the detector and their expected rates can be found in Section 4.1.2.

2.2.2 Inner Detector Components

Acrylic Vessel, Flow Guides and Light Guides

THE acrylic vessel, a hollow acrylic sphere of inner radius 85 cm and thickness 5 cm, serves as the cryostat containing 3279 kg of LAr target. A 25 cm inner diameter acrylic neck at the top of the acrylic vessel provides an opening for a stainless steel detector cooling coil, which maintains the temperature of the LAr. Inside the neck at the bottom of the coil are two acrylic flow guides, the inner flow guide and outer flow guide, designed to boost LAr convective flow and protect the inner acrylic vessel from rogue scintillation light produced in the neck region. On the outer surface of the acrylic vessel there are 255 acrylic stumps, upon which light guides are directly bonded for optimum light transmission from the LAr volume.

The light guides are made from a different type of acrylic to the acrylic vessel and flow guides. The main goal of the light guides is to propagate photons to the PMTs

(through total internal reflection) and thus require a less stringent radiopurity level to the acrylic vessel and flow guides; the 90% upper limit on the total activities of the acrylic vessel and light guides are determined from the results of gamma assays, and are reported in [73] to be < 3 mBq/kg and < 10 mBq/kg respectively. The light guides however require a higher light transmission, as a loss in light yield can lead to reduced background discrimination power and signal sensitivity. At a wavelength of 440 nm, the mean re-emission wavelength of the TPB, the attenuation length of the light guide acrylic was found to be $\lambda_{\text{att}} = 6.2 \pm 0.2$ m after the annealing process [73]. The light guides also double as a thermal insulator, acting as a neutron shield from the PMTs and allowing the PMTs to be operated at non-cryogenic temperatures (~ 260 K) at their highest quantum efficiency.

Tetraphenyl Butadiene Wavelength Shifter

THE inner acrylic vessel is coated with a 3 μm -thick layer of organic TPB to shift VUV scintillation light produced in the LAr volume to the visible region of the electromagnetic spectrum. When VUV scintillation photons emitted in the LAr arrive at the TPB layer, the majority of them are absorbed and re-emitted by the TPB; photons may be backscattered towards the AV upon arrival at the TPB layer, depending on the scattering length of photons in the TPB.

Figure 2.4 shows the TPB wavelength re-emission spectra for incident light of 4 different wavelengths, taken from [76]. For 128 nm scintillation light, the peak wavelength of TPB re-emitted photons is 420 nm, close to the optimum quantum efficiency of the PMTs. Under the assumption that the angular re-emission of TPB photons follows a Lambertian distribution, a reasonable assumption for a surface in which the properties are not known, the total integrated TPB emission efficiency (defined as the ratio of emitted photons to incident photons) was calculated as a function of incident wavelength in [76]. At 128 nm, the efficiency was calculated to

be 1.2 (120%), indicating that the TPB can sometimes fluoresce additional photons.

In order to achieve the target radioactivity level of ~ 18.5 $\mu\text{Bq/kg}$ [73], during TPB production, great care was taken to ensure chemicals used in the process had an assay result of 99% purity or higher [73]. Once the TPB was complete, it was then sealed in a vessel that prevented any exposure to UV light and humidity before it was deposited on the inner acrylic vessel surface. The 90% upper limit on the total activity of the TPB is determined from the results of a gamma assay, reported in [73] to be < 12.6 mBq/kg .

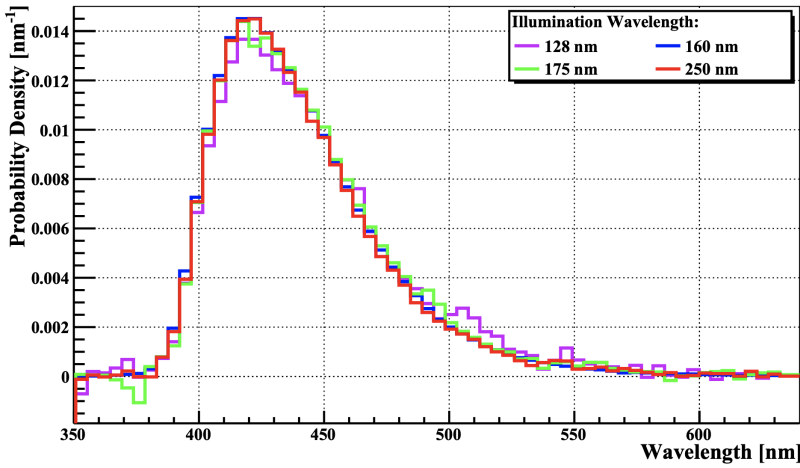


Figure 2.4: TPB wavelength re-emission spectra for incident light of four different wavelengths. The re-emission angular distribution is assumed to follow a Lambertian distribution. From [76].

Photomultiplier Tubes and Filler Blocks

LIGHT from the inner acrylic vessel is detected by 255 Hamamatsu R5912-HQE high quantum efficiency PMTs that provide a $\sim 75\%$ coverage of the inner acrylic vessel. PMTs typically consist of a photocathode, a focusing electrode, a dynode stack and an anode inside a vacuum tube, as illustrated by Figure 2.5. When a photon strikes the photocathode, it ejects a photoelectron (PE) due to the

photoelectric effect. The PE is guided to the first dynode by the focusing electrode, where secondary electrons are ejected. Each dynode is held at a higher potential than the previous one so that ejected electrons are accelerated towards the next dynode by the electric field. The total number of electrons exponentially increases across the dynode stack. Once the cascade of electrons reaches the anode, there is a large enough current to produce an electrical pulse.

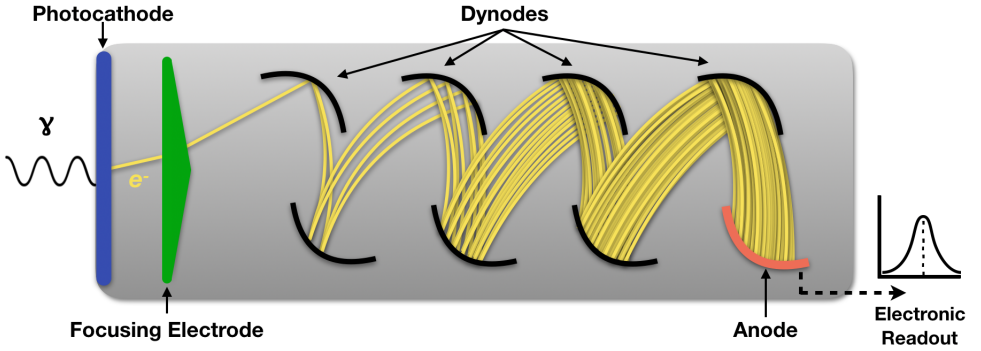


Figure 2.5: Diagram illustrating the typical internal structure of a PMT. The main components are the photocathode, the focusing electrode, the dynode stack and the anode, all labelled.

Each R5912-HQE PMT is made with an 8 inch-diameter low radioactivity borosilicate glass bulb and a bi-alkali photocathode promoting a high quantum efficiency, reaching $\sim 40\%$ at a wavelength of 420 nm; the quantum efficiency is displayed as a function of wavelength in Figure 2.6. The dynode stack consists of 10 stages, providing a typical gain factor of 10^7 for bias voltages between 1500 V - 1800 V [77]. Operating the PMTs at high, positive voltages also enables the use of a single cable for both signal readout and high voltage (HV) supply per PMT [78]. PMT operating temperatures vary across the detector, with PMTs at the top of the detector operating at 280 ± 2 K and PMTs near the bottom of the detector operating at 260 ± 2 K [73]. Since the PMT dark noise rate R_{DN} is heavily dependent on the PMT operating temperature T , $R_{\text{DN}} \propto T^2 \exp(1/T)$, PMTs located at the top

of the detector will have a reduced signal-to-noise ratio compared to PMTs at the bottom. The PMTs are regularly monitored and calibrated with the use of an LED calibration system, explained in detail in Section 2.4.

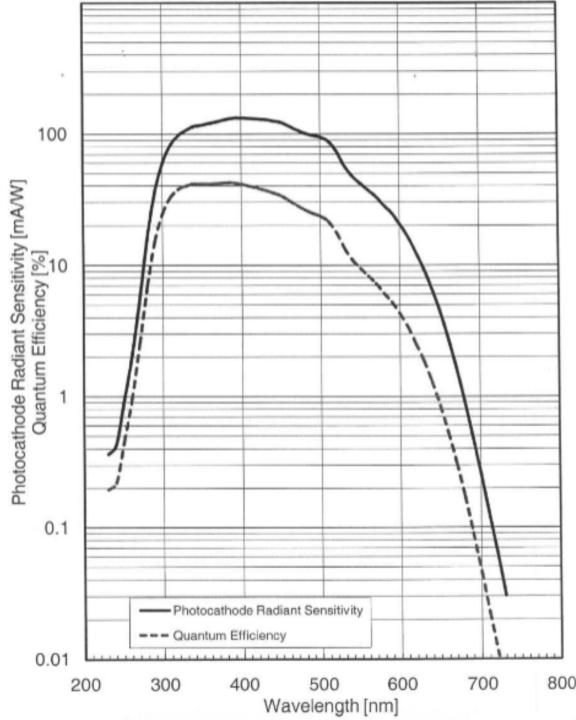
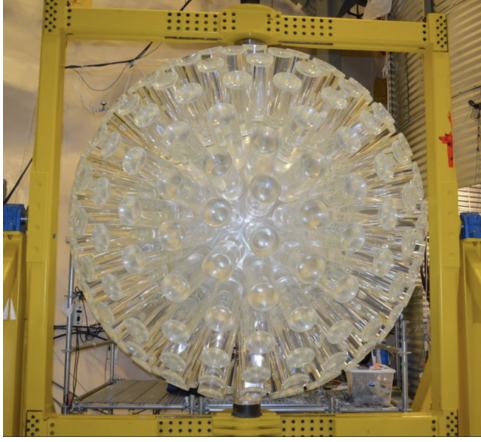
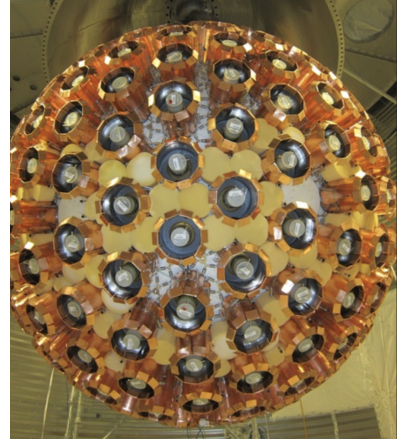


Figure 2.6: R5912-HQE PMT photocathode quantum efficiency [%] as a function of incident wavelength, depicted by the dashed line. At 420 nm, the quantum efficiency is $\sim 40\%$. Also shown is the photocathode radiant sensitivity (solid line), defined as the photocathode photoelectric current divided by the incident radiant power [mA/W]. Image taken from [2].

Completing the inner detector are 486 filler blocks located between the light guides. Composed of alternating high-density polyethylene and polystyrene layers, the filler blocks provide thermal insulation and neutron shielding; approximately 6×10^{-5} of the total neutrons produced in the inner detector components produce a signal in the detector. The blocks are positioned at a distance of 5 mm from the light guides, to protect the acrylic vessel against stress generated by thermal expansion



(a) Completed acrylic vessel with light guides bonded.



(b) Completed acrylic vessel with light guides bonded, during the assembly of PMTs and filler blocks.

Figure 2.7: Images taken during two different stages of construction of the DEAP-3600 inner detector.

[73]. The images in Figures 2.7a and 2.7b show two different construction stages of the inner detector: the completed acrylic vessel with bonded light guides and the completed acrylic vessel with bonded light guides during the PMT and filler block assembly phase respectively.

2.2.3 Outer Detector Components

Steel Shell

THE inner detector is contained inside a 3.4 m diameter spherical stainless steel shell. The light-tight and water-tight steel shell is designed to tolerate a maximum pressure of 30 pounds per square inch gauge (psig) in the event of overpressurisation such as from acrylic vessel failure, which would result in the sudden release of a large gas volume following argon boil-off. The steel shell is suspended from a 45 cm diameter steel outer neck and attached to the deck located above the detector, which provides support to the hardware for the process systems as well

as the electronics. Inside the steel outer neck coaxially hangs a steel inner neck of length 3 m and diameter 30 cm, that supports the $\sim 13,000$ kg load from the inner detector [73].

Water Tank Veto

THE steel shell is submerged in a large cylindrical tank, of diameter 7.8 m and height 7.8 m, filled with ultra pure water (UPW). The water tank is used to mitigate cosmic ray muons and cosmogenic neutrons, which can be produced by interactions in the rock above and around SNOLAB. The average rate of high energy, fast neutrons incident on the water tank has been calculated to be 13.4 ± 6.7 neutrons/day [79]. Upon arrival at the water tank, these neutrons are elastically scattered by hydrogen and oxygen nuclei in UPW, which moderates their energy. Once the neutrons are slow enough, they are absorbed by UPW; according to [80], 99% of 500 keV neutrons are absorbed in 30 cm of UPW.

Cosmic muons are the most difficult particle to shield from as they are not easily attenuated. As outlined in Section 2.2.1, SNOLAB's location significantly reduces the cosmic muon flux down to $0.27 \text{ muons m}^{-2}\text{day}^{-1}$, however unlike neutrons produced in the rock, cosmic muons that make it into the detector are not stopped by the water tank. Instead, muons traversing the water tank produce Cherenkov light. If this Cherenkov light is detected by any of the 48 outward-facing PMTs mounted on the outside of the steel shell, cosmic ray muon events can be removed. The current muon tagging probability in the DEAP-3600 veto is calculated to be $\sim 95\%$. The images in Figures 2.8a and 2.8b show two different construction stages of the outer detector: the inner detector after encapsulation inside the steel shell vessel and the construction phase of the water tank around the steel shell respectively.



(a) Completed inner detector encapsulated in the steel shell vessel.



(b) Steel shell vessel located in its final position during the construction of the water tank.

Figure 2.8: Images taken during two different stages of construction of the DEAP-3600 outer detector.

2.2.4 Cryogenic System

THE cryogenic system is comprised of two parallel systems: a LAr purification loop and a liquid nitrogen (LN_2) cooling system. The LAr purification loop reduces the level of electronegative impurities in the LAr to < 1 ppb [73]; the presence of impurities on the order of $\sim \text{ppm}$ can severely reduce the light yield as discussed in Section 2.1.2. The LAr purification loop is also designed to keep the radon contamination level to < 5 μBq [73].

The main components of the LAr purification loop are the process pump, a getter, a custom-built charcoal radon trap, a condenser column and a boiler. Argon gas, stored in a separate dewar and kept at ~ 300 K, is fed into the purification loop just before the process pump which pushes the gas around the system. Argon gas is chemically purified after passing through the getter, removing contaminants to < 1 ppb. Radon activity in the gas is reduced to < 5 μBq after passing through the radon trap, whereby the gas is cooled to 100 K and passed through a charcoal

column in which radon contaminants become entrapped in the pores of the charcoal. The pre-cooled gas is transferred to the condenser column where it is liquified and supplied to the acrylic vessel. To complete the purification loop, LAr is warmed and removed from the acrylic vessel by the boiler. Extracted LAr can then either re-enter the purification loop or be transferred and stored back in the dewar.

A dedicated LN_2 cooling system is used to keep the LAr at cryogenic temperatures. Stored in a dewar on the deck above the detector, LN_2 is fed down into the detector cooling coil located in the acrylic vessel neck, as outlined in Section 2.2.2. The 1000 W of cooling power provided by the LN_2 keeps the LAr at temperatures of 84 - 87 K, below its boiling point. LAr convection is managed with the use of acrylic flow guides located below the cooling coil, also outlined in Section 2.2.2. The geometry of the inner and outer flow guides were optimised using a Computational Fluid Dynamics (CFD) analysis [73], such that warmer LAr is directed upwards to the cooling coil and cooler LAr is directed downwards back into the acrylic vessel as efficiently as possible.

2.3 Detector Electronics

ALL of the electronics for the DEAP-3600 experiment are located together on the deck above the detector, housed in three standard computer racks. The electronics are split into three different systems, specifically designed to handle both a wide range of energies, from < 100 keV WIMP interactions to $\mathcal{O}(\text{MeV})$ α -background interactions, and a high trigger rate from ^{39}Ar of ~ 3300 β -decays per second. The electronics consist of a front end system, a Digitiser and Trigger Module (DTM) and a Data Acquisition (DAQ) system, all displayed by the diagram in Figure 2.9.

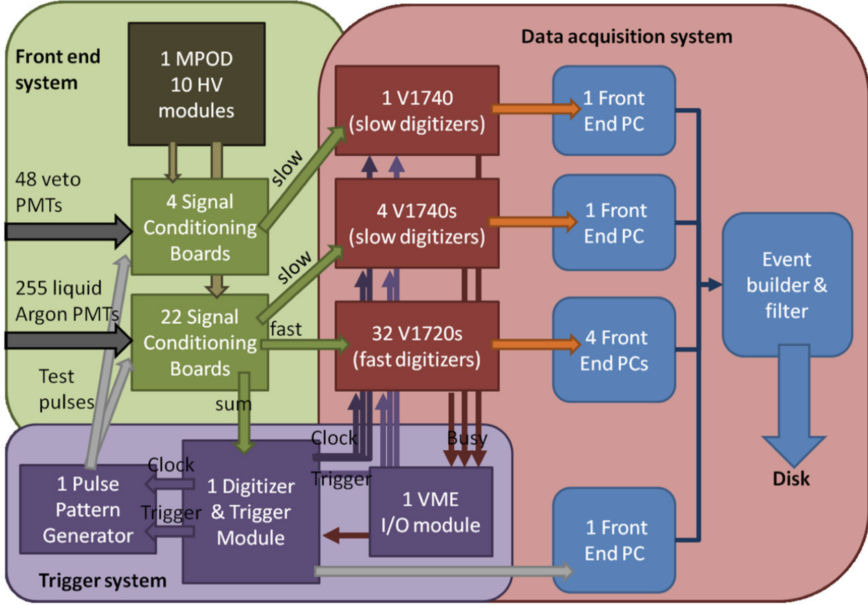


Figure 2.9: Diagram displaying the overall concept of the electronics used in the DEAP-3600 experiment, from [81].

2.3.1 Front End System

THE front end system consists of an MPOD HV supply and 26 signal conditioning boards (SCBs) [81]. The MPOD supplies each PMT with a variable HV, to maintain a uniform gain factor of 10^7 across the detector. The output signals of the PMTs are decoupled, then fed into the SCBs, where they are shaped and amplified. In total, there are 22 SCBs responsible for the 255 LAr PMTs and 4 SCBs responsible for the 48 muon veto PMTs, where each board is connected to up to 12 PMTs. The SCBs first shape and amplify the signal before splitting it into three pathways: high-gain, low-gain and the analog sum.

The high-gain pathway consists of 32 CAEN V1720 fast waveform digitisers, with a digitisation rate of 250 MHz. This fast rate is chosen to optimise the single photoelectron (SPE) signal-to-noise ratio, to ensure SPE pulses are not discarded

as noise by the trigger. An example SPE pulse measured on a particular V1720 channel is shown in Figure 2.10 [73]. The low-gain channel consists of 4 CAEN V1740 slow waveform digitisers, with a much lower digitisation rate of 62.5 MHz. The main role of the low-gain pathway is to measure the pulses which saturate the high-gain pathway with a slower digitisation rate; the pulses are also broadened to more closely match this slower digitisation rate. Output signals from the veto PMTs are fed into their own V1740 board. The third and final pathway, known as the ASUM, creates the analog sum of the 12 separate waveforms arriving from each of the PMTs. The 22 ASUMs from each of the SCBs are then summed together to create the ASUMSUM waveform, which is sent to the Digitiser and Trigger Module (DTM).

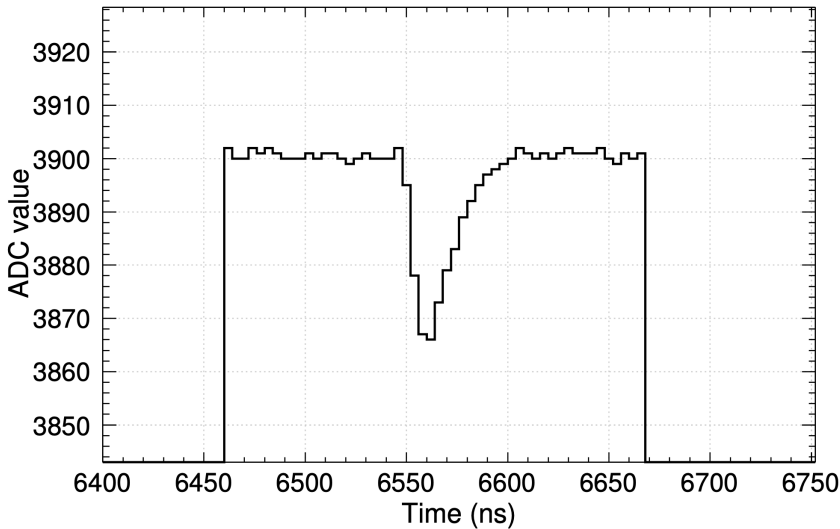


Figure 2.10: Example SPE pulse as measured on one V1720 channel, taken during Zero Length Encoding (ZLE) mode described later. The channel baseline is set at 3900 ADC; the threshold for saving data is set at 3895 ADC. From [73].

2.3.2 Digitiser and Trigger Module

THE DTM has three main functions. Firstly, it makes the decision on whether an event should trigger from the ASUMSUM channel. Secondly, it provides the master clock to all of the digitisers to ensure synchronisation over all SCBs. Finally, it produces the digitised ASUMSUM waveforms to be read by the DAQ system. The trigger system also has a Pulse Pattern Generator board (PPG), which can inject a pre-programmed pulse pattern directly into the SCBs that then distribute the signal to the channels. This enables PMT signal simulation without a physical PMT output and is used to calibrate the channel timing offsets.

The logic of the trigger is established on a collection of trigger sources and outputs. The trigger sources decide whether an event should trigger or not based on two parameters, E_{short} and F_{prompt} . If an event triggers, the trigger outputs then chooses which hardware devices to send the signal to, such as the V1720 and V1740 digitisers. The trigger output also decides whether the event should be “pre-scaled”. Pre-scaling is used to handle the abundant number of triggers from ^{39}Ar β -decays, by deciding whether to save an event based on its “trigger type”. There are 6 different trigger regions defined by E_{short} and F_{prompt} , illustrated by Figure 2.11. In reality, there are actually 5 trigger regions, since events placed in the “very low energy” region are discarded as noise.

The physics trigger algorithm works by computing rolling integrals over the ASUMSUM. Integrals are calculated in two time intervals relative to the same start time; the short window is 177 ns long and the long window is 3100 ns long. The narrow energy, E_{short} is the number of integral ADC counts in the short window of the ASUMSUM. ADC counts are an arbitrary amplitude unit and arise as a result of the digitisation of the waveform from an analogue to a digital signal. For DEAP-3600, 1 ADC corresponds to 0.5 mV. The F_{prompt} parameter is defined as the ratio of E_{short} to E_{long} . The use of rolling integrals enables the computation of

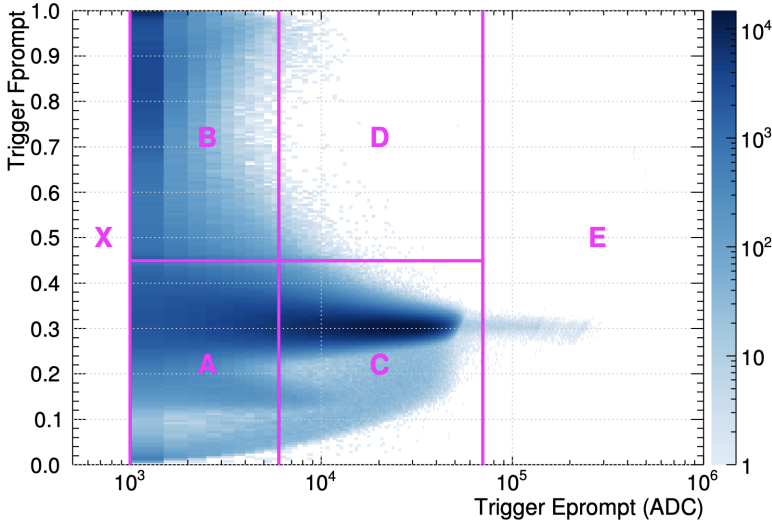


Figure 2.11: F_{prompt} vs E_{short} parameter space for a subset of physics-triggered data (no data-cleaning cuts applied), illustrating the 5 different trigger conditions (separated by pink lines). From [73].

various E_{short} and E_{long} values whilst simultaneously processing new ASUMSUMs. With each new ASUMSUM value, the DTM checks whether the current E_{short} and F_{prompt} both exceed the thresholds to satisfy the next trigger region. During regular physics running:

- The minimum ADC threshold in the narrow energy E_{short} for an event to trigger is set to 1000 ADC,
- The two low E_{short} triggers do not fire the low-gain V1740 digitizers (intended for high-energy saturated events), and
- The medium E_{short} , low F_{prompt} trigger fires the digitisers only 1% of the time; the other 99% of the time only the DTM summary information of the event is saved. This configuration suppresses the rate of ^{39}Ar triggers with total energies $\gtrsim 500$ PE by a factor of 0.99.

Alongside the physics triggers, there are two further trigger sources used in

regular running:

- Periodic trigger: runs at a frequency of 40 Hz and is used to monitor PMT health as well as inject test pulses, and
- External trigger: from the muon veto system.

2.3.3 Data Acquisition System

CONCLUDING the electronics is the DAQ, a system based on the MIDAS software infrastructure for event readout [81][82]. The DAQ consists of the 32 V1720 fast digitising boards connected to 4 front end PCs, the 4 V1740 slow digitising boards connected to 1 front end PC and the single V1740 slow digitising board (veto PMTs) connected to another front end PC. An additional front end PC is directly connected to the DTM. The digitiser information is readout by dedicated software on the front end PCs and then sent to a master PC, where the event is “built” with the event builder program. The master PC also runs the logger program that compresses and saves the complete event. Summary information from the DTM, V1720 and V1740 digitisers about the individual pulses in the full 10 μ s-long event, as well as the veto V1740 board and calibration hardware if applicable, is saved to disk. MIDAS files containing many events can then be reprocessed into ROOT files [83] for analysis purposes, which saves information in the TTree format.

V1720 digitising boards are able to record data through two different modes: Full Waveform (FWF) or Zero-Length Encoding (ZLE). FWF mode stores the full raw waveform, regardless of its properties. ZLE mode runs an algorithm on the raw waveform, only storing the data when a number of samples consistently exceed the ZLE threshold of 5 ADC, in addition to 20 pre-samples and 20 post-samples. ZLE mode is used to filter out triggers from noise and to save disk space; events can be reduced by at least a factor of 10 [81]. The V1740 digitising boards on the other hand only save FWF data, however since a significant portion of events do not fire

the V1740 boards, the need for stringent data storage is less important. The author served as a DAQ expert for a one year duration, between June 2018 - June 2019.

2.4 Calibration Systems

LED Light Injection

UNDERSTANDING the optical properties of the detector is a necessity, for both monitoring detector stability and event reconstruction. The PMTs are regularly calibrated in-situ with a permanent LED light injection system, consisting of 20 aluminium coated acrylic reflectors (AARFs) each attached to the end of a light guide, uniformly distributed across the detector. Coupled to the AARFs are optical fibres that guide injected LED light towards the AARFs, which reflect light onto the face of the PMT attached to the light guide. This setup is illustrated by the diagram in Figure 2.12. Also shown is the PMT occupancy [78], defined as the ratio of the number of times that a PMT observes a pulse at the time of the LED flash to the total number of LED flashes, as a function of each PMT position relative to the LED flash PMT. This shows that whilst the majority of the light is registered by the LED flash PMT, the other PMTs also register some small amount of reflected light. The LED calibration system is used to calculate and track the mean SPE charge value over time and to monitor various time-dependent PMT effects, both essential for event reconstruction as discussed in Section 3.2.1.

Internal/External Radioactive Sources

THE detector is calibrated on a monthly basis using two external radioactive sources:

- Americium-Beryllium (AmBe) neutron source: emits neutrons up to 10 MeV with coincidence 4.4 MeV photons, used to study the detector response to

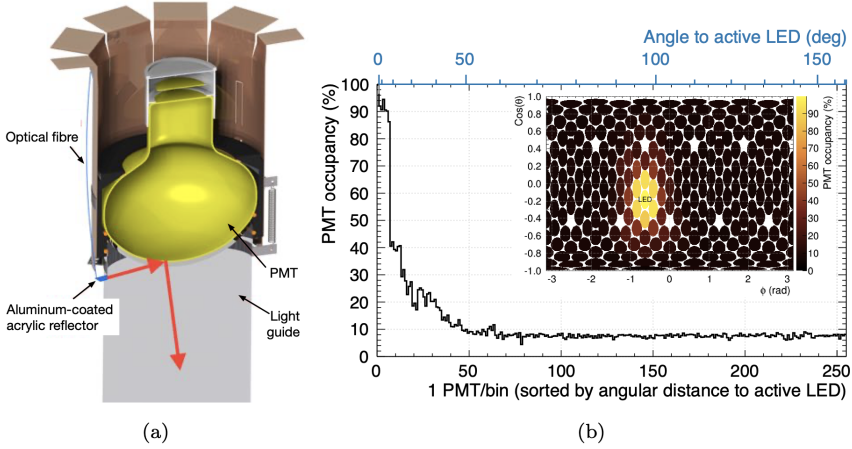


Figure 2.12: Left (a): Diagram illustrating the configuration of the PMT and light guide, with an attached AARF and optical fibre. Right (b): PMT occupancy [%] as a function of PMT position relative to the LED injection PMT. Also shown is a 2D map of the PMT locations in spherical coordinates, where the z -axis colour scheme represents the PMT occupancy. Both (a) and (b) are from [78].

WIMP interactions by mimicking the expected signal with neutron-induced NRs, and,

- Sodium-22 (^{22}Na) γ -ray source: emits a 1.27 MeV photon, used to study the energy and position response with induced ERs.

The sources are deployed in specific calibration tubes, all located outside the steel shell. In total there are 4 calibration tubes: Cal A, Cal B, and Cal E are stainless steel tubes that hang vertically down from the deck at different (x, y) positions around the detector and Cal F is a high density polyethylene tube that diagonally wraps around the detector. Tubes Cal A, Cal C and Cal F can be seen in Figure 2.8a. The sources can be deployed to different positions in the tubes by a motorised pulley and carriage system, measured ex-situ to have a source position uncertainty of ~ 1 cm [73]. Collecting calibration data from various locations around the detector is important for quantifying the position response of the detector.

In addition to external calibration sources, the intrinsic radioactivity from ^{39}Ar

β -decays in the LAr volume offers a uniformly distributed source of ER signals that can be used to study the detector energy response and position reconstruction algorithm biases for events up to ~ 5000 PE.

Chapter 3

Detector Simulation and Event Reconstruction

*“Measure what can be measured,
and make measureable what cannot be measured.”*

—Galileo Galilei

THIS chapter describes how particle interactions are simulated in the DEAP-3600 detector, and how simulated events and real data are reconstructed for analysis. Section 3.1 focuses on detector simulation, first introducing the main analysis framework utilised by the DEAP-3600 experiment, the Reactor Analysis Tool. This is followed by a brief outline of the simulation chain, from the initial generation of particle interactions in the detector to the data acquisition and processing. Section 3.2 focuses on event reconstruction, presenting three of the main reconstructed variables used to characterise the nature of an event in DEAP-3600: the total charge,

the particle identification parameter and the reconstructed event position. For each of these variables, the various challenges faced with event reconstruction, related to different detector effects, are explored.

3.1 Detector Simulation

SIMULATION of the DEAP-3600 detector is performed using the Reactor Analysis Tool, or RAT [84] software package, which utilises Geant4 [85] and ROOT [83] libraries to carry out and analyse Monte Carlo (MC) simulations of particle interactions taking place inside and around the detector. Geant4 handles the propagation of particles through the detector geometry, described by the pre-defined processes for hadronic, electromagnetic and decay physics as well as some additional packages specific to DEAP-3600. Some examples of these include [73],

- A detailed liquid argon (LAr) scintillation model for electronic recoils (ERs) and nuclear recoils (NRs), based on [86],
- A model to describe NRs originating from “rough” surfaces, designed to accurately model the topology of background events from the inner surface of the acrylic vessel such as from α -particles, and
- The energy spectrum of radiogenic neutrons coming from inner detector components (PMTs, for example), obtained from SOURCES-4C [87] and verified with NeuCBOT [88].

The full detector geometry is constructed within the RAT framework using Geant4 geometry classes, describing each of the inner and outer detector components as outlined in Sections 2.2.2 and 2.2.3 as well as the cavity in which the experiment is located and the rock enclosing it. “RATDB” files provide detector material properties to Geant4 during simulation, taken from literature. Material properties are of

fundamental importance when modelling the detector response because the energy loss per unit distance in each material, dE/dx , is directly proportional to the detected signal, $N_\gamma \propto dE/dx$. dE/dx is governed entirely by the physical properties of the material the particle is traversing, such as its composition or density.

Scintillation photons produced in response to a charged particle traversing the detector media, determined by the relevant Geant4 physical processes, are propagated in RAT using a detailed optical model based on ex-situ measurements as inputs for the various optical parameters. Examples of these parameters which have the biggest effect on event reconstruction include the wavelength-dependent LAr refractive index, the photon group velocity in LAr and the Rayleigh length in LAr described in Section 2.1.2, which are all highly correlated with one another. A full description of the optical model implemented in simulation is provided in Section 3.1.1.

A designated PMT response class in RAT handles the simulation of the PMT response to incident scintillation light. The class uses a comprehensive PMT response model to simulate characteristic pulses for each PMT, with charges and times drawn from pre-determined pulse charge-time distributions from in-situ calibration data taken during the commissioning phase. The response model developed for the DEAP-3600 PMTs is discussed in further detail in Section 3.2.1. Each simulated pulse for every PMT is recorded by a dedicated pulse class in RAT, which is used as the input for the data acquisition (DAQ) simulation processor.

Simulation of the full electronics chain on the PMT pulses is achieved with the DAQ processor. Analogous to real data, a combined ASUMSUM waveform from all the PMTs is passed onto the simulated trigger module, the “DTM”, upon which the simulated trigger algorithm is performed. Waveforms of simulated events passing the “physics trigger” condition, which is as closely matched to the real physics trigger condition as possible, are then broadened and conditioned with a simulated Signal

Conditioning Board (SCB) response function, designed to mimic the response of the real SCBs. Events are then digitised using a simulation of the V1720 low-gain and V1740 high-gain waveform digitisers, upon which Zero-Length Encoding (ZLE) data processing can be applied. The final outputs from the simulated waveform digitisers are sent to the “event builder” program, which saves events in the same TTree format as the MIDAS/ROOT files in real data processing. Configuring the “raw” data structure of simulations to match real data is extremely advantageous for the purposes of downstream processing, since the same reprocessing algorithms are applied to both simulations and real data from within the RAT framework.

3.1.1 Optical Model

As outlined earlier, the LAr scintillation process described in Section 2.1.2 is performed in simulation using a specific RAT class which uses the Geant4 package. In simulation, the probability of Rayleigh scattering is handled in the same way as the attenuation probability, using the Beer-Lambert Law $P(x) = \exp(-x/l)$, where l is the Rayleigh scattering length. This expression yields the probability that a particle that has travelled a distance x into a simulated material has not yet undergone scattering [3]. As described in Section 2.1.2, the Rayleigh scattering length l is dependent on the wavelength-dependent refractive index $n(\lambda)$. The values of the Rayleigh scattering length, wavelength-dependent refractive index and photon group velocity implemented in the simulation are given in Section 2.1.2. The uncertainty on the wavelength-dependent refractive index has been shown to have a significant impact on the WIMP region-of-interest (ROI) background expectation for neck α -decays in [4], one of the dominant sources of background to the dark matter search; an uncertainty of -42% was measured on the inner flow guide inner surface ROI background expectation.

Geant4 documents each step of a particle track propagating through LAr; at

each step, Geant4 records the energy loss, dE/dx , which determines the number of scintillation photons produced as described in Section 2.1.2. The total scintillation yield is calculated once the track is complete, after the particle has deposited all of its energy in the LAr. Described in Section 2.1.2, due to nuclear quenching, the number of photons produced per energy deposited differs between ERs and NRs; this is accounted for by implementing the mean energy-dependent quenching factor shown in Figure 2.2 in the simulation.

Scintillation photons are emitted with a time distribution described by Equation 3.6, governed by the fraction of single state excimers compared to triplet state excimers produced in the LAr by the propagating particle as outlined in Section 2.1.2. These fractions are calculated explicitly as a function of charge in Table 2 of [89], the values of which are implemented in the simulation.

Photons incident on the LAr-TPB interface are absorbed and re-emitted with their wavelength shifted into the visible region, as described in Section 2.2.2. The TPB is implemented on the inside of the inner acrylic vessel as a perfect 3 μm layer in simulation. The propagation of photons through the TPB is performed using a separate RAT class to the LAr scintillation process. Upon absorption at the TPB surface, a new photon is initiated in the simulation, emitted from the TPB with a wavelength drawn randomly from the re-emission spectrum shown in Figure 2.4 from [76] at 128 nm. The value of the TPB scattering length implemented in the simulation, which determines how many photons are backscattered at the TPB layer compared to how many are absorbed, is $3^{+3}_{-1.5}$ μm ; the uncertainty on the TPB scattering length is another systematic shown to have a significant impact on the ROI background expectation for neck α -decays in [4], yielding a +82% uncertainty on the inner flow guide inner surface ROI background expectation in the worst-case scenario. A measurement of the TPB light yield induced from α -particles of 882 ± 210 photons/MeV is also implemented in the simulation; as discussed in [90],

scintillation in the TPB could lead to additional background signals from α -decays from within the acrylic vessel or the TPB layer itself.

Before reaching the PMTs, photons must first be propagated from the TPB surface through the acrylic vessel and acrylic light guides. Since Rayleigh scattering in acrylic was found to be insignificant from measurements taken from acrylic samples as discussed in [3], the scattering of photons in acrylic is instead treated as absorption, based on the attenuation lengths of the acrylic vessel and light guides implemented in the simulation. At 440 nm, the mean re-emission wavelength of the TPB, the attenuation lengths were found to be 3.5 m [3] and 6.2 m for the acrylic vessel and light yield respectively, a factor of ~ 70 and 13.5 greater than the acrylic vessel width and light guide length.

3.2 Event Reconstruction

EVENTS that satisfy the trigger conditions set out in Section 2.3.2 in both MC simulations and real data are characterised by reconstructed variables. Some of the most important variables include the reconstruction of the total event charge, the particle identification parameter and the event position. Reconstructed variables are saved to the data structure after applying a number of reprocessing algorithms to the raw “data” from within the RAT framework. Collectively, these variables describe the nature of the event, and are used to differentiate signal interactions from background interactions by their varying event properties. One of the main challenges with event reconstruction is dealing with various detector effects, which can skew the reconstruction and result in signal and background events becoming less distinguishable from each other. Understanding the influence that these detector effects have on event reconstruction, and how they can be accounted for or mitigated against for the three reconstructed variables stated above, is the main focus of this section.

3.2.1 Charge Estimation

IN DEAP-3600, the energy of an event is characterised by the amount of charge it induces in the PMTs. More specifically, the charge of an event is measured by the total number of photoelectrons (PEs) that are produced. The total number of PEs produced in the PMTs is directly proportional to the number of incident photons on the PMTs, which itself is directly proportional to the amount of energy deposited in the LAr from the particle interaction as discussed in Section 3.1, $N_{\text{PE}} \propto N_{\gamma} \propto dE/dx$. The conversion factor between the number of PEs produced and the total energy deposited in the detector has units of [PE/keV] and is referred to as the light yield, calculated explicitly for the DEAP-3600 detector in Section 4.1.1.

Once an event triggers the detector, the DAQ begins recording data for the next 10 μs ; this is defined as the event window. The total charge an event produces in the DEAP-3600 detector is therefore defined as the total number of PEs produced in each PMT, summed across all PMTs, over the 10 μs event window. In order to calculate the total number of PEs produced in each PMT, the mean single photoelectron (SPE) charge for each PMT is required. This is determined from fitting the low-light charge distribution, obtained from data using the LED calibration system discussed in Section 2.4.

The low-light charge model is comprised of a zero-PE contribution known as the pedestal, an SPE contribution and a multi-PE contribution of N-PEs where $N \geq 2$. The zero-PE peak is governed by electronics noise and can be modelled by a simple Gaussian distribution. Described in [78], the SPE charge model consists of three components. The first component accounts for electron multiplication at the first dynode, and is modelled by a Polya distribution. For large numbers of PEs, the Polya approaches the Gamma distribution [78],

$$\Gamma(q; \mu, b) = \frac{1}{b\mu\Gamma(\frac{1}{b})} \left(\frac{q}{b\mu}\right)^{\frac{1}{b}-1} e^{-\frac{q}{b\mu}}, \quad (3.1)$$

where μ is the Gamma mean and b is a shape parameter. The second component is an additional Gamma distribution that accounts for incomplete electron multiplication, which occurs when the initial PE skips the first dynode and instead strikes the second. The third component is an exponentially falling term truncated at the mean value of the first Gamma distribution, empirically chosen to model the scattering of PEs on the dynodes. The full SPE model is written as [78],

$$\text{SPE}(q) = \eta_1 \Gamma(q; \mu, b) + \eta_2 \Gamma(q; \mu f_\mu, b f_b) + \begin{cases} \eta_3 l e^{-ql}, & q < \mu \\ 0, & q > \mu \end{cases} \quad (3.2)$$

where the η_i parameters are the relative component amplitudes, f_μ and f_b are the relative means and widths of the two Gamma distributions and μ is the fit parameter corresponding to the mean SPE charge. Each N-PE component in the multi-PE distribution is modelled as a convolution of the SPE model N times with itself and then convolved with the pedestal term, $\text{Ped}(PE)$, once. The complete function fit to the low-light charge distribution is given by [78],

$$f(PE) = A \cdot [B \cdot \text{Ped}(PE) + \text{Pois}(1, \lambda) \cdot \text{Ped}(PE) \otimes \text{SPE}(PE) + \text{Pois}(2, \lambda) \cdot \text{Ped}(PE) \otimes \text{SPE}(PE) \otimes \text{SPE}(PE) + \dots], \quad (3.3)$$

where A and B are arbitrary constants and λ is the mean amount of PE produced per LED flash. An example of the complete fit for a given PMT is shown in Figure 3.1. The final mean SPE charge, $\hat{\mu}$, is then calculated by taking the SPE contribution separately, post-fit, and calculating its mean. Since LED calibration runs are performed daily, deviations in $\hat{\mu}$ as a function of time can be accounted for in energy reconstruction on a run-to-run basis. A value of 3% is assigned to the systematic uncertainty on $\hat{\mu}$ [78], derived from the deviation δ in the mean charge measured for an SPE pulse, $(1 - \delta)\hat{\mu}$, due to the Zero Length Encoding (ZLE) threshold described

in Section 2.3.3.

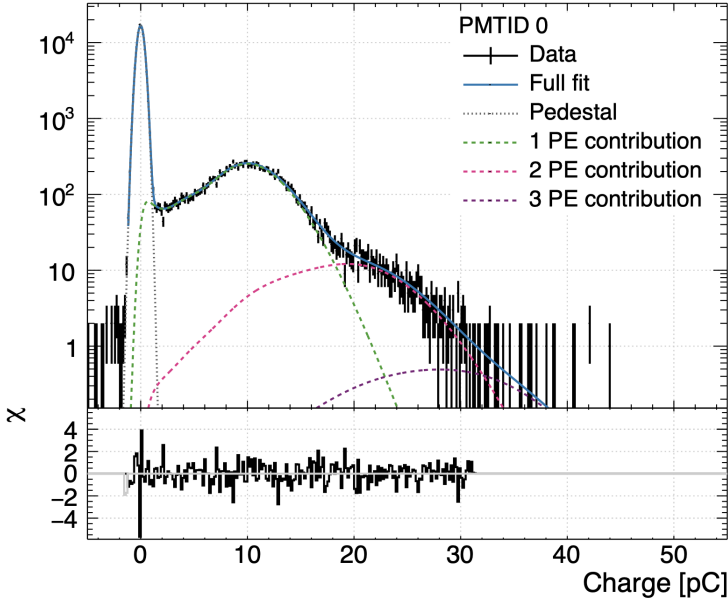


Figure 3.1: Low-light charge distribution for given PMT during an LED calibration run, fit with the summed model for the pedestal, SPE and multi-PE contributions. From [78]. From this fit alone, the mean SPE charge is 9.6 pC.

Two different energy estimators are currently used in DEAP-3600. The first estimator, which was used for the first dark matter search result published by the DEAP-3600 experiment in [91], is calculated by integrating each PMT waveform $\Psi(t)$ over the event window and dividing by the mean SPE charge,

$$q_{\text{PE}} [PE] = \sum_{N_{\text{PMT}}} \left[\frac{\int_{t=-28\text{ns}}^{10\mu\text{s}} \Psi(t) dt}{\hat{\mu}} \right], \quad (3.4)$$

summed over all 255 PMTs. Whilst simple to calculate, this estimator leads to a worse energy resolution, attributed to the wide SPE charge distribution as can be seen in Figure 3.1. Statistical fluctuations at each dynode stage as well as physical PMT effects, such as afterpulsing, are responsible for the width of the SPE charge distribution. This motivated the development of a second energy estimator, denoted

nSCBayes, designed to yield a more accurate light yield and to improve the energy resolution by removing the effect of PMT noise contributions. Improving the energy resolution is particularly important for the WIMP search; a better energy resolution leads to enhanced separation power from ERs at energies near threshold, the region where direct detection experiments are at their optimum WIMP sensitivity.

3

PMT Effects

DOUBLE pulsing, late pulsing and afterpulsing are three examples of internal PMT processes that widen the SPE charge distribution. These effects are explained in this section, with a focus on the dominant effect, PMT afterpulsing.

Double and Late Pulsing

PEs produced at the photocathode have a non-zero probability to backscatter either inelastically or elastically off of the first dynode. In the case of an inelastic backscatter, the backscattered PE loses a fraction of its initial energy in the backscattering process resulting in two separate pulse signals in the PMT; the first pulse created by the initial backscatter is followed by a second pulse created by the backscattered PE drifting back towards the dynode chain. This effect is referred to as double pulsing. Since the integrated charge of the two separate pulses are attributed to the emission of a single PE, double pulsing contributes to the SPE charge distribution; this is accounted for by the falling exponential term in Equation 3.2 described previously. Late pulsing refers to when the PE backscatters elastically off of the first dynode, where only one delayed pulse (< 100 ns after the initial light flash [78]) signal in the PMT is observed from the backscattered PE drifting back towards the dynode chain.

Afterpulsing

AFTERPULSES are produced when residual gas atoms, ionised by electrons inside the PMT bulb, drift to the photocathode or towards the first dynode. When secondary electrons are liberated upon collision, they undergo electron multiplication in the dynode stack to produce an additional PMT signal pulse, adding charge to the event waveform that does not originate from the scintillation photons produced in the detector. Afterpulses are a correlated source of noise, appearing anywhere between ~ 200 ns to ~ 10 μ s after the primary PMT signal pulse. Characterising the effect of PMT afterpulsing is not only important for energy reconstruction, but also for Pulse-Shape Discrimination, which relies solely on the pulse-time distribution.

Three afterpulsing populations are visible in DEAP-3600 PMTs, separated in time ranges 200 ns - 800 ns, 800 ns - 3 μ s and 3 μ s - 10 μ s after the primary signal pulse; these are illustrated in Figure 3.2. Afterpulse charges can range anywhere from <1 PE to ~ 30 PE, however the average afterpulse charge for the three populations are 0.1 PE, 2.1 PE and 1 PE respectively [78]. The total afterpulsing probability, defined as the probability to observe an afterpulse of any charge at any time in the waveform, was found to be function of the primary signal pulse charge. For each PMT, the afterpulsing probability can be described with a linear polynomial. The mean total afterpulsing probability, averaged over all PMTs, is calculated to be $7.6 \% \pm 1.9 \%$ [4].

The **nSCBayes** estimator is calculated by performing a Bayesian PE-counting analysis on every PMT pulse in the 10 μ s event window and summing together the outputs [92]. For each pulse, the Bayesian analysis calculates the most probable number of PEs produced from scintillation in LAr, PE_{scint} . Probabilities are assigned for each detected pulse to originate from scintillation, dark rate, late and double pulsing, early pulsing and afterpulsing based on input prior distributions; the scintillation probabilities are summed to estimate the PE coming from LAr scintil-

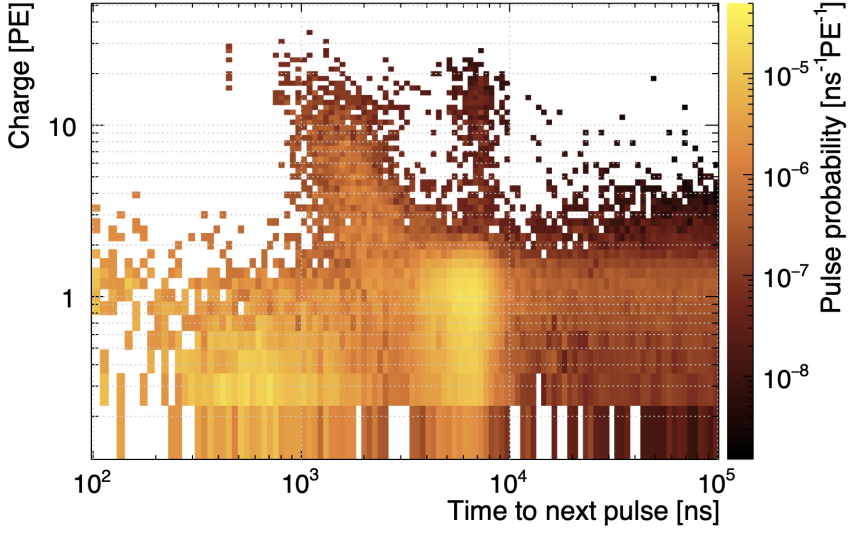


Figure 3.2: Probability for an example PMT to observe a second pulse after a primary scintillation pulse as a function of the follower's pulse charge [PE] and time difference between the pulses [ns]. In this example, events were selected only if the primary scintillation pulses had a charge between 10 pC and 14 pC. From [78].

lation [93]. The scintillation prior is constructed from the LAr scintillation timing PDF and the afterpulsing prior is built from the afterpulsing characteristics of the PMT in question. The posterior distribution is then calculated using a combination of the SPE charge distribution and the prior distribution to yield PE_{scint} , taken as the mean of the posterior distribution. Further information on the construction of the prior and calculation of the posterior can be found in [94]. The nSCBayes of an event can be written as,

$$\text{nSCBayes} [PE] = \sum_{N_{\text{PMT}}} \left[\sum_{t=28\text{ns}}^{10\mu\text{s}} \text{PE}_{\text{scint}}(t) \right]. \quad (3.5)$$

A comparison of the two estimators for a subset of low energy ^{39}Ar β -decay events is illustrated by Figure 3.3. For any given qPE value, Figure 3.3 shows a spread of nSCBayes values that increases with energy; this is attributed to the correlation of afterpulsing probability and charge with the initial pulse charge of the event. The

slope of Figure 3.3, which represents the overall energy scale calibration, is found to be $\text{nSCBayes} = 0.85 \times \text{qPE}$.

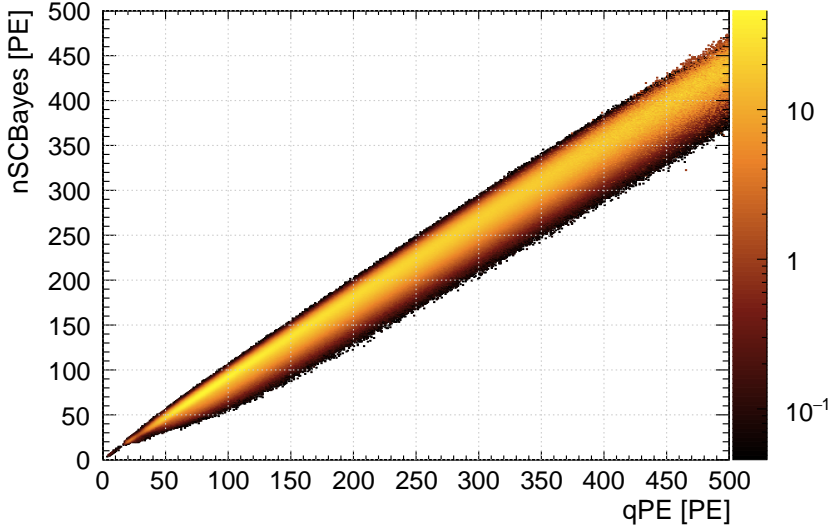


Figure 3.3: 2D distribution comparing the nSCBayes and qPE values of low energy ^{39}Ar β -decay events in the DEAP-3600 detector. The slope of this 2D distribution, which represents the overall energy scale calibration, is found to be $\text{nSCBayes} = 0.85 \times \text{qPE}$.

3.2.2 Pulse-Shape Discrimination

THE scintillation photon time profile in LAr can be described by the sum of two exponentials,

$$f(t) = \frac{\rho_s}{\tau_s} \exp\left(-\frac{t}{\tau_s}\right) + \frac{1-\rho_s}{\tau_t} \exp\left(-\frac{t}{\tau_t}\right), \quad (3.6)$$

where ρ_s is the fraction of singlet state excimers produced in the interaction, $1-\rho_s \equiv \rho_t$ is the fraction of triplet state excimers, and τ_s and τ_t are the decay constants of the singlet and triplet states respectively, defined earlier in Section 2.1.2. It has been found that for ERs, $\rho_s \sim 0.3$ and for NRs, $\rho_s \sim 0.7$ [89]. These values are approximately constant as a function of energy, except at very low energies where

ρ_s tends towards higher (lower) values for ERs (NRs) for decreasing energy. This, combined with the large difference in τ_s and τ_t , leads to two different scintillation time profiles for ERs and NRs, as demonstrated by Figure 3.4.

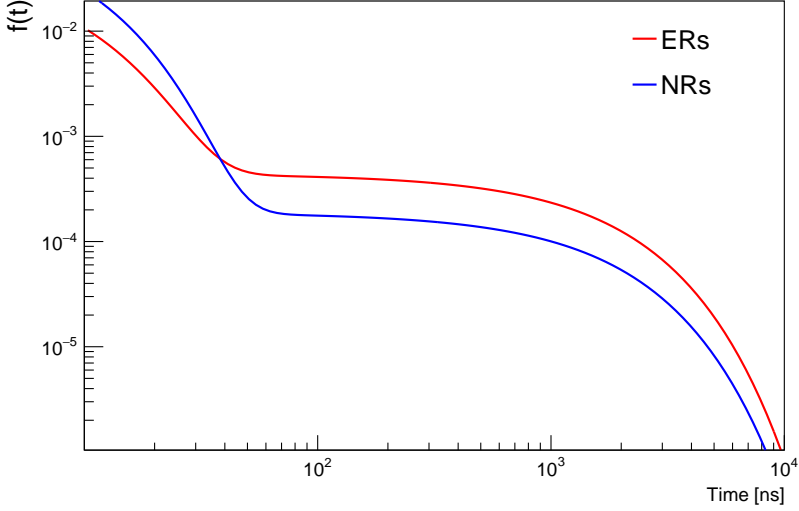


Figure 3.4: Theoretical scintillation decay time profile of ERs (red) and NRs (blue) in LAr, using Equation 3.6 and parameter values $\tau_s = 7$ ns, $\tau_t = 1.6$ μ s. Singlet state fractions for ERs and NRs are taken to be $\rho_s = 0.3$ and $\rho_s = 0.7$ respectively.

Exploiting the difference in the shapes of these time profiles for particle identification is a technique called Pulse-Shape Discrimination (PSD), and has been shown by the DEAP-3600 collaboration to be a very effective tool for background discrimination in LAr [91][4]. The particle identification PSD parameter in DEAP-3600, F_{prompt} , characterises the fraction of the total scintillation light that was recorded in the prompt region of the event window.¹ Since there are two different energy estimators used in DEAP-3600, there are two possible definitions of F_{prompt} . The first definition of F_{prompt} is given by,

¹It should be pointed out that this reconstructed F_{prompt} variable is not the same as the F_{prompt} variable used by the DTM system described in Section 2.3.2. The DTM definition integrates over ADC counts instead of charge [pC], and considers different “short” and “long” windows.

$$F_{\text{prompt}} = \frac{\sum_{N_{\text{PMT}}} \left[\int_{t=-28\text{ns}}^{t_{\text{pr}}} \Psi(t) dt \right]}{\sum_{N_{\text{PMT}}} \left[\int_{t=-28\text{ns}}^{10\mu\text{s}} \Psi(t) dt \right]}, \quad (3.7)$$

where the upper bound of the “prompt” region is taken to be at time t_{pr} after the event time. In DEAP-1, t_{pr} was taken to be 150 ns, however DEAP-3600 now chooses t_{pr} to be 60 ns after particle identification optimisation studies have shown that this definition provides better discrimination between ERs and NRs. Optimisation studies were also performed in order to determine the end of this window, 10 μs . The second definition of F_{prompt} is given by,

$$F_{\text{prompt}} = \frac{\sum_{N_{\text{PMT}}} \left[\sum_{t=-28\text{ns}}^{t_{\text{pr}}} \text{PE}_{\text{scint}}(t) \right]}{\sum_{N_{\text{PMT}}} \left[\sum_{t=-28\text{ns}}^{10\mu\text{s}} \text{PE}_{\text{scint}}(t) \right]}. \quad (3.8)$$

For the analysis presented in the remainder of this thesis, unless stated otherwise, the default energy estimator used is **nSCBayes** and the default PSD parameter used is the second definition of F_{prompt} given by Equation 3.8.

A 2D distribution of F_{prompt} versus **nSCBayes**, taken during an AmBe neutron calibration source run in the DEAP-3600 detector, is shown in Figure 3.5. There are two distinct bands, corresponding to the ER and NR populations. The upper band, peaked at an F_{prompt} value of ~ 0.7 , is the NR band induced by neutron interactions and is the region where WIMP signal events are expected; the red box shows the location of the WIMP ROI used for the dark matter search analysis presented by the DEAP-3600 collaboration in [4]. The lower band, peaked at an F_{prompt} value of ~ 0.3 , is the ER band where the overwhelming source of ^{39}Ar β -decay background events reside. The sparse population between the two bands comes from multiple scatter neutrons and single scatter neutrons that pile up with correlated ERs produced from 4.4 MeV γ -rays emitted by the AmBe source during neutron production, which pull down the F_{prompt} value expected from single scatter neutrons towards the ER band.

In order to determine the leakage probability of ER background events into the NR band and WIMP search region, the ER F_{prompt} distribution is fit with a two-dimensional effective model that describes the ER F_{prompt} as a function of total charge [95]. For an ER with a total charge n_{SCBayes} in [PE], the probability of observing a given F_{prompt} value, f , can be described by the convolution of a Gamma function with mean \bar{f} and shape parameter b , with a Gaussian function centred about zero and width σ ,

$$F^{\text{ER}} = \Gamma(f; \bar{f}, b) \otimes \text{Gaus}(f; \sigma), \quad (3.9)$$

where these three parameters are modelled as charge-dependent,

$$\bar{f} \rightarrow \bar{f}(PE) = m_0 + \frac{m_1}{PE - m_3} + \frac{m_2}{(PE - m_4)^2}, \quad (3.10)$$

$$b \rightarrow b(PE) = b_0 + \frac{b_1}{PE} + \frac{b_2}{PE^2}, \quad (3.11)$$

$$\sigma \rightarrow \sigma(PE) = s_0 + \frac{s_1}{PE} + \frac{s_2}{PE^2}. \quad (3.12)$$

In this parameterisation, there are 11 fit parameters which describe the evolution of the $\bar{f}(PE)$, $b(PE)$ and $\sigma(PE)$ parameters with total charge. Figure 3.6 shows the leakage probability of an ER event being observed above a given F_{prompt} value, in the lowest energy bin of the WIMP ROI used in [4]. Also drawn are the vertical lines which indicate the values of F_{prompt} above which 90% and 50% of NRs are detected. This work presented by the DEAP-3600 collaboration demonstrates the strongest ER background suppression from PSD in LAr, delivering an average leakage probability of $4.1_{-1.0}^{+2.1} \times 10^{-9}$ at 90% NR acceptance in the full WIMP ROI of 15.6 keV – 32.9 keV for a light yield of 6.1 ± 0.4 PE/keV[4].

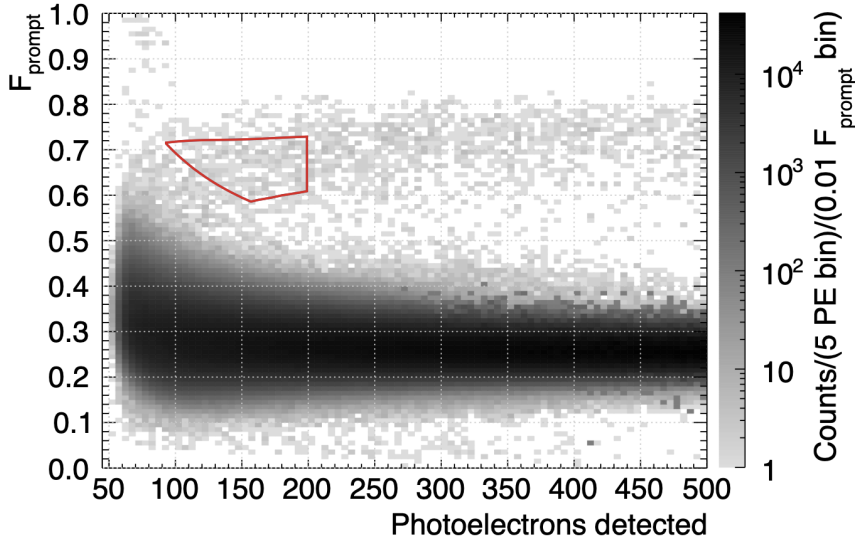


Figure 3.5: 2D distribution of F_{prompt} versus $n\text{SCBayes}$ during an AmBe neutron calibration source run with the DEAP-3600 detector, depicting the ER band at $F_{\text{prompt}} \sim 0.3$ and the NR band at $F_{\text{prompt}} \sim 0.7$. The region between the two bands is populated by NR events piled up with ERs and neutron multiple scatter events, which pull the expected F_{prompt} value from neutron single scatters down towards the ER band. The red box indicates the WIMP ROI used for the dark matter search analysis performed by the DEAP-3600 collaboration reported in [4].

Trigger Efficiency

DESCRIBED earlier in Section 2.3.2, the DEAP-3600 trigger algorithm works by calculating rolling integrals across the event waveform; when the charge of a rolling integral is determined to have exceeded some threshold value, the trigger module (DTM) triggers an event. Understanding the efficiency of the trigger algorithm is most important for PSD, since the calculation of the leakage probability depends on the ability to accurately model the ER F_{prompt} distribution in the lowest energy bin of the WIMP ROI. The algorithm is optimised to detect 100% of prompt low energy NRs and is thus less efficient for low energy ERs, which are dominated by the late light component. The trigger could miss up to 3% of low energy ER events from ^{39}Ar β -decay. As such, the low end of the observed ER F_{prompt} distribution

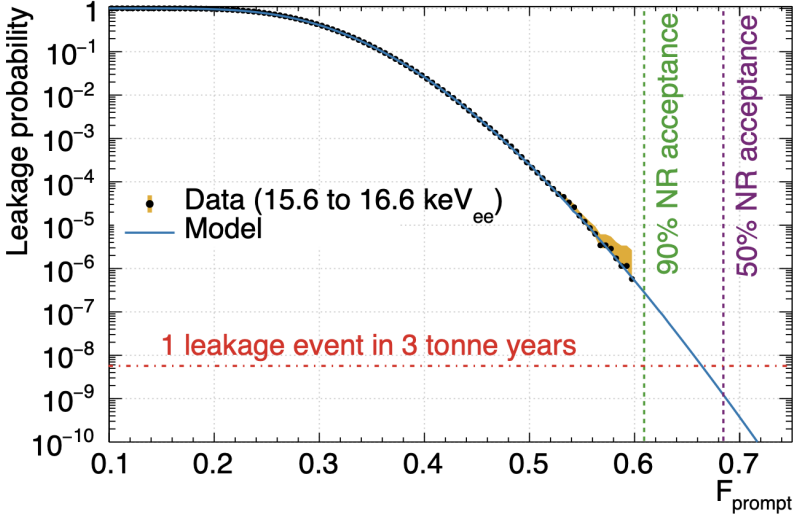


Figure 3.6: ER leakage probability as a function of F_{prompt} in the lowest energy bin of the WIMP ROI used in [4]. Also drawn are the vertical lines which indicate the values of F_{prompt} above which 90% (green) and 50% (purple) of NRs are detected. For a light yield of 6.1 ± 0.4 PE/keV, the average leakage probability in the full WIMP ROI of 15.6 keV – 32.9 keV is $4.1^{+2.1}_{-1.0} \times 10^{-9}$ at 90% NR acceptance. From [4].

can not be described by the effective model from Equation 3.9. Using ER events from ^{39}Ar β -decay, a study was performed to calculate the trigger efficiency of the DEAP-3600 detector.

Generally speaking, the trigger efficiency ϵ_T can be written as the ratio of the number of detected events remaining after applying some trigger condition, N_f , to the initial number of total events occurring in the detector, N_i ,

$$\epsilon_T = \frac{N_f}{N_i}. \quad (3.13)$$

In order to make this measurement, a denominator which is truly “all” events is required. One method of calculating ϵ_T , which can provide the correct denominator, is by replicating the physics trigger algorithm on periodically-triggered data. The benefit of using periodically-triggered data is that since there are no requirements on the event to trigger, the data acquired is an unbiased and random sampling of

activity in the detector. By replicating the physics trigger on this random data, one is able to reproduce the decision the DTM would have made in the given situation.

As discussed in Section 2.3.2, during regular physics running there is a periodic trigger that continuously fires. However, these periodically-triggered events do not quite give an unbiased sample of events, since the physics trigger can “steal” events from the periodic trigger: when the physics trigger fires and the digitisers are read out, the digitisers cannot then be read out for a further 16 μs . If a periodic trigger fires within this 16 μs “deadtime”, the periodic trigger will still be recorded in the trigger summary information, but the 16 μs of waveform data is assigned to the physics trigger. This issue can be resolved with a dedicated data run, where only the periodic trigger fires. A new run type was specifically designed for this study, configured to acquire data with only the periodic trigger firing at a rate of 1 kHz. Events were saved with a 64 μs -long event window each time, six times longer than the regular 10 μs event window saved when the physics trigger is fired. This extended event window is chosen to increase the probability of randomly observing an ^{39}Ar β -decay event by approximately a factor of 5.

A loose set of cuts were applied to the random data for this analysis. These include:

- Low-level cuts, which remove events affected by instrumental effects. Examples of events failing this cut include if any of the high-gain V1720 digitisers had a bad baseline, or if the DAQ was busy and suppressing readout of the digitisers. These cuts are standard data-cleaning cuts that are applied to any data acquired by the detector,
- Pile-up cuts, which remove events which are suspected to be coincidence events (more than one physics signal inside one event waveform) or events with suspected light leakage from a previous event. These are listed later in Section 5.1, and

- Fiducial cuts, which remove events with reconstructed radii within 50 mm of the acrylic vessel surface or with reconstructed positions along the z -axis greater than the LAr fill level. Events are also cut if any one of the PMTs saw more than 40% of the total event charge, which primarily is applied to remove events caused by Cherenkov radiation in the light guides, but also doubles as a very loose fiducial radius cut.

The calibrated 64 μ s random event waveforms are stored in the DEAP-3600 data structure. To replicate the physics trigger algorithm, a rolling integral is performed across the calibrated event waveform, checking at each step whether the E_{short} exceeded the low energy trigger threshold of 1000 ADC. Just like the DTM described in Section 2.3.2, the short window used to calculate E_{short} is defined to be 177 ns long. In order to apply this threshold to the calibrated waveforms, the conversion between the charge measured in the V1720 reconstructed waveform, measured in pico-coulombs [pC], and the charge measured in the DTM ASUMSUM, measured in ADC counts [ADC], is required.

Physics-triggered data can be used to find the mapping between V1720 charge and DTM ADC charge. The same data-cleaning cuts as above are applied to the data, including an additional trigger source cut to remove events which are periodically triggered or triggered independently of the physics trigger. In physics-triggered data, the DTM E_{short} and E_{long} variables from Section 2.3.2 are saved in the data structure; these are called q_{Narrow} and q_{Wide} respectively. The final values of q_{Narrow} and q_{Wide} recorded in the data structure are the values corresponding to the time bin where q_{Narrow} reaches its maximum value in the highest trigger region from Figure 2.11. In order to find the equivalent threshold used by the DTM for the standard physics trigger, a direct one-to-one mapping between the q_{Narrow} from the DTM and the charge from the V1720s in the same time window, denoted as q_{Max} , is required. This is achieved by performing a rolling integral over the calibrated 10 μ s

event waveforms, starting from time $T_0 - 150$ ns, where T_0 is the event time of the event. T_0 is defined as the time with respect to the beginning of the waveform at which the rolling integral crossed the threshold. For each 4 ns step, i , of the rolling integral, the q_{Max} in units of pC is stored. To find the time at which q_{Max} reaches its maximum value, the following condition must be satisfied:

$$q_{\text{Max}, i+1} - q_{\text{Max}, i} < 0. \quad (3.14)$$

Once this condition is satisfied, the algorithm stops and $q_{\text{Max}, i} = q_{\text{Max}}$. The q_{Max} value is then compared with the q_{Narrow} recorded in the data structure. The 2D distribution of q_{Max} and q_{Narrow} is shown in Figure 3.7.

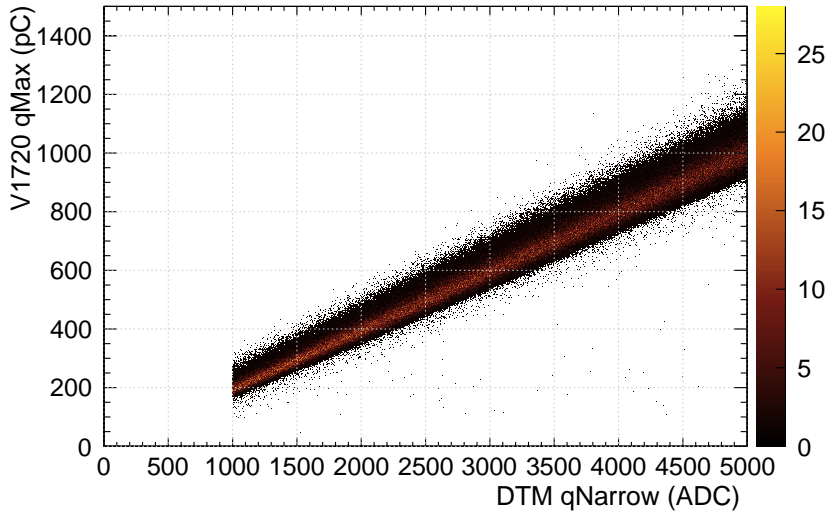


Figure 3.7: 2D distribution of the maximum charge recorded in the V1720s in $E_{\text{short}} = 177$ ns, q_{Max} , and the maximum charge recorded in the DTM in $E_{\text{short}} = 177$ ns, q_{Narrow} , from physics-triggered data.

The step function at 1000 ADC on the x -axis of Figure 3.7 is a direct result of the low energy physics trigger threshold in the DTM. Using this cut-off, the corresponding q_{Max} in pC at the low energy threshold in the DTM is obtained by

projecting the q_{Max} distribution onto the y -axis at q_{Narrow} equal to 1000 ADC; this distribution is shown in Figure 3.8. For a q_{Narrow} value of 1000 ADC, there is a non-symmetric spread of q_{Max} found in the V1720 calibrated waveforms. The spread in the q_{Max} distribution can be attributed to a time offset between the DTM and the V1720 digitisers. When the DAQ is restarted, the DTM clock resets, introducing a time offset with respect to the V1720 digitisers. The non-symmetry in Figure 3.8 can be explained by the pulse-shape; these signals are from ERs (^{39}Ar β -decays), which have a less pronounced “prompt” peak and a long tail. The effect of this long tail is depicted in Figure 3.8, whereby random time offsets in the rolling integral cause a non-symmetry around the peak $q_{\text{Max}} \simeq 190$ pC. To emulate the q_{Max} distribution as a physics trigger threshold on the random data, the threshold applied to the random data is not a constant value, but rather changed on an event-by-event basis by randomly drawing from the distribution in Figure 3.8.

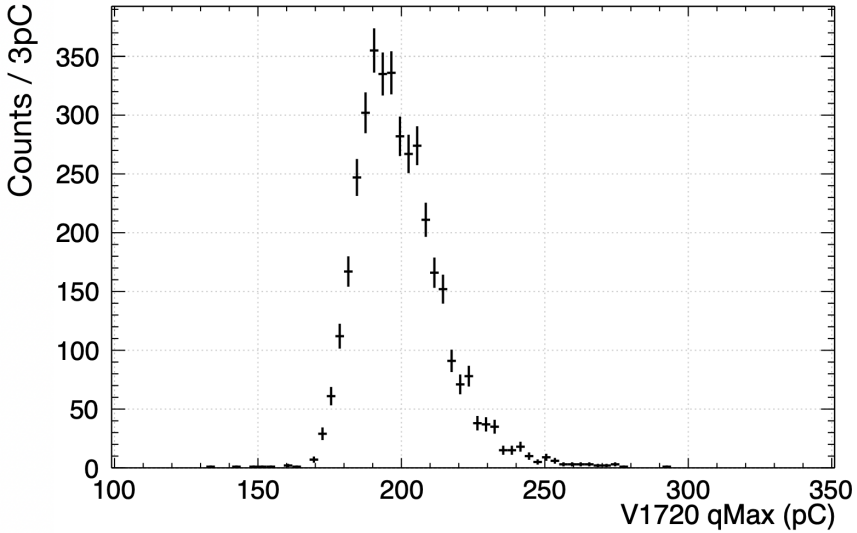


Figure 3.8: Distribution of q_{Max} at the point $q_{\text{Narrow}} = 1000$ ADC, used to find the equivalent threshold of the low energy trigger in units of V1720 charge.

In order to calculate the trigger efficiency measurement, a sample of events orig-

inating from LAr scintillation are selected for the denominator. To do this, an extremely low threshold is applied to the calibrated 64 μ s random event waveforms, to cut out pure noise coming from the PMT dark rate, for example. Events are selected for the study if whilst performing the rolling integral across the waveform, the charge in the narrow window ever exceeds 20 pC,

$$q_{\text{Max}, i} > 20\text{pC}, \quad (3.15)$$

To calculate the numerator, another rolling integral is performed on the event waveform, this time with a higher threshold that is equivalent to the physics trigger threshold of 1000 ADC. This higher threshold is generated randomly from Figure 3.8, and changes for every event. Events are said to have passed the physics trigger condition if whilst performing the rolling integral across the event waveform, the charge in the narrow window ever exceeds this higher threshold,

$$q_{\text{Max}, i} > q_{\text{thresh}}. \quad (3.16)$$

The final trigger efficiency is defined as the ratio of the number of events passing both the low and physics trigger conditions to the number of events passing only the low trigger condition, defined in Equation 3.13. A 2D measurement of the trigger efficiency is illustrated in Figure 3.9, as a function of F_{prompt} and the estimated number of “prompt” PE, produced in the first 60 ns of the event. The **promptPE** variable of an event is defined as,

$$\text{promptPE} [PE] = \begin{cases} F_{\text{prompt}} \times \text{qPE}, & [PE] = \text{qPE} \\ F_{\text{prompt}} \times \text{nSCBayes}, & [PE] = \text{nSCBayes} \end{cases} \quad (3.17)$$

The trigger efficiency is modelled as a function of the number of **promptPE** produced in the event rather than the number of total PE ($\text{qPE}/\text{nSCBayes}$) such that the

trigger efficiency measurement, which is determined using ERs, can also be applied to NRs.

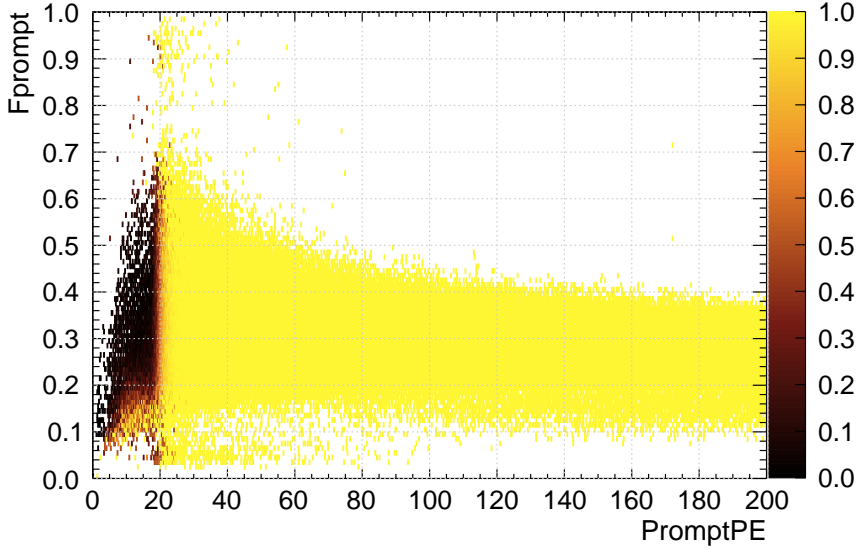


Figure 3.9: Trigger efficiency of the DEAP-3600 detector obtained using three days of periodically-triggered data, measured in 2D as a function of F_{prompt} and promptPE registered in the first 60 ns. For this measurement, the trigger efficiency reaches 10%, 50% and 90% at 18.5, 20.5 and 24 promptPE respectively.

A second method of calculating the trigger efficiency without the use of a dedicated data-taking run was developed by a fellow DEAP-3600 collaborator, Tina Pollmann. In this approach, the trigger efficiency is determined using regular physics-triggered data, known as “boot-strapping”. Details on the methodology of this approach are given in [1]. Given the vast amount of physics-triggered data acquired by the detector, provided that this method returns the correct trigger efficiency, it is a much more sustainable method of regularly calculating the trigger efficiency. The validity of this method is checked by comparing the trigger efficiency curve obtained from the “boot-strapping” method with the conventional method described above, ensuring that the two independent methods yield consistent results.

The trigger efficiency has to be recalculated on a regular basis mainly due to shifts in the mean SPE charge, which causes the biggest change to the trigger efficiency over time. Other effects can also cause the trigger efficiency to behave in unpredictable ways, such as varying noise levels and random time offsets between the DTM and the V1720 digitisers described earlier. To minimise the discrepancy caused by the mean SPE charge drift, the trigger efficiency from the “boot-strapping” method was obtained using physics-triggered data runs taken within a week of the periodically-triggered data that was used to calculate the trigger efficiency through the conventional method. The comparison of the trigger efficiency curves as a function of `promptPE` between the two methods illustrated in Figure 3.10 demonstrate that the results are in agreement with one another.

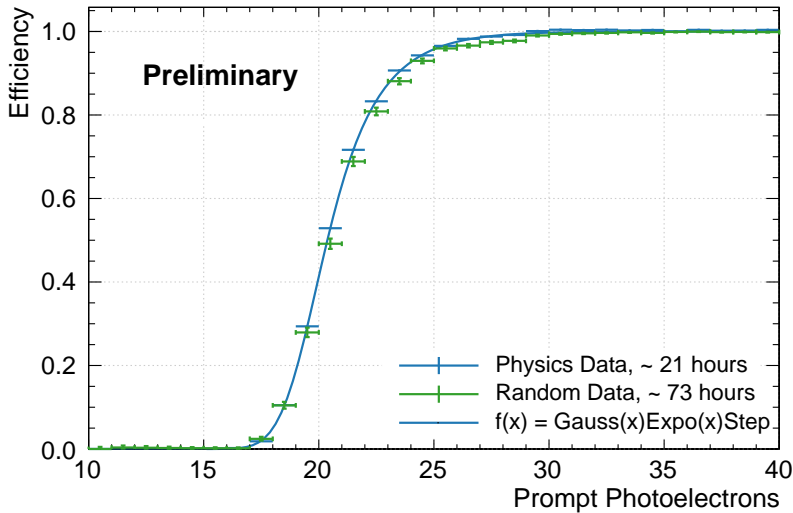


Figure 3.10: Comparison of the 1D trigger efficiency curves as a function of the number of `promptPE` calculated with the conventional method from periodically-triggered data (green) and the “boot-strapping” method from physics-triggered data (blue). The trigger efficiency is calculated over all F_{prompt} . The solid blue line indicates the function used to fit to the trigger efficiency curve from the physics-triggered data. The agreement between the two independently obtained curves implies that the “boot-strapping” technique is a valid method that can be used to regularly calculate the trigger efficiency.

The final trigger efficiency curve can then be used to correct for the loss of events observed in the physics data, in order to validate the effective model described by Equation 3.9, used to extrapolate the leakage of ER events into the WIMP ROI in the low energy, low F_{prompt} regime. Figure 3.11 displays the ER F_{prompt} distribution for 231 live-days exposure, for events between 100 - 240 PE in qPE or equivalently 93 - 200 PE in nSCBayes. As Figure 3.11 shows, at decreasing values of F_{prompt} , the data (in black) diverges from the effective model (in grey). After applying the trigger efficiency correction, the data (in pink) at low F_{prompt} becomes fully consistent with the model, indicating that the trigger efficiency is wholly responsible for this loss of events.

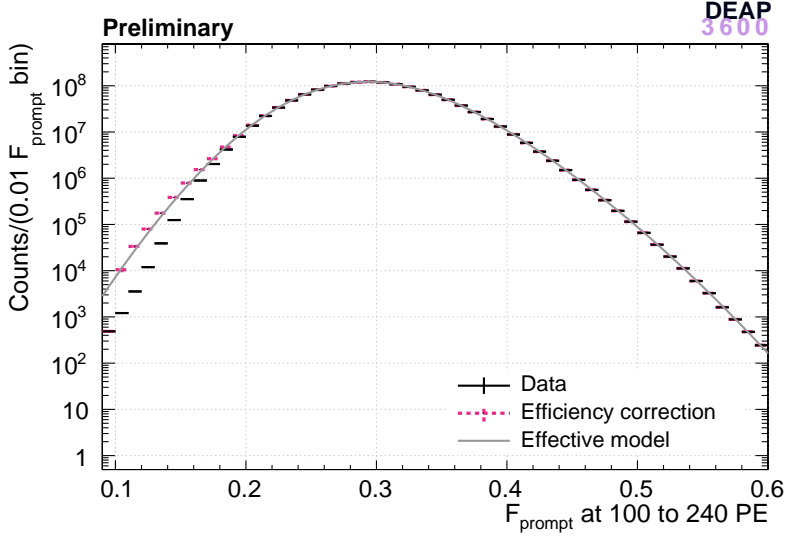


Figure 3.11: ER F_{prompt} distribution for 231 live-days exposure, for events between 100 - 240 PE in qPE or equivalently 93 - 200 PE in nSCBayes. The original data is shown in black, the effective model fit to the data is shown in grey and the trigger efficiency corrected data is shown in pink. Before applying the correction, at low F_{prompt} the data diverges from the model. After applying the correction, the data is once again in agreement with the model. The fit is performed only on F_{prompt} values where the trigger efficiency is $\geq 99\%$.

3.2.3 Event Position

TWO different position reconstruction algorithms developed by the DEAP-3600 collaboration are considered in this thesis. The first algorithm, called “MB-Likelihood”, relies solely on the spatial distribution of charge across the PMTs for position reconstruction. The second algorithm, called “TimeFit2”, uses photon arrival times combined with the PMT charge distribution for position reconstruction.

MBLikelihood: Charge-Based Algorithm

MBLIKELIHOOD compares the observed distribution of PE in each PMT with the predicted distribution given a hypothesised event vertex. These hypothesised distributions are fits to MC simulation, which includes the full model of detector response. The reconstructed event vertex returned by MBLikelihood corresponds to the event vertex in which the PE distribution in each PMT is the most consistent with the predicted distribution.

Consider a likelihood function $\mathcal{L}(\vec{x})$ that describes the probability of observing an event given a hypothesised position \vec{x} , where $(\vec{x}) = (x, y, z)$ [4],

$$\mathcal{L}(\vec{x}) = \prod_{i=0}^{N_{\text{PMT}}} \text{Pois}(n_i | \lambda_i). \quad (3.18)$$

For PMT i located at position $\vec{r}_i = (x_i, y_i, z_i)$, $\text{Pois}(n_i | \lambda_i)$ is the Poisson probability of detecting n_i PE within the 10 μs event window. The expected number of PE detected by PMT i , λ_i , is dependent on $|\vec{x}|$ and the angle between \vec{x} and PMT i and the total number of observed PE across all PMTs [4],

$$\lambda_i \rightarrow \lambda_i(|\vec{x}|, \cos(\theta), N). \quad (3.19)$$

The likelihood function refers to look-up tables to find λ_i values, which are generated using high statistics, MC simulations of scintillation events produced in the detector

at discrete vertex positions along the (x, y, z) axes. The origin of the reconstruction coordinate system, $(x, y, z) = (0, 0, 0)$, is the centre of the detector. The simulations are performed assuming a perfectly spherical geometry and a completely filled detector. The final reconstructed position, saved to the data structure, is given by the value of \vec{x} which maximises $\mathcal{L}(\vec{x})$.

3

TimeFit2: Time Residual Based Algorithm

A_{KIN} to MBLikelihood, this algorithm determines the reconstructed event vertex by finding the hypothesised value \vec{x} that maximises a likelihood function, however this algorithm considers time rather than charge. Consider a likelihood function that describes the probability of observing an event given a hypothesised position and event time, t [4],

$$\mathcal{L}(t, \vec{x}) = \prod_{i=0}^{N_{\text{PE}}} \mathcal{L}^{t, \text{res}}(t_i - t | \vec{x}, \text{PMT}_i), \quad (3.20)$$

where t_i is the time of the i 'th PE observed by PMT i , N_{PE} is the number of promptly arriving PE detected in the first 40 ns of the event and $\mathcal{L}^{t, \text{res}}$ is the time residual distribution. The time difference between the actual time a pulse was registered by a PMT compared to the predicted time from time-of-flight (TOF) calculations is defined as the time residual. For a set of discrete vertex points inside the detector, $\mathcal{L}^{t, \text{res}}$ is determined a priori for each PMT. The combined values of (t, \vec{x}) that maximise $\mathcal{L}(t, \vec{x})$ are returned and saved to the data structure as the reconstructed event time and position.

$\mathcal{L}^{t, \text{res}}$ is predicted based on the optical model, described in detail in Section 3.1.1. The photon arrival time depends on a number of different optical parameters that define light propagation, such as the time constants of LAr scintillation and TPB fluorescence, the group velocity of UV light emitted by LAr and TPB, the average time it takes for visible photons to traverse the acrylic vessel and light guides and

the PMT response time. For simplicity, some effects are not included in the model, such as photon scattering off of and within the TPB and Rayleigh scattering of photons in the LAr [4].

Fitter Algorithm Reconstruction Bias

PERFORMANCE of both fitters can be evaluated using ^{39}Ar β -decays, which are uniformly distributed up to the LAr fill level. The detector can be split into regions of equal volumes, as illustrated by the example in Figure 3.12, by looking at the normalised reconstructed radius cubed distribution, $(\mathbf{R}_{\text{rec}}/R_0)^3$, where \mathbf{R}_{rec} is the reconstructed radial variable and R_0 is the outermost acrylic vessel radius ($R_0 = 851 \text{ mm}$).

If the LAr mass contained in each volume is the same, an equal rate of ^{39}Ar β -decay triggers is expected; since for radii greater than the fill level ($(\mathbf{R}_{\text{rec}}/R_0)^3 > 0.27$) there is less LAr mass contained in each volume, there will be less triggers in each volume than for radii less than the fill level. Therefore if the fitters were to reconstruct events perfectly, the $(\mathbf{R}_{\text{rec}}/R_0)^3$ distribution should be completely flat up to $(\mathbf{R}_{\text{rec}}/R_0)^3 \simeq 0.27$, whereafter the distribution would be pulled downwards for increasing $(\mathbf{R}_{\text{rec}}/R_0)^3$. A comparison of the reconstructed $(\mathbf{R}_{\text{rec}}/R_0)^3$ distributions obtained from the two fitters for ^{39}Ar β -decays is shown in Figure 3.13. As shown in Figure 3.13, the MBLikelihood $(\mathbf{R}_{\text{rec}}/R_0)^3$ distribution spikes at the very edge of the detector and the TimeFit2 $(\mathbf{R}_{\text{rec}}/R_0)^3$ distribution drives upwards for increasing $(\mathbf{R}_{\text{rec}}/R_0)^3$, indicating that both fitters experience bias in their algorithms. Figure 3.13 also shows that the effect of the fill level is negligible.

The reconstruction bias from the fitters can be characterised by a charge-dependent, Gaussian radial resolution function, determined by comparing an event's true position with its reconstructed position. Following the prescription described in [3], the radial resolution function is obtained using MC simulations of ^{39}Ar β -decays,

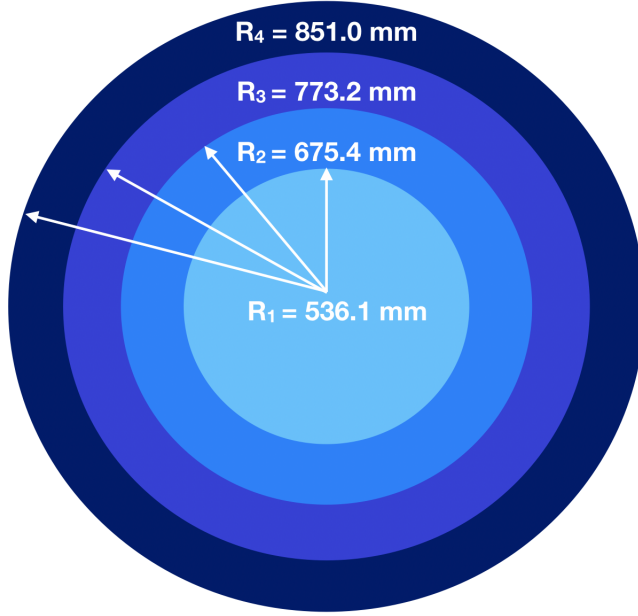


Figure 3.12: Cross-sectional diagram of the acrylic vessel, indicating four regions of equal LAr volume depicted by different shades of blue. The radii values R_1 , R_2 , R_3 and R_4 correspond to $(R_{\text{rec}}/R_0)^3$ values of 0.25, 0.5, 0.75 and 1 respectively.

generated uniformly across the detector volume.

Consider a set of events with the same true radial position R_{MC} , but a range of reconstructed radial positions R_{rec} . For values of R_{rec} greater than some cut-off radius R_{cut} , the cubic reconstructed radial distribution R_{rec}^3 can be well described by a Gaussian. In other words, $(R_{\text{rec}}/R_0)^3 \sim \text{Gaus}(\mu_C, \sigma_C)$, where μ_C is the mean reconstructed cubic radius and σ_C is the cubic radial resolution. For simplicity, everything is normalised to R_0 . For $R_{\text{rec}} > R_{\text{cut}}$, where the cubic reconstructed radial distribution can be modelled with a Gaussian, the linear radial bias is given by,

$$\mu/R_0 = (\mu_C)^{1/3} - R_{\text{MC}}/R_0. \quad (3.21)$$

This yields two linear radial resolution terms,

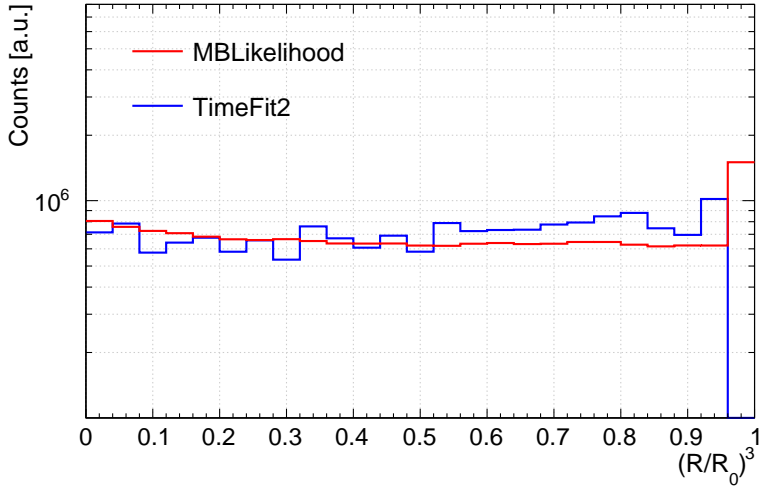


Figure 3.13: Cubed normalised reconstructed radius $(R_{\text{rec}}/R_0)^3$ for ^{39}Ar β -decays from the MBLikelihood position reconstruction algorithm (red) and TimeFit2 position reconstruction algorithm (blue).

$$\sigma_{\pm}/R_0 = |(\mu_C \pm \sigma_C)^{1/3} - \mu_C^{1/3}|, \quad (3.22)$$

where $\sigma_+ < \sigma_-$. This arises as a consequence of the fact that the $(R_{\text{MC}}/R_0)^3$ distribution is flat across the detector; for a constant change in $(R_{\text{rec}}/R_0)^3$, there is a larger change in (R_{rec}/R_0) for smaller values of R_{rec} compared to larger ones. To construct the resolution function, the smaller resolution term σ_+ is considered.

This prescription cannot be used for $R_{\text{rec}} < R_{\text{cut}}$, due to the fact that R_{rec} is truncated at $R_{\text{rec}} = 0$ and thus radii which are lower than the cut-off radius will be truncated at $R_{\text{rec}} = 0$ in the $(R_{\text{rec}}/R_0)^3$ distribution. Instead, for low radii, the reconstructed radial distribution is modelled with a Gaussian, $R_{\text{rec}} \sim \text{Gaus}(\mu, \sigma)$, where μ and σ are the linear radial bias and resolution parameters respectively. Studies performed using simulations of monoenergetic electrons generated at various fixed radial positions in the detector by Navin Seeburn in [3] show that the shell defined

by $R_{\text{MC}} = 553.15$ mm corresponds to a truncation in the $(R_{\text{rec}}/R_0)^3$ distribution $> 2\sigma$ deviation from the mean, and thus this value is chosen for R_{cut} .

The charge-dependent radial resolution function is obtained by studying how the linear radial bias and resolution parameters vary as a function of both `nSCBayes` and R_{rec} . To do this, ^{39}Ar β -decays are simulated at 18 different true radial positions R_{MC} between the centre and the edge of the detector. The values of R_{MC} that are chosen correspond to locations in the detector equally spaced in $(R_{\text{MC}}/R_0)^3$, between 0.05 and 0.95. The normalised linear bias and resolution parameters (μ/R_0 and σ/R_0) are calculated using the extracted Gaussian fit result parameters and Equations 3.21 and 3.22 for μ and σ as described above. Two example Gaussian fits to these distributions between 50 PE - 250 PE for $R_{\text{MC}} < R_{\text{cut}}$ and $R_{\text{MC}} > R_{\text{cut}}$ are shown in Figures 3.14 and 3.15 respectively.

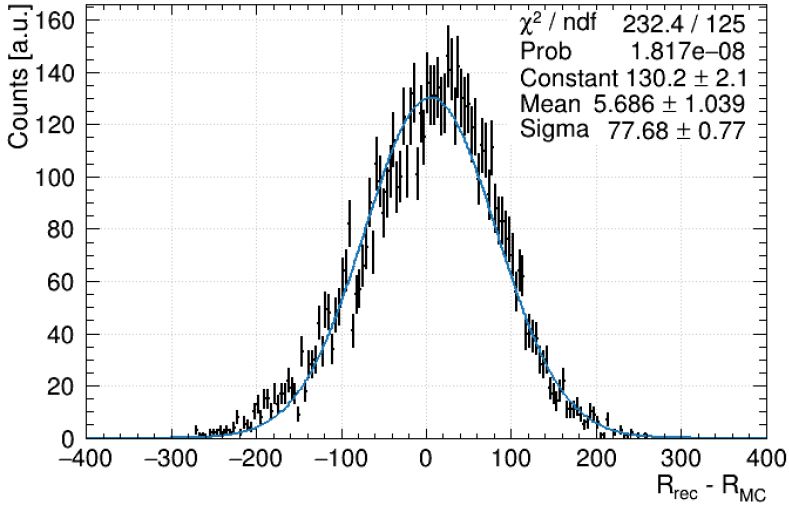


Figure 3.14: Gaussian fit to the $R_{\text{rec}} - R_{\text{MC}}$ [mm] distribution for simulated ^{39}Ar β -decays with $R_{\text{MC}} = 313.51$ mm in the 50 PE - 250 PE bin.

The μ/R_0 and σ/R_0 parameters are plotted as a function of $(R_{\text{MC}}/R_0)^3$ and each fit with a quintic polynomial, which describes how the reconstruction bias and resolution changes as a function of true radius. In order to account for the

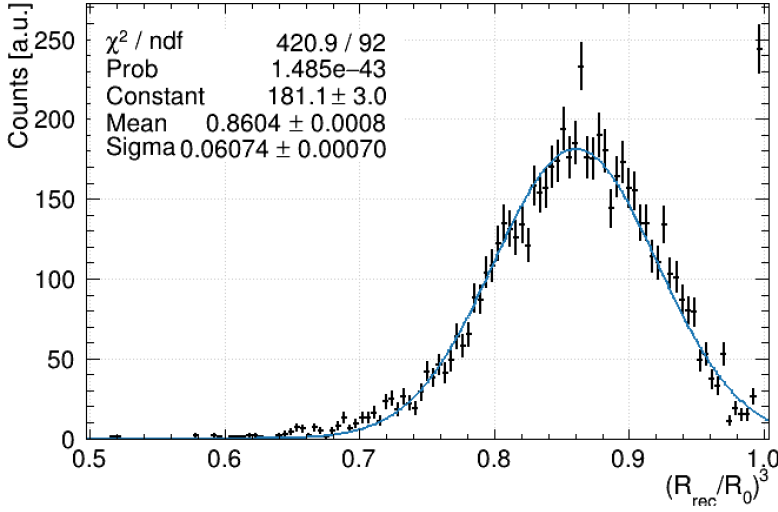


Figure 3.15: Gaussian fit to the $(R_{\text{rec}}/R_0)^3$ distribution for simulated ^{39}Ar β -decays with $R_{\text{MC}} = 821.63$ mm in the 50 PE - 250 PE bin.

charge-dependence on the radial resolution, this process is repeated for 15 bins in `nSCBayes`, starting from 50 PE and spanning out to 3050 PE. The evolution of each of the 6 parameters from the polynomials with `nSCBayes` are then described themselves with a quintic polynomial. Example polynomial fits to the linear bias and resolution parameters as a function of $(R_{\text{MC}}/R_0)^3$ between 50 PE - 250 PE are shown in Figures 3.16 and 3.17. The polynomial fits to the linear bias parameter were required to have a $\chi^2/\text{NDF} \leq 3$ and to the linear resolution parameters ≤ 7 ; for the resolution parameter, the χ^2/NDF is driven up by the choice to use σ_+ which causes a discontinuity at the cut-off radius. This charge-dependent radial resolution function is used to construct a two-dimensional model of ^{39}Ar β -decays in `nSCBayes- R_{rec}` parameter space required for the Profile Likelihood Ratio analysis, described later in Section 5.3.

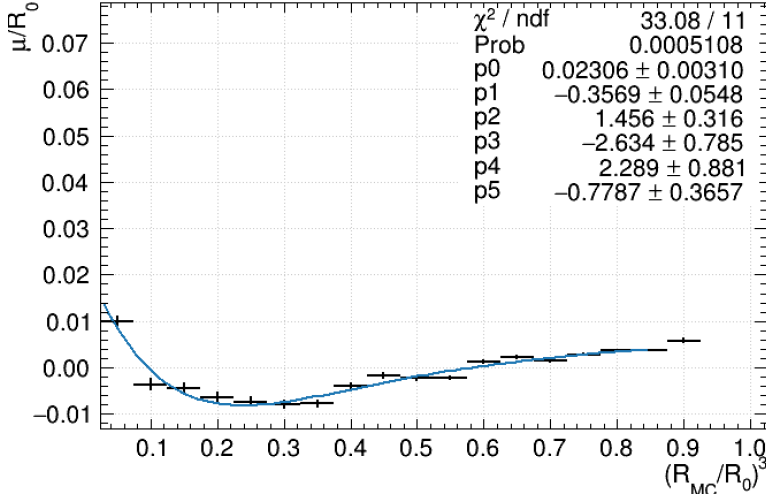


Figure 3.16: Linear radial bias as a function of truth MC reduced radius between 50 PE - 250 PE, fit with a quintic polynomial.

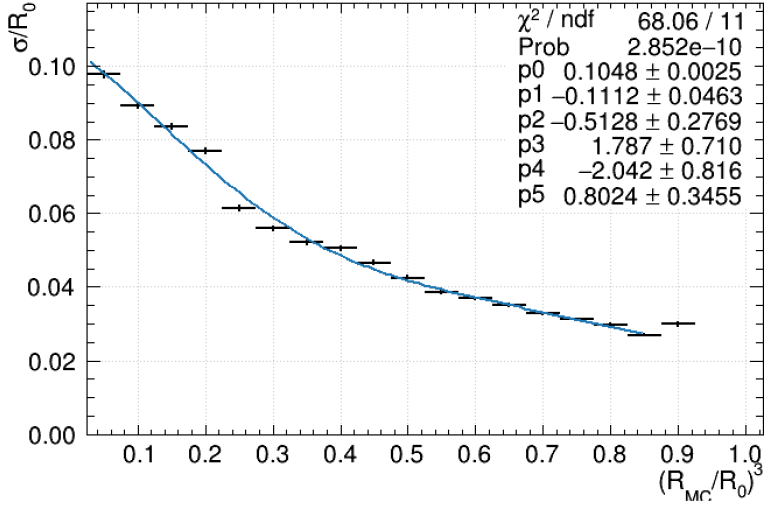


Figure 3.17: Linear radial resolution as a function of truth MC reduced radius between 50 PE - 250 PE, fit with a quintic polynomial.

Optical Model Reconstruction Bias

Out of all three reconstructed variables considered in this thesis, variations in the optical model parameters described in Sections 2.1.2 and 3.1.1 have the largest effect

on position reconstruction. This is demonstrated in Figure 3.18 for neck α -decays, one of the most significant background sources to the WIMP dark matter search. Figure 3.18 shows the two $(R_0 - R_{\text{rec}})$ [mm] distributions constructed using the charge-based position reconstruction algorithm (inside the WIMP ROI, 93 PE - 200 PE) constructed from MC simulations with the LAr refractive index, photon group velocity and Rayleigh scattering length parameters at their nominal values and at their $+1\sigma$ values. The correlations between these three parameters are already accounted for in these $+1\sigma$ variations, derived from the covariance between the Sellmeier coefficients.

Figure 3.18 shows that uncertainties in these particular optical model parameters can cause significant deviations in the reconstructed radial distribution. As discussed in Section 3.1.1, this also has a significant impact on the ROI background expectation for neck α -decays; by integrating the two distributions in Figure 3.18 between 0 - 800 mm in R_{rec} , the number of expected neck α -decays in the WIMP energy ROI when the optical model parameters are varied by $+1\sigma$ is found to be 15% less than the nominal case. Uncertainties on the optical model parameters are included as systematics in the Profile Likelihood Ratio software used to perform the WIMP dark matter search presented in this thesis, described in detail in Section 6.2.

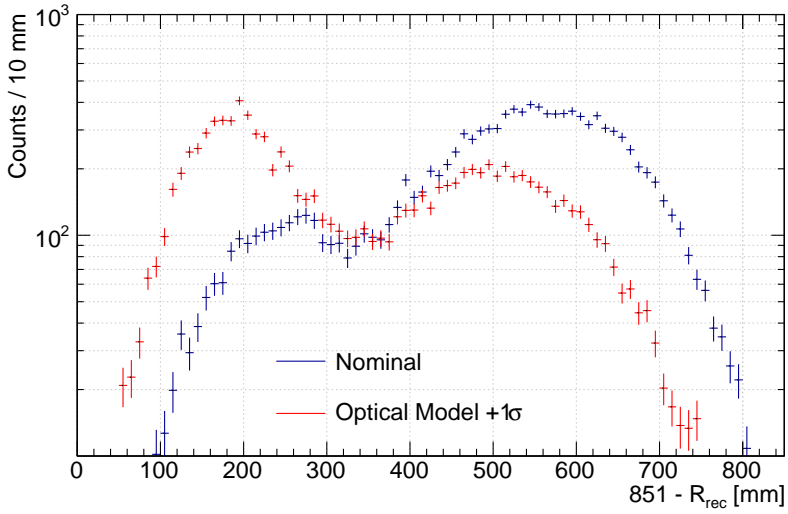


Figure 3.18: $(R_0 - R_{\text{rec}})$ [mm] distribution for neck α -decays constructed from MC simulations, with the LAr refractive index, photon group velocity and Rayleigh scattering length optical parameters at their nominal values (blue) and at their $+1\sigma$ variations (red).

Chapter 4

Review of Backgrounds in DEAP-3600

*“Physics is really nothing more than a search for ultimate simplicity,
but so far all we have is a kind of elegant messiness.”*

–Bill Bryson

FOR experiments searching for rare event signals, understanding the impact of background interactions is of the highest priority. DEAP-3600 has developed a comprehensive background model, with contributions from β -particles and γ -ray interactions, α -decays and neutrons. These backgrounds can originate from a variety of locations, such as from within the liquid argon target and from the surfaces and bulk of the surrounding detector component materials. This chapter reviews the relevant electronic recoil and nuclear recoil background sources considered in the Profile

Likelihood Ratio analysis, including a summary of their event topologies and rates in the detector.

4.1 Electromagnetic Recoils

4.1.1 ^{39}Ar Decay

INTRINSIC ^{39}Ar β -decays produce the highest trigger rate in the detector out of all of the background sources, providing a substantial data sample that is used in the Profile Likelihood analysis as a sideband to constrain systematics related to the energy scale. This section reviews the characterisation of the ^{39}Ar β -decay nSCBayes spectrum.

Overview

ARGON is the third most abundant gas on Earth, constituting approximately 0.93% of Earth's atmosphere by volume [96]. Argon contains the long-lived isotope ^{39}Ar , produced in the atmosphere by cosmic-ray interactions at a rate of (759 ± 128) atoms $\text{kg}^{-1} \text{ day}^{-1}$ at sea-level [96]. Since atmospheric argon is used to produce liquid argon (LAr) at dedicated facilities, where the argon is extracted from liquified atmospheric gas, there is a trace amount of ^{39}Ar present in LAr.

^{39}Ar has a half-life of $t_{1/2} = 268$ years [56] and decays by β^- emission into ^{39}K , releasing an electron antineutrino $\bar{\nu}_e$ in the process,

$$^{39}\text{Ar} \rightarrow ^{39}\text{K} + e^- + \bar{\nu}_e, \quad (4.1)$$

The specific activity of ^{39}Ar in LAr has been calculated to be 1.00 ± 0.02 (stat) ± 0.08 (syst) Bq/kg [57]. Consequently, DEAP-3600 has access to an extremely large sample of electronic recoils (ERs) events over the 3 year duration of the experiment. As ERs are not subject to nuclear quenching as described in Section 2.1.2, the ^{39}Ar

β -decay spectrum can be used to perform the energy calibration of the detector.

The β^- decay spectrum for a single transition in a nucleus of proton number Z and mass number A can be written as an expansion of the underlying electron wave functions [97],

$$S(E, Z, A) = S_0(E)F(E, Z, A)C(E)(1 + \delta(E, Z, A)), \quad (4.2)$$

where E is the total electron energy, E_ν is the total antineutrino energy, $E_0 = E + E_\nu$ is the endpoint energy, $F(E, Z, A)$ is the Fermi function that accounts for the Coulomb interaction between the outgoing electron and the daughter nucleus, $S_0(E) = G_F^2 p E (E_0 - E)^2 / 2\pi^3$, G_F is the Fermi coupling constant, p is the total electron momentum and $C(E)$ is the shape factor required for forbidden transitions. The decay spectrum is also subject to a number of additional corrections, $\delta(E, Z, A)$, as described below.

^{39}Ar β -decay is a unique first forbidden transition, which is a parity-violating decay characterised by a spin-parity change of $|\Delta\vec{J}|^\pi = 2^- \ (\frac{7}{2}^+ \rightarrow \frac{3}{2}^-)$. The “forbiddenness” of a β -decay is a measure of how suppressed the transition probability is, which depends on the difference between the initial state nuclear spin (7/2) and parity (+) of the parent nuclei and final state nuclear spin (3/2) and parity (−) of the daughter nuclei, $(|\Delta\vec{J}|, \Delta\pi)$. The larger the value of $|\Delta\vec{J}|$, the more forbidden a transition is. Decays which violate parity are also more forbidden than decays which do not violate parity. Unique decays are parameterised by $|\Delta\vec{J}| = 2$. Forbidden decays exhibit a different spectral shape to allowed decays, characterised by an energy-dependent shape factor $C(E)$ that parameterises all information of the underlying nuclear structure [98]. For allowed transitions, the shape factor $C(E) = 1$.

Other effects can also alter the shape of the decay spectrum; these include, but are not limited to atomic screening, radiative effects and weak magnetism: $\delta(E, Z, A) = \delta_s + \delta_r + \delta_{wm}$. These particular corrections are considered in this

thesis as they have been already calculated and/or parameterised in literature, discussed below. Atomic screening corrections to the Coulomb function account for the decrease in charge “seen” by the outgoing electron from the nucleus, which is shielded by atomic electrons [99]. Radiative corrections account for the reduction in outgoing electron energy from bremsstrahlung and virtual photon emission in the electromagnetic field of the nucleus [100]. Weak magnetism corrections are induced by the vector current component of the axial-vector (V-A) theory of the weak interaction [99].

4

Modelling the ^{39}Ar β -decay Spectrum

THE energy response of the DEAP-3600 detector is obtained from fitting ^{39}Ar physics-triggered data with a model that relates the true energy of an event in [keV] to the reconstructed energy in `nSCBayes` [PE]. The fit function calculates the amplitude for each [PE] bin in data by evaluating the joint probability of the theoretical ^{39}Ar β -decay spectrum, $S(E)$, with a Gaussian detector response model,

$$f_0(PE) = \int_0^{E_{\max}} S(E) \frac{1}{\sqrt{2\pi\sigma^2(PE)}} e^{-\frac{1}{2}\left(\frac{PE - \mu(E)}{\sigma(PE)}\right)^2} dE, \quad (4.3)$$

where E_{\max} is the maximum energy that the function is evaluated over, $\mu(E)$ is the expected number of PE and $\sigma(PE)$ is the energy resolution. The expected number of PE is a function of the true energy, and can be described with three energy scale parameters, a_0 , a_1 and a_2 ,

$$\mu(E) = a_0 + a_1 \cdot E + a_2 \cdot E^2. \quad (4.4)$$

The energy resolution is a function of the expected number of PE, and can also be described with three parameters, c_0 , c_1 and c_2 ,

$$\sigma(PE) = \sqrt{c_0 + c_1 \cdot PE + c_2 \cdot PE^2}, \quad (4.5)$$

Typically, the parameters a_2 , c_0 and c_2 are fixed to zero, as they are not physically motivated.

Two additional background contributions are included in the total fit function applied to data. These include ^{39}Ar coincidence events, defined as when two individual ^{39}Ar β -decays appear in the same 10 μs event waveform, and other ER backgrounds from internal and external β/γ -ray interactions, described in Section 4.1.2. For both of these contributions, the theoretical spectrum $S(E)$ is replaced with a histogram obtained from Monte Carlo (MC) simulations of the total energy deposited in the LAr in [keV]. Assuming the particle loses all of its energy in the LAr, the total deposited energy is equivalent to the kinetic energy. Figure 4.1 shows the single ^{39}Ar theoretical spectrum $S(E)$, the coincidence ^{39}Ar spectrum from MC simulations $B_0(E)$ and the ER spectrum from other β/γ background sources from MC simulations $B_1(E)$, all normalised to unit area. The total fit function is written as,

$$\begin{aligned} f(PE) = & N_0 \cdot \int_0^{E_{\max}} S(E) \frac{1}{\sqrt{2\pi\sigma^2(PE)}} e^{-\frac{1}{2}\left(\frac{PE - \mu(E)}{\sigma(PE)}\right)^2} dE \\ & + \sum_i^{N_{\text{Bkgd}}} N_i \cdot \int_0^{E_{\max}} B_i(E) \frac{1}{\sqrt{2\pi\sigma^2(PE)}} e^{-\frac{1}{2}\left(\frac{PE - \mu(E)}{\sigma(PE)}\right)^2} dE, \end{aligned} \quad (4.6)$$

where N_0 is an overall normalisation parameter related to the ^{39}Ar rate, $N_{\text{Bkgd}} = 2$ is the total number of background sources and N_i are normalisation parameters related to the rates of coincidence ^{39}Ar and other ER β/γ backgrounds. The physics trigger rates of coincidence ^{39}Ar events and ER β/γ events are estimated to be $< 0.2\%$ and $< 0.4\%$ of the physics trigger rate of single ^{39}Ar events respectively. E_{\max} is set at

900 keV to ensure that all background components are properly accounted for near the ^{39}Ar endpoint, $E_0 = 565 \pm 5$ keV [101].

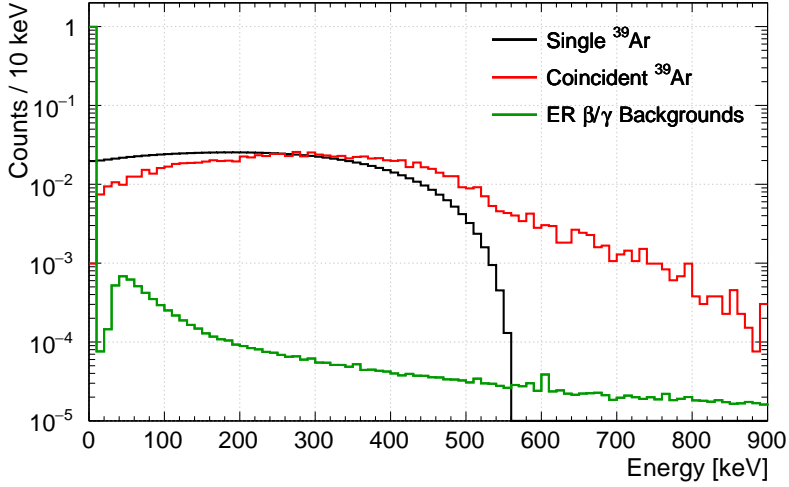


Figure 4.1: Energy spectra [keV] of all three components used in the total fit function defined in Equation 4.6 to fit ^{39}Ar physics-triggered data: single ^{39}Ar (black), coincidence ^{39}Ar (red) and other ER β/γ background (green). For shape comparison, all histograms are normalised to unit area.

The theoretical ^{39}Ar spectrum $S(E)$ used for the fit is obtained from the BetaShape [100] program, written by X. Mougoet. The program can be used to calculate the theoretical energy spectrum for a variety of allowed and forbidden β -decays, for a set of input parameters such as the average energy, endpoint energy, half-life and $\log(ft)$ value. The ft value is referred to as the comparative half-life, given by $\ln(2) \propto |M|^2 ft_{1/2}$, where $|M|$ is the nuclear matrix element that characterises the change in wave function during the β -decay [102]. BetaShape calculates the theoretical shape factor $C_{\text{theo}}(E)$ for the unique first forbidden ^{39}Ar β -decay using the following expression [100],

$$C_{\text{theo}}(E) = (2L - 1)! \sum_{k=1}^L \lambda_k \frac{p^{2(k-1)} q^{2(L-k)}}{(2k - 1)! [2(L - K) + 1]!}, \quad (4.7)$$

where $L = \Delta J = 2$, p and q are the total momenta of the electron and antineutrino respectively, and λ_k are parameters of the Coulomb function, which typically have values close to unity. The Coulomb function describes how charged particles behave in the presence of a Coulomb field.

However, it has been experimentally observed for unique first forbidden β -decays that the experimental spectral shape deviates from the theoretical “unique” spectral shape predicted by $C_{\text{theo}}(E)$. In [103], this deviation is attributed to “third-forbidden contributions and weak magnetism effects”, and is modelled by the following expression,

$$\frac{C_{\text{exp}}(E)}{C_{\text{theo}}(E)} = C_{\text{dev}}(E) = 1 + a_{\text{dev}} \cdot E, \quad (4.8)$$

where E is the total electron energy and a_{dev} is a parameter that can be deduced from a fit to data.

Since BetaShape also allows the user to switch on and off screening and radiative corrections, one is able to probe the effect that these corrections have on the shape of the ^{39}Ar β -decay spectrum. BetaShape is used to calculate the theoretical ^{39}Ar β -decay spectrum with each of these corrections switched on one at a time, $S_s(E)$ and $S_r(E)$, and then compared with the spectrum without corrections, $S_0(E)$. Deviations in the shape of the spectrum can be seen in Figure 4.2, for $S_s(E)/S_0(E)$ and $S_r(E)/S_0(E)$ (for screening and radiative corrections respectively). Figure 4.2 shows that radiative corrections have a negligible effect, whilst screening corrections can cause up to a 0.6% deviation in the shape of the β -decay spectrum. As such, only the effect of screening corrections are considered in this thesis.

In order to account for deviations in the experimental spectral shape, Equation 4.6 is modified to include an additional parameter for a_{dev} from Equation 4.8, yielding the final fit function,

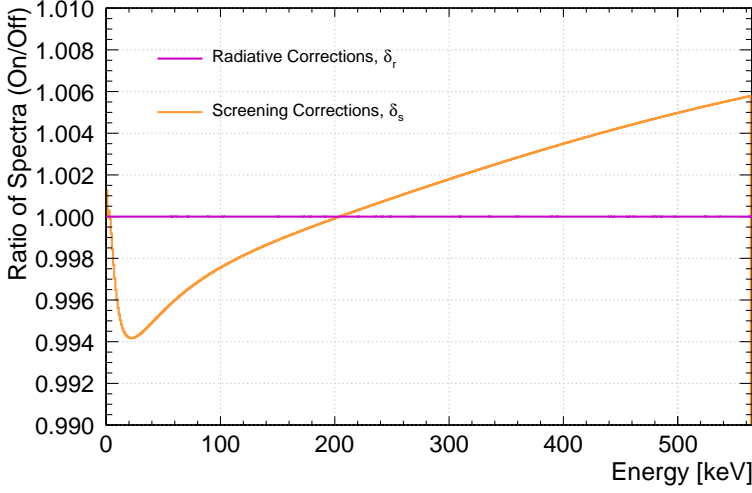


Figure 4.2: Deviations in the theoretical ^{39}Ar β -decay spectrum due to the effects of screening (orange) and radiative (pink) corrections. Quantities shown are $S_s(E)/S_0(E)$ and $S_r(E)/S_0(E)$ for screening and radiative corrections respectively, as a function of energy [keV]. Only screening has a noticeable effect on the shape of the spectrum, causing up to 0.6% deviation.

$$\begin{aligned}
 f(PE) = & N_0 C_{\text{dev}}(E) \cdot \int_0^{E_{\text{max}}} S_s(E) \frac{1}{\sqrt{2\pi\sigma^2(PE)}} e^{-\frac{1}{2}\left(\frac{PE-\mu(E)}{\sigma(PE)}\right)^2} dE \\
 & + N_1 C_{\text{dev}}^2(E) \cdot \int_0^{E_{\text{max}}} B_1(E) \frac{1}{\sqrt{2\pi\sigma^2(PE)}} e^{-\frac{1}{2}\left(\frac{PE-\mu(E)}{\sigma(PE)}\right)^2} dE \\
 & + N_2 \cdot \int_0^{E_{\text{max}}} B_2(E) \frac{1}{\sqrt{2\pi\sigma^2(PE)}} e^{-\frac{1}{2}\left(\frac{PE-\mu(E)}{\sigma(PE)}\right)^2} dE.
 \end{aligned} \tag{4.9}$$

where $S_s(E)$ is the theoretical ^{39}Ar β -decay spectrum from BetaShape with the screening corrections turned on. The deviation term C_{dev} is squared in the case of ^{39}Ar coincidence, since the ^{39}Ar coincidence spectrum can be, to a good approximation, treated as the single ^{39}Ar β -decay spectrum convolved with itself.

An example fit to the nSCBayes distribution of ^{39}Ar physics-triggered data using this functional form is shown in Figure 4.3 for one run of exposure 1.013 live-days.

Only basic low-level and pile-up cuts are applied to the data; fiducial cuts are not applied as this could introduce a bias from position dependence in the detector. Figure 4.4 shows the relative residuals in [%] between the best fit model and the data, defined as $(\text{data} - \text{model})/\text{data}$. The fit is performed between 100 PE and 3200 PE using a binned likelihood analysis. From this fit, the light yield and energy resolution of the detector are found to be $a_1 \equiv \text{LY} = 6.153 \pm 0.003$ [PE/keV] and $\sigma^2(\text{PE}) = (1.51 \pm 0.13)$ [PE²] respectively; however, these values have been shown to fluctuate by approximately 3% as the detector stability changes.

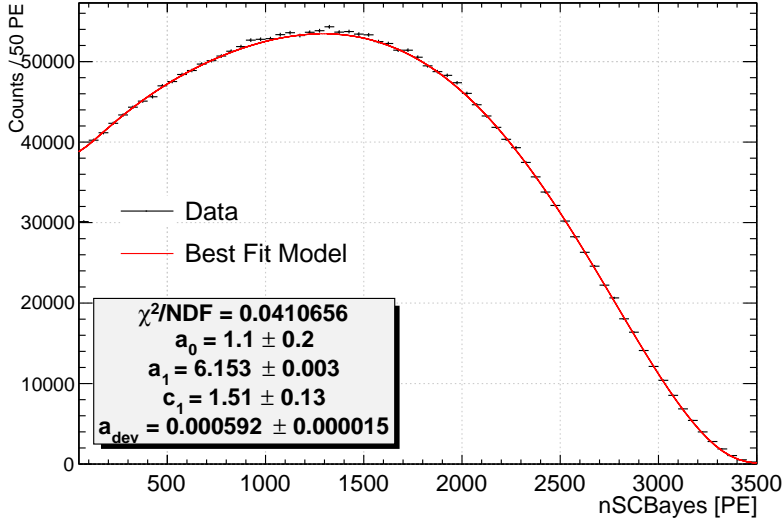


Figure 4.3: Example fit (red) to the ^{39}Ar nSCBayes spectrum from physics-triggered data (black) using functional form defined in Equation 4.9 for one run with exposure 1.013 live-days. Fit range considered is 100 PE - 3200 PE. Also shown are the χ^2 statistic per degrees of freedom (NDF), the linear and offset energy scale parameters a_0 , a_1 , the linear energy resolution parameter c_1 and the experimental shape deviation parameter a_{dev} .

Over the duration of the experiment, the mean light yield has been observed to drift. This is illustrated by Figure 4.5, which shows the mean light yield parameter a_1 extracted from the fit to the ^{39}Ar spectrum, as a function of run number. The range of run numbers shown in this plot corresponds to one full year of data-taking,

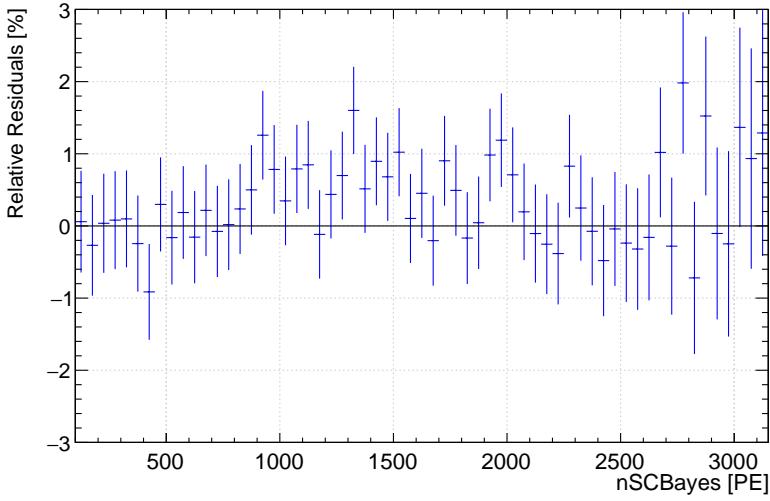


Figure 4.4: Relative residuals in [%] between the best fit model and ^{39}Ar nSCBayes spectrum from physics-triggered data shown in Figure 4.3 as a function of nSCBayes [PE]. Residuals are defined as (data - model)/data.

equating to 231 live-days of exposure. Figure 4.5 demonstrates that in one year of data-taking, the mean light yield shifts from ~ 6.2 PE/keV to ~ 6 PE/keV. The uncertainty on the mean light yield is one of the largest systematics on the WIMP dark matter search. For example, in the WIMP region-of-interest (ROI) energy range of $15 < E_{ee} [\text{keV}] < 30$, a light yield increase of 0.2 from 6 PE/keV would increase the predicted number of WIMP ROI events by 5%. Reducing the uncertainty on this parameter is therefore vital for improving the detector's sensitivity to dark matter.

Similarly to Figure 4.5, the fluctuation of the ^{39}Ar rate over the course of the 231 live-day dataset has also been quantified on a run-to-run basis; this is illustrated by Figure 4.6, which shows the mean ^{39}Ar rate as a function of run number. The rate is calculated by integrating over the best fit function between 100 PE - 3500 PE and dividing by the livetime of the run. The lower bound is chosen to be where the trigger efficiency is expected to be 100%. The mean rate is found to be at 2940 Hz. This calculated rate is expected to be smaller than the actual rate, by up to 10%:

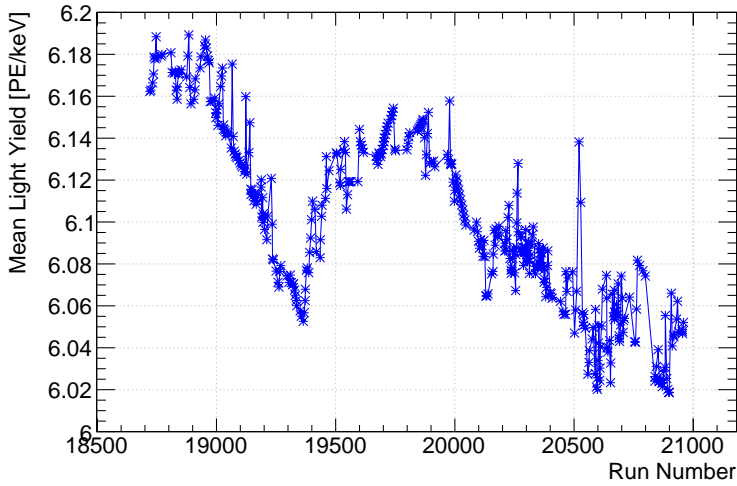


Figure 4.5: Mean light yield [PE/keV] of the DEAP-3600 detector, extracted from fits to the ^{39}Ar nSCBayes spectrum from physics-triggered data, as a function of run number [equivalent to time]. The range of run numbers shown in this plot corresponds to one full year of data-taking (231 live-days exposure). Over one year of data-taking, the mean light yield is observed to drift from ~ 6.2 PE/keV to ~ 6 PE/keV.

the basic data cleaning-cuts applied to this data have a 94% acceptance and events with nSCBayes < 100 PE are not included in the calculation. Figure 4.6 shows that the ^{39}Ar rate is stable during the 231 live-day dataset to within 0.5%.

4.1.2 Internal & External β/γ -ray Interactions

RADIOACTIVITY in various detector materials can produce β -particles and γ -rays with the potential to produce additional ER background signals on top of the dominant background from ^{39}Ar β -decay. The total activity of these various additional β/γ -ray backgrounds were measured in-situ by the DEAP-3600 collaboration [104], the results of which are summarised in this section.

β/γ backgrounds from intrinsic detector radioactivity can be split into two categories:

- *Internal sources:* backgrounds originating from within the LAr target or from

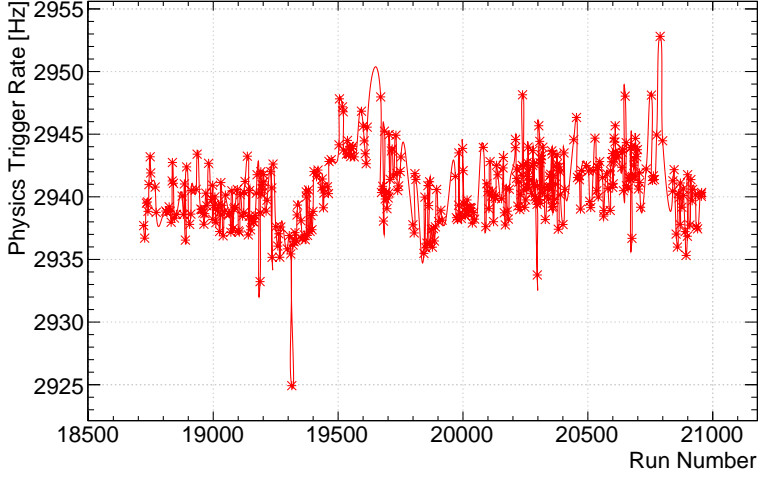


Figure 4.6: Mean ^{39}Ar rate [Hz] of the DEAP-3600 detector, determined from integrating the function fit to the ^{39}Ar `nSCBayes` spectrum from physics-triggered data between 100 PE - 3500 PE, as a function of run number [equivalent to time]. The range of run numbers shown in this plot corresponds to one full year of data-taking (231 live-days exposure). Over one year of data-taking, the ^{39}Ar rate is stable to within 0.5%.

the inner detector surfaces (TPB layer/ acrylic vessel surface), or

- *External sources:* backgrounds originating from the acrylic vessel bulk, the PMTs or the stainless steel shell.

Excluding ^{39}Ar β -decay, the various internal and external sources are summarised below.

LAr target: trace amounts of Argon-42 (^{42}Ar), another long-lived isotope of argon, are also measured to be present in the LAr. Similarly to ^{39}Ar , it decays via β^- emission with an energy endpoint $E_0 = 599 \pm 6$ keV [104]. However, the specific activity of ^{42}Ar is ~ 4 times smaller than ^{39}Ar and thus it is subdominant [104]. The β -decay of its daughter however, Potassium-42 (^{42}K), has an endpoint energy of $E_0 = 3525.2 \pm 0.2$ keV [104] and is therefore significant at higher energies. The β -decays of Bismuth-214 (^{214}Bi) and Thallium-208 (^{208}Tl), with respective endpoint

energies of 3270 keV and 4999 keV [104], also contribute to the high energy spectrum. ^{214}Bi and ^{208}Tl originate from radon gas, which can enter the inner detector via the process systems described in Section 2.2.4. Potential contamination of LAr with Krypton-85 (^{85}Kr) was not considered in this model, as a dedicated analysis showed the contribution to be negligible (0.1% of the specific activity of ^{39}Ar). This study is described in detail in Section 4.1.3.

TPB layer, acrylic vessel surface: the dominant background contribution comes from the β -decay of ^{210}Bi . This is identified as the dominant contribution from the measurement of Polonium-210 (^{210}Po) α -decays originating from the acrylic vessel bulk and/or interface between the TPB and acrylic vessel. Primordial long-lived Lead-210 (^{210}Pb) residing on the surfaces of the TPB and acrylic vessel can decay into ^{210}Bi via β^- emission. ^{210}Bi has a much shorter half-life ($t_{1/2} \sim 5$ days) than ^{210}Pb , and decays via β^- emission with an endpoint energy of 1162 keV [104].

Acrylic vessel/ light guide bulk: All isotopes below Radium-226 (^{226}Ra) in the Uranium-238 (^{238}U) decay chain that emit β -particles and γ -rays are considered in the background model [104]. At high energies, characteristic γ -rays of 2614 keV [104] produced during the β^- decay of primordial ^{208}Tl , from the Thorium-232 (^{232}Th) decay chain, could also be significant to the energy spectrum; it is unlikely for β -particles to enter the LAr, but the γ -ray does have enough energy to reach the LAr after multiple scatters and produce a signal.

PMTs: the majority of external ER background comes from the PMT components, in particular, the PMT glass. Neutrons produced in (α, n) reactions in the borosilicate glass can be captured via (n, γ) reactions in surrounding detector materials, producing γ -rays in multiple locations spanning a wide energy range (up to 10 MeV [104]). High energy γ -rays produced through the primordial decay series of ^{226}Ra , ^{232}Th and Potassium-40 (^{40}K) are also included for all PMT components, which are all still energetic enough to reach the LAr [104].

Stainless steel shell: only γ -rays from the primordial decay series of ^{226}Ra and ^{232}Th , like the PMTs, have a high enough energy to reach the LAr from the steel shell. The steel shell also contains small amounts of Cobalt-60 (^{60}Co), which also produces high energy γ -rays.

The total activity of β/γ backgrounds in the DEAP-3600 detector is determined from fitting the low F_{prompt} qPE spectrum in data ($F_{\text{prompt}} < 0.55$) with a model comprised of all the background components described above and ^{39}Ar . The predicted spectra from each background component is generated using MC simulations, and fit to the data up to ~ 5 MeV (~ 30000 PE). The fit is performed using the Bayesian Analysis Toolkit (BAT) software [105] on the aforementioned 231 live-day exposure dataset from Section 4.1.1 and shown in Figure 4.5, with only basic data-cleaning cuts applied such as low-level cuts and pile-up cuts. The summed best fit result and data are shown in the top panel of Figure 4.7; also shown are the contributions from each individual background component. The bottom panel of Figure 4.7 shows the relative residuals between the best fit model and the data, with the 1, 2 and 3σ confidence bands from the uncertainty as calculated by the user-defined likelihood function utilised by the BAT software.

Excluding the ^{39}Ar contribution, the total activity of other β/γ backgrounds in the DEAP-3600 detector is calculated to be $\mathcal{A}_{\text{ER}} = 1046.67$ Bq. However, as the majority of external sources do not actually make it into the LAr to produce a detectable signal, the total physics trigger rate is significantly lower than the total activity. The total β/γ background physics trigger rate is calculated to be $\mathcal{R}_{\text{ER}} = 12.2$ Hz. The ^{39}Ar -subtracted β/γ background energy spectrum obtained from this analysis, as discussed earlier in Section 4.1.1, is included as an additional component in the fit to the ^{39}Ar β -decay spectrum. The spectrum is shown in Figure 4.1. The total physics trigger rate \mathcal{R}_{ER} is used as the prior normalisation for this β/γ background component, $N_2 = 12.2$ Hz, in Equation 4.9.

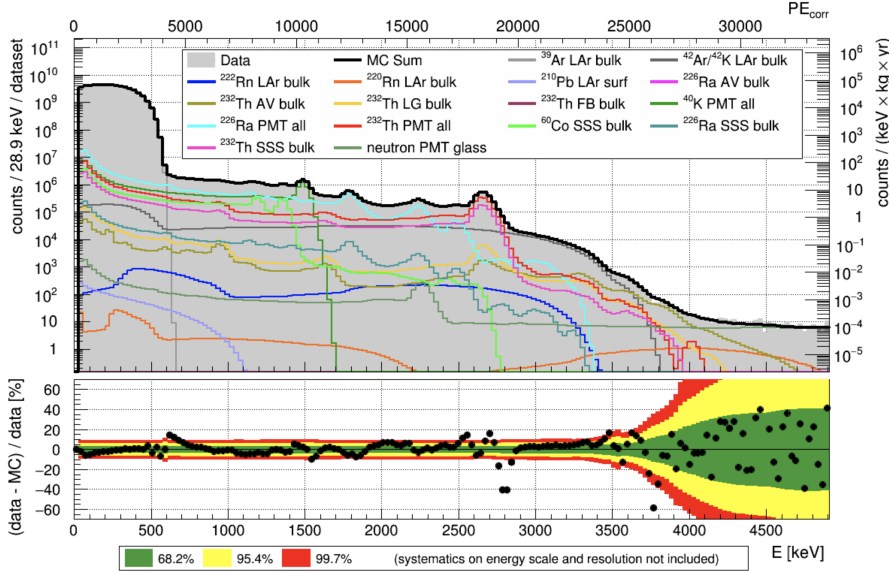


Figure 4.7: Top: β/γ ER background energy spectrum in data (grey) [keV], shown with the summed best fit result from all background contributions (black). Each background contribution, scaled to its best fit activity, is also shown in varying colours. Bottom: relative residuals between the data and the best fit result [%]. The 1, 2 and 3σ confidence bands calculated by BAT are shown in green, yellow and red respectively. From [104].

4.1.3 ^{85}Kr Decay

SINCE LAr is made from atmospheric argon, the LAr used by the DEAP-3600 Experiment could be contaminated with atmospheric Krypton-85 (^{85}Kr), which could give rise to additional backgrounds in the ER band. To assess the impact of potential ^{85}Kr background, an in-situ measurement of the ^{85}Kr activity was performed. ^{85}Kr was an important background in the DarkSide-50 LAr dark matter search, which further motivated this dedicated measurement. This analysis showed that the activity of ^{85}Kr is negligible in comparison to the other dominant background contributions in the same energy regime, and thus the decision was made to not include ^{85}Kr in the overall DEAP-3600 background model or the Profile Likelihood Ratio analyses.

Overview

KRYPTON-85, an isotope of Krypton, is produced in Earth's atmosphere from both natural and anthropogenic processes. ^{85}Kr is produced naturally in the atmosphere due to interactions between cosmic-rays and stable Krypton-84. The abundance of ^{85}Kr produced naturally is small however compared to the abundance of ^{85}Kr produced at nuclear power plants via the nuclear fission of ^{235}U . At the time of publication, the artificial production rate of ^{85}Kr was estimated as 3916 PBq per year; eight orders of magnitude greater than the natural production rate, which at the time of publication, was estimated as 26 GBq per year [106].

^{85}Kr is an unstable isotope of half-life $t_{1/2} = 10.76$ years, that decays into stable Rubidium-85 (^{85}Rb), via two main decay channels. The most probable channel (99.57%) is via β -decay, with a maximum and average energy of 687 keV and 251 keV respectively. The second most probable channel (0.43%) consists of two separate decays: the first to a metastable state of ^{85}Rb through β^- emission with maximum energy of 173 keV, the second to a stable state of ^{85}Rb by the emission of a single γ -ray of fixed energy 514 keV.

In-Situ ^{85}Kr Activity Measurement

THE ^{85}Kr activity is determined by searching for evidence of ^{85}Kr decay in the detector. Due to the high rate of ^{39}Ar β -decays (~ 3300 per second), only the second decay channel was considered for the search, as the experimental signature of the first decay channel would be difficult to distinguish from ^{39}Ar . ^{85}Kr that decays through the second channel in the DEAP-3600 detector manifests as two time-correlated ERs caused by the separate β^- and γ -ray emissions: the time difference Δt between these two recoils follows an exponential relationship with mean lifetime of $\tau = 1.464$ μs , which can be exploited for background rejection.

For this search, the dominant background is the coincidence of two ^{39}Ar β -

decays, producing two uncorrelated ERs of energies comparable with the energies expected from the two-stage ^{85}Kr decay. Since the coincidence of two independent ^{39}Ar β -decays is a random process, the Δt between two coincidence ^{39}Ar decays does not follow an exponential relationship. This time difference can be used to differentiate between background (coincidence ^{39}Ar β -decays) and signal (^{85}Kr decays) by searching for an exponential on top of a flat continuum in the Δt distribution.

A processor named `multievent`, developed by previous DEAP-3600 PhD student Tom McElroy for the purpose of identifying candidate coincidence/pile-up events, is used in this analysis. When two separate particle interactions occur within the same 10 μs DAQ event window, this is referred to as a pile-up event. The processor searches for evidence of more than one physics event occurring in the event window by determining whether the distribution of pulse times and charges are more consistent with a single cluster of pulses or multiple clusters. The output of the processor is the `subeventN` variable, which returns an integer value corresponding to the number of suspected independent physics clusters, or “subevents”, occurring in the event window.

To select candidate ^{85}Kr decays, only events with `subeventN` = 2 are considered for analysis. Other cuts applied in order to select candidate events include low-level and fiducial cuts (as outlined in Section 3.2.2). The `multievent` processor not only outputs the `subeventN` variable, but also estimates the times, relative to the start of the 10 μs DAQ event window, that each of the subevents occur. For a candidate `subeventN` = 2 event, these times are denoted $t_{\text{sub},0}$ and $t_{\text{sub},1}$ respectively; these times are used to define the time difference between the two subevents, $\Delta t = t_{\text{sub},1} - t_{\text{sub},0}$.

The probability of a second ^{39}Ar β -decay occurring in a time window t of 10 μs given a decay has already occurred can be calculated using the Poisson distribution,

$$P(k=1; r, t) = \frac{(rt)^k e^{-rt}}{k!} \equiv \frac{(rt)^1 e^{-rt}}{1!}, \quad (4.10)$$

where r is the ^{39}Ar decay rate, ~ 1 Bq/kg. This yields a coincidence probability of 3%. If all of these coincidence events were included in the dataset used for the ^{85}Kr search, the background would completely dominate the Δt distribution. To reduce the background contamination, instead of looking at the Δt distribution over all energies, only a specific energy range is considered. For this particular decay channel, the only part of the process which is identical for every ^{85}Kr decay is the energy of the single γ -ray as metastable ^{85}Rb decays into stable ^{85}Rb . By only analysing the Δt distribution for candidate events where the energy of the second subevent is 514 keV, a considerable amount of coincidence ^{39}Ar background can be eliminated. However, trying to decouple the true energies of the two subevents is not trivial.

As discussed in Section 3.2.1, the total energy of an event is expected to be contained within the range $[T_0 - 28 \text{ ns}, T_0 + 10 \mu\text{s}]$ of the event waveform, where T_0 is the event time. The upper limit of this range is chosen to ensure that, given LAr scintillation properties, all of the scintillation light generated by an event is recorded. This means that for events with `subeventN` = 2 and $\Delta t < 10 \mu\text{s}$, the measured energy of the second subevent will include some of the scintillation light from the first subevent and thus the observed energy of each subevent is greater than the true energy. Without knowing the true energy of the subevent, it is not possible to only select candidate events where the energy of the second subevent is 514 keV. In light of this, a new processor was developed to correct for light leakage from the first subevent into the second subevent on an event-by-event basis.

Calibrated waveforms of single ^{39}Ar events are stacked on top of one another to create an averaged single ^{39}Ar waveform of $10 \mu\text{s}$ length. Based on their charge, events are split into five different categories, resulting in five different averaged

waveforms. The energy leakage as a function of time after the event is calculated, for each of these five charge bins. The fraction of energy leaking after a time t is calculated, for each averaged waveform $\psi(t)$, by,

$$f_{\text{leak}} = \frac{\int_{t_i}^{10\mu s} \Psi(t) dt}{\int_{-28\text{ns}}^{10\mu s} \Psi(t) dt}, \quad (4.11)$$

for varying values of t_i . The numerator is the integral of the waveform from a time t_i to the end of the waveform, and the denominator is the integral of the full waveform. This equation yields the fraction of the total energy of the first subevent, f_{leak} , that leaks into the calculation of the second subevent energy given the Δt between the event time of the first subevent and the beginning of the energy window of the second subevent.

The subevent energy correction was calculated using calibrated single ^{39}Ar waveforms from both MC simulations and data, so that the correction can be correctly applied to both MC and data events accordingly. Events are split based on their prompt charge **promptPE** defined by Equation 3.17, instead of total charge since in real data, the true energy of the first subevent is unknown. Figure 4.8 shows f_{leak} as a function of Δt for ^{39}Ar data for two of the five different **promptPE** bins. Using these f_{leak} curves and the Δt between the two subevents, the corrected energy of the second subevent can be determined.

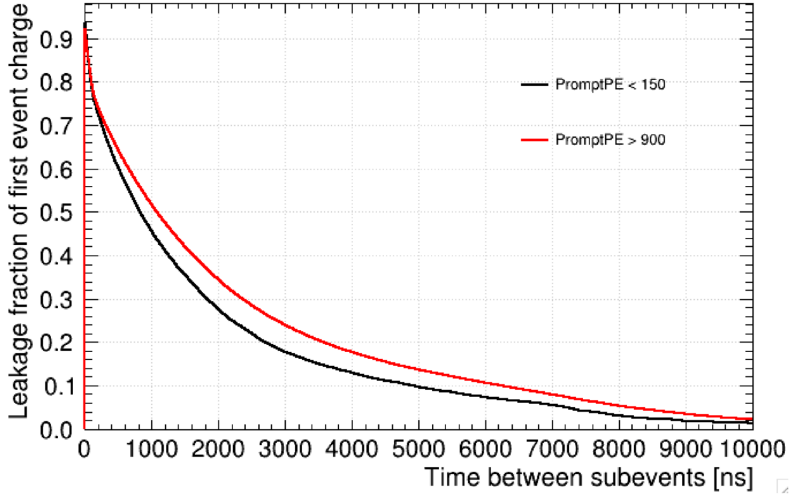


Figure 4.8: Fraction of the first subevent energy which leaks into the energy window of the second subevent, f_{leak} as a function of Δt , obtained from single ^{39}Ar events in data. The f_{leak} distribution is shown for two different energy bins, `promptPE < 150` and `promptPE > 900`.

The subevent energy correction method is verified using MC simulations of background coincidence ^{39}Ar β -decays and signal ^{85}Kr decays, where the true energies of the two individual subevents are known. There are only two requirements made on the simulated events at this stage, these are:

- The event caused a trigger in the detector, and
- The `multievent` processor identified `subeventN = 2`.

The subevent energy correction is first tested on the background events. The two-dimensional distributions of the second subevent energy versus the Δt between the two subevents for coincidence ^{39}Ar β -decays before and after applying the subevent energy correction are shown in Figures 4.9 and 4.10.

For random processes, such as coincidence ^{39}Ar β -decays, the Δt distribution should be flat. As shown in Figure 4.9, before applying a subevent energy correction, for smaller values of Δt the second subevent energy is higher than it should be,

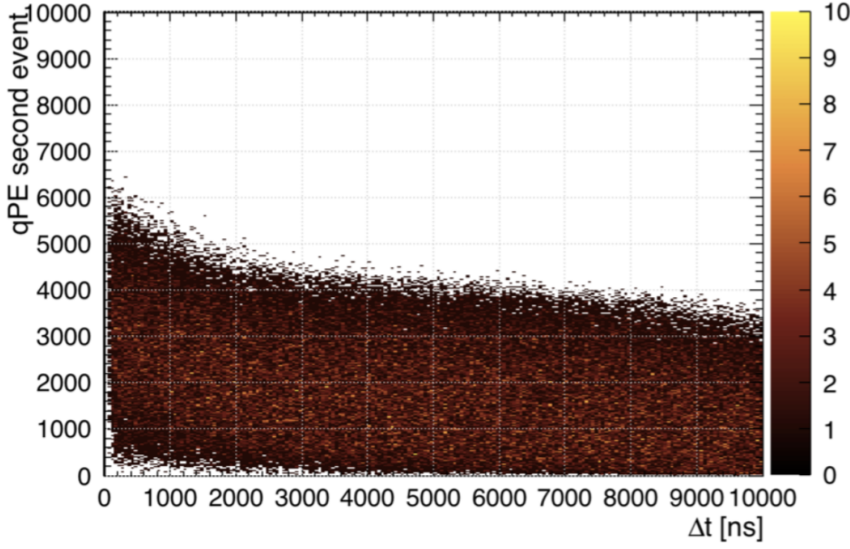


Figure 4.9: Two-dimensional distribution of the second subevent energy against Δt between the two subevents for two simulated coincidence ^{39}Ar β -decays before applying a subevent energy correction on the second subevent. The upturn at low Δt values demonstrates the leakage of the first subevent into the second subevent energy window.

resulting in an upturn in the distribution. Once the subevent energy correction is applied in Figure 4.10, this effect is no longer visible and by eye, the distribution looks “flat”. The downward slope in the distribution after a Δt of approximately 4 μs is expected. The second subevent energy is estimated by considering the time window $[t_{\text{sub},1} - 28 \text{ ns}, t_{\text{sub},1} + 10 \mu\text{s}]$, however given that the 10 μs acquisition window starts with respect to the time of the first subevent, for increasing values of Δt , the more scintillation light from the second subevent will be missed by the 10 μs acquisition window.

A more quantitative sanity check was performed by comparing the projection of Figure 4.10 onto the y -axis with the nominal MC simulated single ^{39}Ar β -decay spectrum, which should match if the energy correction is working as expected. Figure 4.11 shows the comparison of the projection of Figure 4.10 onto the y -axis between $500 \text{ ns} < \Delta t < 4000 \text{ ns}$ with a nominal MC simulated ^{39}Ar β -decay spectrum. The

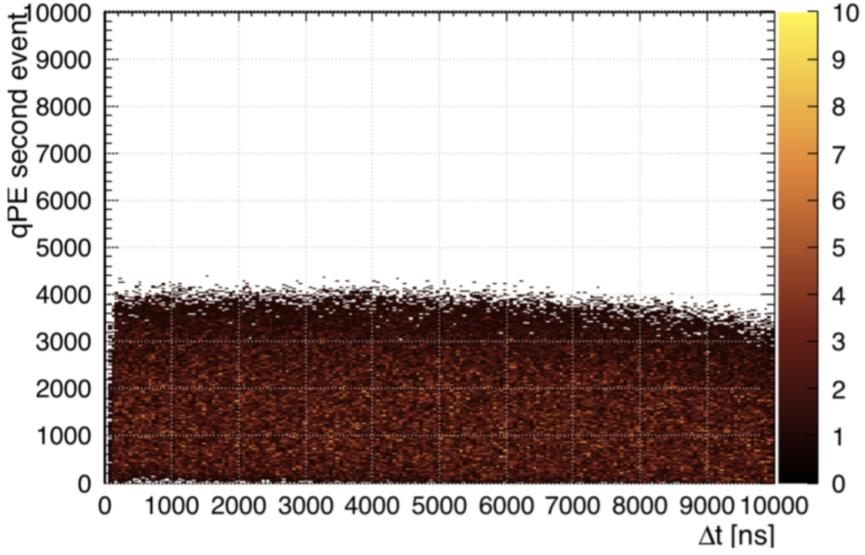


Figure 4.10: Two-dimensional distribution of the second subevent energy against Δt between the two subevents for two simulated coincidence ^{39}Ar β -decays after applying a subevent energy correction on the second subevent. There is no longer the upturn at low Δt values, illustrating the effect of the correction from the leakage of the first subevent into the second subevent energy window.

spectra are normalised such that the peak heights at ~ 1500 qPE, the average β^- energy, are equal. Overall, the spectra are in agreement; the only discrepancy lies at $\text{qPE} < 200$, attributed to a combination of the efficiency of the `multievent` processor and the trigger efficiency. However, given that the spectra match well in the energy range of the 514 keV γ -ray emission, $\sim 3000 < \text{second subevent qPE} < 4000$, this discrepancy is not a cause for concern.

The subevent energy correction was also validated on simulated ^{85}Kr events, to ensure that after applying the subevent energy correction and selecting a specific energy range for analysis ($3000 < \text{second subevent qPE} < 4000$), the observed mean lifetime of the ^{85}Kr decay does not change. To verify that this is not the case, the Δt distribution for events that satisfy the condition $3000 < \text{second subevent qPE} < 4000$ is fit with an exponential function of the form,

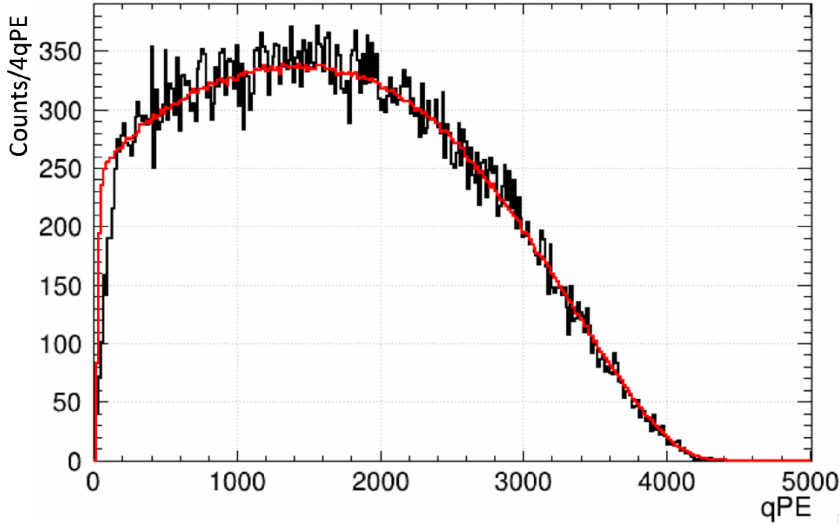


Figure 4.11: Comparison of the single ^{39}Ar qPE spectrum produced by projecting Figure 4.10 onto the y -axis between $500 \text{ ns} < \Delta t < 4000 \text{ ns}$ after applying a subevent energy correction (black) to a nominal MC simulated single ^{39}Ar β -decay spectrum (red). The spectra are normalised such that the peak heights, corresponding to the average β^- energy at approximately 1500 qPE, are equal.

$$f(t; a, \tau) = a \cdot e^{-t/\tau}, \quad (4.12)$$

where a is the normalisation and τ is the mean lifetime of the ^{85}Rb decay. This fit is performed on the Δt distribution obtained from selecting ^{85}Kr events that satisfy the condition $3000 < \text{second energy subevent qPE} < 4000$, using both truth and reconstructed energy information.

Selecting ^{85}Kr events with $3000 < \text{second energy subevent qPE} < 4000$ using MC truth information and fitting the Δt distribution yields $\tau = (1443 \pm 6.9) \text{ ns}$; the fit result is shown in Figure 4.12. The small discrepancy between this value and the true value of $\tau = 1464 \text{ ns}$ is driven by the `subeventN = 2` requirement made on `subeventN = 2` events; repeating the fit on ^{85}Kr events without this requirement gives a mean lifetime of $\tau = (1464 \pm 7.0) \text{ ns}$. Selecting ^{85}Kr events with $3000 <$

second energy subevent $qPE < 4000$ using reconstructed information after applying the subevent energy correction and fitting the Δt distribution yields $\tau = (1442 \pm 7.6)$. Since the two τ fit parameters are within 1σ of each other, it was concluded that the subevent energy correction does not change the observed mean lifetime.

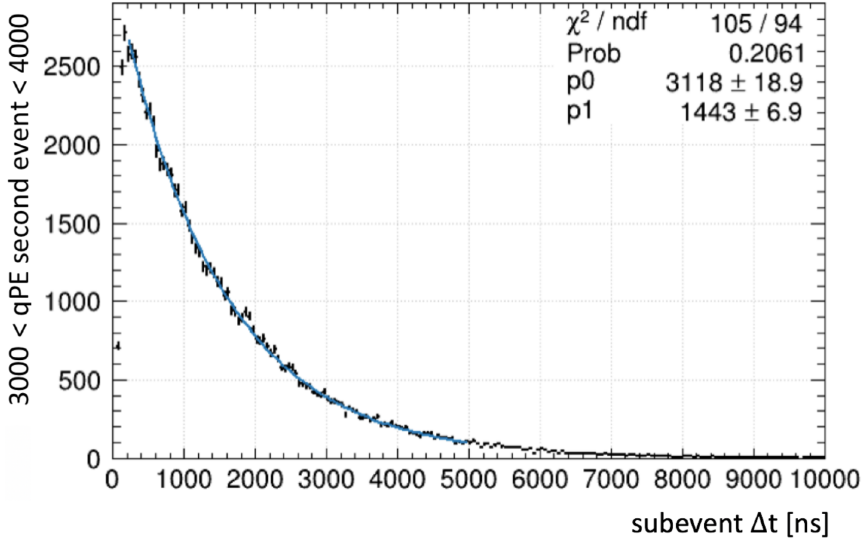


Figure 4.12: ^{85}Kr decay Δt spectrum for signal MC events with `subeventN` = 2 and $3000 < \text{second energy subevent } qPE < 4000$, selected using MC truth information. The distribution is fit with an exponential function described by Equation 4.12, and yields a mean lifetime parameter of $\tau = (1443 \pm 6.9)$ ns.

The ^{85}Kr search was performed on 10% of the 231 live-day dataset, equivalent to 24.72 live-days exposure. This is due to the fact that at the time of the analysis, only 10% of the 231 live-day dataset was reprocessed with the individual pulse-level information required for this analysis. The majority of physics-triggered data does not typically contain pulse-level information in order to save disk space. Candidate events are accepted from the data after applying basic low-level cuts as well as three additional cuts:

- The time difference between the event in question i and event $i - 1$ must be greater than $20 \mu\text{s}$. This excludes the leakage of scintillation light from event

$i - 1$ into the window of event i ,

- The **subeventN** variable must be equal to 2, to ensure that the energy of the second subevent can be calculated, and,
- The energy of the first subevent is between 120 qPE and 1400 qPE. The upper limit is derived from the knowledge that the maximum energy of the initial β -decay can not exceed 173 keV; a broad qPE window, where the upper bound is above the maximum energy expected for the β^- particle, is used to maximise the efficiency of observing the β^- . The lower limit of 120 qPE ensures that no strange effects are observed due to the trigger efficiency.

The two-dimensional distribution of the corrected second subevent qPE versus the Δt in data is shown in Figure 4.13. Projecting Figure 4.13 onto the x -axis between $3000 < \text{second subevent qPE} < 4000$ yields the Δt distribution, which is fit with the following fit function,

$$f(t; a, b, \tau) = a \cdot e^{-t/\tau} + b, \quad (4.13)$$

where a is the normalisation of the exponential term, b is the normalisation of the constant, flat background from coincidence ^{39}Ar β -decays and τ is the mean lifetime of the metastable ^{85}Rb decay process. The τ parameter is fixed in the fit to $\tau = 1442$ ns, the value obtained from fitting the Δt distribution for signal MC events with $3000 < \text{second subevent qPE} < 4000$ after applying the same cut flow as is applied to the data. Figure 4.14 shows the Δt distribution with the fit result from fitting the data with Equation 4.13.

The ^{85}Kr activity is calculated using the following expression,

$$\mathcal{A}_{\text{Kr85}} = \frac{N_{\text{Kr85}}}{p_{\text{decay}} \cdot \epsilon_{\text{det}} \cdot t_{\text{live}} \cdot M_{\text{LAr}}}, \quad (4.14)$$

where N_{Kr85} is the integral number of candidate ^{85}Kr decays in the data in the search region [$3000 < \text{second subevent qPE} < 4000$, $500 \text{ ns} < \Delta t < 4000 \text{ ns}$], p_{decay} is the decay probability (0.43%), ϵ_{det} is the ^{85}Kr detection efficiency in the search region, t_{live} is the corrected livetime [s] and M_{LAr} is the LAr mass [kg]. Using the parameter values a , b extracted from the fit in Figure 4.14 and the fixed value for τ , N_{Kr85} is calculated by integrating the fit function between $500 \text{ ns} < \Delta t < 4000 \text{ ns}$. The ^{85}Kr detection efficiency ϵ_{det} is obtained from MC simulations, and is defined as the ratio of signal events residing in the search region after applying the same cut flow as applied to data to all simulated signal events. The final parameter values used to calculate $\mathcal{A}_{\text{Kr85}}$ are displayed in Table 4.1.

Table 4.1: Parameter values used to calculate the ^{85}Kr activity in the DEAP-3600 detector, using Equation 4.14.

| Parameter | Value |
|-------------------------|-------------------------------------|
| N_{Kr85} | 287.3 ± 53.5 |
| p_{decay} | 0.0043 |
| ϵ_{det} | 0.1732 ± 0.0119 |
| t_{live} | 2007415.87 [s] |
| M_{LAr} | $(3256.59 \pm 111.91) \text{ [kg]}$ |

In order to obtain the final ^{85}Kr activity, the value of $\mathcal{A}_{\text{Kr85}}$ calculated from Equation 4.14 is scaled up by an additional 3% to account for the ^{85}Kr signal loss due to the `subeventN = 2` cut. There is a 3% probability for a genuine ^{85}Kr decay to pile-up with a coincidence ^{39}Ar event. In this scenario, the `multievent` processor could identify `subeventN = 3` and as such, the ^{85}Kr decay would be missed from the analysis. If the assumption is made that all piled-up ^{85}Kr decays are missed, a conservative measurement of the ^{85}Kr activity is obtained,

$$\mathcal{A}_{\text{Kr85}} = (1.15 \pm 0.23) \text{ mBq/kg.} \quad (4.15)$$

Given that the measured ^{85}Kr activity is 0.1% of the ^{39}Ar activity, it was determined

that the background contribution from ^{85}Kr decay is negligible and is therefore not included in the overall DEAP-3600 background model or the Profile Likelihood Ratio analysis.

The ^{85}Kr activity obtained from this analysis is comparable with the result obtained by the DarkSide-50 collaboration in [107], which measured $\mathcal{A}_{\text{Kr}85} = (2.05 \pm 0.13)$ mBq/kg. However, DarkSide-50 uses low radioactivity underground argon (UAr), which reduces the ^{39}Ar activity by a factor of $(1.4 \pm 0.2) \times 10^3$ compared to atmospheric argon, as used by DEAP-3600. Thus, the ^{85}Kr activity measured by DarkSide-50 was found to be comparable to the measured ^{39}Ar activity, $\mathcal{A}_{\text{Ar}39} = (0.73 \pm 0.11)$ mBq/kg. As discussed in [107], the presence of ^{85}Kr in UAr is unexpected; it has been hypothesised that the presence of ^{85}Kr in UAr could come from atmospheric leaks, or from natural fission underground.

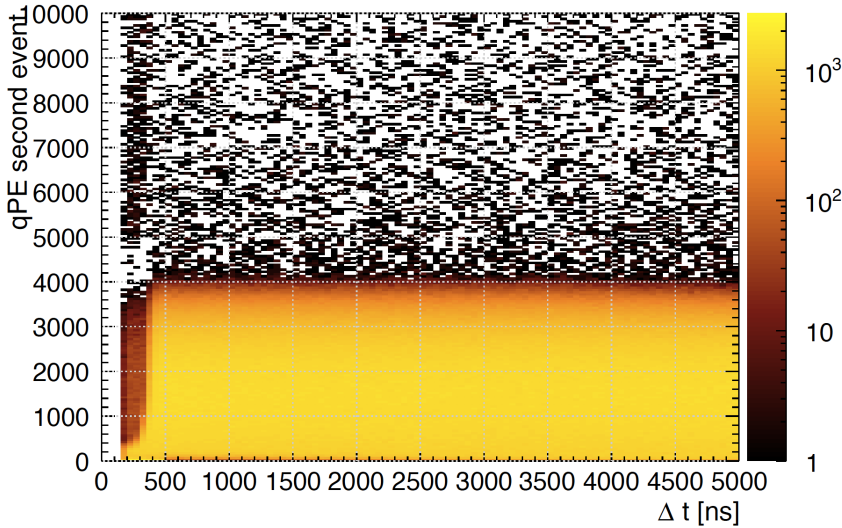


Figure 4.13: Two-dimensional distribution of the corrected second subevent $q\text{PE}$ versus Δt for physics-triggered events with `subeventN` = 2, acquired by the DEAP-3600 detector in 24.72 live-days.

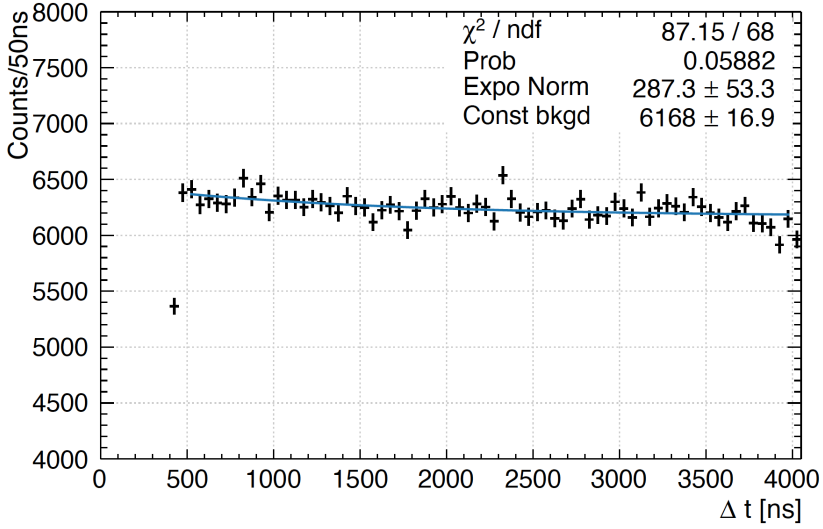


Figure 4.14: Δt distribution obtained by projecting Figure 4.13 onto the x -axis between the y -axis range $3000 < \text{second subevent } qPE < 4000$. The distribution is fit with an exponential function plus a constant background as defined by Equation 4.13 between $500 \text{ ns} < \Delta t < 4000 \text{ ns}$, in order to calculate $\mathcal{A}_{\text{Kr85}}$.

4.2 Nuclear and Nuclear-Like Recoils

4.2.1 Radiogenic Neutrons

RADIOGENIC neutrons are the most detrimental source of background to the WIMP search as they can induce high F_{prompt} nuclear recoil (NR) signals that can deposit enough energy to wind up inside the WIMP ROI ($< 200 \text{ PE}$). Unlike cosmogenic neutrons which can be effectively removed (producing < 0.2 events in the WIMP ROI in this dataset [4]) using signals from the water tank veto PMTs, radiogenic neutrons are nearly impossible to mitigate in analysis. At the time of writing, only background events induced from radiogenic neutrons are considered in the Profile Likelihood Ratio WIMP search analysis. The expected production rates of radiogenic neutrons from different detector components are summarised briefly below.

Trace amounts of primordial ^{238}U and ^{232}Th present in the detector materials can give rise to radiogenic neutrons through spontaneous fission (^{238}U) and (α, n) reactions from α -decays (^{238}U , ^{232}Th). In order to calculate the amount of ^{238}U and ^{232}Th present in the detector components, comprehensive gamma assays were performed on each of the detector materials. The specific activities of ^{238}U and ^{232}Th in the major detector components, including the acrylic vessel, PMTs, filler blocks and steel shell, are summarised in [73] (Table 6).

The predicted (α, n) neutron yields for these various detector materials, defined as the number of neutrons produced per decay, are calculated independently using the SOURCES-4C [87] and NeuCBOT [88] software tools; comparisons between the two enables some level of probing into (α, n) yield calculation uncertainties. These can be used in conjunction with the detector component activities obtained from [73] to determine the expected rate of radiogenic neutrons from each individual component; these are summarised in Table 4.2 for the leading contributions, from the PMTs, neck veto PMTs, filler blocks, filler foam and steel shell. The rates from the acrylic vessel and light guides are not included, as these rates are subdominant in comparison to the other components considered.

Out of all of the detector components, the PMTs have the highest level of radioactivity; Table 4.2 shows that in the 231 live-day dataset, 47500 - 81230 radiogenic neutrons are produced through (α, n) reactions in the PMTs alone. The total radiogenic neutron rate observed in a dedicated neutron capture analysis however, is significantly lower than the sum of the production rates quoted in Table 4.2. The majority of neutrons are stopped by the filler blocks and light guides and thus do not make it into the LAr target to generate a signal. In the second WIMP dark matter search conducted by the DEAP-3600 collaboration, the number of neutron events from the PMTs expected inside the WIMP ROI after applying a fiducial radius cut of $R_{\text{rec}} < 630$ mm and several background mitigation cuts, as described in [4], was

calculated to be between 0.015 - 0.192 [4].

The prior normalisation of radiogenic neutrons in the Profile Likelihood Ratio analysis are based on the production rates calculated in Table 4.2, taking into account the fraction of neutrons that pass the physics trigger condition. For each signal and background source, the Profile Likelihood Ratio uses a detailed model of the source combined with the expected rates/activities to predict the number of signal or background events in the WIMP ROI for the 231 live-day dataset. Each model is comprised of multi-dimensional PDFs that together describe the topology of these events in the detector. For radiogenic neutrons, these PDFs are built using MC simulations; the details of which are discussed in Section 5.3.

Table 4.2: Radiogenic neutron production rates in the DEAP-3600 detector for the major inner detector components: PMTs, neck veto PMTs, filler blocks, filler foam and steel shell. The acrylic vessel and light guides are a subdominant contribution and are not included.

| Component | Rate [Hz] (SOURCES-4C) | Rate [Hz] (NeuCBOT) |
|----------------|------------------------|-----------------------|
| PMTs | 2.38×10^{-3} | 4.07×10^{-3} |
| Filler blocks | 5.55×10^{-7} | 8.59×10^{-7} |
| Filler foam | 1.40×10^{-6} | 2.58×10^{-6} |
| Steel shell | 1.64×10^{-5} | 2.32×10^{-5} |
| Neck veto PMTs | 3.15×10^{-5} | 1.85×10^{-5} |

4.2.2 α -decays from the Acrylic Vessel

DECAYS of long-lived and short-lived radon progeny in the detector can be problematic for WIMP dark matter searches as they emit high energy α -particles with the ability to produce high F_{prompt} NR-like signals. Potentially detrimental to the WIMP search are α -decay backgrounds from the surface and bulk of the acrylic vessel, because these α -particles have degraded energies. The activities of these backgrounds, measured in-situ by the DEAP-3600 collaboration [4], are summarised below.

Energy-degraded α -decay backgrounds come from long-lived ^{210}Po decays that

produce 5.3 MeV α -particles. The majority of these backgrounds come from decays of residual ^{210}Po on the surface of the acrylic vessel, however they can also originate from within the bulk of the acrylic vessel as well as from within the TPB layer [4]. Since α -decays from these surfaces have to traverse up to 3 μm of TPB layer and tens of microns of acrylic in order to reach the LAr, they can deposit a significant portion of their initial energy into these media. The NR-like signals they produce in the LAr can therefore span a wide range of energies; α -decays on the very surface of the acrylic vessel can produce signals of ~ 20000 PE, compared to α -decays from within the acrylic vessel bulk which can produce signals with low enough energies to leak into the WIMP ROI.

Surface and bulk α -decay activities are deduced from fitting the high $\mathbf{F}_{\text{prompt}}$ **nSCBayes** spectrum in data ($\mathbf{F}_{\text{prompt}} > 0.55$) outside of the WIMP ROI with a model of the predicted total ^{210}Po activity in the detector. The model includes three main components: ^{210}Po decays in the acrylic vessel bulk, occurring up to a depth of 50 μm from the surface, ^{210}Po decays on the acrylic vessel surface and TPB interface and ^{210}Po decays occurring on the surface of the TPB layer and LAr interface as well as within the 3 μm layer of TPB. The predicted spectra from each component of the model is generated using MC simulations. The fit is performed on the 231 live-day dataset, once again with low-level and pile-up cuts applied to the data, across an energy range of ~ 8000 PE - 22000 PE. The final fit result, superimposed on the data, is shown in Figure 4.15 [4]; also shown are the spectra of the individual components, each normalised according to their best fit rates. Figure 4.15 clearly illustrates the tail of energy-degraded surface and bulk α -decays tending towards lower energies from a mean value of ~ 20000 PE.

The combined surface α -decay activity from the TPB and acrylic vessel is calculated to be (0.26 ± 0.02) mBq/m² and from the acrylic vessel bulk the α -decay activity is (2.82 ± 0.05) mBq [4]. These activities correspond to physics trigger rates

in the detector of (1.31 ± 0.11) mHz from surface decays and (0.51 ± 0.02) mHz from bulk decays [4], summarised in Table 4.3. Similarly to radiogenic neutrons, these rates are required for the Profile Likelihood Ratio analysis prior normalisation. In conjunction with a detailed surface and bulk α -decay model constructed from MC simulations, these rates are used to estimate the number of expected events in the WIMP ROI from surface and bulk α -decays in the 231 live-day dataset. Details on the implementation of the surface and bulk α -decay model in the Profile Likelihood Ratio analysis can be found in Section 5.3.

4

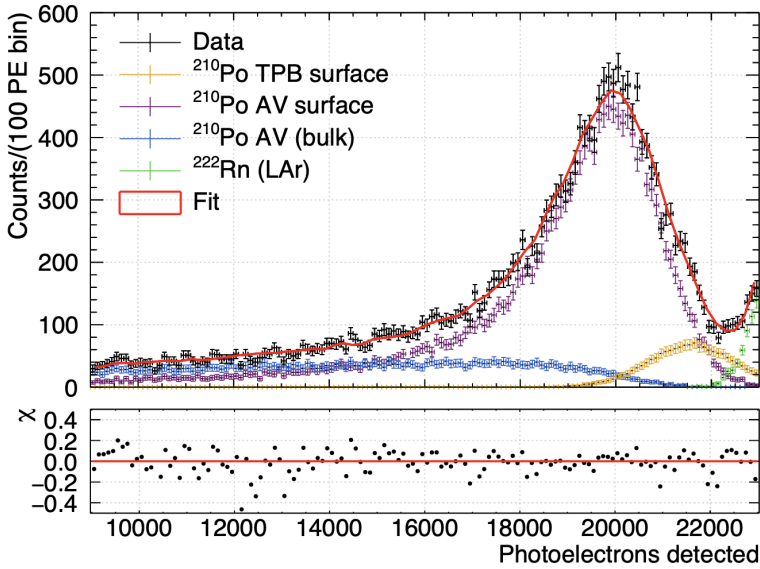


Figure 4.15: nSCBayes spectrum [PE] of candidate surface and bulk α -decays from high $F_{\text{prompt}} (> 0.55)$ data (black). The spectra of simulated ^{210}Po α -decays from the surface of the acrylic vessel and TPB interface (purple), from within the 3 μm TPB layer and LAr/TPB interface (yellow) and from the bulk of the acrylic vessel up to a depth of 50 μm (blue) are also shown. The combined fit of these three components to the data is overlaid in red. From [4]. This plot clearly shows the tail of surface and bulk α -decays from ~ 20000 PE with degraded energies that can leak down towards the WIMP ROI.

Table 4.3: Combined activities and physics trigger rates of surface α -decays, from the TPB and acrylic vessel surface, and bulk α -decays, from the acrylic vessel, in the DEAP-3600 detector.

| α -decay Source | Activity | Physics Trigger Rate [mHz] |
|-------------------------------|------------------------------------|----------------------------|
| Surface (TPB, acrylic vessel) | 0.26 ± 0.02 mBq/m ² | 1.31 ± 0.11 |
| Bulk (acrylic vessel) | 2.82 ± 0.05 mBq | 0.51 ± 0.02 |

4.2.3 α -decays from the Acrylic Neck Flow Guides

THE largest α -decay background contribution to the WIMP search comes from long-lived ^{210}Po α -decays on the surfaces of the acrylic flow guides located in the neck of the detector. These are termed neck α -decays. Whilst surface and bulk α -decays from the acrylic vessel, which reconstruct near the very edge of the detector $R_{\text{rec}} > 800$ mm, can generate high F_{prompt} signals with low WIMP-like energies, they can be almost entirely mitigated in analysis with position reconstruction algorithms. Position reconstruction is not as powerful a mitigation technique however for neck α -decays, many of which survive fiducial reconstructed radius cuts. A detailed model of neck α -decay backgrounds developed by the DEAP-3600 collaboration [4] was used to estimate the expected event rate from neck α -decays in the detector.

Two acrylic flow guides are located in the acrylic vessel neck: the inner (IFG) and outer (OFG) flow guide. On these flow guides, there are three distinct surfaces that can give rise to neck α -decays: the inner surface of the inner flow guide (IFGIS), the outer surface of the inner flow guide (IFGOS) and the inner surface of the outer flow guide (OFGIS); these are illustrated by the cross-sectional diagram of the neck in Figure 4.16 [4]. The outer surface of the outer flow guide does not contribute to the neck α -decay background as it is attached to the wall of the acrylic vessel, and thus has no direct line of sight to the LAr target [4].

Since the flow guides are located above the LAr fill level, the only manner in which scintillation light from neck α -decays can be observed is if there is some

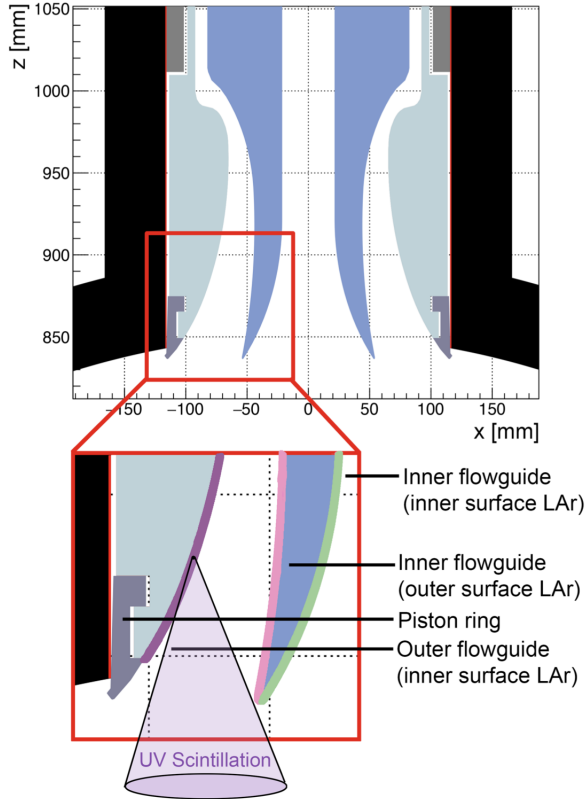


Figure 4.16: Cross-sectional diagram of the acrylic vessel neck, illustrating the inner (IFG) and outer (OFG) flow guides. Also shown are the three flow guide surfaces that are considered in the neck α -decay background model: the inner flow guide inner surface (IFGIS), inner flow guide outer surface (IFGOS) and outer flow guide inner surface (OFGIS). From [4].

residual LAr on the surfaces of the flow guides, as the scintillation yield of GAR alone is too low to produce a signal in the detector. A model of ^{210}Po α -decays occurring on the three aforementioned surfaces of the flow guides, each coated with a thin layer (50 μm) of LAr, was implemented into MC simulations. The flow guides are implemented into simulation as two rotational bodies made from acrylic. Their shape is defined as a 2D polygonal contour in $\rho = \sqrt{x^2 + y^2}$ and z , which is then rotated around the z -axis. LAr films residing on the surfaces of the flow guides are approximated by three further rotational bodies for the inner flow guide inner

surface, inner flow guide outer surface and outer flow guide inner surface, created from polygons made from the corresponding flow guide surface, and the same surface shifted by $50\text{ }\mu\text{m}$ in ρ with the appropriate sign.

Simulated neck α -decays from each of the three sources are compared to the high $F_{\text{prompt}} (> 0.55)$ population in data, outside of the WIMP ROI. A nominal LAr layer of thickness of $50\text{ }\mu\text{m}$ was chosen as it is just enough for the α -particle to stop in the LAr, and simulated events with a $50\text{ }\mu\text{m}$ LAr film yield an F_{prompt} distribution consistent with the one observed in data [4]. MC simulations show that 5.3 MeV neck α -decays from ^{210}Po scintillating in LAr films on the IFGIS, IFGOS and OFGIS produce three populations consistent with data. These populations are most clearly visible in the two-dimensional plane of reconstructed z position and $n\text{SCBayes}$, shown in Figure 4.17, as three “arm”-like features [4].

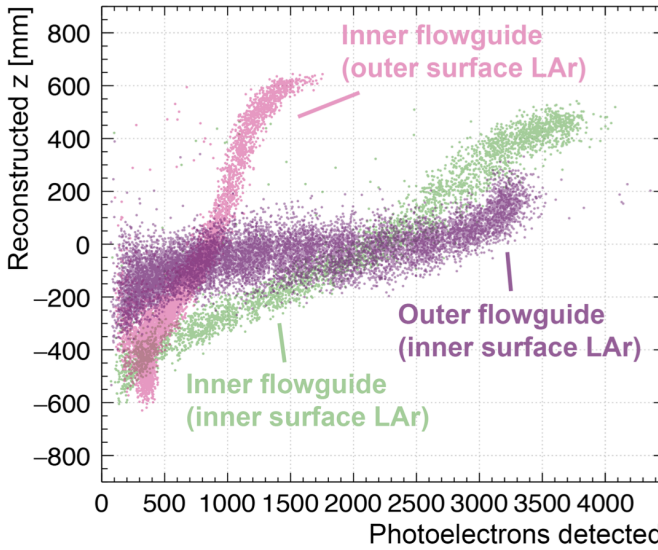


Figure 4.17: Two-dimensional plane of reconstructed z position vs $n\text{SCBayes}$ [PE] for simulated ^{210}Po neck α -decays on the IFGIS (green), IFGOS (pink) and OFGIS (purple). The three populations produce “arm”-like features. From [4].

Figure 4.17 shows that neck α -decays can produce signals ranging between ~ 100

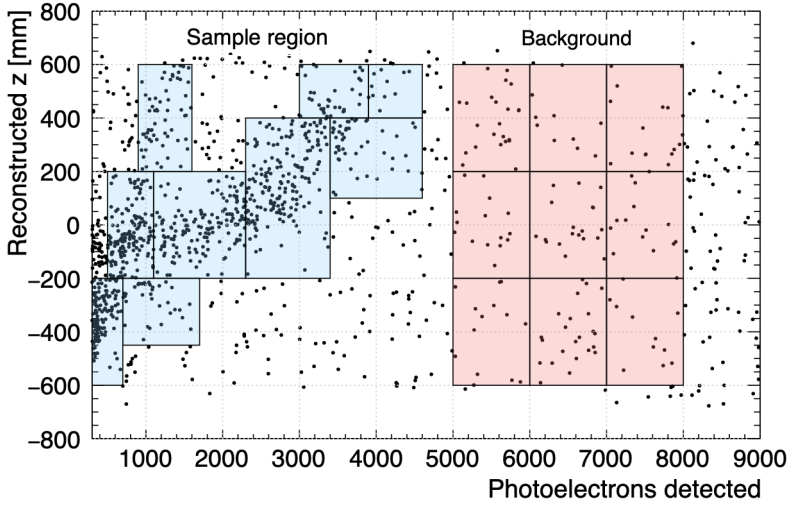


Figure 4.18: Two-dimensional plane of reconstructed z position vs charge [PE] for candidate ^{210}Po neck α -decays from high F_{prompt} data. Blue boxes depict sample control regions used by the fit to compare the observed spectra with the expected spectra. Pink boxes depict background control regions in order to deduce a background component. The “arm”-like feature predicted from MC simulations in Figure 4.17 is clearly visible in data. From [4].

PE - 5000 PE, at least 6 times smaller than the initial α -decay energy. This is due to a “shadowing” effect, whereby the majority of scintillation photons produced from neck α -decays incident on the flow guides are absorbed by the acrylic. Consequently, the reconstructed charge of a neck α -decay is highly correlated with the true position of its decay, since the position determines the amount of shadowing. [4].

Position reconstruction is a challenge for neck α -decays due to a combination of shadowing effects and complex event topologies involving the GAR-LAr interface. Depending on the location of such flow guide events, scintillation light produced in the LAr film can either be absorbed or reflected by the neighbouring flow guides before reaching the inner acrylic vessel; upon entering the inner acrylic vessel, some photons could also be reflected at the GAR-LAr interface. As a result, the number of photons that make it into the LAr is a small fraction of the initial decay.

Since the position reconstruction algorithms are based on a perfect spherical ge-

ometry and do not include the neck (flow guides), this complicated event topology results in the majority of neck α -decays reconstructing closer to the centre of the detector and thus they are not removed with a fiducial radius cut, nominally chosen as $R_{\text{rec}} < 630$ mm in the second dark matter search published in [4]. In this analysis, the DEAP-3600 collaboration constructed a new event variable, referred to as **PulseIndexFirstGAR**, to reject neck α -decay backgrounds. **PulseIndexFirstGAR** quantifies the location of the PMTs which first registered the early pulses in the event window; since the group velocity of UV photons is three times greater in GAR compared to LAr [4], the PMTs located above the LAr fill level in the GAR region will register reflected photons from neck α -decays before the LAr PMTs will register transmitted photons.

If any of the GAR PMTs above the fill level detect a pulse, the **PulseIndexFirstGAR** variable returns an integer value corresponding to the pulse index. By definition, **PulseIndexFirstGAR** ≥ 0 . Using MC simulations, it was found that rejecting events with **PulseIndexFirstGAR** ≤ 2 produces a predicted neck α -decay background leakage of < 0.5 in the WIMP ROI [4]. This cut was shown to be extremely effective at removing neck α -decays, with a rejection efficiency inside the fiducial volume ($R_{\text{rec}} < 630$ mm) of 80%, 85% and 81% for neck α -decays from the IFGIS, IFGOS and OFGIS respectively [4]. However, this cut also corresponds to approximately a 40% loss in WIMP signal acceptance inside the fiducial volume. This motivated the concept of including the **PulseIndexFirstGAR** variable in the Profile Likelihood Ratio analysis as an additional “dimension”, described in detail in Chapter 5.

To determine the total rate of neck α -decay backgrounds, a combined model of neck α -decays including contributions from all three surfaces was fit to the high $F_{\text{prompt}} (> 0.55)$ **nSCBayes** spectrum in data, outside of the WIMP ROI. The expected spectra for IFGIS, IFGOS and OFGIS neck α -decays used by the fit were generated with MC simulations. A flat “background” component is also included

in the fit, taken directly from sideband data between 5000 PE – 8000 PE. A component from simulated ^{210}Po α -decays on the piston ring, labelled in Figure 4.16, is also included, however it was found to be negligible compared with the three surfaces identified above. The fit is performed on the 231 live-day dataset, with low-level and pile-up cuts applied. An additional cut is also applied to the data to mitigate leakage from surface and bulk α -decays: no more than 4% of the total event charge can be observed in one PMT. The post-fit spectra of the individual IFGIS, IFGOS and OFGIS components, each accordingly normalised to their best fit rates, is shown overlaid on the data in Figure 4.19 [4]. In particular, Figure 4.19 highlights the severity of neck α -decays to the WIMP search, which implies that for the high F_{prompt} region, the majority of neck α -decays peak near the lower bound of the WIMP energy ROI.

The neck α -decay physics trigger rates for the IFGIS, IFGOS and OFGIS are calculated to be (14.1 ± 1.3) μHz , (16.8 ± 1.4) μHz and (22.7 ± 1.6) μHz respectively; these are summarised in Table 4.4. Activities cannot be calculated for neck α -decays as it is unknown what fraction of the surfaces are coated with a LAr layer [4]. The thickness of the LAr film is another unknown and one of the largest systematics with the neck α -decay model. Other systematics on the neck α -decay model, which are also applicable to all background models constructed using MC simulations are discussed further in Section 6.2.

Akin to surface and bulk α -decays and radiogenic neutrons described above, the neck α -decay rates quoted above are a required input to the Profile Likelihood Ratio analysis for the neck α -decay background model prior normalisation, which is also constructed using MC simulations. These rates are used to correctly predict the number of expected events from neck α -decays in the WIMP ROI for the 231 live-day dataset. Details on the implementation of the neck α -decay model in the Profile Likelihood Ratio analysis is described in Section 5.3.

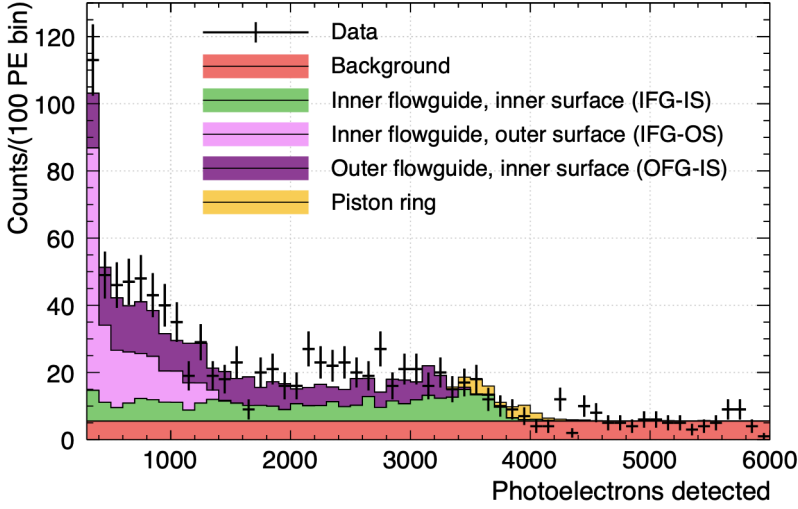


Figure 4.19: nSCBayes spectrum [PE] of candidate neck α -decays from high F_{prompt} (> 0.55) data (black). Overlaid are the spectra of simulated ^{210}Po α -decays from the IFGIS (green), the IFGOS (pink) and OFGIS (purple), all normalised according to their best fit rates. The small contributions from a flat “background” component (red) and the piston ring (yellow) are also shown. From [4]. This plot illustrates the severity of neck α -decays to the WIMP search, with the majority of neck α -decays peaked < 200 PE, within the WIMP ROI.

Table 4.4: Physics trigger rates of neck α -decays from the inner flow guide inner surface, inner flow guide outer surface and outer flow guide inner surface, in the DEAP-3600 detector.

| Neck α -decay Source | Physics Trigger Rate [μHz] |
|-----------------------------|---|
| IFGIS | 14.1 ± 1.3 |
| IFGOS | 16.8 ± 1.4 |
| OFGIS | 22.7 ± 1.6 |

4.2.4 α -decays from Dust Particulates

An excess of high F_{prompt} events extending out in energy from the WIMP ROI to ~ 20000 PE has been observed to reconstruct across the full volume of the detector; this has been attributed to α -decays from dust particulates circulating within the LAr target. Metallic dust from cryogenic liquid nitrogen is the current leading candidate, however norite dust (from rocks inside the mine) and residual

acrylic dust (from the sanding of the inner acrylic vessel during construction) have also been considered as candidates. MC simulations of copper dust particulates ranging in size from 1 μm to 50 μm are used to estimate the total dust α -decay event rate inside the detector.

During the construction phase of the DEAP-3600 detector, the inner acrylic vessel was sanded using a resurfacer robot, described in Section 2.2.1. Throughout the 198 integrated hours of sanding time, the acrylic vessel was continuously purged with radon-scrubbed nitrogen gas (boil-off) [73] to reduce the total radon activity. During the purge, metallic dust from erosion of the inner surface of the tank storing the liquid nitrogen could have been deposited inside the acrylic vessel. After resurfacing, the acrylic vessel was flushed with ultra-pure water; however it is possible that some fraction of these dust particulates remained inside. This hypothesis is supported by measurements taken at Carleton University (Ottawa, Canada), in which dust samples from liquid nitrogen collected using filter paper were analysed with a scanning electron microscope. The samples indicated an abundance of particulates ($> 10^6$ in 10 L of liquid nitrogen) ranging in diameters of 1 μm - 50 μm mainly comprised of elemental copper and zinc.

Trace amounts of primordial ^{238}U and ^{232}Th present in the metallic dust give rise to a range of high energy α -decays (~ 5 MeV) that produce energy-degraded signals in the LAr upon exiting the particulate. The number of scintillation photons produced by the α -decay is proportional to the total energy deposited in the LAr. In a simple model, this deposited energy in the LAr $= E_{\text{LAr}} = E - E_{\text{dust}}$, where E and E_{dust} are the initial α -particle energy and the total energy deposited in the particulate respectively. E_{dust} depends on the linear energy transfer LET of the α -particle in the particulate, which in this energy regime follows the relationship $dE/dx \propto 1/v^2$, where v is the α -particle velocity ($\propto E$). E_{dust} also depends on how much dust the α -particle traverses before reaching the LAr, determined by the

origin and direction of the decay in the particulate as well as the particulate size.

The observed α -decay energy is further degraded by a “shadowing” effect, in which scintillation photons directed back towards the particulate, contained inside the cone subtended by the solid angle Ω between the α -particle track and particulate surface, are absorbed. This is illustrated by the diagram in Figure 4.20. The fraction of light shadowed is also dependent on the α -range in the LAr; simulations show that for a 10 MeV (0.1 MeV) α -decay emitted from a 50 μm particulate ($r_{\text{dust}} = 25 \mu\text{m}$), $\sim 5\%$ (50%) of the initial α -particle energy is lost to shadowing.

4

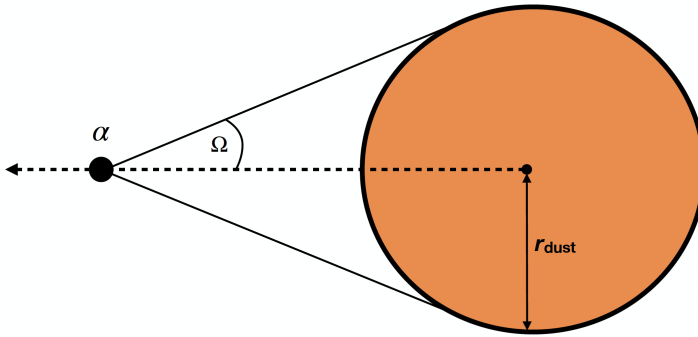


Figure 4.20: Diagram illustrating the effect of shadowing from a dust particulate of radius r_{dust} . In this example, the α -decay is emitted from the centre of the particulate; the dotted black line indicates the α -particle track. The cone subtended by the solid angle Ω between the α -particle track and particulate surface is indicated by solid black lines. Scintillation photons directed back towards the particulate inside this cone are absorbed by the particulate, resulting in a reduced observed energy. Diagram is not to scale.

To calculate the total dust α -decay rate in the detector, the high $F_{\text{prompt}} (> 0.55)$ nSCBayes spectrum in data is fit outside of the WIMP ROI with a superposition of the spectra produced from α -decays in dust particulates of varying sizes. Five template histograms $h_i(PE)$ are used in the fit, generated from MC simulations of α -decays from copper dust particulates; the following bins in particulate diameter are used to construct the histograms: 1-10 μm , 11-20 μm , 21-30 μm , 31-40 μm and 41-50 μm . Motivated by observations from the SNO collaboration [108], the

particulate size distribution can be well-modelled by a power law. The fit function used to fit the data is written as,

$$f(PE) = \sum_{i=1}^5 N(D_{\text{lower}}^p - D_{\text{upper}}^p) \cdot h_i(PE), \quad (4.16)$$

where N is an overall normalisation parameter, p is the power parameter, and D_{lower} and D_{upper} are the lower and upper boundaries of the particulate diameter bin considered in histogram $h_i(PE)$. Prior to performing the fit, each histogram $h_i(PE)$ is renormalised such that the y -axis of the histogram is in units of counts/particulate; this normalisation assumes a copper density of $\rho = 8960 \text{ kg/m}^3$ and a ^{238}U , ^{232}Th activity of 1 mBq/kg in the copper dust. This activity is arbitrarily chosen to normalise the histograms relative to one another, as there is not yet a measurement of this activity. This does not affect the total number of dust α -decays predicted from the fit to the data, since this is accounted for in the overall normalisation parameter. Figure 4.21 shows the five normalised histograms $h_i(PE)$ used by the fit. Figure 4.21 clearly demonstrates that α -decays from larger particulates have the potential to generate LAr signals that could contribute to the background rate in the WIMP ROI, unlike smaller particulates (between 1-10 μm in diameter) which cannot produce a signal smaller than $\sim 13000 \text{ PE}$.

The fit is performed on the 231 live-day dataset, with basic low-level and pile-up applied. A fiducial radius cut of $R_{\text{rec}} < 630 \text{ mm}$ is chosen, to reduce the leakage of surface and bulk α -decays in the dust α -decay control (fit) region, selected to be 6000 PE - 20000 PE. The lower bound of 6000 PE is chosen to mitigate neck α -decay backgrounds in the dust α -decay control region, which as shown earlier in Section 4.2.3, extends out to $\sim 5000 \text{ PE}$. The fit result overlaid on the data is shown in Figure 4.22; also shown are the five template histograms $h_i(PE)$ used by Equation 4.16 for the fit, each weighted relative to their best fit contributions.

The dust α -decay physics trigger rate for each of the five particulate diameter

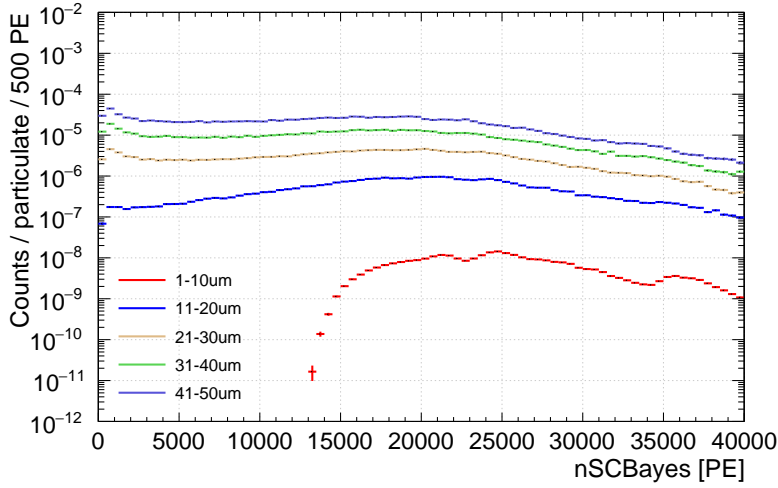


Figure 4.21: nSCBayes spectra [PE] of α -decays from copper dust particulates of various sizes, generated using MC simulations. The five distributions are separated based on particulate diameter: 1-10 μm (red), 11-20 μm (blue), 21-30 μm (yellow), 31-40 μm (green) and 41-50 μm (purple). Each histogram is normalised to /particulate, and used by the fit function expressed in Equation 4.16.

bins considered are extracted from the fit result displayed in Figure 4.22; these rates are summarised in Table 4.5. In total, 2.1×10^{-4} triggered events from dust α -decays are expected per second in the DEAP-3600 detector. These rates are used as a priori estimates for the Profile Likelihood Ratio analysis, to estimate the number of expected events expected in the WIMP ROI from dust α -decays in the 231 live-day dataset. Like the other background sources discussed in this section, the background model implemented in the Profile Likelihood Ratio is also constructed from MC simulations; the same simulations used to determine the rates quoted here. Details on the implementation of the dust α -decay model in the Profile Likelihood Ratio analysis is described in Section 5.3.

Table 4.5: Total physics trigger rate of dust α -decay events in the DEAP-3600 detector, split into five regions based on particulate diameter. Rates are extracted from the fit result displayed in Figure 4.22

| Particulate Diameter [μm] | Physics Trigger Rate [μHz] |
|--|---|
| 1-10 | 76.7 ± 3.1 |
| 11-20 | 31.2 ± 1.3 |
| 21-30 | 33.0 ± 1.3 |
| 31-40 | 34.0 ± 1.5 |
| 41-50 | 33.0 ± 1.4 |

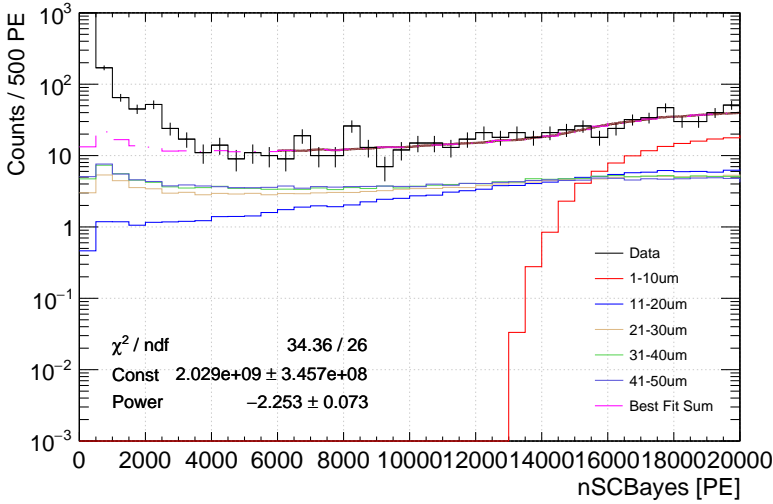


Figure 4.22: nSCBayes spectrum [PE] of high $F_{\text{prompt}} (> 0.55)$ (candidate dust α -decay) events in the 231 live-day dataset. A fiducial radius cut of $R_{\text{rec}} < 630$ mm cut is made on the data to remove leakage of surface and bulk α -decay events. The data is fit outside of the WIMP ROI, between 6000 PE - 20000 PE with the functional form described by Equation 4.16, using MC-simulated templates of the expected spectra for α -decays from copper dust particulates with particulate diameters in the following bins: 1-10 μm , 11-20 μm , 21-30 μm , 31-40 μm and 41-50 μm .

4.2.5 Data - MC Validation

THE Profile Likelihood Ratio software developed in this thesis relies heavily on MC simulations to build background models in three-dimensional parameter space, defined by the nSCBayes, F_{prompt} and R_{rec} variables. The MC simulations used to construct the surface α -decay, neck α -decay and dust α -decay models are

validated by comparing the **nSCBayes**, F_{prompt} and R_{rec} distributions from these three MC components to a high F_{prompt} (> 0.55) sideband, located outside of the WIMP ROI, from the 231 live-day dataset.

The sideband is defined to be between 1000 PE - 20000 PE. Low-level and pile-up cuts detailed in Section 5.1 are applied to the dataset and the MC simulations. A fiducial cut of $R_{\text{rec}} < 630$ mm is also applied. PMT saturation is not currently modelled in MC simulation; high energy surface α -decays taking place at the edge of the detector are biased towards lower **nSCBayes** in data, an effect not reflected in MC simulations. For the surface α -decay activity measurement described in Section 4.2.2, MC simulations were fit to high **nSCBayes** (> 20000 PE) high F_{prompt} (> 0.55) events in data, where numerous smearing parameters were introduced into the fit to account for the effect of saturation. Since a smearing factor is not applied here, a fiducial cut of $R_{\text{rec}} < 630$ mm is applied to remove surface α -decays most likely to saturate the PMTs, reducing the expected surface α -decay contribution in the sideband to 1.5%.

The surface, neck and dust α -decay distributions in the three dimensions are scaled by their expected contributions in the sideband in the 231 live-day dataset. These are calculated using their relative activities and physics trigger rates, given in Tables 4.3, 4.4 and 4.5 respectively. Figures 4.23, 4.24 and 4.25 show the individual MC distributions from surface α -decays, neck α -decays and dust α -decays and the summed MC distribution superimposed on the distribution from the 231 live-day dataset for the **nSCBayes**, F_{prompt} and R_{rec} dimensions respectively. Uncertainties on the background activities/physics trigger rates are not accounted for. In all three dimensions, the summed distribution from these three MC components are mainly consistent with the data in this sideband. Figure 4.24 indicates a potentially small discrepancy in the mean F_{prompt} peak, attributed to uncertainties in the α -particle scintillation parameters as discussed in [4].

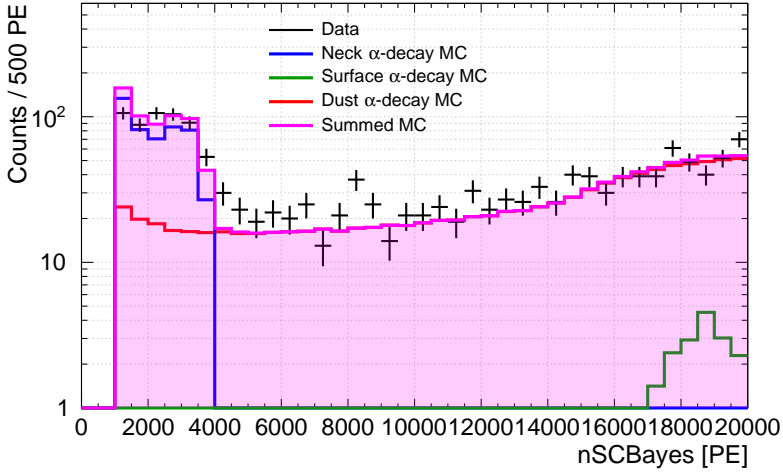


Figure 4.23: Individual $nSCBayes$ distribution from MC simulations of surface α -decays (green), neck α -decays (blue) and dust α -decays (red) and the summed distributions from all three components (pink), superimposed on the $nSCBayes$ distribution from the 231 live-day dataset (black). Only events with $R_{rec} < 630$ mm are considered. The number of expected events from surface α -decays, neck α -decays and dust α -decays are calculated using background activities/physics trigger rates based on in-situ measurements, detailed in Tables 4.3, 4.4 and 4.5 respectively.

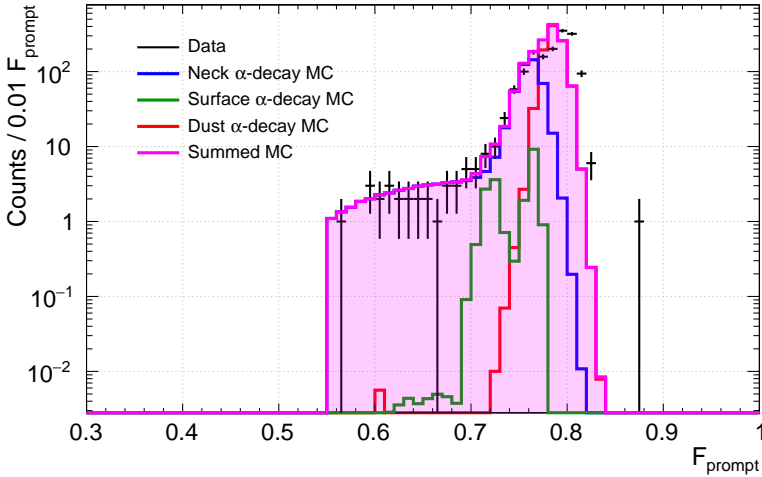


Figure 4.24: Individual F_{prompt} distribution from MC simulations of surface α -decays (green), neck α -decays (blue) and dust α -decays (red) and the summed distributions from all three components (pink), superimposed on the $nSCBayes$ distribution from 231 live-day dataset (black). Only events with $R_{rec} < 630$ mm are considered. The number of expected events from surface α -decays, neck α -decays and dust α -decays are calculated using background activities/physics trigger rates based on in-situ measurements, detailed in Tables 4.3, 4.4 and 4.5 respectively.

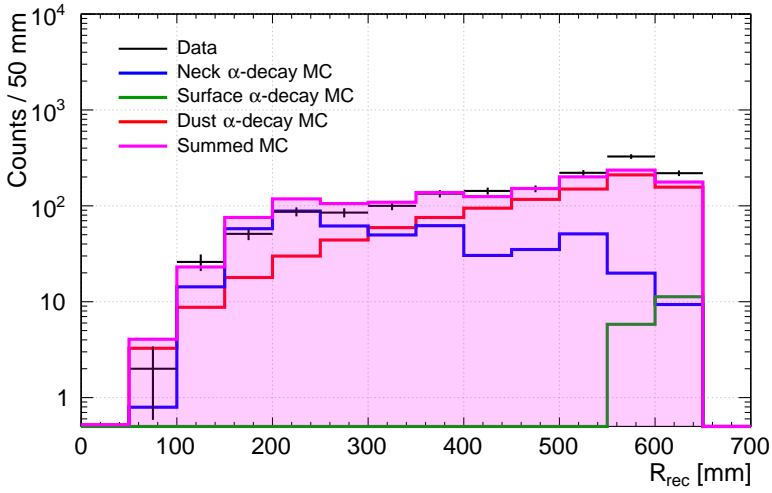


Figure 4.25: Individual R_{rec} distribution from MC simulations of surface α -decays (green), neck α -decays (blue) and dust α -decays (red) and the summed distributions from all three components (pink), superimposed on the `nSCBayes` distribution from the 231 live-day dataset (black). Only events with $R_{\text{rec}} < 630$ mm are considered. The number of expected events from surface α -decays, neck α -decays and dust α -decays are calculated using background activities/physics trigger rates based on in-situ measurements, detailed in Tables 4.3, 4.4 and 4.5 respectively.

Chapter 5

Development of the Profile Likelihood Ratio Software

*“The development of physics, like the development of any science,
is a continuous one. ”*

—Owen Chamberlain

THIS chapter presents the development of a multi-dimensional Profile Likelihood Ratio analysis software. The software is written in C++, and uses the MIGRAD algorithm in the TMinuit class from ROOT [83] to perform the maximisation of the likelihood function. A full description of the implementation and validation of the three-dimensional signal and background models currently incorporated in the software is provided, including a detailed discussion on the addition of a new dimension into the Profile Likelihood Ratio analysis.

5.1 Cut Selection and Region-of-Interest

THE Profile Likelihood Ratio (PLR) WIMP search is performed on 231 live-days of DEAP-3600 detector data, corresponding to an exposure of 757.5 ± 22.2 tonne-days. A selection of cuts are applied to the data, grouped into four categories:

- Low-level cuts,
- Pile-up cuts,
- Fiducial cuts,
- Background rejection cuts.

Low-level cuts were first introduced in Section 3.2.2, and are standard instrumental data-cleaning cuts that are applied to any data acquired by the detector. Pile-up cuts, also introduced in Section 3.2.2, are designed to remove events that are suspected to be coincidence events. There are four pile-up cuts applied to the 231 live-day dataset; events are selected if:

- $2250 \text{ ns} < \text{eventTime} < 2700 \text{ ns}$: the trigger time of the event with respect to the start of the waveform must be within the range 2250 ns - 2700 ns, to remove coincidence events occurring before or after the main physics event that can drive the trigger time outside of the expected range,
- $\text{numEarlyPulses} \leq 3$: the number of pulses registered in the first 1600 ns of the event waveform must be less than or equal to three, an indication of light leakage from the previous event,
- $\text{deltaT} < 20 \text{ } \mu\text{s}$: the time between the event in question, i , and the event preceeding it, $i - 1$, must be greater than 20 μs , to avoid leakage of scintillation light from the previous event, and,

- **subeventN == 1**: the **subeventN** variable discussed in Section 4.1.3 must be equal to 1. This indicates that there is no evidence of multiple physics signals in the event waveform.

As outlined in Section 3.2.2, fiducial cuts are used to remove events that reconstruct near the edge of the detector or the liquid argon (LAr) fill level. These are most important for removing α -decay and radiogenic neutron background events, originating from radioactivity in the surface and bulk of the inner detector materials. In total, five fiducial cuts are applied to this dataset; events are selected if:

- **fmaxpe < 0.4**: this cut removes events for which more than 40% of the total event charge is observed in just one PMT. As described in Section 3.2.2, this cut was initially developed to remove Cherenkov background events, however it can also serve as a very loose fiducial radius cut,
- **chargeTopTwoRings/qPE < 0.04**: this cut removes events where more than 4% of the total event charge is detected in the PMTs located in the highest two rows at the top of the detector, designed to remove events originating near the top of the detector,
- **chargeBottomThreeRings/qPE < 0.1**: this cut removes events where more than 10% of the total event charge is detected in the PMTs located in the lowest three rows at the bottom of the detector, designed to remove events originating near the bottom of the detector,
- **Z_{rec} < 550 mm**: this cut removes events that reconstruct along the z -axis at a position above the LAr fill level, not originating from LAr scintillation, and,
- **R_{rec} < 720 mm**: this cut removes events that reconstruct at a radius greater than 720 mm. This defines a fiducial volume that is 1.5 times larger than the fiducial volume used in the published analysis of this dataset [4], to enhance the WIMP sensitivity.

Finally, several background rejection cuts developed specifically to remove background events, primarily neck α -decay events, are applied to the data. Events are selected if,

- **neckVetoN == 0**: this cut removes events if any of the four neck veto PMTs described in Section 2.2.1 observe light, an indication of scintillation originating from the neck,
- **R_{rec} consistency**: this cut removes events if the difference between the reconstructed radial positions determined from the TimeFit2 and MBLikelihood fitters is greater than what is expected for 85% of ^{39}Ar events, designed to remove neck α -decay events,
- **Z_{rec} consistency**: this cut removes events if the TimeFit2 returns a z coordinate higher than the MBLikelihood fitter, with a difference greater than what is expected for 90% of ^{39}Ar events, designed to remove neck α -decay events.

In the WIMP dark matter search published in [4], an additional background rejection cut specifically designed to remove neck α -decay backgrounds was applied:

- **PulseIndexFirstGAR > 2**: events are rejected if any of the first three pulses in the event waveform are registered in the GAR PMTs located above the LAr fill level. The calculation of the **PulseIndexFirstGAR** variable is described in Section 4.2.3.

Currently, there is no cut made on signals from the water tank veto PMTs, as optimisation studies are still ongoing. Without a cut on the water tank veto, cosmogenic muon/neutron backgrounds could be present in this dataset. A water tank veto cut is expected to be added to this analysis in the near future.

Table 5.1 displays the integrated cut acceptances inside the ROI for different cut streams, measured using ^{39}Ar data and ^{40}Ar MC, simulated nuclear recoils (NRs), to

ensure that the simulated acceptance for each cut is in agreement with the measured acceptance. The first row in Table 5.1 yields the cut acceptance for the five fiducial cuts listed above, given an event has already passed the low-level and pile-up cuts. The remaining four rows yield the cut acceptances for the four background rejection cuts individually, given an event has already passed low-level, pile-up and fiducial cuts.

Table 5.1: Integrated ROI acceptances for various WIMP dark matter search cut flows, calculated using ^{39}Ar data and ^{40}Ar MC (simulated NRs). The first row in Table 5.1 yields the cut acceptance for the five fiducial cuts listed above, given an event has already passed the low-level and pile-up cuts. The remaining four rows denoted with a * yield the cut acceptances for the four background rejection cuts individually, given an event has already passed low-level, pile-up and fiducial cuts.

| Cuts Applied | ^{40}Ar MC | ^{39}Ar Data |
|---|---------------------|-----------------------|
| Fiducial | 39.7% | 40.2% |
| Neck Veto* | 98.6% | 98.4% |
| Reconstructed R_{rec} Consistency* | 82.2% | 84.7% |
| Reconstructed Z_{rec} Consistency* | 89.8% | 90.5% |
| PulseIndexFirstGAR* | 52.5% | 53.6% |

5

Figure 5.1 shows the WIMP acceptance as a function of nSCBayes [PE] for two different cut-streams, calculated using ^{39}Ar data. The purple curve corresponds to the probability of a candidate WIMP event passing background rejection cuts including **PulseIndexFirstGAR**, given that it has already passed low-level, pile-up and fiducial cuts. The green curve corresponds to the probability of a candidate WIMP event passing background rejection cuts not including **PulseIndexFirstGAR**, given that it has already passed low-level, pile-up and fiducial cuts. The integrated WIMP acceptance inside the region-of-interest (ROI), 93 PE - 200 PE, when applying the **PulseIndexFirstGAR** cut is $\sim 46\%$, compared to an integrated WIMP acceptance of 81% when the **PulseIndexFirstGAR** cut is not applied; this illustrates that a large chunk of this acceptance loss is driven by the **PulseIndexFirstGAR** cut.

In an attempt to gain back WIMP sensitivity, the **PulseIndexFirstGAR** cut is

not applied to the 231 live-day dataset for the PLR WIMP analysis, and is instead modelled in the analysis as an additional parameter “dimension”. This is achieved as follows. Each signal and background model included in the PLR analysis is described by a three-dimensional PDF, based on the `nSCBayes`, `Fprompt` and `Rrec` variables. The `nSCBayes` variable is modelled as one-dimensional, whilst the `Fprompt` and `Rrec` variables are modelled as two-dimensional, as functions of `nSCBayes`, to account for the correlation between the `Fprompt`, `Rrec` variables with the event charge. Multiple three-dimensional PDFs are constructed per model, for different values of the `PulseIndexFirstGAR` variable. For each observed event in the dataset with `nSCBayes`, `Fprompt`, `Rrec` and `PulseIndexFirstGAR` values, the three-dimensional PDF which corresponds to the `PulseIndexFirstGAR` value of the event is used to calculate the expected probability for that event to reside inside the ROI for the source (signal or background) in question.

This method is motivated not only by the observed signal acceptance loss of the `PulseIndexFirstGAR` cut, but by the separation power it could provide between WIMP events and neck α -decays in addition to the other three variables. The `PulseIndexFirstGAR` distribution between WIMPs and neck α -decays varies considerably, with neck α -decays typically having much lower values of `PulseIndexFirstGAR` compared to WIMPs. This affects the number of events in each `PulseIndexFirstGAR` bin and changes the shape of the `nSCBayes`, `Fprompt` and `Rrec` distributions, due to correlations between these variables and `PulseIndexFirstGAR`. In the PLR approach, unlike a standard cut-and-count analysis, a non-zero number of events in the ROI does not necessarily degrade the WIMP sensitivity under the assumption that all background components are accurately accounted for. Including `PulseIndexFirstGAR` as an additional dimension in this way could therefore provide additional separation power between WIMPs and neck α -decays without the 35% acceptance loss, for increased WIMP sensitivity.

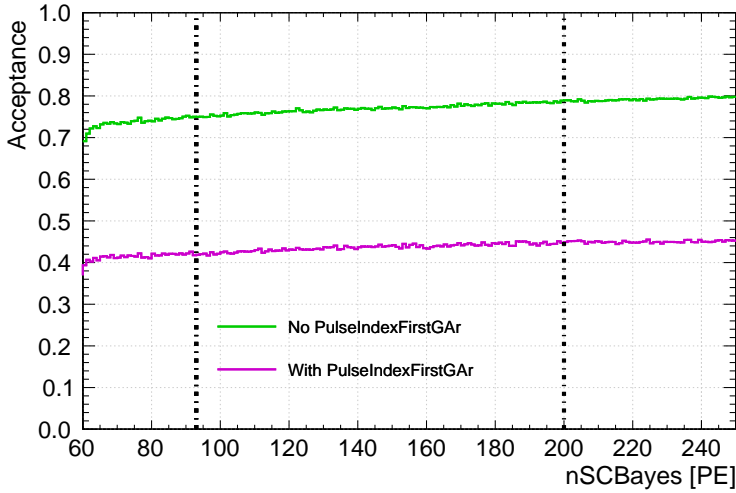


Figure 5.1: WIMP acceptance curves [%] as a function of `nSCBayes` [PE] for two different cut-streams, calculated using ^{39}Ar data: background rejection cuts including `PulseIndexFirstGAR` (purple) and background rejections cuts not including `PulseIndexFirstGAR` (green). Both curves represent the probability of a WIMP event to survive these cuts given that it has already passed the low-level, pile-up and fiducial cuts. The WIMP ROI is enclosed inside the two vertical dashed lines.

The WIMP ROI is defined in the two-dimensional `nSCBayes`- F_{prompt} plane. Since the PLR analysis is not a zero-background approach, the ROI bounds can be relaxed compared to a cut-and-count analysis, in order to enhance sensitivity. Nevertheless, the same `nSCBayes` ROI range of 93 PE - 200 PE is used in this analysis. As sensitivity grows exponentially with decreasing energy threshold, a natural place to expand the ROI would be to decrease the energy threshold, however, without a model to describe potential background events from Cherenkov radiation, the decision was made to constrain this lower bound at 93 PE for this iteration.

The upper and lower F_{prompt} bounds used in the PLR are looser here than in the published analysis [4]. The lower F_{prompt} bound is calculated by finding the value of F_{prompt} that maximises the quantity $s/\sqrt{(s+b)}$ for each `nSCBayes` bin, where s and b are the number of signal and background events respectively. If in each bin, there

are $N = s + b$ expected events, then this quantity represents the signal significance with respect to the 1σ Poisson uncertainty on N . The lower F_{prompt} bound used in [4] is harsher compared to the bound obtained from maximising $s/\sqrt{(s+b)}$ for $\text{nSCBayes} < 155$ PE, since it was constructed to reach the target number of electronic recoil (ER) background events of < 0.05 . The upper F_{prompt} bound is defined by the contour that yields a 10% NR acceptance loss in each nSCBayes bin, compared to the 30% NR acceptance loss contour used in [4] that was used to achieve the target number of neck α -decays of < 0.5 . A 10% NR acceptance loss is chosen as a compromise between an increase in WIMP acceptance (by 20% in each bin), and a loss in sensitivity from un-modelled Cherenkov backgrounds, expected to reside above this contour. A comparison of the two ROIs are shown in Figure 5.2.

After applying all low-level, pile-up, fiducial and background rejection cuts (not including `PulseIndexFirstGAR`) to the 231 live-day dataset, there are 24 surviving events that reside inside the expanded ROI illustrated in blue in Figure 5.2. This is the final data sample used in the PLR analysis.

5.2 Likelihood Function

THE likelihood function for the PLR WIMP search in DEAP-3600 is comprised of three terms:

$$\mathcal{L}(\sigma|\{\theta\}) = \mathcal{L}_{\text{PDF}}(\sigma|\{\theta\}) \cdot \mathcal{L}_{\text{constraint}}(\{\theta\}) \cdot \mathcal{L}_{\text{sideband}}(\{\theta\}), \quad (5.1)$$

where $\{\theta\} = \{\theta_1, \theta_2 \dots \theta_N\}$ are nuisance parameters, $\mathcal{L}_{\text{PDF}}(\sigma|\{\theta\})$ is the PDF term, $\mathcal{L}_{\text{constraint}}(\{\theta\})$ is the constraint term and $\mathcal{L}_{\text{sideband}}(\{\theta\})$ is the sideband term. $\mathcal{L}_{\text{PDF}}(\sigma|\{\theta\})$ is an unbinned term which contains parameter distributions selected for their discriminating power between signal and background models, and is given by,

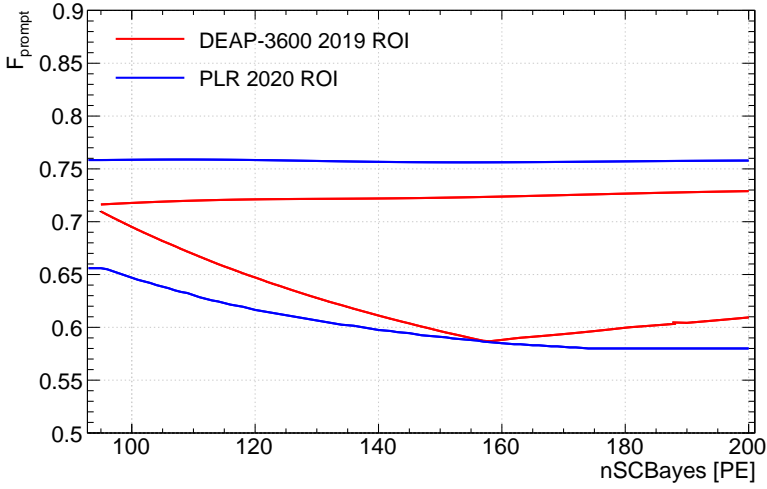


Figure 5.2: Two-dimensional plane of F_{prompt} vs $n\text{SCBayes}$, illustrating the two WIMP ROI boxes used for the cut-and-count analysis used in [4] (red) and for the PLR analysis performed in this thesis (blue).

$$\mathcal{L}_{\text{PDF}}(\sigma; \{\theta\}) = \text{Pois}(N_{\text{obs}}|N_{\text{exp}}) \times \prod_{j=1}^{N_{\text{obs}}} \left(\sum_{i=1}^{N_{\text{PDFs}}} \frac{N_{\text{exp},i}}{N_{\text{exp}}} \times f_i(n\text{SCBayes}, F_{\text{prompt}}, R_{\text{rec}}, \text{PulseIndexFirstGAR}; \{\theta\}) \right), \quad (5.2)$$

where N_{exp} is the total number of expected events in the ROI from all models (signal + background), N_{obs} is the total number of observed events in the ROI in data. As previously outlined, each model PDF f_i is built in three dimensions based on three event observables: $n\text{SCBayes}$ [PE], F_{prompt} and R_{rec} [mm]. Each 3D model is built in five different `PulseIndexFirstGAR` bins: $= 0$, $= 1$, $= 2$, $= 3$, or ≥ 4 . These five bins were chosen as a compromise between optimising the separation power between WIMPs and neck α -decays using the `PulseIndexFirstGAR` variable, and computing time to produce sufficient PDF statistics. The probability for each event to reside in the ROI, given its $n\text{SCBayes}$, F_{prompt} , R_{rec} and `PulseIndexFirstGAR` values, is

computed, and multiplied by the ratio of the number of expected events in the ROI from the model in question, $N_{\text{exp},i}$ to N_{exp} . This probability is summed over all models. The total term is the product of this quantity for each observed event. Finally, the total term is multiplied by a Poisson term, which compares N_{obs} with N_{exp} .

The constraint term $\mathcal{L}_{\text{constraint}}(\{\theta\})$ incorporates systematic uncertainties into the PLR in the form of nuisance parameters, and is given by,

$$\mathcal{L}_{\text{constraint}}(\{\theta\}) = \prod_{j=1}^{n_{\theta}} f(\theta_j), \quad (5.3)$$

where n_{θ} is the total number of nuisance parameters and $f(\theta_j)$ are constraint PDFs. Each nuisance parameter has an associated constraint PDF, which contributes to the likelihood function proportionally with the relevant level of systematic uncertainty. Most systematic uncertainties are modelled with Gaussian uncertainties; this results in a constraint PDF of the form $\text{Gaus}(\mu, \sigma)$, with the μ parameter set to the nominal value of the nuisance parameter and σ set to the size of the uncertainty. The values of μ and σ come from measurements made in calibration datasets or sidebands, outside the ROI. For example, the mean light yield of the detector is determined from fitting the `nSCBayes` distribution of ^{39}Ar data, similarly to the method described in Section 4.1.1; the mean light yield for this dataset is calculated to be $\text{LY} = 6.1 \pm 0.4 \text{ PE/keV}$ [4]. The associated constraint PDF for this nuisance parameter is $\text{Gaus}(6.1, 0.4) [\text{PE/keV}]$. There are just two nuisance parameters not modelled with a Gaussian constraint PDF; these are detailed in a full table that lists all of the nuisance parameters and their constraint PDFs, and whether they are being allowed to float in the fit, in Section 6.2. Section 6.2 motivates why these particular systematics are used in the PLR. The total term added to the likelihood, $\mathcal{L}_{\text{constraint}}(\{\theta\})$, is the product of all of the constraint PDFs when evaluated at the test value of the nuisance parameter.

The final term, $\mathcal{L}_{\text{sideband}}(\{\theta\})$, is based on using internal ^{39}Ar calibration data to further constrain certain nuisance parameters and reduce the overall systematic uncertainty. The sideband term is constructed as a binned likelihood evaluated over three dimensions,

$$\mathcal{L}_{\text{sideband}}(\{\theta\}) = \prod_i^{N_i} \prod_j^{N_j} \prod_k^{N_k} \text{Pois}(N_{\text{obs};i,j,k} | N_{\text{exp};i,j,k}), \quad (5.4)$$

where $N_{\text{obs};i,j,k}$ corresponds to the the number of observed ^{39}Ar events in data for a given **nSCBayes**, $\mathbf{F}_{\text{prompt}}$ and \mathbf{R}_{rec} bin, denoted $\{i, j, k\}$, and $N_{\text{exp};i,j,k}$ corresponds to the number of expected ^{39}Ar events in the same bin predicted by the ^{39}Ar model. Currently, the sideband term is configured to integrate over the $\mathbf{F}_{\text{prompt}}$ dimension. It is used to constrain systematics such as the light yield, energy resolution and reconstructed position bias, described earlier in Section 3.2.

The selection criteria used to construct the sideband include the following. The same low-level and pile-up cuts as applied for the WIMP search are applied. An $\mathbf{F}_{\text{prompt}}$ selection criterion of $0.1 < \mathbf{F}_{\text{prompt}} < 0.5$ is applied to the data, to ensure a clean sample of single ^{39}Ar events are selected. No fiducial cuts, such as a \mathbf{R}_{rec} cut, are applied; fiducial cuts can distort the shape of the ^{39}Ar spectrum. One run from the 231 live-day dataset, corresponding to 0.9 live-days ($\sim 2.5 \times 10^8$ ^{39}Ar events) is used to build the three-dimensional histogram used for the sideband.

A “median” run is selected for the sideband, located approximately six months into the full one year of data acquisition from which the 231 live-day dataset is derived. When all 231 live-days are considered in the sideband data, the fit quality from just fitting the **nSCBayes** distribution becomes considerably worse; the χ^2/NDF was observed to increase by at least a factor of 10. This is attributed to the change in detector stability over the duration of the dataset. In lieu of this, only one run is used in the sideband, to ensure a good fit quality ($\chi^2/\text{NDF} \leq 1$). A median run located (in time) at the centre of the dataset is chosen due to the fact that the mean

light yield is observed to decrease as a function of time, illustrated by Figure 4.5. The mean light yield value obtained from a fit to this particular run corresponds to a near central value (6.068 PE/keV) between the mean light yield at the start of the dataset (~ 6.16 PE/keV) and the end of this dataset (~ 6.02 PE/keV).

5.3 Signal and Background Model Construction

5.3.1 WIMPs and ^{39}Ar

nSCBayes Model

THE nSCBayes dimension of the WIMP signal and ^{39}Ar background models are both constructed from theoretical distributions convolved with a Gaussian detector response model. The six detector response parameters (three energy scale parameters defined in Equation 4.4 and three energy resolution parameters defined in Equation 4.5), are first obtained from fitting the ^{39}Ar nSCBayes distribution, described in Section 4.1.1. The functional form described by Equation 4.9 is implemented in the PLR to describe the ^{39}Ar nSCBayes distribution. With the exception of the mean light yield parameter, the parameters used to describe the ^{39}Ar nSCBayes distribution, such as the energy resolution, the three relative normalisations from single ^{39}Ar , coincidence ^{39}Ar and additional ER background contributions and the “experimental shape” deviation are “fixed” in the final configuration for the PLR WIMP search. This means that the values of these parameters are not allowed to change in the likelihood, and thus the systematic uncertainties from these parameters are not accounted for. The a-priori values for each of these parameters that are fixed in the PLR are determined from a separate fit to the ^{39}Ar sideband data only, and are summarised in Table 6.1.

The WIMP differential recoil rate dR/dE_R , given in Equation 1.26, describes the expected energy distribution of WIMPs as a function of their recoil energy,

E_{nr} [keV_{nr}]; this is translated into electron-equivalent energy in the detector [keV_{ee}] using Equation 2.3 and the quenching factor $q_n(E_{\text{nr}})$, described in Section 2.1.2. Once in electron-equivalent energy, the distribution is convolved with the detector response model given by Equation 4.3, using the same energy response parameters as obtained from the fit to the ^{39}Ar spectrum. An example **nSCBayes** distribution for a 100 GeV/ c^2 WIMP with a WIMP-nucleon cross-section of 10^{-44} cm^2 is shown in Figure 5.3, drawn using the nominal values for the energy scale parameters, energy resolution parameters and $q_n(E_{\text{nr}})$.

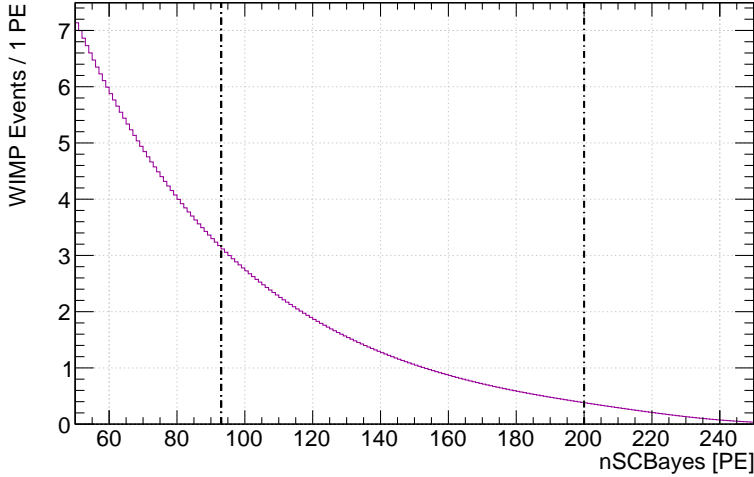


Figure 5.3: Number of events [PE^{-1}] for a 100 GeV/ c^2 WIMP as a function of **nSCBayes** [PE], using a WIMP-nucleon cross-section of 10^{-44} cm^2 (purple). The WIMP ROI is enclosed inside the two vertical dashed lines (black), between 93 PE - 200 PE.

F_{prompt} Model

IN Section 3.2.2, an 11-parameter effective model (Equation 3.9) was introduced that describes the ER **F_{prompt}** distribution as a function of **nSCBayes**. By fitting ^{39}Ar data, the DEAP-3600 collaboration determined the values of these 11 parameters which describe the evolution of the mean **F_{prompt}** $\bar{f}(PE)$, the skew $b(PE)$ and

the width $\sigma(PE)$ of the ER F_{prompt} distribution with **nSCBayes**.

This same model can be used to describe the NR F_{prompt} distribution, F^{NR} , by inverting the skew of the distribution,

$$F^{\text{NR}} = \Gamma(1 - f; 1 - \bar{f}, b) \otimes \text{Gaus}(f; \sigma), \quad (5.5)$$

where $\bar{f} \rightarrow \bar{f}(PE)$, $b \rightarrow b(PE)$ and $\sigma \rightarrow \sigma(PE)$. The assumption is made that the skew in the F_{prompt} distribution behaves the same for NRs as it does for ERs, and thus the same functions for $b(PE)$ can be used.

The mean NR F_{prompt} , $\bar{f}(PE)$, is derived from the f_{90} ratio measurements reported by the SCENE experiment [63], which consists of a dual-phase LAr time projection chamber; f_{90} is a discrimination parameter, defined as the fraction of light detected in the first 90 ns of the S1 signal [63]. The f_{90} ratios are converted into LAr scintillation singlet-to-triplet ratios, which are then implemented into the Reactor Analysis Tool (RAT) framework as an MC simulation input. Simulations of ^{40}Ar NRs uniformly distributed across the detector are used to obtain the mean NR F_{prompt} as a function of E_{nr} . This is transformed to be a function of **nSCBayes**, $\bar{f} \rightarrow \bar{f}(PE)$, using the quenching factor $q_n(E_{\text{nr}})$.

In order to assess the importance of detector systematic uncertainties on Pulse-Shape Discrimination (PSD), this technique was repeated with variations on the PMT afterpulsing probabilities, the LAr scintillation triplet lifetime and the LAr scintillation singlet-to-triplet measurements reported by SCENE to produce $\pm 1\sigma$ curves; all three curves are shown in Figure 5.4. This systematic uncertainty is not currently considered in the PLR however as it is subdominant compared to other systematics considered in this analysis, such as $q_n(E_{\text{nr}})$ and the mean light yield.

The effect of the energy resolution is important on the NR F_{prompt} distribution. Since the mean NR F_{prompt} depends on E_{nr} , a given F_{prompt} value can populate multiple **nSCBayes** given the energy resolution. The correlation of these two parameters

in the PLR is accounted for as follows:

1. The mean NR F_{prompt} is calculated as a function of **nSCBayes**, $\bar{f}(PE)$, using E_{nr} and $q_n(E_{\text{nr}})$,
2. A normalised Gaussian of μ equal to **nSCBayes** and σ equal to the energy resolution is constructed,
3. For each of the **nSCBayes** values that span $\pm 3\sigma$ of the mean value, the Gaussian is evaluated to give the probability that a WIMP with recoil energy E_{nr} and mean $\bar{f}(PE)$ contributes to that particular **nSCBayes** bin; this value is filled into a 2D histogram of F_{prompt} versus **nSCBayes**, and is repeated over all recoil energies,
4. A projection of the 2D histogram onto the F_{prompt} axis is made for the **nSCBayes** bin in question. The width of this histogram is fed into Equation 5.5 as the $\sigma(PE)$ parameter.

Since the uncertainty on the energy resolution is not currently considered in PLR, this width $\sigma(PE)$ does not change. However, this dependence on the energy resolution results in a wider F_{prompt} distribution for NRs as expected for ERs. This is illustrated by Figure 5.5, which shows the expected F_{prompt} distribution for WIMPs and ^{39}Ar inside the WIMP ROI [93 PE - 200 PE] as implemented in the PLR.

R_{rec} Model

SINCE the WIMP-nucleon cross section is so small, the probability of a WIMP scattering off of a nucleon is equal across the LAr volume. This means that the same reconstructed radial model can be used for both WIMPs and ^{39}Ar β -decays, which also occur uniformly across the LAr volume.

The R_{rec} dimension for WIMPs (and ^{39}Ar) is implemented as a convolution of the expected probability of a scattering event to take place at a given true radius R_{MC}

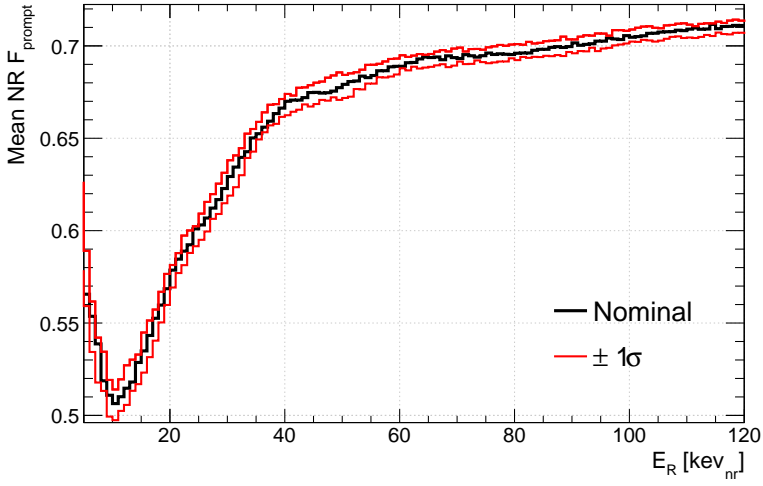


Figure 5.4: Mean NR F_{prompt} as a function of recoil energy [keV_{nr}] (black), implemented for the WIMP F_{prompt} dimension in the PLR. The two red curves depict the $\pm 1\sigma$ uncertainty bounds, driven by PMT afterpulsing probabilities in simulation, the LAr scintillation triplet lifetime and the LAr scintillation singlet-to-triplet measurements reported by SCENE. These uncertainties are not currently treated as a systematic in the PLR.

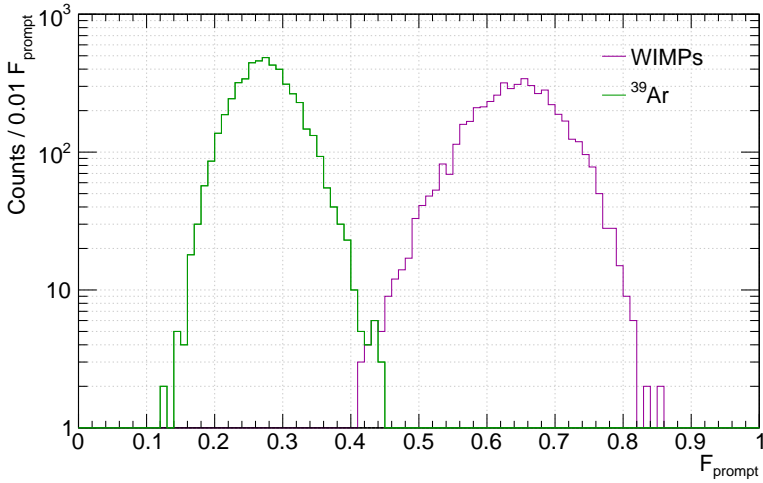


Figure 5.5: F_{prompt} distributions of WIMPs (pink) and ^{39}Ar β -decays (green) inside the WIMP ROI [93 PE - 200 PE], drawn randomly from the two-dimensional models of F_{prompt} vs nSCBayes implemented in the PLR. Both histograms are normalised to unit area.

with an `nSCBayes` and `Rrec` dependent Gaussian radial resolution function. Given spherical geometry, the probability for a scatter to occur in the LAr volume as a function of R_{MC} can be written as,

$$P(R_{MC}) = \frac{3R_{MC}^2}{R_0^2}, \quad (5.6)$$

where $R_0 = 851$ mm. The LAr fill level is neglected in this parameterisation, due to the fact that the deviation from a uniform radial distribution as a result of the fill level is itself negligible. To account for the fact that position reconstruction algorithms do exhibit some bias, the true distribution is convolved with a Gaussian radial resolution function, obtained using the method described in Section 3.2.3. The charge-dependent two-dimensional model of `Rrec` versus `nSCBayes` for uniformly distributed events as implemented in the PLR is displayed in Figure 5.6. Two nuisance parameters were introduced in the PLR to allow the nominal values of the radial bias μ and resolution σ parameters of the Gaussian radial resolution function to shift, however these systematics are not currently considered in the PLR analysis.

PulseIndexFirstGAR Model

ONCE the three-dimensional PDF has been constructed from the `nSCBayes`, `Fprompt` and `Rrec` dimensions, the PDF is further separated into five different `PulseIndexFirstGAR` bins. For WIMPs and ^{39}Ar , "binning" in `PulseIndexFirstGAR` is not so simple as the models are constructed from analytical or empirical functions determined from theory or from fits to data, which are only applicable over all `PulseIndexFirstGAR` values. In order to develop five different `PulseIndexFirstGAR` PDFs, various empirical "reweighting" functions are applied to the nominal `nSCBayes`, `Fprompt` and `Rrec` dimensions described above, which consider all `PulseIndexFirstGAR` values. These functions account for the shape deviation and overall rate change in the different distributions between various `PulseIndexFirstGAR` bins. These

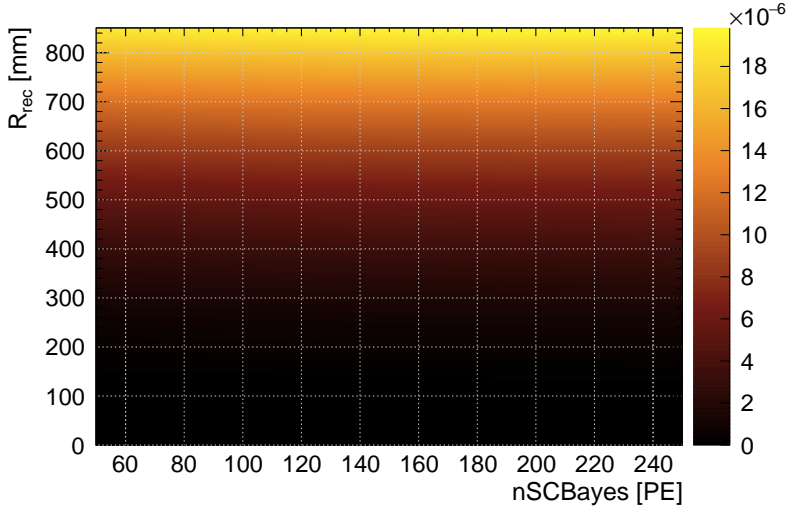


Figure 5.6: Illustration of the two-dimensional radial R_{rec} model implemented in the PLR for both WIMPs and ^{39}Ar , against `nSCBayes` [PE]. Events are distributed uniformly throughout the detector volume. The histogram is arbitrarily normalised to unity.

reweighting functions can be determined from ^{39}Ar data. The same reweighting functions are used for both WIMPs and ^{39}Ar , given that their expected event topology is the same. Differences in the `nSCBayes` spectrum of WIMPs and ^{39}Ar are factored out in this method, described below.

For the `nSCBayes` dimension, six one-dimensional histograms of the `nSCBayes` spectrum for ^{39}Ar data are built; one over all `PulseIndexFirstGAR` values, and one for each of the following `PulseIndexFirstGAR` bins: 0, 1, 2, 3, 4+. Each of the histograms corresponding to each of the `PulseIndexFirstGAR` bins are then divided by the histogram over all `PulseIndexFirstGAR` values; this results in a distribution which describes how the nominal model shape deviates when considering a particular `PulseIndexFirstGAR` bin. The rate variation in each `PulseIndexFirstGAR` bin is also intrinsically accounted for using this method. The shape deviation for each bin is modelled with a quartic polynomial, which acts as the reweighting function. An example quartic polynomial fit to the shape deviation in the `nSCBayes` distribution

from the `PulseIndexFirstGAR = 0` bin is shown in Figure 5.7. Depending on what value of `PulseIndexFirstGAR` an event has, the corresponding reweighting function is multiplied by the nominal model implemented in the PLR. After this procedure, when the `nSCBayes` portion of the PDF is evaluated for a given event, the correct `nSCBayes` spectrum corresponding to the equivalent `PulseIndexFirstGAR` bin is evaluated.

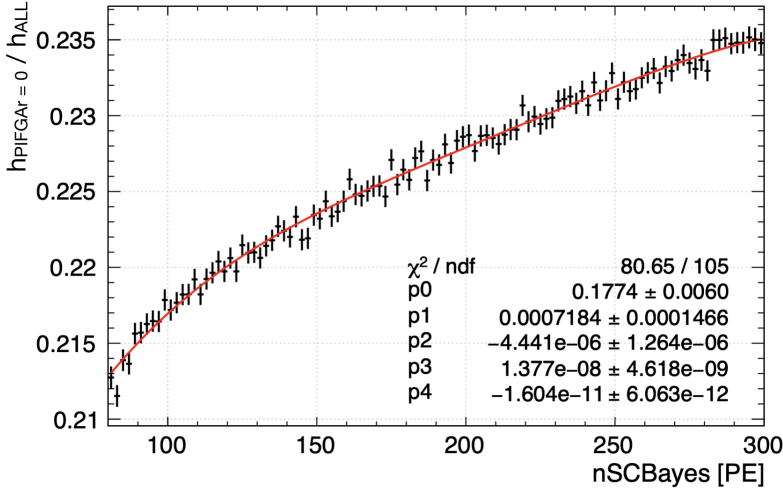


Figure 5.7: Ratio of the `nSCBayes` spectrum from ^{39}Ar events with `PulseIndexFirstGAR = 0` to the `nSCBayes` spectrum from ^{39}Ar events over all `PulseIndexFirstGAR` values. The distribution is fit with a quartic polynomial over the range 80 PE - 300 PE to determine the reweighting function.

The same approach is taken for the F_{prompt} and R_{rec} dimensions, instead using two-dimensional histograms of F_{prompt} vs `nSCBayes` and R_{rec} vs `nSCBayes` so that the approach described above can be repeated in three `nSCBayes` bins spanning 80 PE - 380 PE; this conserves the charge-dependence in the F_{prompt} and R_{rec} models across the ROI and marginally above and below the ROI, in case the ROI is expanded in the future. Only three bins in `nSCBayes` are chosen since the charge dependence is not expected to change drastically across this limited range. The shape deviation between the nominal F_{prompt} distribution compared to the distribution in a given

`PulseIndexFirstGAR` bin can be modelled with a quadratic polynomial, as shown in Figure 5.8. Figure 5.8 shows an example fit to the shape deviation in the F_{prompt} distribution shape from the `PulseIndexFirstGAR` = 0 bin, between 80 PE - 180 PE. The fit is only performed between 0.1 - 0.42 in F_{prompt} , where there are sufficient statistics; the assumption is made that the F_{prompt} reweighting functions used for ERs can be applied to the $(1 - F_{\text{prompt}})$ distribution for NRs, since NRs are expected to have an inverted skew in the F_{prompt} distribution.

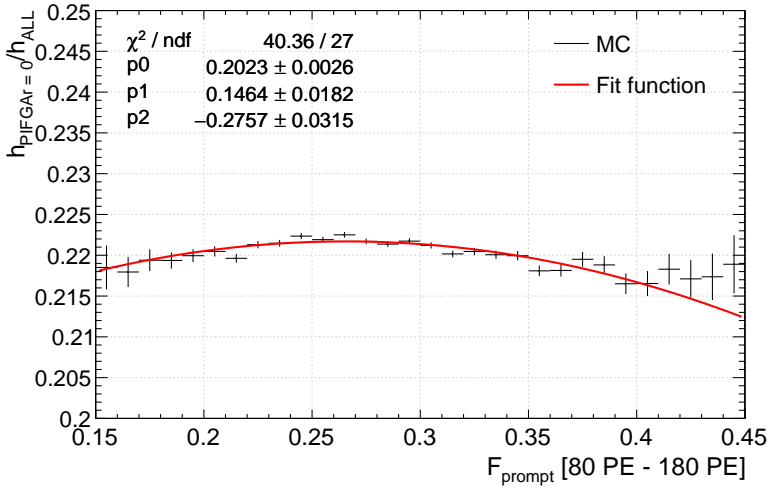


Figure 5.8: Ratio of the F_{prompt} spectrum from ^{39}Ar events with `PulseIndexFirstGAR` = 0 between 80 PE - 180 PE to the F_{prompt} spectrum from ^{39}Ar events over all `PulseIndexFirstGAR` values between 80 PE - 180 PE. The distribution is fit with a quadratic polynomial over the range 0.1 - 0.42 F_{prompt} , to determine the reweighting function.

The evolution of each of the three parameters from the quadratic polynomial are then described as a function of `nSCBayes` with a quadratic polynomial themselves. This results in a set of five two-dimensional reweighting functions, dependent on both F_{prompt} and `nSCBayes`; depending on what value of `PulseIndexFirstGAR` an event has, the corresponding two-dimensional reweighting function will be multiplied by the nominal two-dimensional F_{prompt} model implemented in the PLR. In

this way, when the F_{prompt} portion of the PDF is evaluated for a given event, the correct F_{prompt} spectrum corresponding to the equivalent `PulseIndexFirstGAR` bin is evaluated.

The implementation of the two-dimensional F_{prompt} -`nSCBayes` reweighting functions in the PLR are validated by comparing the ^{39}Ar F_{prompt} distribution from data over all `PulseIndexFirstGAR` bins with the sum of the five separate ^{39}Ar F_{prompt} distributions from different `PulseIndexFirstGAR` bins, constructed by drawing from the nominal ^{39}Ar F_{prompt} model and applying the corresponding reweighting functions. This is validated at a single `nSCBayes` value near the centre of the WIMP ROI energy range (150 PE), displayed in Figure 5.9. The summed ^{39}Ar F_{prompt} distribution from the PLR is consistent with the ^{39}Ar F_{prompt} distribution from data, confirming that the reweighting functions are correctly implemented.

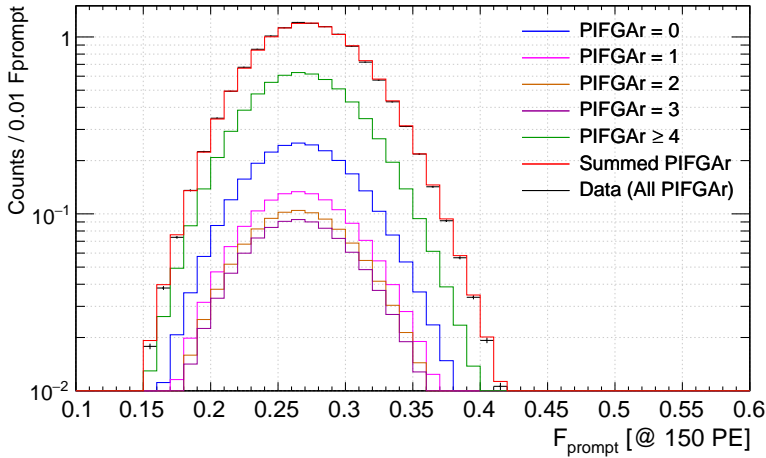


Figure 5.9: Comparison the ^{39}Ar F_{prompt} distribution from data over all `PulseIndexFirstGAR` bins with the sum of the five separate ^{39}Ar F_{prompt} distributions from different `PulseIndexFirstGAR` bins, constructed by drawing from the nominal ^{39}Ar F_{prompt} model and applying the corresponding reweighting function.

The shape deviation between the nominal R_{rec} distribution compared to the distribution in a given `PulseIndexFirstGAR` bin cannot be modelled with a simple

polynomial, as illustrated by Figures 5.10 and 5.11; this is due to the fact that `PulseIndexFirstGAR` is highly correlated with the location of an event inside the detector. It was found that for `PulseIndexFirstGAR` bins = 0, 1, 2 and 3, the best functional form to describe the shape deviation of the reduced radial distribution cubed $(R_{\text{rec}}/R_0)^3$, from different `PulseIndexFirstGAR` bins was the sum of an exponential and a quadratic polynomial. For the `PulseIndexFirstGAR` ≥ 4 bin, the best functional form was found to be the sum of a logarithm and a quadratic polynomial:

$$f(\bar{R}, PE) = \begin{cases} \exp(p_0(PE) + p_1(PE)\bar{R}) + p_2(PE) + p_3(PE)\bar{R} + p_4(PE)\bar{R}^2, \\ (1.0/p_0(PE)) \log(p_1(PE)\bar{R}) + p_2(PE) + p_3(PE)\bar{R} + p_4(PE)\bar{R}^2, \end{cases} \quad (5.7)$$

where $\bar{R} = (R_{\text{rec}}/R_0)^3$ and $p_i(PE)$ are the charge-dependent empirical fit parameters. The first expression in Equation 5.7 is for `PulseIndexFirstGAR` < 4 and the second is for `PulseIndexFirstGAR` ≥ 4 . As with the `Fprompt` dimension, this process is repeated over multiple `nSCBayes` bins; the evolution of each of the five parameters with `nSCBayes` from the functions described in Equation 5.7 are modelled with cubic polynomials. Two example fits to the $(R_{\text{rec}}/R_0)^3$ distributions for `PulseIndexFirstGAR` = 0 and `PulseIndexFirstGAR` ≥ 4 bins, divided by the $(R_{\text{rec}}/R_0)^3$ distribution over all `PulseIndexFirstGAR` values, for the 80 PE - 180 PE range are shown in Figures 5.10 and 5.11 respectively. The fit range is defined to be 0 - 0.85 in $(R_{\text{rec}}/R_0)^3$ (equivalently 0 mm - 800 mm in R_{rec}); the fit is not performed up to the very edge of the detector as shown in Figure 3.13, the `MBLikelihood` fitter algorithm experiences bias, causing a sharp spike at the edge of the detector.

Once again, this yields a set of five two-dimensional reweighting functions, dependent on R_{rec} and `nSCBayes`. For an event with a given `PulseIndexFirstGAR`, the corresponding two-dimensional reweighting function as obtained from Equation 5.7 is multiplied by the nominal two-dimensional radial model implemented in the

PLR. In that way, when the R_{rec} portion of the PDF is evaluated for a given event, the correct R_{rec} distribution corresponding to the equivalent `PulseIndexFirstGar` bin is evaluated.

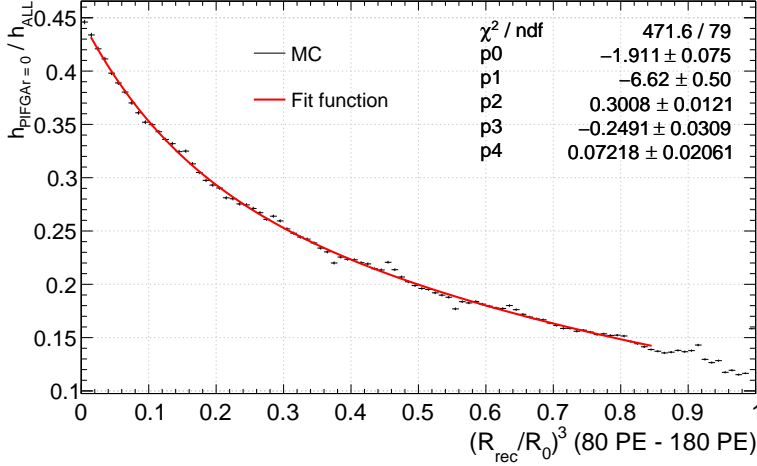


Figure 5.10: Ratio of the $(R_{\text{rec}}/R_0)^3$ distribution of ^{39}Ar events between 80 PE - 180 PE for the `PulseIndexFirstGar` = 0 bin to the $(R_{\text{rec}}/R_0)^3$ distribution of ^{39}Ar events over all `PulseIndexFirstGar` values, fitted with an exponential + polynomial as described in Equation 5.7.

The implementation of the two-dimensional R_{rec} -`nSCBayes` reweighting functions in the PLR are validated using the same method as described for the F_{prompt} dimension. The ^{39}Ar R_{rec} distribution from data over all `PulseIndexFirstGar` bins is compared with the sum of the five separate distributions from the five `PulseIndexFirstGar` bins, constructed by drawing from the nominal ^{39}Ar R_{rec} model with the corresponding reweighting functions applied. This is validated for just one `nSCBayes` value near the centre of the WIMP ROI energy range (150 PE) displayed in Figure 5.12. The summed ^{39}Ar R_{rec} distribution from the PLR is consistent with the ^{39}Ar R_{rec} distribution from data, confirming that the reweighting functions are correctly implemented.

For generating pseudoexperiments, described in Section 6.1, a `PulseIndexFirstGar`

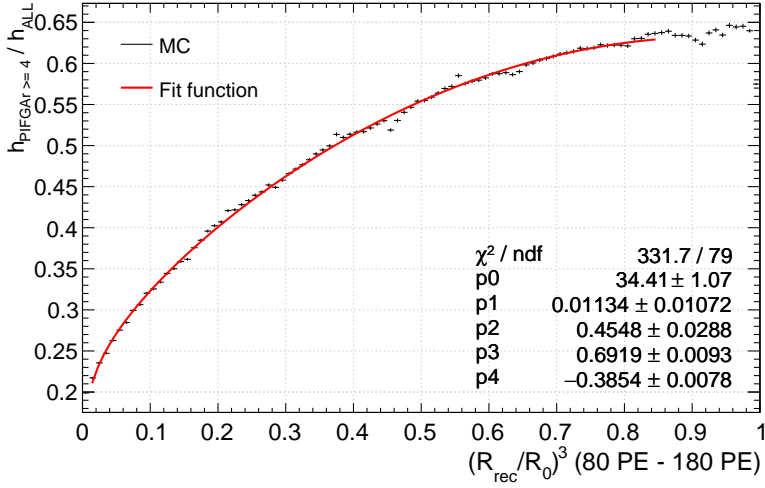


Figure 5.11: Ratio of the $(R_{\text{rec}}/R_0)^3$ distribution of ^{39}Ar events between 80 PE - 180 PE for the $\text{PulseIndexFirstGAR} \geq 4$ bin to the $(R_{\text{rec}}/R_0)^3$ distribution of ^{39}Ar events over all $\text{PulseIndexFirstGAR}$ values, fitted with a logarithm + polynomial as described in Equation 5.7.

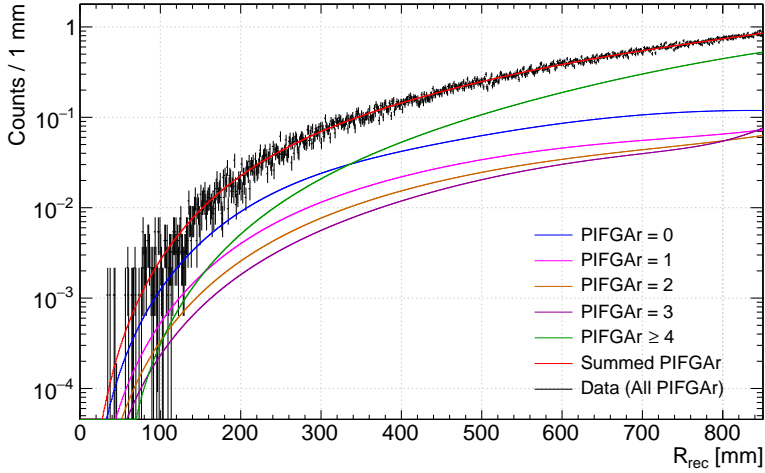


Figure 5.12: Comparison of the ^{39}Ar R_{rec} distribution from data over all $\text{PulseIndexFirstGAR}$ bins with the sum of the five separate ^{39}Ar R_{rec} distributions from different $\text{PulseIndexFirstGAR}$ bins, constructed by drawing from the nominal ^{39}Ar R_{rec} model and applying the corresponding reweighting function.

model for each event type is required in order to generate a random `PulseIndexFirstGar` value for an event of given `nSCBayes`, F_{prompt} and R_{rec} values. The `PulseIndexFirstGar` distribution for WIMPs and ^{39}Ar is modelled directly from ^{39}Ar data, with the sum of a Gaussian distribution and exponential. The functional form implemented in the PLR can be seen in Figure 5.13, shown superimposed on the `PulseIndexFirstGar` distribution obtained from simulated ^{40}Ar NRs, to ensure that the simulated WIMP `PulseIndexFirstGar` distribution is in reasonable agreement with the measured distribution determined from ^{39}Ar data.

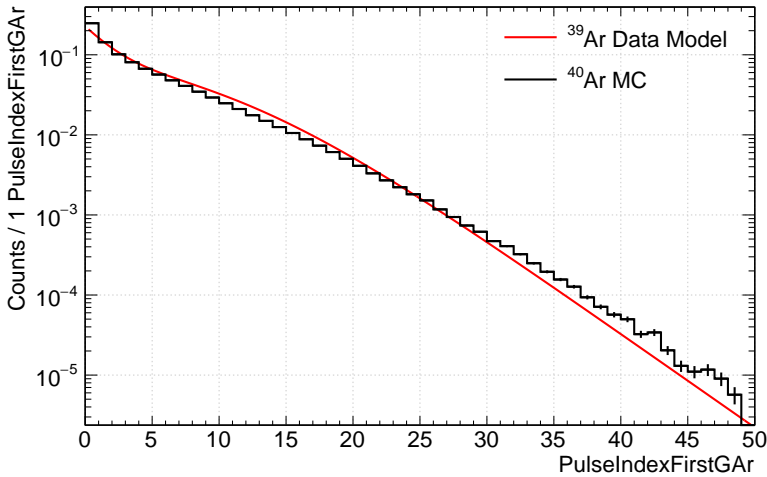


Figure 5.13: The model implemented in the PLR for the ^{39}Ar /WIMP `PulseIndexFirstGar` distributions, as determined from fitting ^{39}Ar data (red), shown superimposed on the raw `PulseIndexFirstGar` distribution from simulated ^{40}Ar NRs (black). The simulated WIMP `PulseIndexFirstGar` distribution is in reasonable agreement with the measured distribution determined from ^{39}Ar data.

5.3.2 Neck α -decays

THE approach taken to construct the remaining background models in the PLR software (neck α -decays, surface α -decays, dust α -decays and radiogenic neutrons) is the same for each background source. The three-dimensional PDFs are

built from one and two-dimensional empirical functions, determined from fitting the **nSCBayes**, F_{prompt} and R_{rec} distributions obtained from high-statistics MC simulations after applying the WIMP dark matter search cuts listed in Section 5.1. Empirical functions are chosen to model the distributions due to the fact that after applying the WIMP dark matter search cuts to the MC events, the shape of the distributions can be changed in a non-trivial way.

For each **nSCBayes** dimension, a one-dimensional empirical function is used to describe the distribution. The empirical fit parameters obtained from these fits are not considered as nuisance parameters in the PLR, and are therefore not allowed to vary. For the F_{prompt} and R_{rec} dimensions, which are constructed to be correlated with **nSCBayes**, two-dimensional empirical functions are used to describe the distributions. This is achieved by performing multiple one-dimensional fits to the F_{prompt} and R_{rec} distributions using empirical functions in numerous **nSCBayes** bins, spanning from 50 PE up to ~ 1000 PE. Each of the empirical fit parameters from these one-dimensional fits are then modelled as a function of **nSCBayes**, $a \rightarrow a(PE)$, typically with a simple quadratic polynomial unless otherwise stated.

The quadratic polynomial parameters, which describe the evolution of the parameters with **nSCBayes** are also not implemented as nuisance parameters in the PLR, and thus are not allowed to vary. The motivation to call these empirical fit parameters rather than incorporate them as individual systematic uncertainties in the PLR is two-fold. Firstly, this method from a computing perspective is favourable; reducing the overall number of free parameters helps to speed up the code as well as help the stability of the fit itself. Secondly, it has been observed that uncertainties in the modelling of the distributions are smaller than the systematic uncertainties already considered in the PLR, from the mean light yield, LAr optical model, TPB scattering length, PMT afterpulsing probabilities, relative PMT efficiencies and overall background normalisations. This is discussed in detail in

Section 6.2.

To incorporate the `PulseIndexFirstGAR` dimension into the models, MC events are first separated based on their `PulseIndexFirstGAR` value into one of the following bins: 0, 1, 2, 3 or 4+. This yields five sets of one and two-dimensional histograms for the `nSCBayes`, F_{prompt} and R_{rec} dimensions, used to construct the distributions. The procedure described above is repeated for each of these five `PulseIndexFirstGAR` bins, to yield five sets of one and two-dimensional empirical functions, each corresponding to a particular `PulseIndexFirstGAR` bin. This is not the case however for the radiogenic neutron background, which is not binned in `PulseIndexFirstGAR` in this way. The motivation for this and how this is handled mathematically in the PLR is explained later in this chapter. The following subsections individually describe the characterisation of each of the remaining background sources in the PLR analysis.

nSCBayes Model

APPROXIMATELY 10^6 events are simulated for each of the different neck α -decay sources discussed in Section 4.2.3, the inner flow guide inner surface (IFGIS), inner flow guide outer surface (IFGOS) and outer flow guide inner surface (OFGIS); the exact number of events simulated at each source reflects the relative trigger rates tabulated in Section 4.2.3. All of the WIMP dark matter search cuts listed in Section 5.1, with the exception of `PulseIndexFirstGAR`, are then applied to the simulated events. For each source, events that survive all cuts are filled into a one-dimensional `nSCBayes` histogram and two, two-dimensional F_{prompt} vs `nSCBayes` and R_{rec} vs `nSCBayes` histograms.

Since each source corresponds to neck α -decays originating from a different location, the event topologies from each source differ from one another. Consequently, there are variations in the `nSCBayes`, F_{prompt} and R_{rec} distributions between the

different sources that need to be reflected in the construction of the total neck α -decay model. As such, before fitting the distributions, the one and two-dimensional histograms from the three separate sources are summed together. Whilst the uncertainties on the individual trigger rates are not explicitly accounted for in this parameterisation, they are also determined to be smaller than the uncertainties from the other systematics considered in the neck α -decay model.

The **nSCBayes** distribution for the summed neck α -decay PDF is fit between 80 - 600 PE with the sum of four Gaussians for each of the five **PulseIndexFirstGar** bins,

$$f(PE) = \sum_{i=1}^4 N_i \exp\left(-\frac{1}{2}\left(\frac{PE - \mu_i}{\sigma_i}\right)^2\right). \quad (5.8)$$

An example fit is shown in Figure 5.14 for the **PulseIndexFirstGar** = 0 bin. The fit range 80 PE - 600 PE is chosen as a control region, used to constrain the overall neck α -decay ROI normalisation in the PLR. This fit function was originally chosen to attempt to model the individual “peak” features seen in Figure 5.14. This fit function was also found to be the only function that can consistently model the distribution in all **PulseIndexFirstGar** bins, as well as for all MC parameter systematic variations; this is explained further in Section 6.2.

After neck α -decays are simulated, a post-processing weighting is applied to each event, to ensure that events are simulated uniformly along the z -axis of the flow guides. These weights introduce a “peak-like” structure to the **nSCBayes** distribution, enhanced by the event selection cuts as illustrated in Figure 5.14. It was found that the fit function described by Equation 5.8 does not have sensitivity to resolve all of these individual features outside of the ROI in all **PulseIndexFirstGar** bins, due to the fact that these features are not physical. Figure 5.15 shows the five best fit functions corresponding to each of the **PulseIndexFirstGar** bins drawn on top of each other. There is only sensitivity to the peak at ~ 350 PE in the

$\text{PulseIndexFirstGAR} = 1$ bin, which is more pronounced in this bin than in the other $\text{PulseIndexFirstGAR}$ bins. The effect on the prediction of the ROI normalisation from mismodelling these bumps is found to be smaller than from the systematic uncertainties already considered in the PLR, from the mean light yield, LAr optical model, TPB scattering length, PMT afterpulsing probabilities, relative PMT efficiencies and overall background normalisation, discussed in detail in Section 6.2.

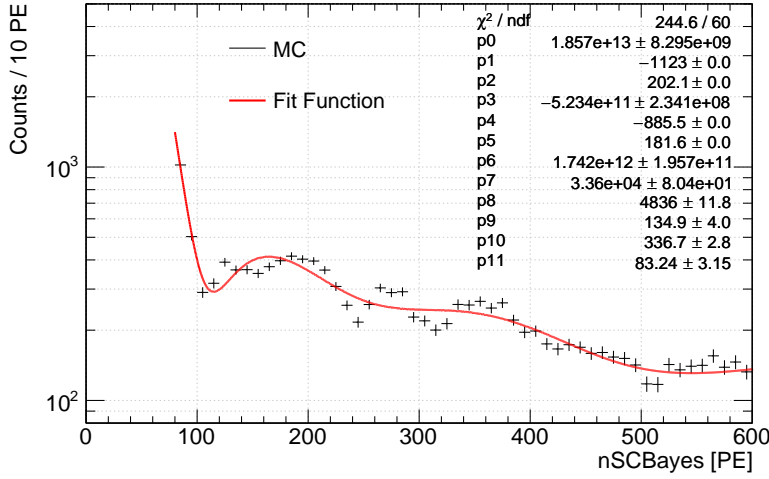


Figure 5.14: nSCBayes distribution of the neck α -decay PDF from MC simulations for the $\text{PulseIndexFirstGAR} = 0$ bin, where the three individual IFGIS, IFGOS and OFGIS sources are summed together. The distribution is fit with an empirical model, described by Equation 5.8.

$\mathbf{F}_{\text{prompt}}$ Model

EVEN after applying all of the WIMP dark matter search cuts, the same two-dimensional empirical functional form used to describe the $\mathbf{F}_{\text{prompt}}$ distribution as a function of nSCBayes for WIMPs and ^{39}Ar can be used for neck α -decays. The evolution of the mean $\mathbf{F}_{\text{prompt}}$ $\bar{f}(PE)$, skew $b(PE)$ and width $\sigma(PE)$ parameters with nSCBayes however are explicitly determined for neck α -decays. It cannot be assumed that the same 11 parameters that describe the WIMP and ^{39}Ar charge-

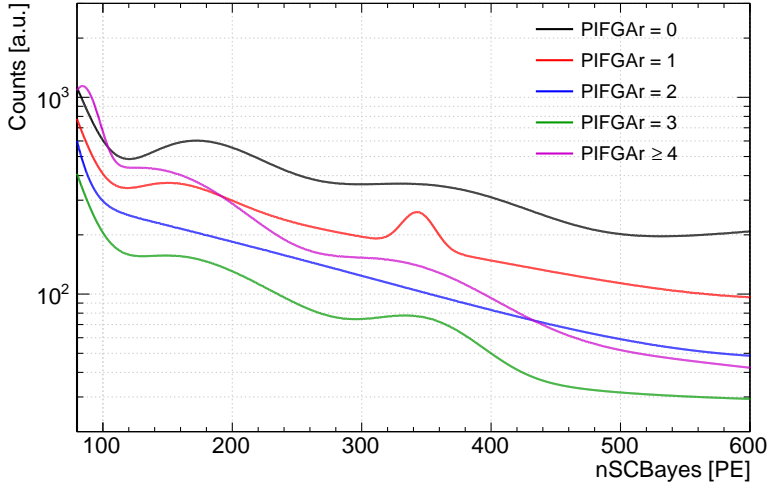


Figure 5.15: Best fit functions obtained from fitting Equation 5.8 to the `nSCBayes` distribution from the summed neck α -decay PDF from MC simulations, for the five individual `PulseIndexFirstGAR` bins: 0, 1, 2, 3, 4+.

dependent F_{prompt} parameters from Equation 3.9 also apply to neck α -decays, which have an entirely different event topology.

The values of these 11 parameters are obtained by fitting the functional form described in Equation 3.9 to the $(1 - F_{\text{prompt}})$ distribution in 6 `nSCBayes` slices of 100 PE width starting from 80 PE, to ensure that the F_{prompt} distribution is modelled across the range of the control region in `nSCBayes` (80 PE - 600 PE). Figure 5.16 shows an example fit to the $(1 - F_{\text{prompt}})$ distribution between 80 PE - 180 PE, in the `PulseIndexFirstGAR` = 0 bin. The $(1 - F_{\text{prompt}})$ distribution is fit over the range 0.1 - 0.42 (equivalently 0.58 - 0.9 in F_{prompt}) which defines the control region used to constrain the overall neck α -decay ROI normalisation in the PLR. At low `nSCBayes` (< 300 PE), a small fraction ($< 10\%$) of additional events at $F_{\text{prompt}} < 0.58$ have been observed, which cannot be easily modelled by the empirical functional form used to fit the main F_{prompt} peak. In lieu of this, a cut of 0.58 was made on the F_{prompt} distribution. This effect of this structure can be seen in Figure 5.16,

beginning to leak into the main F_{prompt} peak at the $F_{\text{prompt}} = 0.58$ boundary.

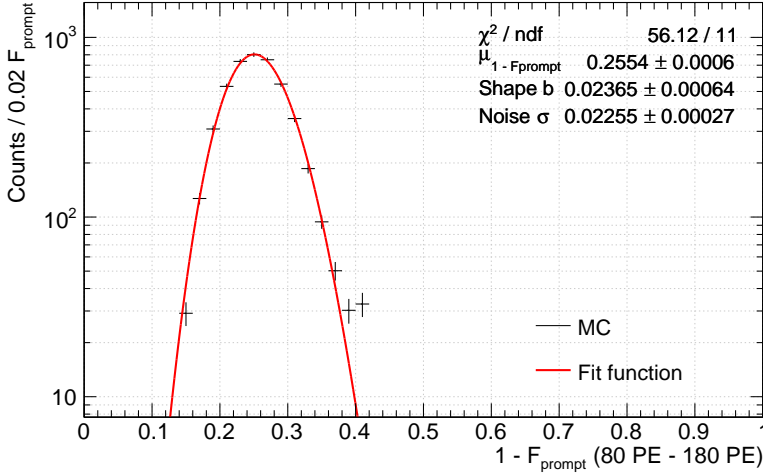


Figure 5.16: $(1 - F_{\text{prompt}})$ distribution from the summed neck α -decay PDF between 80 PE - 180 PE, in the `PulseIndexFirstGar` = 0 bin. The distribution is fit with the empirical fit function described by the first expression in Equation 3.9.

All α -particles have an F_{prompt} distribution more consistent with a NR, and as such the $(1 - F_{\text{prompt}})$ distribution is fit. Since the fit function described by the first expression in Equation 3.9 is with respect to the ER band, for neck α -decays, the skew of the Gamma needs to be reversed. The mean $(1 - \bar{f}(PE))$, $b(PE)$ and $\sigma(PE)$ parameters determined from the 6 individual fits are then plotted as a function of `nSCBayes` and fit with the last three functions described by Equation 3.9. Figure 5.17 shows the evolution of the $(1 - \bar{f}(PE))$ parameter as a function of `nSCBayes` in the `PulseIndexFirstGar` = 0 bin.

The procedure described above is repeated for each of the five `PulseIndexFirstGar` bins using an automated script that performs the 30 individual $(1 - F_{\text{prompt}})$ fits over all `nSCBayes` and `PulseIndexFirstGar` parameter space. To ensure the fit quality is satisfactory across all of this parameter space, the script constructs a two-dimensional histogram and records, for each $(1 - F_{\text{prompt}})$ fit performed in a given

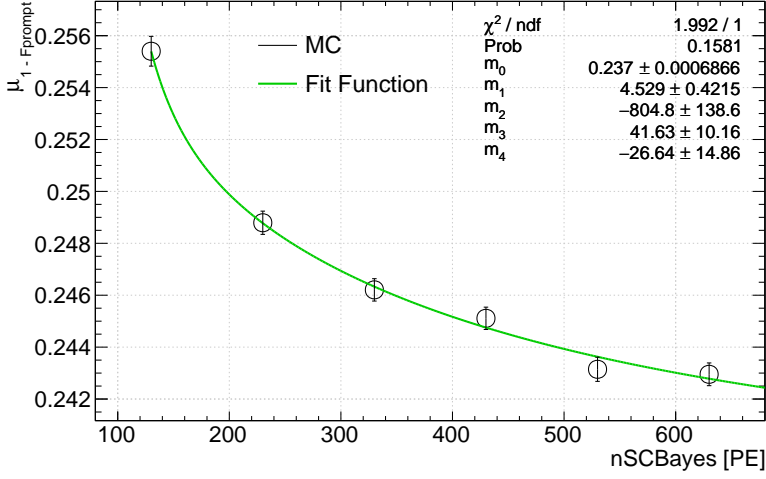


Figure 5.17: Evolution of the $(1 - \bar{f}(PE))$ parameter as a function of `nSCBayes` [PE] for the summed neck α -decay PDF in the `PulseIndexFirstGar` = 0 bin, fit with the second expression defined in Equation 3.9. Each data point is the mean $(1 - \bar{f}(PE))$ parameter as extracted from the individual fits to the $(1 - F_{\text{prompt}})$ distributions in separate `nSCBayes` bins, an example of which is shown in Figure 5.16.

`nSCBayes` and `PulseIndexFirstGar` bin, the χ^2/NDF of each fit in the corresponding bin in the histogram; this is shown in Figure 5.18. This is important to show that the functional forms implemented in the PLR analysis to construct the background models are a good description of the MC simulations. In the two lowest `nSCBayes` bins, the χ^2/NDF values are systematically worse than the remaining bins. This is driven by the additional low F_{prompt} population as described earlier; at the tail of the fit range ($F_{\text{prompt}} = 0.58$), the model diverges from the data due to this extra population. However, by integrating the functional form over the range 0 - 0.58 in F_{prompt} in Figure 5.16 and comparing this value with the total integral of the F_{prompt} distribution, it is found that the model under-predicts the number of events in this region by $< 0.5\%$, and thus the model is still an acceptable description of the MC. This is found to be the case in all `PulseIndexFirstGar` bins.

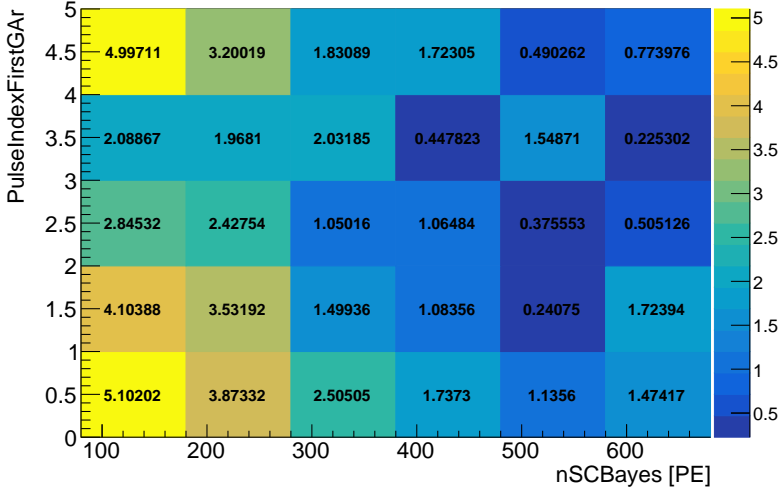


Figure 5.18: Two-dimensional histogram illustrating the χ^2/NDF value from each (1 - F_{prompt}) fit performed in each `nSCBayes`, `PulseIndexFirstGar` bin for neck α -decays, as a verification of the goodness of fit across all parameter space.

R_{rec} Model

THE best fit function found to consistently model the R_{rec} dimension of the neck α -decay model in all `PulseIndexFirstGar` bins is the sum of two Gaussians,

$$f(R', PE) = \sum_{i=1}^2 N_i(PE) \exp\left(-\frac{1}{2}\left(\frac{R' - \mu_i(PE)}{\sigma_i(PE)}\right)^2\right), \quad (5.9)$$

where $R' = (R_0 - R_{\text{rec}})$ and $N_i(PE)$, $\mu_i(PE)$ and $\sigma_i(PE)$ are the charge-dependent normalisation, mean and width parameters of the i 'th Gaussian respectively. Since there is some intrinsic charge-dependence on position reconstruction, the R_{rec} dimension for the neck α -decay is modelled by a two-dimensional function of both `nSCBayes` and R_{rec} ; this is achieved by fitting Equation 5.9 to the $(R_0 - R_{\text{rec}})$ distribution in 6 `nSCBayes` bins of 100 PE width starting from 80 PE, to ensure that the R_{rec} distribution is modelled across the range of the control region in `nSCBayes` (80 PE - 600 PE). Figure 5.19 shows an example fit to the $(R_0 - R_{\text{rec}})$ distribution

between 80 PE - 180 PE, in the `PulseIndexFirstGAR = 0` bin. The $(R_0 - R_{\text{rec}})$ distribution is fit over the range 50 mm - 800 mm (equivalently 51 mm - 801 mm in R_{rec}). The control region used to constrain the overall neck α -decay ROI normalisation in the PLR is taken to be 0 mm - 800 mm in R_{rec} , however the model is extrapolated down to 0 mm since there are no events there to fit the model to. The two normalisation parameters $N_1(PE)$, $N_2(PE)$, two mean parameters $\mu_1(PE)$, $\mu_2(PE)$ and two width parameters $\sigma_1(PE)$, $\sigma_2(PE)$ are then individually plotted as a function of `nSCBayes` and each fit with a quadratic polynomial, which describes the evolution of these parameters with `nSCBayes`. Figure 5.20 shows the evolution of the $\sigma_2(PE)$ parameter as a function of `nSCBayes` in the `PulseIndexFirstGAR = 0` bin.

5

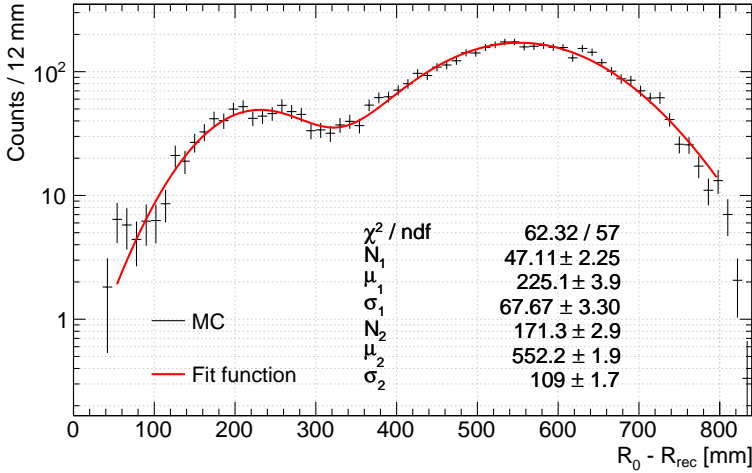


Figure 5.19: $(R_0 - R_{\text{rec}})$ [mm] distribution from the summed neck α -decay PDF between 80 PE - 180 PE, in the `PulseIndexFirstGAR = 0` bin. The distribution is fit with the empirical fit function described by Equation 5.9.

This procedure is repeated for each of the five `PulseIndexFirstGAR` bins using an automated script that performs the 30 individual $(R_0 - R_{\text{rec}})$ fits over all `nSCBayes` and `PulseIndexFirstGAR` parameter space. To ensure a satisfactory fit quality across all of this parameter space, another two-dimensional histogram was

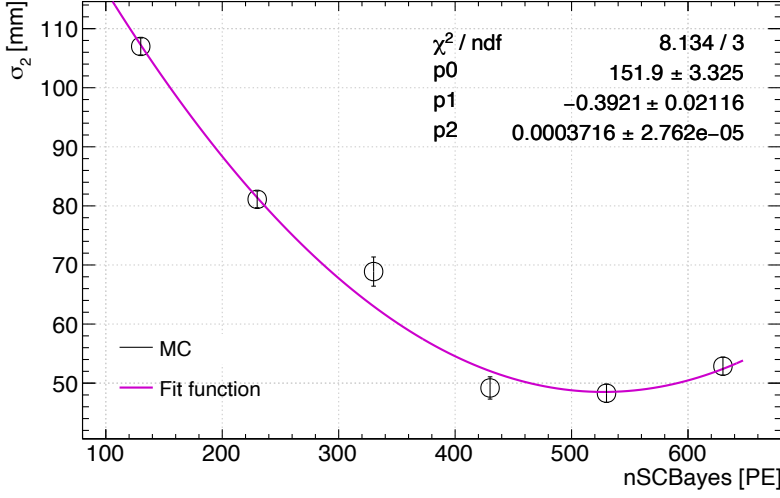


Figure 5.20: Evolution of the $\sigma_2(\text{PE})$ parameter as a function of `nSCBayes` [PE] for the summed neck α -decay PDF in the `PulseIndexFirstGar` = 0 bin, fit with a quadratic polynomial. Each data point is the mean $\sigma_2(\text{PE})$ parameter as extracted from the individual fits to the $(R_0 - R_{\text{rec}})$ distribution in separate `nSCBayes` bins, an example of which is shown in Figure 5.19.

constructed and filled with the χ^2/NDF value extracted from each $(R_0 - R_{\text{rec}})$ fit in each `nSCBayes` and `PulseIndexFirstGar` bin considered; this is shown in Figure 5.22. Figure 5.22 illustrates a consistent fit quality over all parameter space, with all χ^2/NDF values < 2 .

The correlation between `PulseIndexFirstGar` and R_{rec} is observed to be more prominent than in the `nSCBayes` and F_{prompt} dimensions; this is illustrated by Figure 5.21, which show the expected R_{rec} distributions from neck α -decays in the WIMP ROI (93 PE - 200 PE), in the `PulseIndexFirstGar` = 0 and ≥ 4 bins, drawn from the fit functions implemented in the PLR. Both histograms are normalised to unity. Figure 5.21 shows that the means of both Gaussians shift towards higher values between the `PulseIndexFirstGar` = 0 and ≥ 4 bins, and the integral under the

second Gaussian increases relative to the first between the `PulseIndexFirstGar` = 0 and ≥ 4 bins.

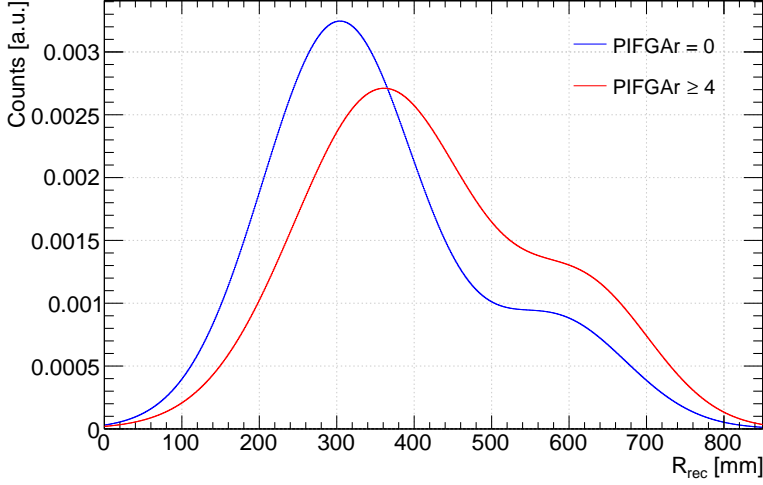


Figure 5.21: Comparison of the expected R_{rec} distributions from neck α -decays in the WIMP ROI (93 PE - 200 PE), in the `PulseIndexFirstGar` = 0 (blue) and ≥ 4 (red) bin, as implemented in the PLR, highlighting the correlation between R_{rec} and `PulseIndexFirstGar`. Both histograms are normalised to unity.

`PulseIndexFirstGar` Model

THE expected `PulseIndexFirstGar` distribution for each event type included in the PLR is required. For all sources (WIMPs and all backgrounds), the `PulseIndexFirstGar` distribution can be modelled with the sum of a Gaussian and an exponential distribution,

$$f(P') = \frac{N}{\sqrt{2\pi}\sigma} \exp\left(-\frac{(P' - \mu)^2}{2\sigma^2}\right) + \exp(a + b \cdot P'), \quad (5.10)$$

where $P' = \text{PulseIndexFirstGar}$, N , μ and σ are the normalisation, mean and width parameters of the Gaussian and a and b are the normalisation and scale parameters of the exponential. For each background source, the values of these

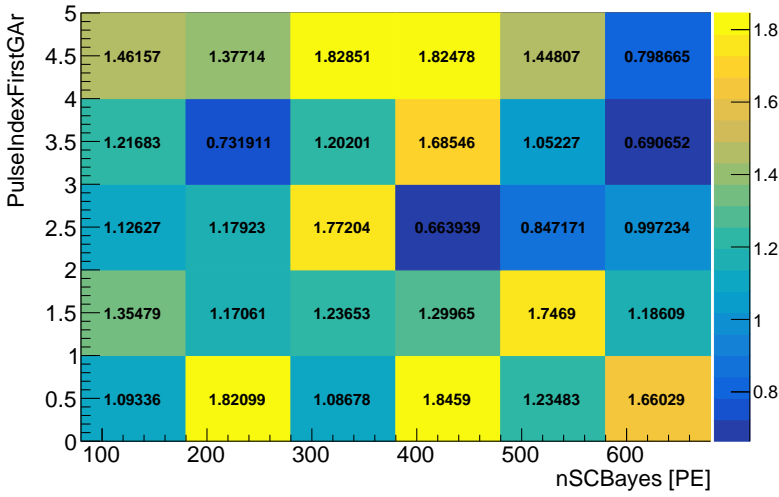


Figure 5.22: Two-dimensional histogram illustrating the χ^2/NDF value from each ($R_0 - R_{\text{rec}}$) fit performed in each nSCBayes, PulseIndexFirstGar bin for neck α -decays, as a verification of the goodness of fit across all parameter space.

parameters are different. Figure 5.23 shows the PulseIndexFirstGar distribution for WIMPs and ^{39}Ar overlaid with the PulseIndexFirstGar distribution for neck α -decays, separated into the same five PulseIndexFirstGar bins as considered in this thesis. Figure 5.23 highlights the separation power between signal (WIMP) and background (neck α -decay) events from the PulseIndexFirstGar variable, further motivating the choice to model it as an additional dimension in the PLR as a method of gaining back WIMP sensitivity.

5.3.3 Surface α -decays

nSCBayes Model

APPROXIMATELY 10^6 surface α -decay events in total are simulated at three different locations: the acrylic vessel bulk, the TPB surface and the TPB bulk. The acrylic vessel surface component is not included in the model, as the contribution from the acrylic vessel surface across the ROI and the control region

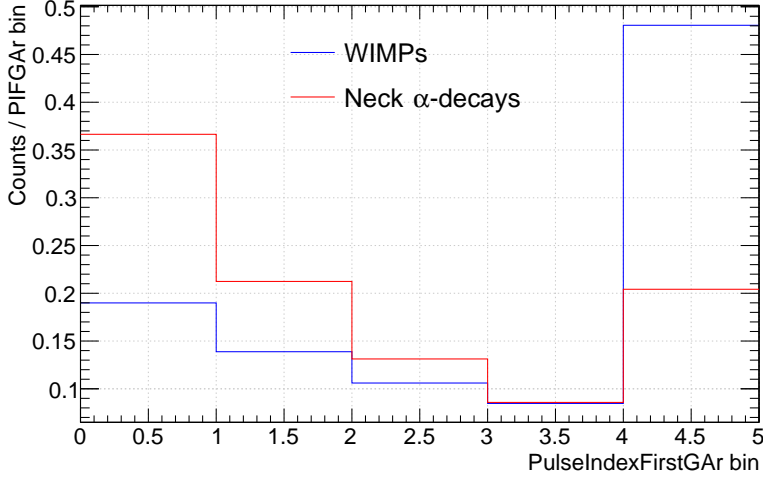


Figure 5.23: `PulseIndexFirstGAR` distributions of signal WIMP events (blue) and background neck α -decay events (red), drawn directly from the functional forms implemented in the PLR, binned in the same five `PulseIndexFirstGAR` bins used in this analysis. Both histograms are normalised to unity for shape comparison.

(80 PE - 600 PE) after event selection cuts is consistent with zero. The relative number of events simulated at each source reflects their relative activities from Section 4.2.2. All of the WIMP dark matter search cuts listed in Section 5.1 are then applied to the simulated events. Following the same procedure as for the neck α -decays, for each source, events that survive all cuts are filled into a one-dimensional `nSCBayes` histogram and two, two-dimensional `Fprompt` vs `nSCBayes` and `Rrec` vs `nSCBayes` histograms. The histograms from the three separate sources are then added together.

In each of the five `PulseIndexFirstGAR` bins, the `nSCBayes` distribution for the summed surface α -decay PDF is modelled with the sum of two Landau distributions multiplied by a Sigmoid curve,

$$f(PE) = \frac{\sum_{i=1}^2 N_i \text{TMATH}::\text{Landau}(PE; \mu_i, \sigma_i, \text{true})}{1 + e^{-(PE - x_S)/\tau_S}}, \quad (5.11)$$

where `TMath::Landau` is the Landau probability density function called from ROOT [83], μ_i , σ_i are the location and scale parameters of the i 'th Landau distribution and x_S and τ_S characterise the Sigmoid curve's midpoint value and "steepness" respectively. The fit function implemented in the PLR software for the `PulseIndexFirstGAR = 0` bin is shown in Figure 5.24, superimposed on the `nSCBayes` distribution from MC simulations used to obtain the functional form.

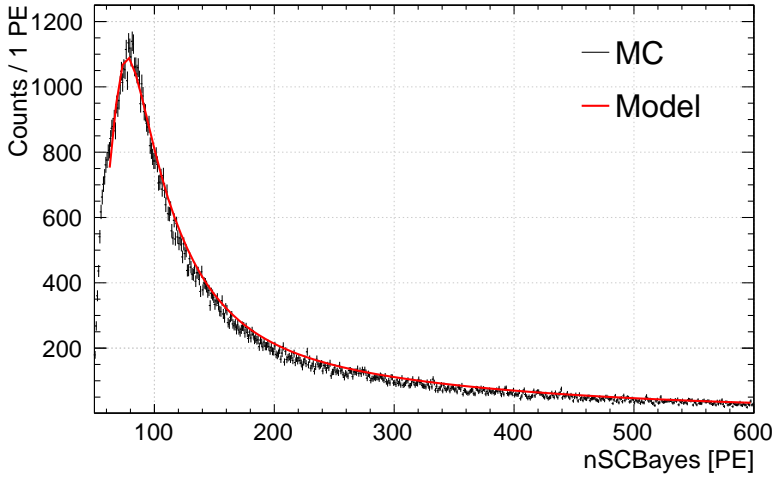


Figure 5.24: Functional form implemented in the PLR to describe the `nSCBayes` distribution of surface α -decays with `PulseIndexFirstGAR = 0` (red) described by Equation 5.11, superimposed on the `nSCBayes` distribution from MC simulations used to determine the functional form (black).

F_{prompt} Model

A customised model is required to describe the F_{prompt} distribution of surface α -decays over all five `PulseIndexFirstGAR` bins, which has a double peak structure. The larger of the two peaks comes from decays occurring within the TPB layer, since α -decays originating from the acrylic vessel have a much higher probability of scintillating in the TPB layer before reaching the LAr to produce a much smaller peak. The F_{prompt} distribution is described by the sum of a Gaussian,

to describe the TPB peak, and a skewed Gaussian, to describe the LAr peak,

$$f(f', PE) = \frac{N_{\text{TPB}}(PE)}{\sqrt{2\pi}\sigma_{\text{TPB}}(PE)} \exp\left(-\frac{(f' - \mu_{\text{TPB}}(PE))^2}{2\sigma_{\text{TPB}}^2(PE)}\right) + \frac{N_{\text{LAr}}(PE)}{2} \exp\left(-\frac{(f' - \mu_{\text{LAr}}(PE))^2}{2\sigma_{\text{LAr}}^2(PE)}\right) \left[1 + \operatorname{erf}\left(\frac{\alpha_{\text{LAr}}(PE)(f' - \mu_{\text{LAr}})}{\sqrt{2}\sigma_{\text{LAr}}(PE)}\right)\right], \quad (5.12)$$

where $f' = (1 - F_{\text{prompt}})$, $N_{\text{TPB}}(PE)$, $\mu_{\text{TPB}}(PE)$ and $\sigma_{\text{TPB}}(PE)$ are the charge-dependent normalisation, mean and width parameters of the TPB Gaussian peak, $N_{\text{LAr}}(PE)$, $\mu_{\text{LAr}}(PE)$ and $\sigma_{\text{LAr}}(PE)$ are the charge-dependent normalisation, mean and width parameters of the LAr skewed Gaussian peak, characterised by the charge-dependent skew parameter $\alpha_{\text{LAr}}(PE)$. An example fit to the $(1 - F_{\text{prompt}})$ distribution with this functional form is shown in Figure 5.25, between 150 PE - 250 PE, for the `PulseIndexFirstGAR` = 0 bin. The $(1 - F_{\text{prompt}})$ distribution is fit over the range 0.2 - 0.6 (equivalently 0.4 - 0.8 in F_{prompt}) which defines the control region used to constrain the overall surface α -decay ROI normalisation in the PLR. The $(1 - F_{\text{prompt}})$ distribution is fit in 6 `nSCBayes` bins of 100 PE width between 50 PE - 650 PE, such that the 7 parameters defined in Equation 5.12 can each be modelled as a function of `nSCBayes` with a quadratic polynomial.

As with neck α -decays, this procedure is repeated for each of the five `PulseIndexFirstGAR` bins using an automated script that performs the 30 individual $(1 - F_{\text{prompt}})$ fits over all `nSCBayes` and `PulseIndexFirstGAR` parameter space. To ensure a satisfactory fit quality across all of this parameter space, another two-dimensional histogram was constructed and filled with the χ^2/NDF value extracted from each $(1 - F_{\text{prompt}})$ fit in each `nSCBayes` and `PulseIndexFirstGAR` bin considered; this is shown in Figure 5.26. Figure 5.26 illustrates a reasonably consistent fit quality over all parameter space, with the exception of one bin located outside the ROI with a χ^2/NDF value > 0.5 greater than the bin with the second highest χ^2/NDF . Since this is one bin

out of a total of 30, and this is located outside of the ROI, this model is overall a good description of the MC.

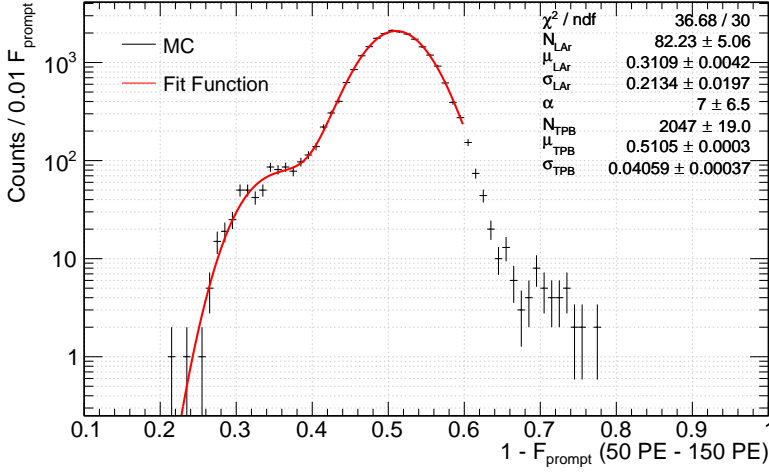


Figure 5.25: $(1 - F_{\text{prompt}})$ distribution from the summed surface α -decay PDF between 150 PE - 250 PE, in the `PulseIndexFirstGar` = 0 bin. The distribution is fit with the empirical fit function described by Equation 5.12.

R_{rec} Model

THE R_{rec} dimension of the surface α -decay model is described over all `PulseIndexFirstGar` bins by the sum of three exponential distributions and one Gaussian distribution,

$$f(R', PE) = \sum_{i=1}^3 \frac{N_i(PE)}{\theta_i(PE)} \exp(-R'/\theta_i(PE)) + \frac{N_G(PE)}{\sqrt{2\pi}\sigma_G(PE)} \exp\left(-\frac{(R' - \mu_G(PE))^2}{2\sigma_G^2(PE)}\right), \quad (5.13)$$

where $R' = (R_0 - R_{\text{rec}})$, $N_i(PE)$ and $\theta_i(PE)$ are the charge-dependent normalisation and scale parameters of the i 'th exponential and $N_G(PE)$, $\mu_G(PE)$ and $\sigma_G(PE)$ are

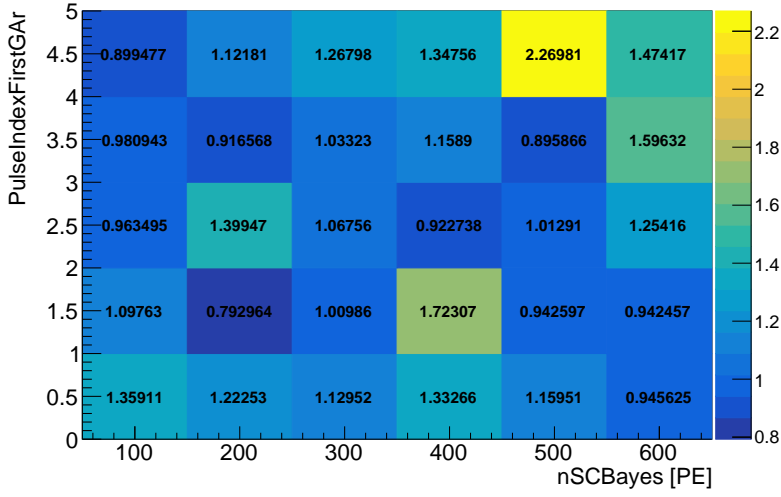


Figure 5.26: Two-dimensional histogram illustrating the χ^2/NDF value from each (1 - F_{prompt}) fit performed in each `nSCBayes`, `PulseIndexFirstGar` bin for surface α -decays, as a verification of the goodness of fit across all parameter space.

the charge-dependent normalisation, mean and width parameters of the Gaussian distribution. An example fit to the $(R_0 - R_{\text{rec}})$ distribution with this functional form is shown in Figure 5.27, between 150 PE - 250 PE, for the `PulseIndexFirstGar` = 0 bin. The $(R_0 - R_{\text{rec}})$ distribution is fit over the range 1 mm - 851 mm (equivalently 0 mm - 850 mm in R_{rec}) which defines the control region used to constrain the overall surface α -decay ROI normalisation in the PLR; the very edge of the detector is excluded from the fit region as the fit function was found to tend towards infinity. The $(R_0 - R_{\text{rec}})$ distribution is fit in 6 `nSCBayes` bins of 100 PE width between 50 PE - 650 PE, such that the 9 parameters defined in Equation 5.13 can each be modelled as a function of `nSCBayes` with a quadratic polynomial.

Like neck α -decays, this procedure is repeated for each of the five `PulseIndexFirstGar` bins using an automated script that performs the 30 individual $(R_0 - R_{\text{rec}})$ fits over all `nSCBayes` and `PulseIndexFirstGar` parameter space. To ensure a satisfactory fit quality across all of this parameter space, another two-dimensional histogram was

constructed and filled with the χ^2/NDF value extracted from each $(R_0 - R_{\text{rec}})$ fit in each `nSCBayes` and `PulseIndexFirstGAR` bin considered; this is shown in Figure 5.28. Figure 5.28 illustrates that the χ^2/NDF values in the first `nSCBayes` bin, 50 PE - 150 PE bin, are systematically higher across all `PulseIndexFirstGAR` bins. These are driven up by the “bump” in the $(R_0 - R_{\text{rec}})$ distribution at approximately $R_{\text{rec}} = 820$ mm, which becomes less prominent with increasing `nSCBayes`. Mis-modelling of the bump is not too concerning in this case; as it is located at a radius greater than the R_{rec} cut applied to the data ($R_{\text{rec}} < 720$ mm), the model is still an accurate description of the MC simulations inside the ROI. Additionally, the integral of this bump comprises less than 1.5% of the total R_{rec} distribution.

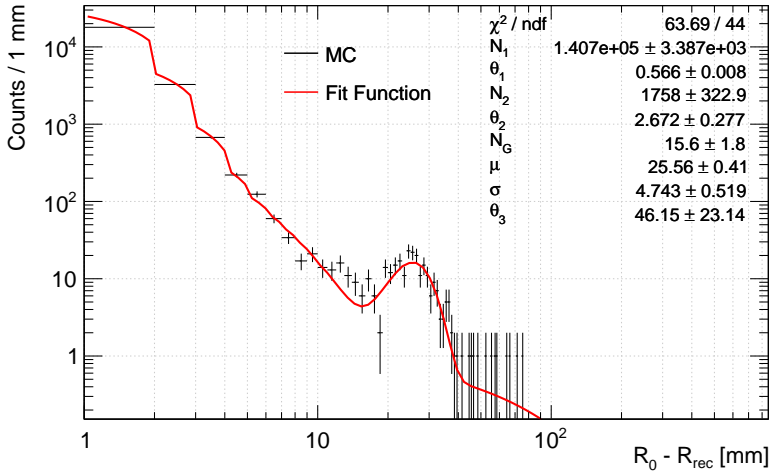


Figure 5.27: $(R_0 - R_{\text{rec}})$ distribution from the summed surface α -decay PDF between 150 PE - 250 PE, in the `PulseIndexFirstGAR` = 0 bin. The distribution is fit with the empirical fit function described by Equation 5.13.

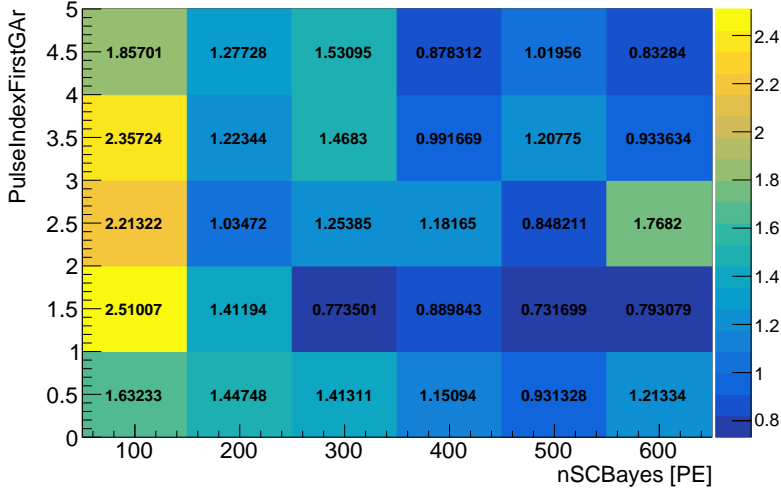


Figure 5.28: Two-dimensional histogram illustrating the χ^2/NDF value from each ($R_0 - R_{\text{rec}}$) fit performed in each `nSCBayes`, `PulseIndexFirstGar` bin for surface α -decays, as a verification of the goodness of fit across all parameter space.

5.3.4 Dust α -decays

`nSCBayes` Model

APPROXIMATELY 10^6 dust α -decay events are simulated in total, corresponding to $\sim 200,000$ events per diameter size: 2 μm , 10 μm , 20 μm , 34 μm and 50 μm . These dust sizes are chosen based on the in-situ rate measurements performed in Section 4.2.4. All of the WIMP dark matter search cuts listed in Section 5.1 are then applied to the simulated events. For each of the five components, events that survive all cuts are filled into a one-dimensional `nSCBayes` histogram and two, two-dimensional F_{prompt} vs `nSCBayes` and R_{rec} vs `nSCBayes` histograms. The histograms from the five individual dust components are then added together with a weighting scheme reflective of their relative physics trigger rates quoted in Table 4.5, multiplied by the 231 live-day dataset exposure.

The `nSCBayes` distribution of the summed dust α -decay PDF can be described

in all `PulseIndexFirstGar` bins with a simple Gaussian,

$$f(PE) = \frac{N}{\sqrt{2\pi}\sigma} \exp\left(-\frac{(PE - \mu)^2}{2\sigma^2}\right) \quad (5.14)$$

where N , μ and σ are the normalisation, mean and width parameters of the Gaussian distribution. The fit function implemented in the PLR software for the `PulseIndexFirstGar` = 0 bin is shown in Figure 5.29, superimposed on the `nSCBayes` distribution from MC simulations used to obtain the functional form. The `nSCBayes` control region used to constrain the overall number of dust α -decay ROI events is 50 PE - 1000 PE; almost a factor of 2 larger than the control regions defined for the neck and surface α -decay models. This choice is a consequence of less statistics; larger `nSCBayes` bins are required to model the charge-dependence in the F_{prompt} and R_{rec} dimensions, described in the next subsections.

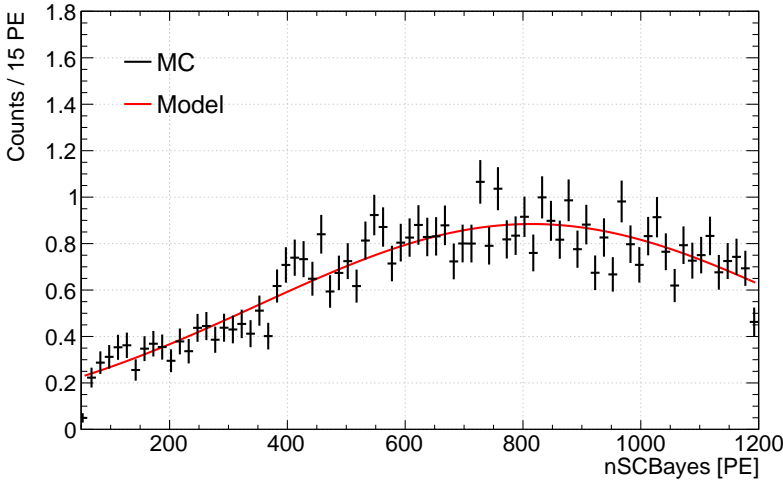


Figure 5.29: Functional form implemented in the PLR to describe the `nSCBayes` distribution of dust α -decays with `PulseIndexFirstGar` = 0 (red) described by Equation 5.14, superimposed on the `nSCBayes` distribution from MC simulations used to determine the functional form (black).

F_{prompt} Model

SINCE the origin of dust α -decay events comes from within the LAr target, the same empirical model defined in Equation 3.9 used to describe the F_{prompt} distribution for WIMPs, ^{39}Ar and neck α -decays can also be used for dust events. However, just like for neck α -decays, the 11 parameters which describe the charge-dependence of the mean F_{prompt} ($1 - \bar{f}(PE)$), skew $b(PE)$ and width $\sigma(PE)$ parameters are determined specifically for dust α -decays. This is achieved by fitting the $(1 - F_{\text{prompt}})$ distribution in 5 **nSCBayes** bins across 50 PE - 1000 PE, using 200 PE **nSCBayes** widths, following the prescription described in Section 5.3.2. Due to the 50 PE cut off, the first bin is only 150 PE wide.

This procedure is repeated for each of the five **PulseIndexFirstGAR** bins using an automated script that performs the 25 individual $(1 - F_{\text{prompt}})$ fits over all **nSCBayes** and **PulseIndexFirstGAR** parameter space. The fit quality across all of this parameter space is again verified using a two-dimensional histogram to display the χ^2/NDF value extracted from each $(1 - F_{\text{prompt}})$ fit in each **nSCBayes** and **PulseIndexFirstGAR** bin considered. This is shown in Figure 5.30. Figure 5.30 illustrates a consistent fit quality over all parameter space, with all χ^2/NDF values < 2 .

R_{rec} Model

THE R_{rec} dimension of the dust α -decay model, over all **PulseIndexFirstGAR** bins, is best described by a two-parameter empirical function of the form,

$$f(\bar{R}, PE) = N(PE)(1 - \exp(\bar{R}/\rho(PE))), \quad (5.15)$$

where $\bar{R} = (R_{\text{rec}}/R_0)^3$ and $N(PE)$ and $\rho(PE)$ are the charge-dependent normalisation and scale parameters of the exponential term respectively. It was first predicted that the same radial model used to describe WIMPs and ^{39}Ar could be used for dust

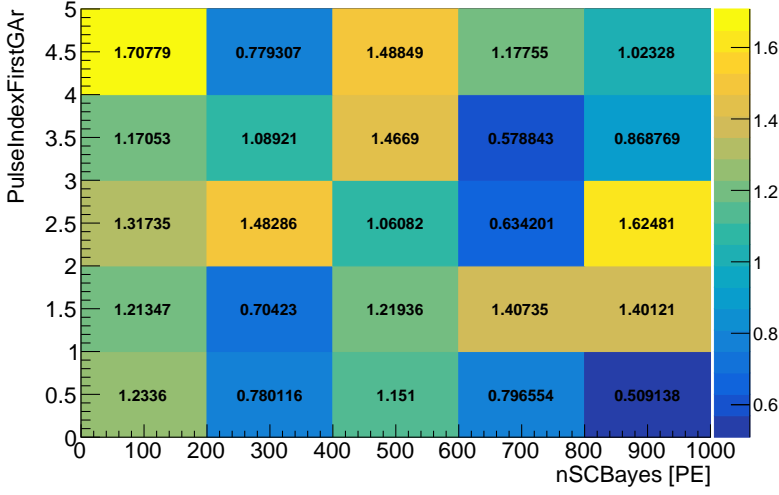


Figure 5.30: Two-dimensional histogram illustrating the χ^2/NDF value from each (1 - F_{prompt}) fit performed in each `nSCBayes`, `PulseIndexFirstGar` bin for dust α -decays, as a verification of the goodness of fit across all parameter space.

α -decays, since dust particulates are assumed to be approximately uniformly distributed throughout the LAr volume through convection. However, it was observed that the reconstructed R_{rec} distribution for dust α -decays tends to bias towards higher radii; a potential consequence of the shadowing effect described in Section 4.2.4.

The charge-dependent $N(PE)$ and $\rho(PE)$ parameters are determined from fitting the $(R_{\text{rec}}/R_0)^3$ distribution in 5 `nSCBayes` bins between 50 PE - 1000 PE, using 200 PE `nSCBayes` widths, and modelling the evolution of these parameters with `nSCBayes` with quadratic polynomials. The functional form implemented in the PLR software for the `PulseIndexFirstGar` = 0 bin between 50 PE - 250 PE is shown in Figure 5.31, superimposed on the `nSCBayes` distribution from MC simulations used to obtain the functional form.

This procedure is repeated for each of the five `PulseIndexFirstGar` bins using an automated script that performs the 25 individual $(R_{\text{rec}}/R_0)^3$ fits over all

`nSCBayes` and `PulseIndexFirstGAR` parameter space. The fit quality across all of this parameter space is again verified using a two-dimensional histogram to display the χ^2/NDF value extracted from each $(R_{\text{rec}}/R_0)^3$ fit in each `nSCBayes` and `PulseIndexFirstGAR` bin considered. This is shown in Figure 5.32, and indicates a reasonably consistent fit quality over all parameter space. The χ^2/NDF is observed to increase marginally with increasing `nSCBayes`, however this is located outside of the ROI, and thus is not a concern for this analysis.

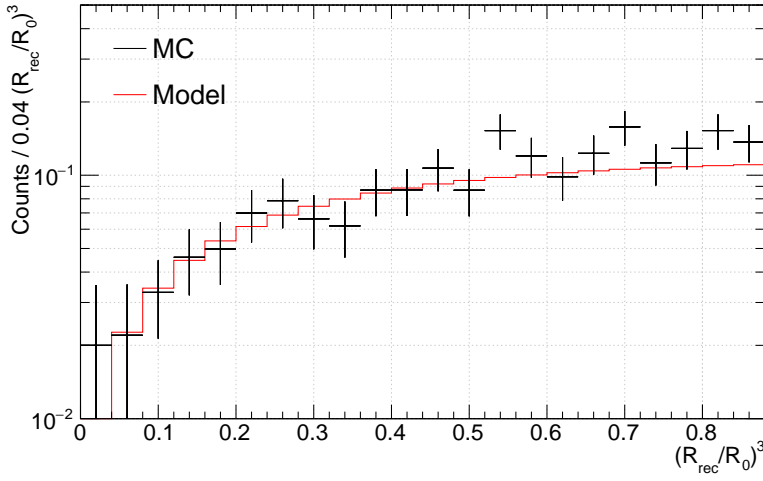


Figure 5.31: Functional form implemented in the PLR to describe the $(R_{\text{rec}}/R_0)^3$ distribution of dust α -decays with `PulseIndexFirstGAR` = 0 between 150 PE - 250 PE (red) described by Equation 5.15, superimposed on the `nSCBayes` distribution from MC simulations used to determine the functional form (black).

5.3.5 Radiogenic Neutrons

`nSCBayes` Model

IN total, approximately 10^7 radiogenic neutrons are simulated to construct the radiogenic neutron background model. Out of these 10^7 simulated neutrons, 99% come from the PMTs; the other 1% are split between the neck veto PMTs, the filler

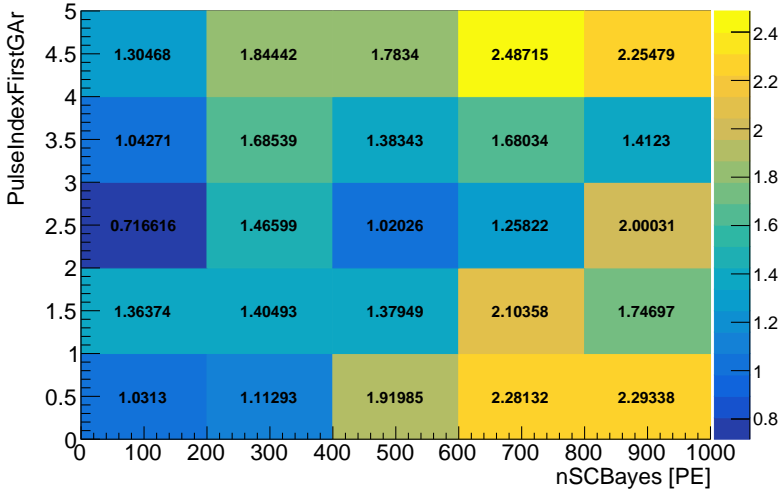


Figure 5.32: Two-dimensional histogram illustrating the χ^2/NDF value from each $(R_{\text{rec}}/R_0)^3$ fit performed in each `nSCBayes`, `PulseIndexFirstGAR` bin for dust α -decays, as a verification of the goodness of fit across all parameter space.

blocks and the filler foam. This is a simulation choice, since physics trigger signals from neutrons are wholly dominated by PMT neutrons. Generating a high statistics sample of simulated radiogenic neutrons that pass all of the WIMP dark matter search cuts is extremely challenging, due to the fact that the majority of neutrons do not make it into the LAr to produce a signal; the average physics trigger rate for neutrons originating from the PMTs is $\sim 1.5\%$. To speed up simulations and save on computing resources, neutrons are simulated with a uniform energy distribution. An event weight, based on the neutron energy spectra from NeucBOT described in Section 4.2.1, is then applied post-simulation in order to obtain the correct distribution shapes. After applying this event weight, the WIMP dark matter search cuts are applied to the events. Following the same procedure as for the neck α -decays, for each source, events that survive all cuts are filled into a one-dimensional `nSCBayes` histogram and two, two-dimensional F_{prompt} vs `nSCBayes` and R_{rec} vs `nSCBayes` histograms. The histograms from the four separate sources

are then added together with a total weighting reflective of their relative production rates quoted in Table 4.2 and their relative physics trigger rates, multiplied by the 231 live-day dataset exposure.

As outlined earlier in Section 5.3.2, the radiogenic neutron model is the only model to not be binned in `PulseIndexFirstGar` in the same way as the other MC-constructed models. This decision was made to further alleviate the heavy load on computing resources to generate a satisfactory number of events to build the model. In order to preserve the probability calculation from the `PulseIndexFirstGar` binning in the PLR, instead of removing the dimension entirely, the same `PulseIndexFirstGar` distribution as calculated for WIMPs and ^{39}Ar in Section 5.3 is assumed for neutrons. Additionally, the `PulseIndexFirstGar` reweighting functions for all three dimensions calculated in Section 5.3.1 for WIMPs and ^{39}Ar are applied to the neutron model. This parameterisation has the effect that `PulseIndexFirstGar` does not provide any discrimination power against radiogenic neutrons.

The `nSCBayes` distribution of the summed radiogenic neutron PDF over all `PulseIndexFirstGar` values is modelled with the sum of two exponentials distributions, multiplied by a Sigmoid curve,

$$f(PE) = \frac{\sum_{i=1}^2 N_i / \theta_i \exp(-PE/\theta_i)}{1 + e^{-(PE-x_S)/\tau_S}}, \quad (5.16)$$

where N_i and θ_i are the normalisation and scale parameters of the i 'th exponential and x_S and τ_S characterise the Sigmoid curve's midpoint value and "steepness" respectively. Figure 5.33 shows the fit to the radiogenic neutron `nSCBayes` distribution with this function, between 50 PE - 1000 PE, defined as the `nSCBayes` control region used to constrain the overall neutron ROI normalisation. This control region is the same as used for the dust α -decays, where there are less statistics and thus larger `nSCBayes` bins are required to model the charge-dependence of the $\mathbf{F}_{\text{prompt}}$ and \mathbf{R}_{rec} dimensions.

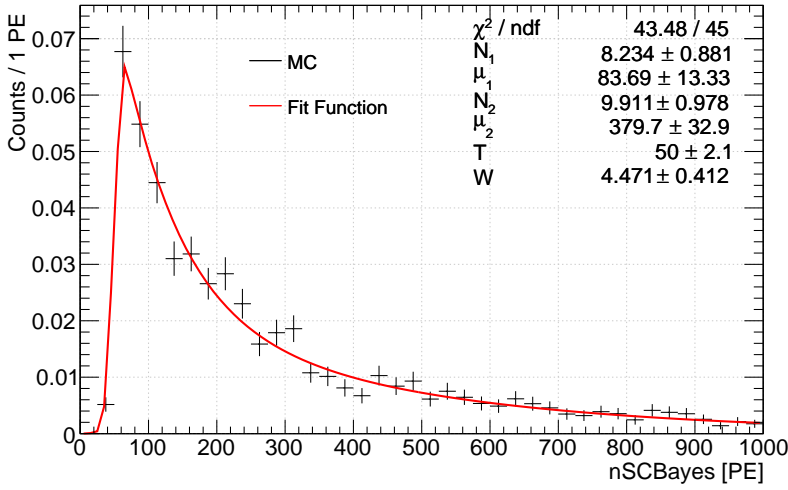


Figure 5.33: nSCBayes distribution of the summed radiogenic neutron PDF from MC simulations over all `PulseIndexFirstGAr` values. The distribution is fit with the sum of two exponentials and a Sigmoid curve, described by Equation 5.16.

F_{prompt} Model

It was observed that the same empirical model used to describe the F_{prompt} distribution for WIMPs can also be used for radiogenic neutrons; the contribution from multi-scatter neutron events, which comprise a lower F_{prompt} population, reside below the lower F_{prompt} ROI bound from Figure 5.2. To account for any differences in the observed neutron F_{prompt} distribution from the WIMP F_{prompt} distribution, potentially from subtle differences in the simulation, the 11 empirical parameters which describe the charge-dependence of the $(1 - \bar{f}(PE))$, $b(PE)$ and $\sigma(PE)$ parameters are determined specifically for neutrons by fitting the $(1 - F_{\text{prompt}})$ distribution from MC simulations in 5 nSCBayes bins between 50 PE - 1050 PE, with 200 nSCBayes bin widths, following the prescription described in Section 5.3.2.

R_{rec} Model

THE R_{rec} dimension for radiogenic neutrons is described by a single exponential distribution,

$$f(R', PE) = N_1(PE)/\theta_1(PE)\exp(-R'/\theta_1(PE)), \quad (5.17)$$

where $R' = (R_0 - R_{\text{rec}})$ and $N_1(PE)$, $\theta_1(PE)$ are the charge-dependent normalisation and scale parameters of the exponential. The functional form implemented in the PLR software between 50 PE - 250 PE is shown in Figure 5.34, superimposed on the $(R_0 - R_{\text{rec}})$ distribution from MC simulations used to obtain the functional form. As evident in Figure 5.34, neutron events have a higher probability of reconstructing at radii nearer the edge of the detector than WIMPs, which have an equal probability of reconstructing anywhere within the target volume. As with all of the other models, the neutron R_{rec} dimension is modelled as charge-dependent. The $(R_0 - R_{\text{rec}})$ distribution from MC simulations is fit in 5 **nSCBayes** bins between 50 PE - 1050 PE using 200 PE **nSCBayes** widths, such that the two parameters $N_1(PE)$, $\theta_1(PE)$ are modelled as a function of **nSCBayes** with quadratic polynomials.

5.3.6 Background Expectation and Model Summary

A summary of the number of expected ROI events in the 231 live-day dataset from each background source, after applying all WIMP dark matter search cuts, is provided in Table 5.2. Out of all the background sources, the largest contribution comes from radiogenic neutrons, which are expected to comprise 8.23 ROI events. The smallest contribution comes from surface α -decays, which are expected to contribute < 1 expected ROI event.

Tables 5.3 and 5.4 summarise the parameterisation of the WIMP, ^{39}Ar β -decay, surface α -decay, neck α -decay, dust α -decay and radiogenic neutron models included

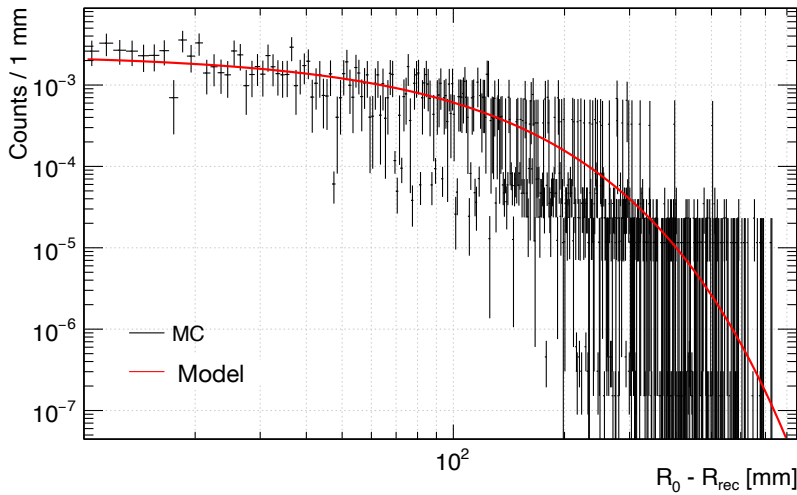


Figure 5.34: Functional form implemented in the PLR to describe the $(R_0 - R_{\text{rec}})$ distribution of radiogenic neutrons over all `PulseIndexFirstGar` values between 50 PE - 250 PE (red) described by Equation 5.17, superimposed on the $(R_0 - R_{\text{rec}})$ distribution from MC simulations used to determine the functional form (black).

in the PLR analysis, as described in detail in this chapter. The tables summarise the following information:

- How the models are determined (from theoretical predictions or from MC simulations or from calibration data),
- Which MC-based systematic uncertainty variations are considered in the model (whether the detector response and optical model parameters are considered only at their nominal values or also at their $\pm 1\sigma$ values). These are described in further detail in Section 6.2,
- If the models are binned in the `PulseIndexFirstGar` variable, and,
- Which functional forms are used to describe the shapes of the `nSCBayes`, F_{prompt} (`nSCBayes`-dependent), R_{rec} (`nSCBayes`-dependent) and `PulseIndexFirstGar`

Table 5.2: Summary table of the number of expected ROI events in the 231 live-day dataset from each background source included in the PLR, after applying all WIMP dark matter search cuts.

| Background Source | N_{ROI} |
|----------------------------------|------------------|
| ^{39}Ar β -decays | 1.64 |
| Neck α -decays | 3.92 |
| Surface α -decays | 0.000337 |
| Dust α -decays | 3.04 |
| Radiogenic Neutrons | 8.23 |
| Total | 16.8 |

distributions for each model, important for determining event probabilities and generating random pseudoexperiments.

Table 5.3: Summary table describing the parameterisation of the WIMP, ^{39}Ar β -decay and surface α -decay models in the PLR analysis.

| | WIMPs | ^{39}Ar β-decays | Surface α-decays |
|---|---|---|--|
| From theory/MC/data? | Theory/data (nSCBayes) Data (F_{prompt}) Theory/MC (R_{rec}) Data (PulseIndexFirstGar) | Theory/data (nSCBayes) Data (F_{prompt}) Theory/MC (R_{rec}) Data (PulseIndexFirstGar) | MC (All) |
| Which MC systematic variations? | Nominal (Restricted due to time limitations) | Nominal (Restricted due to time limitations) | Nominal, LAr optical model, TPB scattering length, PMT afterpulsing, PMT efficiency |
| Binned in PulseIndexFirstGar? | Yes | Yes | Yes |
| nSCBayes parameterisation | Theoretical WIMP recoil rate spectrum convolved with Gaussian response function (Energy response parameters obtained from energy calibration with ^{39}Ar data) | Theoretical ^{39}Ar β -decay spectrum convolved with Gaussian response function (Energy response parameters obtained from energy calibration with ^{39}Ar data) | Empirical function (Sum of 2 Landau distributions multiplied by Sigmoid curve) determined from fit to MC simulations |
| F_{prompt} parameterisation (nSCBayes-dependent) | Empirical function (Gamma function convolved with Gaussian) determined from fit to ^{39}Ar data in F_{prompt} space Mean F_{prompt} / Gamma mean parameter skew is inverted for WIMPs | Empirical function (Gamma function convolved with Gaussian) determined from fit to ^{39}Ar data in F_{prompt} space | Empirical function (Sum of Gaussian and skewed Gaussian) determined from fit to MC simulations in $(1 - F_{\text{prompt}})$ space |
| R_{rec} parameterisation (nSCBayes-dependent) | Uniform radial distribution predicted from spherical geometry, convolved with Gaussian resolution function determined from ^{39}Ar MC | Uniform radial distribution predicted from spherical geometry, convolved with Gaussian resolution function determined from ^{39}Ar MC | Empirical function (Sum of 3 exponentials and single Gaussian) determined from fit to MC simulations in $(R_0 - R_{\text{rec}})$ space |
| PulseIndexFirstGar parameterisation | Empirical function (Sum of Gaussian and exponential) determined from fit to ^{39}Ar data | Empirical function (Sum of Gaussian and exponential) determined from fit to ^{39}Ar data | Empirical function (Sum of Gaussian and exponential) determined from fit to MC simulations |

Table 5.4: Summary table describing the parameterisation of the neck α -decay, dust α -decay and radiogenic neutron models in the PLR analysis.

| | Neck α -decays | Dust α -decays | Radiogenic Neutrons |
|---|--|--|--|
| From theory/MC/data? | MC (All) | MC (All) | MC (nSCBayes, F_{prompt} , R_{rec}) Data (PulseIndexFirstGar) |
| Which MC systematic variations? | Nominal, LAr optical model, TPB scattering length, PMT afterpulsing, PMT efficiency | Nominal (Restricted due to computing resource limitations) | Nominal (Restricted due to computing resource limitations) |
| Binned in PulseIndexFirstGar? | Yes | Yes | Yes & No (Assumptions: Same PulseIndexFirstGar distribution as ^{39}Ar assumed for neutrons) |
| nSCBayes parameterisation | Empirical function (Sum of 4 Gaussians) determined from fit to MC simulations | Empirical function (Single Gaussian) determined from fit to MC simulations | Empirical function (Sum of 2 exponentials multiplied by Sigmoid curve) determined from fit to MC simulations |
| F_{prompt} parameterisation (nSCBayes-dependent) | Empirical function (Gamma function convolved with Gaussian) determined from fit to MC simulations in $(1 - F_{\text{prompt}})$ space | Empirical function (Gamma function convolved with Gaussian) determined from fit to MC simulations in $(1 - F_{\text{prompt}})$ space | Empirical function (Gamma function convolved with Gaussian) determined from fit to MC simulations in $(1 - F_{\text{prompt}})$ space |
| R_{rec} parameterisation (nSCBayes-dependent) | Empirical function (Sum of 2 Gaussians) determined from fit to MC simulations in $(R_0 - R_{\text{rec}})$ space | Empirical function of form $y(x) \sim 1 - \exp(x)$ determined from fit to MC simulations in $(R_{\text{rec}}/R_0)^3$ space | Empirical function (Single exponential) determined from fit to MC simulations in $(R_0 - R_{\text{rec}})$ space |
| PulseIndexFirstGar parameterisation | Empirical function (Sum of Gaussian and exponential) determined from fit to MC simulations | Empirical function (Sum of Gaussian and exponential) determined from fit to MC simulations | Empirical function (Sum of Gaussian and exponential) determined from fit to ^{39}Ar data |

Chapter 6

Limit Setting with the Profile Likelihood Ratio

*“There’s two possible outcomes: if the result confirms the hypothesis,
then you’ve made a discovery. If the result is contrary to the hypothesis,
then you’ve made a discovery.”*

—Enrico Fermi

THIS chapter reports the results of a WIMP dark matter search performed on a 231 live-day dataset collected by the DEAP-3600 detector using the Profile Likelihood Ratio analysis. Section 6.2 provides an overview on the various systematic uncertainties and their implementation into the Profile Likelihood Ratio analysis. Validation studies to verify the stability of the software are performed in Section 6.3. Section 6.4 explores the projected WIMP sensitivity using the Profile Likelihood Ratio analysis, for various different configurations of background rates

and systematic uncertainties. Finally in Section 6.5, the software is used to produce a 90% Confidence Level upper limit on the WIMP-nucleon cross section as a function of WIMP mass for the 231 live-day dataset.

6.1 Calculating an Upper Limit

CALCULATING an upper limit (exclusion) on the WIMP-nucleon cross section using the Profile Likelihood Ratio (PLR) software is as follows. The software first reads in a text file with the `nSCBayes`, `Fprompt`, `Rrec` and `PulseIndexFirstGar` values of each observed event in the dataset. The PLR fits the observed data under the signal (WIMP) hypothesis, defined by an input test WIMP-nucleon cross section σ [cm²] and input test WIMP mass M_χ [GeV/c²]. A “fit” to the data is actually comprised of two separate fits with the likelihood function given in Equation 5.2, to yield the conditional and unconditional maximum likelihoods. Described in Section 1.4.3, the conditional maximum likelihood is defined as the maximum value of the likelihood function when σ is fixed at its test value in the fit and the nuisance parameters return their maximum likelihood estimators. The unconditional maximum likelihood is defined as the maximum value of the likelihood function when both σ and the nuisance parameters return their maximum likelihood estimators. The conditional and unconditional maximum likelihoods define the PLR, λ , from Equation 1.34. The value of λ is used to define the value of the “test statistic” for the observed dataset q_{obs} using the definition from Equation 1.37. The test statistic, q , quantifies the level of discrepancy between the observed data and the signal hypothesis. Larger values of q correspond to worse agreement between the data and hypothesis; as σ increases (relative to its maximum likelihood estimator, $\hat{\sigma}$), the value of q increases.

For a given M_χ , the observed data is fit under multiple signal hypotheses with varying values of σ , to calculate the value of q for the observed dataset at each

test σ value, q_{obs} . Only cases where $\sigma > \hat{\sigma}$ are considered in the calculation of an upper limit; a direct consequence of the definition of q given in Equation 1.37. At each test σ value, the PLR software is then used to generate approximately 500 - 1000 pseudoexperiments, in which fake datasets comprised of a random number of signal and background events are created. The software integrates over each model to calculate the expected number of ROI events N_{exp} from the event type in question, which is used to generate a random number of events by randomly drawing from a Poisson distribution with an expectation value of N_{exp} . For every event generated by each model, a random **PulseIndexFirstGAR** value is drawn from the **PulseIndexFirstGAR** distribution implemented in the model. The **nSCBayes**, **F_{prompt}** and **R_{rec}** values are then drawn randomly from one of the five three-dimensional PDFs, depending on which **PulseIndexFirstGAR** bin the event falls into. If any nuisance parameters are configured as “free” in the fit, these are randomised with respect to their constraint terms in the models prior to the event variables being chosen.

For each test σ value, all of the pseudoexperiments are fit with the PLR software in order to obtain the distribution of q under the test signal hypothesis, $f(q|H_\sigma)$. With $f(q|H_\sigma)$ and q_{obs} determined from fitting the observed data, the signal p -value p_s under the test hypothesis σ can be calculated using Equation 1.38, or equivalently, the number of pseudoexperiments with $q \geq q_{\text{obs}}$. The upper limit is determined from the distribution of p_s as a function of σ . An upper limit on the WIMP-nucleon cross section at 90% Confidence Level (C.L.) is placed on the value of σ which yields $p_s = 0.1$ (10%). In order to calculate an exclusion curve, this procedure is repeated at multiple values of M_χ .

6.2 Systematic Uncertainties

IN total, the PLR software has 20 nuisance parameters, each corresponding to a specific systematic uncertainty. All of the nuisance parameters are summarised in Table 6.1, shown with their respective constraint terms.

Table 6.1: Summary table of the 20 nuisance parameters implemented in the WIMP PLR software, shown with their respective constraint terms (uncertainties) and whether they are fixed or allowed to float in the fit.

| Nuisance Parameter | Constraint Term | Free/Fixed |
|--|---------------------------------|------------|
| | $498 < v_{\text{esc}} < 608,$ | |
| Escape Velocity [km/s] | $v_{\text{esc,med}} = 544$ [46] | Fixed |
| Energy Scale Offset [PE] | Gaus(1.1, 0.2) | Fixed |
| Mean Light Yield [PE/keV] | Gaus(6.1, 0.4) | Free |
| Energy Resolution [PE] | Gaus(1.5, 0.13) | Fixed |
| Mean NR F_{prompt} Error [σ] | Gaus(0, 1) [63] | Fixed |
| Quenching Factor $q_n(E_{\text{nr}})$ Error [σ] | Gaus(0, 1) [63] | Free |
| Single ^{39}Ar Rate Scale | Gaus(0, 0.05) | Fixed |
| Coincidence ^{39}Ar Rate Scale | Gaus(0, 0.05) | Fixed |
| Additional ER Background Rate Scale | Gaus(0, 0.05) | Fixed |
| ^{39}Ar Shape Deviation [keV^{-1}] | Gaus(0.00067, 0.00005) | Fixed |
| Reconstructed Radial Bias Scale | Gaus(0, 0.2) | Fixed |
| Reconstructed Radial Resolution Scale | Gaus(0, 0.05) | Fixed |
| LAr Optical Model Error [σ] | HalfGaus(0, 1) | Free |
| TPB Scattering Length Error [σ] | Gaus(0, 1) | Free |
| PMT Afterpulsing Probability Error [σ] | Gaus(0, 1) | Free |
| Relative PMT Efficiency Error [σ] | Gaus(0, 1) | Free |
| Surface α -decay Normalisation Scale | Gaus(0, 0.5) | Free |
| Neck α -decay Normalisation Scale | Gaus(0, 0.5) | Free |
| Dust α -decay Normalisation Scale | Gaus(0, 0.5) | Free |
| Radiogenic Neutron Normalisation Scale | Gaus(0, 1) | Free |

The implementation of the nuisance parameters are as follows. Parameters which are referred to as “scale” are ones which quantify the fractional level of deviation from the nominal value; these are constructed as linear multipliers of the form: $N = N + p_0 \cdot N$, where N is the nominal value of the parameter and p_0 is the corresponding nuisance parameter. For example, for the neutron ROI background expectation, $p_0 = 0$ returns the nominal background expectation value ($N = 8.23$) whereas $p_0 =$

0.5 corresponds to a 50% increase from the nominal background expectation value ($N = 12.3$). Parameters which are defined in units of $[\sigma]$ are ones which quantify the level of deviation from the nominal value in units of their measured uncertainty σ ; these are constructed as $N = N + p_0 \cdot \sigma$. For example, for the quenching factor, a value of $p_0 = 1$ corresponds to an observed value of $\bar{q}_n(E_{\text{nr}}) + 1\sigma$, where $\bar{q}_n(E_{\text{nr}})$ is the nominal value of $q_n(E_{\text{nr}})$ and σ is the measured error on $q_n(E_{\text{nr}})$. Parameters which do not fall into either of these two categories correspond to systematics whose mean values and uncertainties are directly encoded into their constraint terms.

The prior values of each nuisance parameter, their constraint terms, and their origin are as follows. The escape velocity constraint is derived from measurements taken by the RAVE survey, described further in [46]. The mean values and uncertainties on the nuclear recoil (NR) quenching factor and mean NR F_{prompt} come from ex-situ measurements described in Sections 2.1.2 and 5.3.1 respectively. The mean value of the light yield parameter is taken directly from the results of the energy calibration performed by the DEAP-3600 experiment in [4], unlike the energy scale offset parameter, the energy resolution parameter, the three ^{39}Ar spectrum rate parameters and the ^{39}Ar shape deviation parameter, whose mean values are determined from an independent fit to the ^{39}Ar sideband data. Out of all of these parameters listed above, the mean light yield is the only parameter currently allowed to float in the PLR, which is constrained by the ^{39}Ar sideband data during the fit. The other parameters listed above are instead fixed to their best fit values obtained from the ^{39}Ar sideband data. The constraints on the mean light yield and energy resolution are taken from [4], which account for uncertainties from position dependence and time dependence throughout the 231 live-days of data as well as fit uncertainties. The 5% uncertainty on the single ^{39}Ar rate parameter is derived from an in-situ measurement performed by former DEAP-3600 PhD student Matt Dunford in [109]. The same level of uncertainty is assumed for the ^{39}Ar coincidence

rate and additional electronic recoil (ER) background contributions. The constraint on the ^{39}Ar shape factor is currently taken as the fit uncertainty, as studies on the variation of this parameter with time and position have not yet been conducted.

The mean value of the LAr refractive index, which governs the LAr optical model uncertainty, is determined by an ex-situ measurement performed at $\lambda = 128$ nm by the DUNE collaboration in [71]. The uncertainty on the LAr refractive index is taken to be the difference between the mean value from [71] and the value obtained from an extrapolation down to 128 nm from the measurement performed by E Grace et al in [69] at $\lambda \sim 420$ nm. The mean value and $\pm 1\sigma$ uncertainties on the TPB scattering length are given in Section 3.1.1. The mean value of the afterpulsing probabilities for each PMT are calculated internally by the DEAP-3600 collaboration; a 20% uncertainty is assigned to the afterpulsing probability for all PMTs. The mean value of the relative PMT efficiencies are also calculated internally by the DEAP-3600 collaboration, and are each assigned a 5% uncertainty. The mean values of the radial bias and resolution parameters are determined from ^{39}Ar Monte Carlo (MC) simulations, used to construct the ^{39}Ar R_{rec} model in Section 5.3.1. The uncertainties on these parameters are 20% and 5% respectively, and are derived from comparisons between ^{39}Ar data and MC simulations as described in [4]. The uncertainties on the overall normalisations of the MC-constructed background models are driven by in-situ measurements performed by the DEAP-3600 collaboration internally and in [4].

As summarised in Table 6.1, not all of the systematics listed in Table 6.1 are currently allowed to float in the fit. In the current configuration, one fit to the data takes on average 5 hours. Since each free nuisance parameter can add up to 1 hour to the total fit time, it is important to reduce the number of necessary nuisance parameters where possible. In order to determine which systematics are the most important, a study was performed in which the data was fit under a test signal

hypothesis ($M_\chi = 100 \text{ GeV}/c^2$, $\sigma = 10^{-45} \text{ cm}^2$), where just the light yield was allowed to float and the rest were fixed. One at a time, each systematic uncertainty was unfixed and the data refit, to test whether introducing the systematic had a significant impact on the best fit cross section and its uncertainty. It was determined that the energy scale offset, single ^{39}Ar rate, ^{39}Ar coincidence rate, ER background rate, ^{39}Ar shape deviation and radial bias/ resolution parameters each had $< 1\%$ of an effect on the best fit cross section and its uncertainty, and thus are fixed in the final configuration. The effect of the mean NR F_{prompt} was found to be insignificant compared to the quenching factor $q_n(E_{\text{nr}})$, and so the decision was made to also fix that parameter in the final configuration. The energy resolution was observed to change the best fit cross section and its uncertainty marginally more than the above systematics, by $\sim 3\%$, however the decision was made to fix this parameter in this iteration due to time constraints, as it extended the fit time by up to factor of 2 (~ 10 hours). Work is ongoing to speed up the implementation of the energy resolution in the PLR, in order to include it as a systematic in the next iteration.

6.2.1 Propagation of Systematic Uncertainties in PLR

A new technique was developed in order to propagate additional systematic uncertainties from the detector response and optical model parameters into the PLR, in which MC simulations of the different background sources are generated with each parameter at their nominal value and varied at their $\pm 1\sigma$ values. Four parameters are considered in this analysis:

- Liquid argon (LAr) optical model: this blanket term constitutes three parameters; the LAr refractive index, the group velocity of light in LAr and the Rayleigh scattering length, which are all highly correlated with one another as described in Section 2.1.2. The correlations between these parameters are intrinsically accounted for in one global systematic variation of the LAr

refractive index in simulation,

- Scattering length of light in the TPB,
- PMT afterpulsing probabilities, and
- Relative PMT efficiencies.

Each of these systematics can change the shapes of the `nSCBayes`, `Fprompt` and `Rrec` distributions, which can push potential events into and out of the ROI. The procedure for implementing these systematics into the PLR, described in the context of the neck α -decay model, is described below.

The same number of events as simulated to build the nominal neck α -decay model are simulated with the values of the four parameters listed above at their $\pm 1\sigma$ values. Due to a computing (resource) limitation, the LAr optical model is only simulated at its $+1\sigma$ value, and is implemented in the PLR currently as a one-sided systematic. For each systematically varied MC dataset, the three-dimensional PDFs are constructed the same way as described for the nominal MC in Section 5.3.2. Figure 6.1 shows three example functional forms that describe the neck α -decay `nSCBayes` distribution, obtained from fitting the distribution with Equation 5.8 for the nominal MC dataset, and the two MC datasets which correspond to the MC afterpulsing probability parameter when varied by $\pm 1\sigma$, in the `PulseIndexFirstGAr` = 0 bin.

Systematic uncertainties enter the likelihood function as follows. When the $\mathcal{L}_{\text{PDF}}(\sigma|\{\theta\})$ term is calculated for a set of events in the PLR software, the one and two-dimensional functions that describe the `nSCBayes`, `Fprompt` and `Rrec` dimensions are evaluated at the value of these event variables. To incorporate these four systematics, a set of four associated nuisance parameters θ_i are introduced that modify the functions in each of the three dimensions simultaneously,

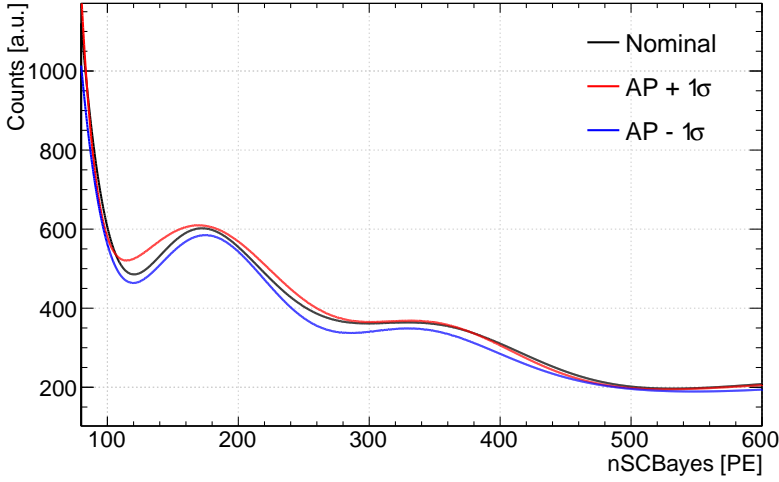


Figure 6.1: Three example fit functions that describe the neck α -decay **nSCBayes** distribution in the **PulseIndexFirstGAR** = 0 bin, obtained from fitting the distribution with Equation 5.8, for the nominal MC dataset (black), and the two MC datasets which correspond to the MC afterpulsing probability parameter when varied by $\pm 1\sigma$ (red and blue respectively).

$$f^j \rightarrow f^{j'} = f_{\text{nom}}^j + \sum_{i=1}^{N=4} \begin{cases} (f_{\text{up},i}^j - f_{\text{nom}}^j)\theta_i, & \theta_i \geq 0 \\ (f_{\text{nom}}^j - f_{\text{down},i}^j)\theta_i, & \theta_i < 0, \end{cases} \quad (6.1)$$

where f_{nom}^j , f_{up}^j and f_{down}^j are the one-dimensional or two-dimensional functions from dimension j , where $j = 1, 2$ or 3 and correspond to the three dimensions: **nSCBayes**, **F_{prompt}** and **R_{rec}**. When any of the θ_i parameters vary, the functions describing the **nSCBayes**, **F_{prompt}** and **R_{rec}** dimensions simultaneously vary according to Equation 6.1. As such, correlations between the event variables and systematics are properly accounted for. In the case of the LAr optical model parameter, which is a one-sided uncertainty, θ_i is constructed to vary only in one direction, ≥ 0 .

The quantities $(f_{\text{up},i} - f_{\text{nom}})$ and $(f_{\text{nom}} - f_{\text{down},i})$ can be written as $\delta(f)$, and correspond to the absolute differences between the functions that model the distributions from the nominal and $\pm 1\sigma$ MC datasets for the i 'th MC systematic. The

fractional quantities $\delta(f)/f_{\text{nom}}$ for the $\pm 1\sigma$ cases are shown in Figure 6.2 for the MC afterpulsing probability systematic variations in the `nSCBayes` dimension for neck α -decays in the `PulseIndexFirstGAR` = 0 bin. Figure 6.2 shows that a symmetric uncertainty in the parameters itself does not necessarily translate to a symmetric change in $\delta(f)$, and thus these quantities are calculated explicitly for the $\pm 1\sigma$ cases with the exception of the LAr optical model, which is only calculated for the $+1\sigma$ case.

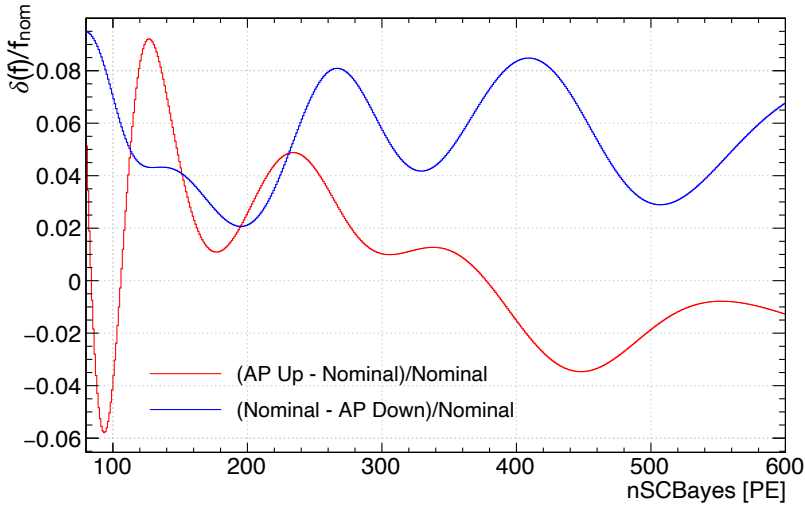


Figure 6.2: The fractional quantities $\delta(f)/f_{\text{nom}}$ for the $\pm 1\sigma$ cases as a function of `nSCBayes` [PE] as calculated for the MC afterpulsing probability systematic variations for neck α -decays shown in Figure 6.1.

This set of four nuisance parameters θ_i can be called in any MC-constructed models with this implementation simultaneously during the fit, ensuring that correlations between the `nSCBayes`, F_{prompt} and R_{rec} event variable parameters and the systematics are fully propagated through all of the models. Correlations between the systematic parameters themselves θ_i are also accounted for in this method, determined directly from the covariance matrix from the fit result. Since all three

dimensions of the MC models can all be simultaneously changed with the use of just four additional parameters, this significantly speeds up operation of the software and helps the stability of the fit. For the result presented in this thesis, the computing resources required to generate the MC systematic variations of dust α -decays were not available; propagation of the LAr optical model, TPB scattering length, PMT afterpulsing probability and PMT efficiency systematics in the PLR is currently only accounted for in surface α -decays and neck α -decays. A further caveat is that this propagation is also not currently implemented for the WIMP model, which means that a change in the θ_i parameters will induce a change in just the surface and neck α -decay backgrounds, and not the WIMP signal. This has the effect that the size of the surface and neck α -decay backgrounds will change relative to the signal larger (or smaller) in an undefined way, and thus a change of 1σ may not necessarily correspond to 1σ . Work is currently ongoing to propagate these systematics through the WIMP model, however it is expected that this will have a small effect on the final result obtained from the PLR analysis.

For the radiogenic neutron model, it was deliberately decided to not generate the full set of MC systematic variations, after it was observed that the normalisation uncertainty on the number of radiogenic neutron ROI events, determined in [4], is greater than the systematic uncertainty. This was evaluated by generating one additional MC dataset for radiogenic neutrons, varying the LAr optical model parameter by its $+1\sigma$ uncertainty. The PDFs are constructed the same way as described for the nominal MC in Section 5.3.5. The LAr optical model parameter was chosen for this study as it is expected to make the largest difference with respect to the nominal case. The functional forms determined from the $+1\sigma$ LAr optical model systematic MC dataset are then implemented into the PLR software and the expected number of radiogenic neutron ROI events recalculated. The change in the number of expected radiogenic neutron ROI events between the nominal and $+1\sigma$

LAr optical model cases is determined to be -30%; less than the $\sim 100\%$ normalisation uncertainty calculated in [4] that is implemented in the neutron normalisation constraint term in Table 6.1.

Figure 6.3 shows the 1σ uncertainty band on the neck α -decay **nSCBayes** model for the `PulseIndexFirstGAR` = 0 bin, based on the 1σ systematic uncertainties from the LAr optical model, TPB scattering length, PMT afterpulsing probability, relative PMT efficiencies, and mean light yield. The overall normalisation systematic is not accounted for in Figure 6.3, which scales only the ROI normalisation. The correlations between these 5 parameters are extracted from one of the fits performed to the 24 surviving events using the PLR software as described in Chapter 6, which are used to correctly propagate the individual uncertainties into a combined 1σ uncertainty band. Superimposed on Figure 6.3 is the **nSCBayes** distribution from the nominal neck α -decay MC simulations. The y -axis has been scaled in Figure 6.3 to match the exposure of the 231 live-day dataset. Figure 6.3 illustrates that currently, the uncertainties from the systematic variations cover variations caused by a mis-modelling of the MC simulations. With the implementation of a two-sided LAr optical model uncertainty, the systematic uncertainty band is expected to increase further, improving the coverage of MC-model mismatches. In order to quantify the size of the systematics compared to the level of agreement between data and MC simulations, the neck α -decay best fit model and 1σ uncertainty band should be compared with candidate neck α -decay data, in a region outside of the ROI. This validation study is planned for the near future.

Table 6.2 summarises the predicted number of ROI events from each background (^{39}Ar β -decays, neck, surface and dust α -decays and radiogenic neutrons) in the 231 live-day dataset, for every $\pm 1\sigma$ variation of systematic uncertainties labelled “free” in Table 6.1.

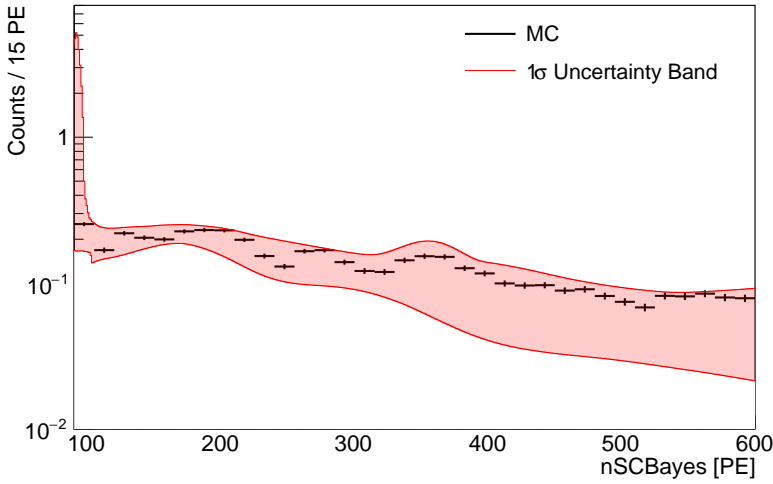


Figure 6.3: 1σ uncertainty band on the neck α -decay **nSCBayes** model for the **PulseIndexFirstGAR** = 0 bin, based on the 1σ uncertainties on the LAr optical model, TPB scattering length, PMT afterpulsing probability, relative PMT efficiencies and mean light yield (red). Superimposed is the **nSCBayes** distribution from nominal neck α -decay MC (black). The y -axis is scaled to match the exposure of the 231 live-day dataset.

Table 6.2: Predicted number of ROI events from each background (^{39}Ar β -decays, neck, surface and dust α -decays and radiogenic neutrons) in the 231 live-day dataset, for every $\pm 1\sigma$ variation of systematic uncertainties labelled “free” in Table 6.1.

| Systematic $[+1/-1]\sigma$ | ^{39}Ar | Neck α | Surface α | Dust α | Neutrons |
|----------------------------|------------------|---------------|-------------------|---------------|-----------|
| Light Yield | 1.53/1.76 | 3.89/3.96 | 0.000321/0.000421 | 2.84/3.25 | 8.06/8.47 |
| Quenching Factor | N/A | N/A | N/A | N/A | 8.01/8.41 |
| LAr Optical Model | N/A | 2.02 | 0.00533 | N/A | N/A |
| TPB Scattering Length | N/A | 3.61/3.97 | 0.00174/0.00954 | N/A | N/A |
| PMT Afterpulsing Prob | N/A | 4.14/3.33 | 0.00530/0.00190 | N/A | N/A |
| Rel. PMT Efficiencies | N/A | 3.89/3.64 | 0.00218/0.00208 | N/A | N/A |
| ROI Normalisation | N/A | 5.88/1.96 | 0.000506/0.000167 | 4.55/1.52 | 16.5/0.00 |

6.3 Software Validation

A series of consistency tests were conducted in order to ensure that the likelihood function implemented in the software performs as expected. The implemen-

tation of the $\mathcal{L}_{\text{PDF}}(\sigma|\{\theta\})$ and $\mathcal{L}_{\text{constraint}}(\{\theta\})$ terms are first verified. For a fake dataset comprised of a large enough number of events, $\mathcal{O}(1000)$, the $\mathcal{L}_{\text{PDF}}(\sigma|\{\theta\})$ and $\mathcal{L}_{\text{constraint}}(\{\theta\})$ terms in the likelihood should be able to reproduce the true values of any floating nuisance parameters if there is no sideband present to constrain certain nuisance parameters. This can be tested by generating and fitting random fake datasets, or pseudoexperiments, where the true values of the nuisance parameters used to generate the dataset, drawn randomly from their corresponding constraint term $\mathcal{L}_{\text{constraint}}(\{\theta\})$, are known.

Given the large number of events required for this study, only one or two nuisance parameters are tested at a time. Currently, one fit to a dataset comprised of 24 events and 10 free nuisance parameters takes ~ 5 hours. Generating such a substantial number of events from models which make use of convolutions, such as the WIMP and ^{39}Ar models, is also very computationally time-consuming. As such, just two parameters (the mean light yield and the overall neck α -decay normalisation scale factor), are considered for this study. In an ideal world, this study would be performed for each nuisance parameter allowed to float in the fit.

Figures 6.4 and 6.5 show the distribution of the fitted nuisance parameter value versus the true nuisance parameter value obtained from fitting 1000 pseudoexperiments using the likelihood function for the mean light yield and neck α -decay normalisation parameters respectively. Both plots are fit with a first order polynomial, with the offset fixed to zero. In both cases, the linear polynomial parameter p_1 is consistent with 1, indicating that the likelihood correctly reproduces the true value of both parameters. The variance of the fitted parameter values as well as their individual error bars are larger in the mean light yield case than in the neck α -decay normalisation case, illustrating that the neck α -decay model has more sensitivity to its normalisation parameter than the mean light yield parameter.

The sideband term $\mathcal{L}_{\text{sideband}}(\{\theta\})$ is then added to the likelihood function. To

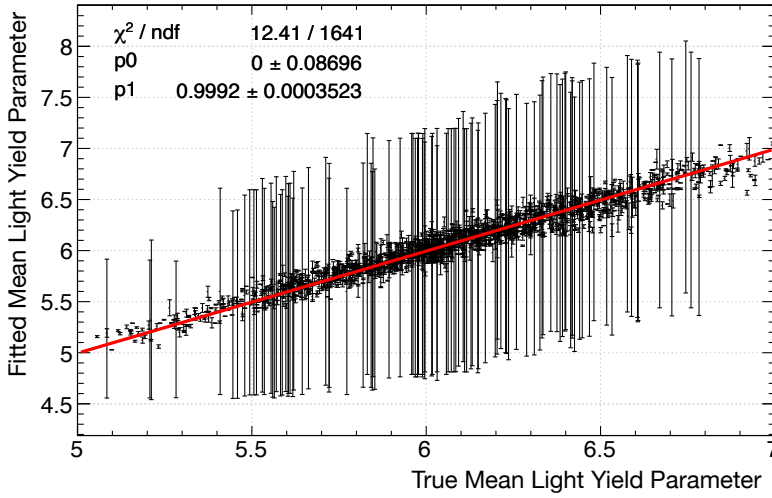


Figure 6.4: Fitted mean light yield parameter versus the true mean light yield parameter obtained from fitting 1000 pseudoexperiments using the likelihood function, including only the $\mathcal{L}_{\text{PDF}}(\sigma|\{\theta\})$ and $\mathcal{L}_{\text{constraint}}(\{\theta\})$ terms. The true values of the mean light yield parameter are drawn randomly from its Gaussian constraint term $\mathcal{L}_{\text{constraint}}(\{\theta\}) \sim \text{Gaus}(6.1, 0.4)$ [PE/keV]. The distribution is fit with a first order polynomial with the offset fixed to zero (red line).

verify that the $\mathcal{L}_{\text{sideband}}(\{\theta\})$ implementation is correct, a further 1000 pseudoexperiments are generated and fit with the likelihood, with both the mean light yield and neck α -decay normalisation parameters drawn randomly from their respective constraint terms and allowed to float in the fit. Figure 6.6 shows the distribution of the fitted mean light yield parameter values obtained from fitting 1000 pseudoexperiments, with the inclusion of $\mathcal{L}_{\text{sideband}}(\{\theta\})$ in the likelihood function. Figure 6.6 demonstrates that the sideband is extremely effective at constraining the mean light yield parameter within its constraint term of $\text{Gaus}(6.1, 0.4)$ [PE/keV]. The mean value of the distribution corresponds to 6.068 PE/keV; this matches the actual value of the mean light yield determined from a separate fit to the ^{39}Ar sideband, which also yields a mean light yield of 6.068 PE/keV.

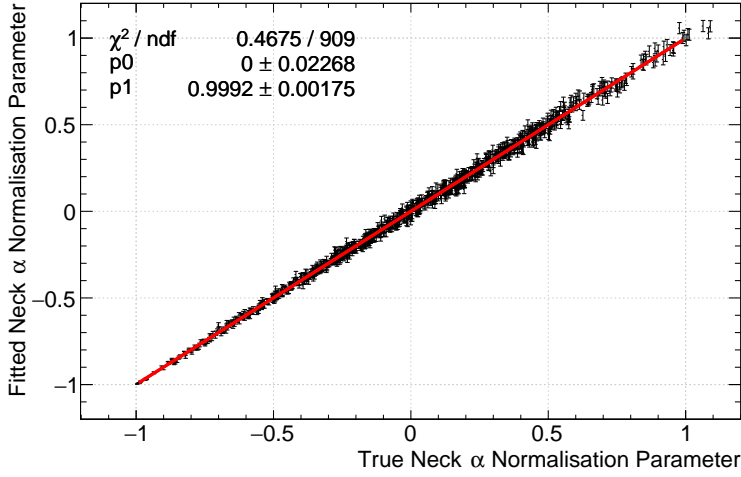


Figure 6.5: Fitted neck α -decay normalisation parameter versus the true neck α -decay normalisation parameter obtained from fitting 1000 pseudoexperiments using the likelihood function, including only the $\mathcal{L}_{\text{PDF}}(\sigma|\{\theta\})$ and $\mathcal{L}_{\text{constraint}}(\{\theta\})$ terms. The true values of the neck α -decay normalisation parameter are drawn randomly from its Gaussian constraint term $\mathcal{L}_{\text{constraint}}(\{\theta\}) \sim \text{Gaus}(0, 0.5)$. The distribution is fit with a first order polynomial with the offset fixed to zero (red line).

Figure 6.7 shows the distribution of the fitted neck α -decay normalisation parameter values obtained from fitting 1000 pseudoexperiments, with the inclusion of $\mathcal{L}_{\text{sideband}}(\{\theta\})$ in the likelihood function. Also drawn is the constraint term from which the true neck α -decay normalisation parameter is drawn from, $\text{Gaus}(0, 0.5)$. Figure 6.7 shows that the distribution of fitted neck α -decay normalisation parameter values is extremely consistent with its constraint term, implying that the likelihood fits out the true value despite the difference between the true and fitted out mean light yield parameter which is constrained by the sideband. This implies that the neck α -decay normalisation parameter is not highly correlated with the mean light yield parameter, as expected.

One further test was performed on the PLR software, to verify how the upper limit calculated by the PLR in the case of a zero background analysis compares

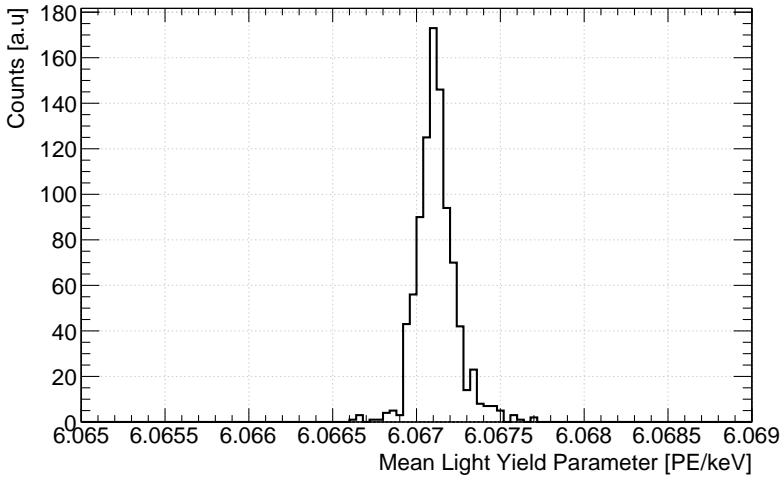


Figure 6.6: Distribution of the mean light yield parameter obtained from fitting 1000 pseudoexperiments where the sideband term is included in the likelihood function. The neck α -decay normalisation parameter is also floated in the fit. The inclusion of the sideband term in the likelihood tightly constrains the mean light yield to the value determined by the separate fit to ^{39}Ar sideband, equal to 6.068 PE/keV.

to the Poisson upper limit. Poisson statistics states that if no events are observed in the WIMP ROI, a 90% C.L. upper limit is placed at the value of the WIMP-nucleon cross section that yields 2.3 expected signal events. The 90% C.L. upper limit obtained from the PLR software in the zero background case was compared to the 90% C.L. Poisson upper limit calculated by the DEAP-3600 collaboration in [4], an analysis in which zero ROI events were observed.

The PLR was tested by fitting a “zero event” dataset using the same ROI and WIMP dark matter search cuts as [4], and assuming a background expectation of zero. The PLR is used to determine the 90% C.L. upper limit on the WIMP-nucleon cross section at just one WIMP mass, $M_\chi = 100 \text{ GeV}/c^2$. Only the mean light yield and quenching factor systematics, which vary the WIMP signal, are considered in this study. Following the procedure described in Section 6.1, the distribution of the signal p -value p_s as a function of test cross section σ is obtained at 5 different test

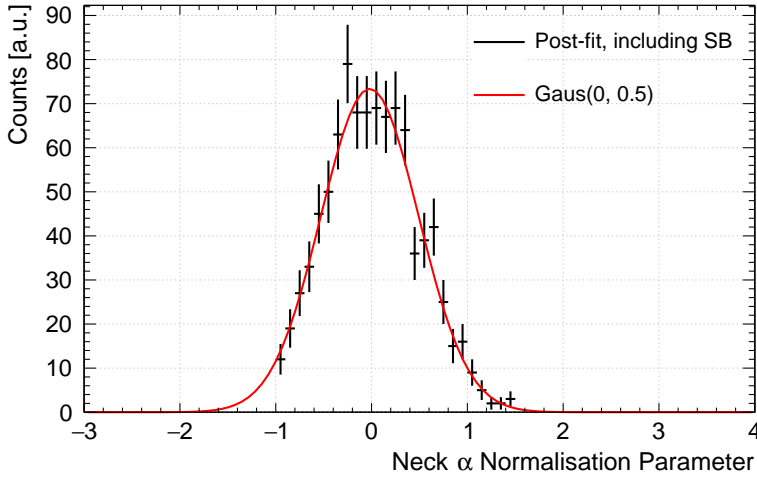


Figure 6.7: Distribution of the neck α -decay normalisation parameter obtained from fitting 1000 pseudoexperiments where the sideband term is included in the likelihood function (black). The mean light yield parameter is also floated in the fit. Shown overlaid is the neck α -decay normalisation constraint term, $\text{Gaus}(0, 0.5)$ (red). The distribution is extremely consistent with its constraint term, confirming that the neck α -decay normalisation is not highly-correlated with the mean light yield.

cross section values; this is shown in Figure 6.8. The y -axis errors on the distribution are calculated from the `TGraphAsymmErrors` class from ROOT. `TGraphAsymmErrors` takes in two input histograms and creates a graph with asymmetric errors by dividing one input histogram by another. `TGraphAsymmErrors` is typically used to correctly calculate the uncertainty on an efficiency curve, which can vary only between 0 and 1. Since p_s is analogous to an efficiency, in that it can only scale between 0 and 1, this functionality is used to ensure that the uncertainties do not extend beyond physical boundaries, such as below 0 or above 1. The x -axis errors are also created as part of the `TGraphAsymmErrors` functionality, however these errors are ignored when the distribution is fit as there is no uncertainty on the value of the test cross section.

The 90% C.L. upper limit is found by fitting the distribution with a half-Gaussian

with the mean parameter fixed at the best fit value of the test cross section, $\hat{\sigma} = 0$. Evaluating the function in Figure 6.8 at $p_s = 0.1$ (10%) yields a 90% C.L. upper limit of $3.62 \times 10^{-45} \text{ cm}^2$ for a 100 GeV WIMP/ c^2 . This value is 7% more sensitive than the 90% C.L. upper limit placed by the DEAP-3600 experiment in [4] ($3.9 \times 10^{-45} \text{ cm}^2$). This is most likely attributed to the fact that only the mean light yield and quenching factor systematics are considered in this study; an additional study including all of the same systematics as [4] should be performed to confirm if this is the source of the discrepancy.

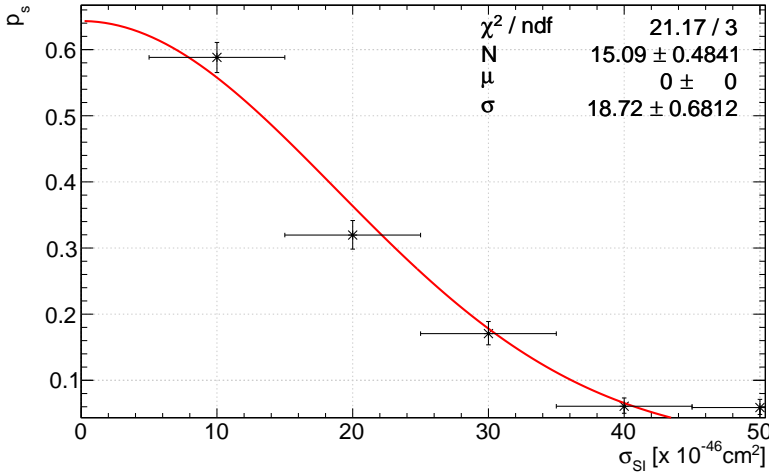


Figure 6.8: Signal p -value p_s as a function of test WIMP-nucleon cross section σ [$\times 10^{-46} \text{ cm}^2$], used to obtain the 90% C.L. upper limit on the WIMP-nucleon cross section for a 100 GeV/ c^2 WIMP for a background-free analysis. As a further sanity check, the software is used to reproduce the Poisson 90% C.L. upper limit set by the cut-and-count analysis performed by the DEAP-3600 experiment in [4]. The upper limit obtained from the PLR software is $3.62 \times 10^{-45} \text{ cm}^2$, 7% more sensitive than the DEAP-3600 limit ($3.9 \times 10^{-45} \text{ cm}^2$).

6.4 Projected Sensitivity

BEFORE performing the WIMP dark matter search on the data, the PLR was used to calculate an upper limit on the WIMP-nucleon cross section for two fake datasets in which the 10 free nuisance parameters from Table 6.1 are added in succession, to explore how the projected WIMP sensitivity scales with the number of observed events N_{obs} , the number of expected background events N_{exp} and the various systematic uncertainties.

Two fake datasets are considered. The event variables for both fake datasets are drawn randomly from the dominant background models in the PLR (neck, dust α -decays and radiogenic neutrons, see Table 5.2), each containing a different number of observed events. Fake dataset X_1 contains $N_{\text{obs}} = 15$ events and fake dataset X_2 contains an additional 10 events, $N_{\text{obs}} = 25$ events. In both cases, the PLR predicts $N_{\text{exp}} = 15$ events from considering only neck, dust α -decays and radiogenic neutron backgrounds. These numbers were chosen to reflect the current number of expected background events in the PLR analysis, $N_{\text{exp}} \simeq 17$, and the current number of observed events in the data, $N_{\text{obs}} = 24$, and to determine how the projected WIMP sensitivity changes when $N_{\text{exp}} \simeq N_{\text{obs}}$ compared to when $N_{\text{exp}} < N_{\text{obs}}$.

The 10 nuisance parameters are separated into three groups, which are added consecutively to the PLR. The three groups are as follows:

- Group 1: Energy scale parameters, including the mean light yield and quenching factor,
- Group 2: Optical model and detector response parameters, including the LAr optical model, TPB scattering length, PMT afterpulsing probabilities and relative PMT efficiencies,
- Group 3: All background normalisation parameters, including the surface, neck and dust α -decay and radiogenic neutron models.

Three levels of systematic uncertainty are considered in the PLR per dataset: the first considers only Group 1 systematics, the second considers Group 1 and Group 2 systematics and the third considers Group 1, Group 2 and Group 3 systematics. This yields a total of 6 test configurations considered for this study.

This study is performed considering only one WIMP test mass, $M_\chi = 100$ GeV/ c^2 . Following the procedure described in Section 6.1, for each of the 6 configurations considered (2 fake datasets, 3 systematic configurations per dataset), the distribution of the signal p -value p_s as a function of test cross section σ is determined. The uncertainties on the values of p_s are calculated using the same method as outlined in Section 6.3. Each distribution is fit with half-Gaussian distribution to interpolate how p_s varies with the test cross section, with the mean of each half-Gaussian fixed to the value of the best fit cross section $\hat{\sigma}$ determined from each different configuration. The values of the WIMP-nucleon cross section that are excluded at 90% C.L. for a 100 GeV/ c^2 WIMP are summarised in Table 6.3 for the X_1 and X_2 fake datasets, where the three different levels of systematic uncertainty are accounted for in the PLR per dataset.

Table 6.3: Summary of the 90% C.L. upper limits placed on the WIMP-nucleon cross section for a 100 GeV/ c^2 WIMP using the PLR software on two fake datasets X_1 and X_2 comprised of 15 and 25 observed events respectively. In both cases, the nominal combined background model in the PLR predicts 15 expected events. For each dataset, 10 systematics, separated into three groups, are added in succession to the PLR, to investigate which systematics are dominant in the calculation of upper limits with the PLR.

| | X_1 ($N_{\text{obs}} = 15$) | X_2 ($N_{\text{obs}} = 25$) |
|------------------------------------|------------------------------------|------------------------------------|
| Group 1 | $1.9 \times 10^{-45} \text{ cm}^2$ | $4.2 \times 10^{-45} \text{ cm}^2$ |
| Group 1 + Group 2 | $2.1 \times 10^{-45} \text{ cm}^2$ | $4.4 \times 10^{-45} \text{ cm}^2$ |
| Group 1 + Group 2 + Group 3 | $3.5 \times 10^{-45} \text{ cm}^2$ | $5.5 \times 10^{-45} \text{ cm}^2$ |

The results from Table 6.3 show that for a dataset with an additional 10 observed events, the WIMP sensitivity worsens by between 60% - 120%, depending on which systematics are being considered in the analysis. The effect of the Group 2 systematics, dominated by the LAr optical model, result in an upper limit 10%

and 5% less sensitive than the effect of just Group 1 systematics for the X_1 and X_2 datasets respectively; however, these systematics are currently only implemented for two of the four MC-constructed background models, and not yet the WIMP model. For both datasets, the largest detriment to the WIMP sensitivity comes from the combined uncertainties on the ROI background predictions described by Group 3 systematics. The effect of the Group 3 systematics result in an upper limit 85% and 30% less sensitive than the effect of just Group 1 systematics for the X_1 and X_2 datasets respectively.

To explore the prospects of improving sensitivity, a further test was performed on the X_1 dataset, in which the constraint terms on the dust, neck α -decay and radiogenic neutron background ROI predictions were reduced by a factor of 2. With the ROI background prediction uncertainties reduced by half, an upper limit on the WIMP-nucleon cross section at 90% C.L. for a 100 GeV/c² is placed at 2.5×10^{-45} cm²; only 30% less sensitive from the case where only Group 1 systematics are included compared to 85% as calculated for the nominal ROI background prediction uncertainties in Table 6.3.

6.5 Final Results

A 90% C.L. upper limit is placed on the WIMP-nucleon cross section at 5 WIMP masses between 50 GeV/c² - 1000 GeV/c² using the PLR method. After applying all of the WIMP dark matter search cuts listed in Section 5.1, 24 remaining events are observed in the ROI; these are shown in Figure 6.9.

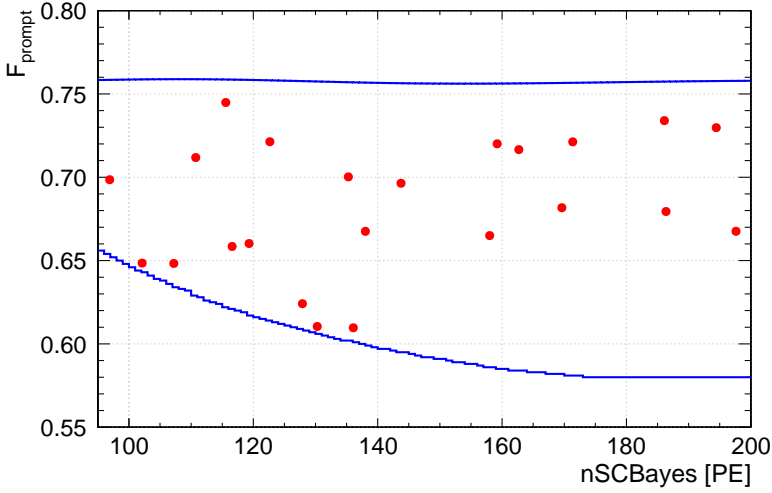


Figure 6.9: Two-dimensional plane of F_{prompt} vs $n\text{SCBayes}$, illustrating the WIMP ROI box defined for the Profile Likelihood Ratio analysis (blue) and the location of the 24 surviving events upon which the analysis is performed (red).

As part of the procedure for determining the upper limit, described in Section 6.1, approximately 10,000 pseudoexperiments in total are generated and fit by the PLR. The posterior values of the nuisance parameters obtained from both the conditional and unconditional likelihood fits for each pseudoexperiment are saved into a ROOT file, such that the posterior nuisance parameter distributions can be compared to their prior constraints. Figures 6.10 - 6.14 show the prior constraints superimposed on the conditional and unconditional posterior distributions of the mean light yield, quenching factor, LAr optical model, neck α -decay ROI normalisation and radiogenic neutron ROI normalisation parameters respectively for 850 pseudoexperiments generated under the signal hypothesis $M_\chi = 100 \text{ GeV}/c^2$, $\sigma = 1 \times 10^{-45} \text{ cm}^2$. The most constrained nuisance parameter is the mean light yield shown in Figure 6.10, as a result of the sideband term in the likelihood function. Figures 6.11 - 6.14 illustrate that the remaining posterior nuisance parameter distributions are mainly constrained by their priors; the wider posterior distributions are indicative of the more dominant systematics uncertainties, such as the overall

background ROI normalisations and the LAr optical model.

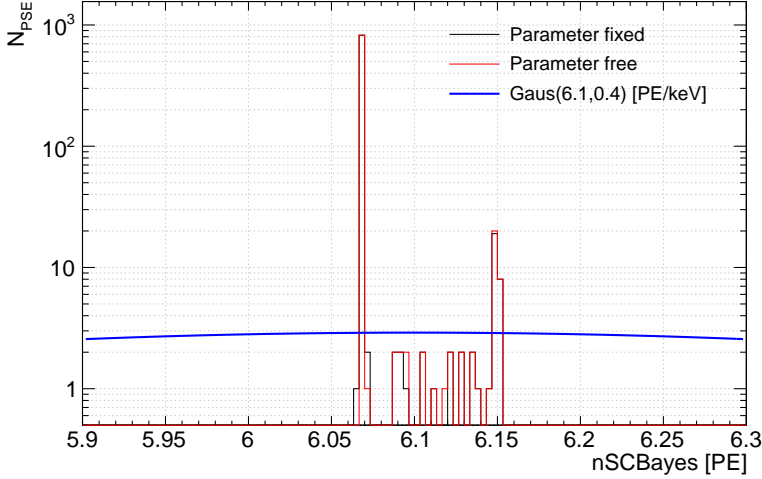


Figure 6.10: Posterior distributions of the mean light yield parameter from the conditional (black) and unconditional (red) likelihoods obtained from fitting 850 pseudoexperiments. The prior constraint term, $\text{Gaus}(6.1, 0.4)$ [PE/keV], is shown in blue.

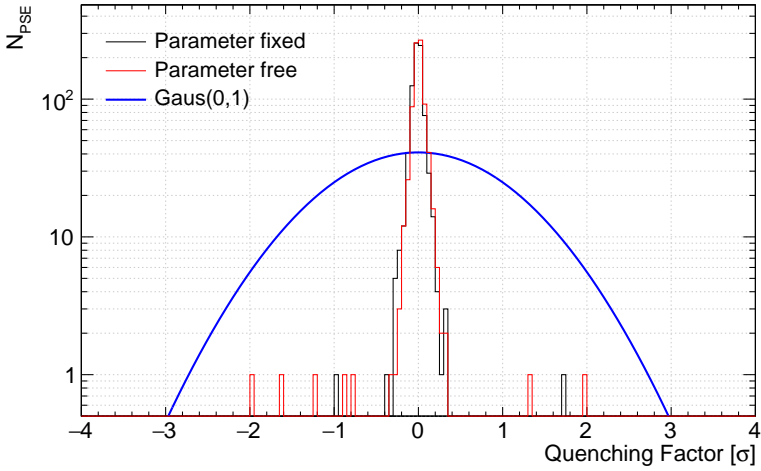


Figure 6.11: Posterior distributions of the quenching factor $q_n(E_{\text{nr}})$ [σ] parameter from the conditional (black) and unconditional (red) likelihoods obtained from fitting 850 pseudoexperiments. Also shown is the prior constraint term used in the PLR (blue), $\text{Gaus}(0, 1)$ [σ].

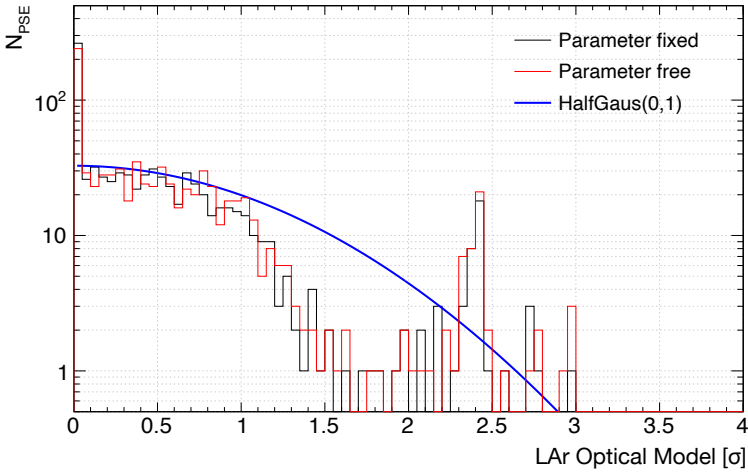


Figure 6.12: Posterior distributions of the LAr optical model $[\sigma]$ parameter from the conditional (black) and unconditional (red) likelihoods obtained from fitting 850 pseudoexperiments. The prior constraint term, $\text{HalfGaus}(0, 1)$ $[\sigma]$, is shown in blue.

6

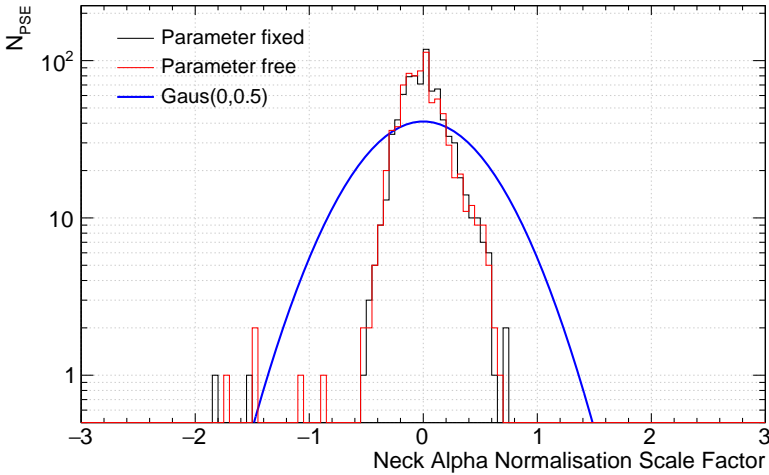


Figure 6.13: Posterior distributions of the neck α -decay ROI normalisation scale parameter from the conditional (black) and unconditional (red) likelihoods obtained from fitting 850 pseudoexperiments. The prior constraint term, $\text{Gaus}(0, 0.5)$, is shown in blue.

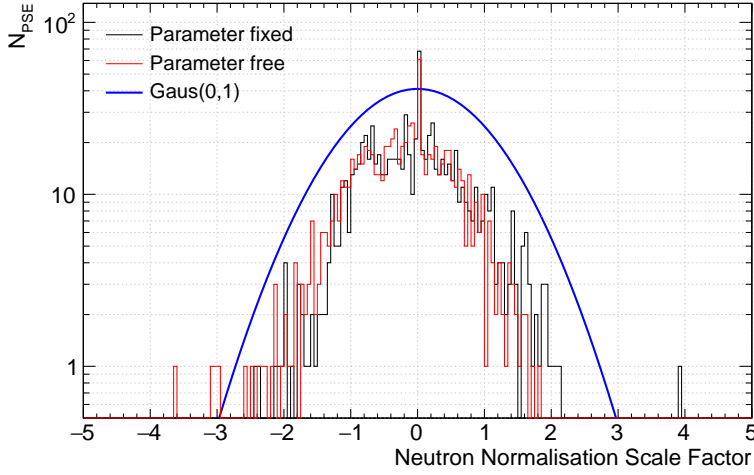


Figure 6.14: Posterior distributions of the radiogenic neutron ROI normalisation scale parameter from the conditional (black) and unconditional (red) likelihoods obtained from fitting 850 pseudoexperiments. The prior constraint term, $\text{Gaus}(0, 1)$, is shown in blue.

6

Following the procedure described in Section 6.1, for each WIMP mass, the distribution of the signal p -value p_s is determined as a function of test cross section. The signal p -value p_s is determined by the number of pseudoexperiments with $q \geq q_{\text{obs}}$. This is illustrated by Figure 6.15, which shows the $f(q|H_\sigma)$ distribution under the signal hypothesis of $M_\chi = 100 \text{ GeV}/c^2$, $\sigma = 3 \times 10^{-45} \text{ cm}^2$; p_s is given by the ratio of the shaded region to the full distribution. The uncertainties on p_s are again calculated using the same method as described in Section 6.3. Each of the five p_s distributions, corresponding to each of the five WIMP masses, are determined as a function of test cross section and fit with a half-Gaussian distribution, with the mean of the half-Gaussian fixed at the value of the best fit cross section $\hat{\sigma}$. Figure 6.16 illustrates an example fit to the p_s distribution for a $200 \text{ GeV}/c^2$ WIMP, which is used to determine the test cross section value that yields a 90% C.L. upper limit ($p_s = 0.1$).

Figure 6.17 shows the final 90% C.L. exclusion curve produced using the PLR for the 231 live-day dataset between $50 \text{ GeV}/c^2$ - $1000 \text{ GeV}/c^2$, compared with the

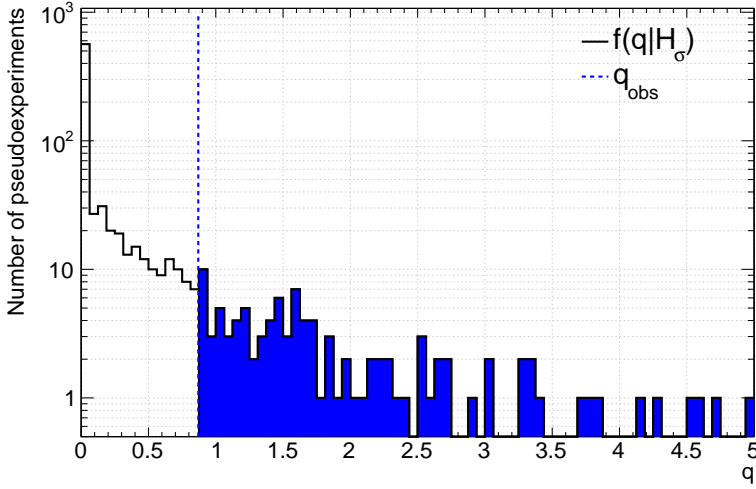


Figure 6.15: The $f(q|H_\sigma)$ distribution generated by ~ 500 pseudoexperiments under the signal hypothesis of $M_\chi = 100 \text{ GeV}/c^2$, $\sigma = 3 \times 10^{-45} \text{ cm}^2$. The blue dotted line indicates the value of the test statistic when the data is fit under the signal hypothesis, $q_{\text{obs}} = 0.928$. The signal p -value p_s is defined as the ratio of the shaded region to the full distribution.

exclusion curve obtained from the DEAP-3600 experiment using the same dataset in [4]. Figure 6.17 indicates that across a WIMP mass range of $50 \text{ GeV}/c^2 \leq M_\chi < 1000 \text{ GeV}/c^2$, the PLR yields a more sensitive limit compared to the DEAP-3600 cut-and-count analysis, more prominent at lower WIMP masses; there is almost a 50% improvement in sensitivity at $M_\chi = 50 \text{ GeV}/c^2$. The limit obtained from the PLR analysis converges with the DEAP-3600 cut-and-count analysis at $1000 \text{ GeV}/c^2$. The projected WIMP sensitivity studies in Section 6.4 show that the largest source of systematic uncertainty on the upper limit produced by the PLR analysis comes from the large uncertainties on the ROI background predictions; the study indicates that reducing the uncertainties on the background ROI predictions by a factor of 2 can improve the WIMP sensitivity by up to 40%.

Since the sensitivity scales as the square root of the exposure, the result determined from this analysis is expected to be at least 20% more sensitive than the DEAP-3600 result obtained in [4], considering just the increase in the fiducial vol-

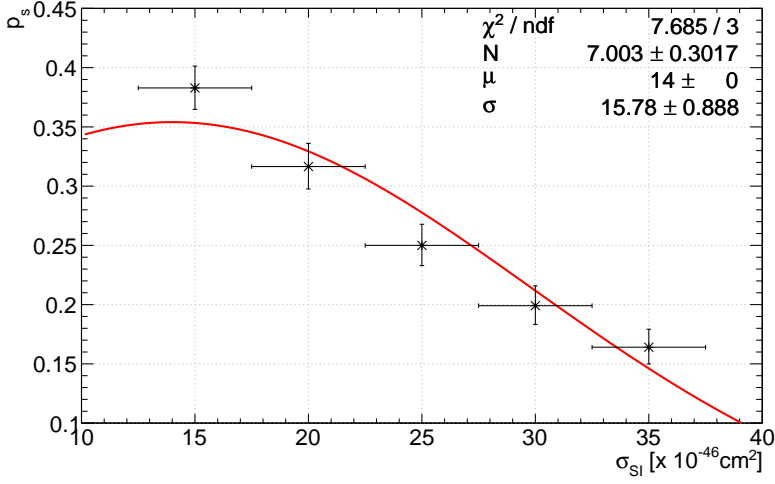


Figure 6.16: Signal p -value p_s as a function of test cross section σ [$\times 10^{-46} \text{ cm}^2$] for a $200 \text{ GeV}/c^2$ WIMP, as calculated from fitting the 24 observed events from the 231 live-day dataset. A half-Gaussian, with the mean parameter fixed to the best fit test cross section $\hat{\sigma}$, is fit to the distribution to calculate the value of the test cross section which yields $p_s = 0.1$ (10%) for a 90% C.L. upper limit. A WIMP-nucleon cross section of $3.90 \times 10^{-45} \text{ cm}^2$ is excluded at 90% C.L. for a $200 \text{ GeV}/c^2$ WIMP.

6

ume. Below $100 \text{ GeV}/c^2$, this level of improvement is achieved and actually surpasses expectation for smaller WIMP masses, as illustrated by the $\sim 50\%$ improvement in sensitivity at $50 \text{ GeV}/c^2$. The improvement at lower WIMP masses is driven by the increase in the WIMP ROI in F_{prompt} near the energy threshold. At WIMP masses of $100 \text{ GeV}/c^2$ and above, the level of improvement is less than expected from the increase in the fiducial volume. In this regime, the large uncertainties on the number of expected ROI background events (from surface α -decays, neck α -decays, dust α -decays and radiogenic neutrons) limit the sensitivity gain. Developing high-level statistical techniques, such as the PLR, is of increasing importance for future dark matter experiments, where the construction of long-running, larger detectors will likely lead to increasing background levels. In particular for single-phase detectors, which do not have an S2 signal from ionisation that can be used for effective position

reconstruction in removing backgrounds originating from detector surfaces.

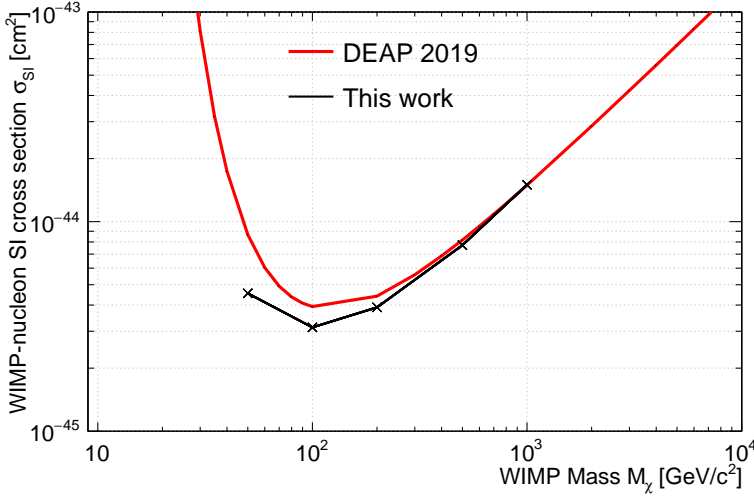


Figure 6.17: 90% C.L. upper limit on the WIMP-nucleon spin-independent cross section σ [cm²] as a function of WIMP mass M_χ [GeV/c²], based on a 231 live-day dataset acquired by the DEAP-3600 detector, using the PLR analysis presented in this thesis (black) and the cut-and-count analysis performed by the DEAP-3600 collaboration in [4] (red).

6.6 Summary and Outlook

THE DEAP-3600 experiment has been actively collecting physics data for over 3 years, in which time the collaboration has published the results of two dark matter searches; the most stringent upper limit placed on the WIMP-nucleon cross section by the DEAP-3600 experiment is based on 231 live days of data, in which a 90% C.L. upper limit of 3.9×10^{-45} cm² is reported for a 100 GeV/c² WIMP. This result uses a cut-and-count analysis, in which zero events are observed in the ROI. The limiting factor on this result comes from the low ($\sim 25\%$) signal acceptance inside the ROI; a combination of the strict ROI bounds and background rejection cuts specifically designed to achieve a background expectation of < 1 event.

A multi-dimensional Profile Likelihood Ratio PLR analysis has been developed

as an alternative statistical technique for setting an upper limit on the WIMP-nucleon cross section. This method has the potential to improve on the current upper limit by increasing the signal acceptance in the ROI, specifically from loosening the ROI bounds and relaxing some of the harshest background rejection cuts. The PLR analysis is developed around three main event reconstruction variables; the total charge **nSCBayes**, the particle identification parameter F_{prompt} and the reconstructed radial position R_{rec} . Potential sources of event reconstruction bias from detector effects, such as the potential loss of observed events if the trigger efficiency of the detector is $< 100\%$, have been investigated and quantified. A procedure to characterise the trigger efficiency as a function of prompt charge **promptPE** was developed using in-situ periodically-triggered ^{39}Ar β -decay data, which confirmed that the trigger efficiency reaches 100% on average at 30 **promptPE**, translating to **nSCBayes** ~ 95 PE for ERs and ~ 40 PE for NRs.

6

The PLR analysis requires a comprehensive background model; all of the sources included in the analysis (^{39}Ar β -decays, surface, neck and dust α -decays and radiogenic neutrons) and their predicted rates in the detector have been discussed in detail. A thorough characterisation of the expected event topologies for all of these background sources in the **nSCBayes**, F_{prompt} and R_{rec} dimensions has been performed and implemented into the PLR analysis, using either theoretical predictions, in-situ calibration data or MC simulations. In addition, an in-situ measurement of the ^{85}Kr activity was performed in order to determine whether it is a significant background component to the ER band and ^{39}Ar β -decay energy spectrum. ^{39}Ar data is used as a sideband in the PLR analysis, to constrain the uncertainty on the mean light yield. The ^{85}Kr activity was measured to be negligible with respect to the ^{39}Ar activity, $\mathcal{A}_{\text{Kr85}} = 1.15 \pm 0.23$ mBq/kg, and as such was not included as a background component in the model.

For two fake datasets comprised of 15 (25) observed events and 15 expected

background events, the PLR projects an optimum upper limit on the WIMP-nucleon cross section at 90% C.L. of $1.90 \times 10^{-45} \text{ cm}^2$ ($4.20 \times 10^{-45} \text{ cm}^2$) for a $100 \text{ GeV}/c^2$ WIMP considering minimal systematic uncertainties (from the mean light yield and quenching factor). With the addition of the remaining systematics, the sensitivity worsens by 85% (30%) compared to the optimum case. This increase is mostly driven by the conservative uncertainties on the ROI background predictions; when the uncertainties on the background ROI predictions are reduced by a factor of 2, the sensitivity improves by up to 40% compared to when the nominal uncertainties are considered.

With 24 observed events in the 231 live-day dataset acquired by the DEAP-3600 detector and ~ 17 expected background events from the background model described in Chapter 4, the PLR analysis calculates a 90% C.L. upper limit of $3.13 \times 10^{-45} \text{ cm}^2$ at $100 \text{ GeV}/c^2$; a limit 20% more sensitive than the upper limit obtained by the DEAP-3600 collaboration in [4]. The result determined from this analysis is expected to be at least 20% more sensitive than the DEAP-3600 result obtained in [4], considering just the increase in the exposure. Below $100 \text{ GeV}/c^2$, this level of improvement is achieved and surpasses expectation for smaller WIMP masses, reaching a $\sim 50\%$ improvement in sensitivity at $50 \text{ GeV}/c^2$. At WIMP masses greater than $100 \text{ GeV}/c^2$, the level of improvement is less than expected from the increase in the fiducial volume; the two results converge at $1000 \text{ GeV}/c^2$. The large uncertainties on the number of expected ROI background events (from surface α -decays, neck α -decays, dust α -decays and radiogenic neutrons) are the main limiting factors to the sensitivity gain.

Investigation is ongoing into reducing the uncertainties on the ROI background predictions, which has been shown in Section 6.4 to significantly improve the sensitivity of the PLR analysis. Further studies are also ongoing to explore additional background rejection cuts to remove radiogenic neutron backgrounds predicted to

be the leading background contribution to the WIMP search using the PLR-specific ROI definition and cutflow. A water tank veto cut is currently in the process of being optimised such that it can be applied to data to remove potential cosmogenic muon and neutron backgrounds. In addition, the prospect of lowering the `nSCBayes` threshold of the ROI for the PLR is being explored. The optical model systematics and detector response systematics discussed in Section 6.2 are currently in the process of being propagated through the remaining background models and WIMP signal model in the PLR; the most significant task remaining for the completion of the analysis. The author intends to publish the PLR analysis presented in this thesis in the near future.

Bibliography

- [1] Tina R Pollmann. “Estimating the efficiency turn-on curve for a constant-threshold trigger without a calibration dataset”. In: *The European Physical Journal C* 79.4 (2019), p. 322.
- [2] Alistair Butcher. “Searching for Dark Matter with DEAP-3600”. PhD thesis. Ph. D. thesis, Royal Holloway University of London, 2016.
- [3] Navin Seeburn. “It Came From Outer Space: Position Reconstruction in the DEAP-3600 Dark Matter Detector”. PhD thesis. Ph. D. thesis, Royal Holloway University of London, 2018.
- [4] DEAP Collaboration et al. “Search for dark matter with a 231-day exposure of liquid argon using DEAP-3600 at SNOLAB”. In: *Physical Review D* 100.2 (2019), p. 022004.
- [5] Fritz Zwicky. “Die rotverschiebung von extragalaktischen nebeln”. In: *Helvetica Physica Acta* 6 (1933), pp. 110–127.
- [6] Martin Lopez-Corredoira. “Problems with the dark matter and dark energy hypotheses, and alternative ideas”. In: *arXiv:1808.09823* (2018).
- [7] Laura Baudis. “WIMP dark matter direct-detection searches in noble gases”. In: *Physics of the Dark Universe* 4 (2014), pp. 50–59.

- [8] Gianfranco Bertone and Dan Hooper. “History of dark matter”. In: *Reviews of Modern Physics* 90.4 (2018), p. 045002.
- [9] Gianfranco Bertone, Dan Hooper, and Joseph Silk. “Particle dark matter: Evidence, candidates and constraints”. In: *Physics reports* 405.5-6 (2005), pp. 279–390.
- [10] David Puglielli, Lawrence M Widrow, and Stéphane Courteau. “Dynamical models for NGC 6503 using a Markov chain Monte Carlo technique”. In: *The Astrophysical Journal* 715.2 (2010), p. 1152.
- [11] Ken Freeman. “Dark matter in galaxies”. In: *Cosmology: The Physics of the Universe* (2008), p. 186.
- [12] Douglas Clowe et al. “A direct empirical proof of the existence of dark matter”. In: *The Astrophysical Journal Letters* 648.2 (2006), p. L109.
- [13] Martin C Weisskopf et al. “Chandra X-ray Observatory (CXO): overview”. In: *X-Ray Optics, Instruments, and Missions III*. Vol. 4012. International Society for Optics and Photonics. 2000, pp. 2–16.
- [14] David Harvey et al. “The nongravitational interactions of dark matter in colliding galaxy clusters”. In: *Science* 347.6229 (2015), pp. 1462–1465.
- [15] Arno A Penzias and Robert Woodrow Wilson. “A measurement of excess antenna temperature at 4080 Mc/s.” In: *The Astrophysical Journal* 142 (1965), pp. 419–421.
- [16] JD Barrow. “What is the principal evidence for the cosmological principle?” In: *Quarterly Journal of the Royal Astronomical Society* 30 (1989), pp. 163–167.
- [17] David L Clements. “An introduction to the Planck mission”. In: *Contemporary Physics* 58.4 (2017), pp. 331–348.

- [18] Planck. *2018 CMB maps - Planck PLA Internal Wiki*. 2018. URL: https://wiki.cosmos.esa.int/planck-legacy-archive/index.php/CMB_maps (visited on 08/27/2019).
- [19] Planck Collaboration. “Planck 2018 results. VI. Cosmological parameters”. In: *Astronomy & Astrophysics* (2020). URL: <https://doi.org/10.1051/0004-6361/201833910> (visited on 07/21/2020).
- [20] Darren J Croton. “Damn you, little h!(or, real-world applications of the hubble constant using observed and simulated data)”. In: *Publications of the Astronomical Society of Australia* 30 (2013).
- [21] Karsten Jedamzik and Maxim Pospelov. “Big Bang nucleosynthesis and particle dark matter”. In: *New Journal of Physics* 11 (2009).
- [22] Atul Kedia et al. “Relativistic Electron Scattering and Big Bang Nucleosynthesis”. In: *APS 2019* (2019), B11–003.
- [23] Peter AR Ade et al. “Planck 2015 results-xiii. cosmological parameters”. In: *Astronomy & Astrophysics* 594 (2016), A13.
- [24] Antonio Peimbert, Manuel Peimbert, and Valentina Luridiana. “The primordial helium abundance and the number of neutrino families”. In: *Revista mexicana de astronomía y astrofísica* 52.2 (2016), pp. 419–424.
- [25] Yu I Izotov, TX Thuan, and NG Guseva. “A new determination of the primordial He abundance using the He I $\lambda 10830$ Å emission line: cosmological implications”. In: *Monthly Notices of the Royal Astronomical Society* 445.1 (2014), pp. 778–793.
- [26] Eric Gawiser and Joseph Silk. “Extracting primordial density fluctuations”. In: *Science* 280.5368 (1998), pp. 1405–1411.
- [27] Margaret J Geller et al. “The century survey: a deeper slice of the universe”. In: *Astron.J* 114 (1997).

- [28] Beth A Reid et al. “Cosmological constraints from the clustering of the Sloan Digital Sky Survey DR7 luminous red galaxies”. In: *Monthly Notices of the Royal Astronomical Society* 404.1 (2010), pp. 60–85.
- [29] Mary K Gaillard, Paul D Grannis, and Frank J Sciulli. “The standard model of particle physics”. In: *Reviews of Modern Physics* 71.2 (1999), S96.
- [30] Particle Data Group. *Review of particle properties*. Vol. 45. 11. American Physical Society, 1992.
- [31] Frank Daniel Steffen. “Dark-matter candidates”. In: *The European Physical Journal C* 59.2 (2009), pp. 557–588.
- [32] Geraldine Servant. “Baryogenesis from Strong C P Violation and the QCD Axion”. In: *Physical review letters* 113.17 (2014), p. 171803.
- [33] Leanne D Duffy and Karl Van Bibber. “Axions as dark matter particles”. In: *New Journal of Physics* 11.10 (2009), p. 105008.
- [34] Gerard Jungman, Marc Kamionkowski, and Kim Griest. “Supersymmetric dark matter”. In: *Physics Reports* 267.5-6 (1996), pp. 195–373.
- [35] Manuel Drees. “Dark Matter Theory”. In: *arXiv preprint hep-ph/1811.06406v1* (2018).
- [36] Bohdan Grzadkowski and Jose Wudka. “Pragmatic approach to the little hierarchy problem: the case for Dark Matter and neutrino physics”. In: *Physical review letters* 103.9 (2009), p. 091802.
- [37] Guang Hua Duan et al. “Probing GeV-scale MSSM neutralino dark matter in collider and direct detection experiments”. In: *Physics Letters B* 778 (2018), pp. 296–302.
- [38] Paola Arias et al. “WISPy cold dark matter”. In: *Journal of Cosmology and Astroparticle Physics* 2012.06 (2012), p. 013.

- [39] Christopher McCabe. “Astrophysical uncertainties of dark matter direct detection experiments”. In: *Physical Review D* 82.2 (2010), p. 023530.
- [40] Markus Weber and Wim de Boer. “Determination of the local dark matter density in our galaxy”. In: *Astronomy & Astrophysics* 509 (2010), A25.
- [41] Paolo Salucci et al. “The dark matter density at the Sun’s location”. In: *Astronomy & Astrophysics* 523 (2010), A83.
- [42] Ulrich Haisch and Felix Kahlhoefer. “On the importance of loop-induced spin-independent interactions for dark matter direct detection”. In: *Journal of Cosmology and Astroparticle Physics* 2013.04 (2013), p. 050.
- [43] Carlos E Yaguna. “New constraints on xenonphobic dark matter from DEAP-3600”. In: *Journal of Cosmology and Astroparticle Physics* 2019.04 (2019), p. 041.
- [44] JD Lewin and PF Smith. “Review of mathematics, numerical factors, and corrections for dark matter experiments based on elastic nuclear recoil”. In: *Astroparticle Physics* 6.1 (1996), pp. 87–112.
- [45] N Wyn Evans, Ciaran AJ O’Hare, and Christopher McCabe. “Refinement of the standard halo model for dark matter searches in light of the Gaia Sausage”. In: *Physical Review D* 99.2 (2019), p. 023012.
- [46] Martin C Smith et al. “The RAVE survey: constraining the local galactic escape speed”. In: *Monthly Notices of the Royal Astronomical Society* 379.2 (2007), pp. 755–772.
- [47] R Agnese et al. “Results from the super cryogenic dark matter search experiment at Soudan”. In: *Physical Review Letters* 120.6 (2018), p. 061802.
- [48] R Agnese et al. “Projected Sensitivity of the SuperCDMS SNOLAB experiment”. In: *Physical Review D* 95.8 (2017), p. 082002.

- [49] XENON Collaboration et al. “Dark matter search results from a one ton-year exposure of XENON1T”. In: *Physical Review Letters* 121.11 (2018), p. 111302.
- [50] DS Akerib et al. “Projected WIMP sensitivity of the LUX-ZEPLIN dark matter experiment”. In: *Physical Review D* 101.5 (2020), p. 052002.
- [51] Shawn Henderson, Jocelyn Monroe, and Peter Fisher. “Maximum patch method for directional dark matter detection”. In: *Physical Review D* 78.1 (2008), p. 015020.
- [52] Steven Yellin. “Finding an upper limit in the presence of an unknown background”. In: *Physical Review D* 66.3 (2002), p. 032005.
- [53] E Aprile et al. “Likelihood approach to the first dark matter results from XENON100”. In: *Physical Review D* 84.5 (2011), p. 052003.
- [54] J Billard, F Mayet, and D Santos. “Exclusion limits from data of directional Dark Matter detectors”. In: *Physical Review D* 82.5 (2010), p. 055011.
- [55] Marc Schumann. “Dark matter search with liquid noble gases”. In: *arXiv preprint arXiv:1206.2169* (2012).
- [56] Jun Chen. “Nuclear Data Sheets for A= 39”. In: *Nuclear Data Sheets* 149 (2018), pp. 1–251.
- [57] P Benetti et al. “Measurement of the specific activity of ^{39}Ar in natural argon”. In: *Nuclear Instruments and Methods in Physics Research Section A: Accelerators, Spectrometers, Detectors and Associated Equipment* 574.1 (2007), pp. 83–88.
- [58] Jean E Sansonetti and William Clyde Martin. “Handbook of basic atomic spectroscopic data”. In: *Journal of Physical and Chemical Reference Data* 34.4 (2005), pp. 1559–2259.

- [59] Akira Hitachi et al. “Effect of ionization density on the time dependence of luminescence from liquid argon and xenon”. In: *Physical Review B* 27.9 (1983), p. 5279.
- [60] M Hofmann et al. “Ion-beam excitation of liquid argon”. In: *The European Physical Journal C* 73.10 (2013), p. 2618.
- [61] Robert L Jaffe and Washington Taylor. *The physics of energy*. Cambridge University Press, 2018.
- [62] Jens Lindhard et al. “Integral equations governing radiation effects”. In: *Mat. Fys. Medd. Dan. Vid. Selsk* 33.10 (1963), pp. 1–42.
- [63] Huajie Cao et al. “Measurement of scintillation and ionization yield and scintillation pulse shape from nuclear recoils in liquid argon”. In: *Physical Review D* 91.9 (2015), p. 092007.
- [64] Tadayoshi Doke et al. “Absolute scintillation yields in liquid argon and xenon for various particles”. In: *Japanese journal of applied physics* 41.3R (2002), p. 1538.
- [65] TH Joshi et al. “First measurement of the ionization yield of nuclear recoils in liquid argon”. In: *Physical Review Letters* 112.17 (2014), p. 171303.
- [66] P Agnes et al. “Simulation of argon response and light detection in the DarkSide-50 dual phase TPC”. In: *Journal of Instrumentation* 12.10 (2017), P10015.
- [67] Ilya Obodovskiy. *Radiation: fundamentals, applications, risks, and safety*. Elsevier, 2019.
- [68] R Acciarri et al. “Effects of Nitrogen contamination in Liquid Argon”. In: *Journal of Instrumentation* 5.06 (2010), P06003.

- [69] Emily Grace et al. “Index of refraction, Rayleigh scattering length, and Sellmeier coefficients in solid and liquid argon and xenon”. In: *Nuclear Instruments and Methods in Physics Research Section A: Accelerators, Spectrometers, Detectors and Associated Equipment* 867 (2017), pp. 204–208.
- [70] AC Sinnock and BL Smith. “Refractive indices of the condensed inert gases”. In: *Physical Review* 181.3 (1969), p. 1297.
- [71] M Babicz et al. “Experimental study of the propagation of scintillation light in Liquid Argon”. In: *Nuclear Instruments and Methods in Physics Research Section A: Accelerators, Spectrometers, Detectors and Associated Equipment* 936 (2019), pp. 178–179.
- [72] M Babicz et al. “Light propagation in liquid argon”. In: *arXiv preprint arXiv:2002.09346* (2020).
- [73] P-A Amaudruz et al. “Design and construction of the DEAP-3600 dark matter detector”. In: *Astroparticle Physics* 108 (2019), pp. 1–23.
- [74] P-A Amaudruz et al. “Measurement of the scintillation time spectra and pulse-shape discrimination of low-energy β and nuclear recoils in liquid argon with DEAP-1”. In: *Astroparticle Physics* 85 (2016), pp. 1–23.
- [75] Mark G Boulay and Andrew Hime. “Technique for direct detection of weakly interacting massive particles using scintillation time discrimination in liquid argon”. In: *Astroparticle Physics* 25.3 (2006), pp. 179–182.
- [76] VM Gehman et al. “Fluorescence efficiency and visible re-emission spectrum of tetraphenyl butadiene films at extreme ultraviolet wavelengths”. In: *Nuclear Instruments and Methods in Physics Research Section A: Accelerators, Spectrometers, Detectors and Associated Equipment* 654.1 (2011), pp. 116–121.
- [77] KK Hamamatsu Photonics. *Photomultiplier Tube-R5912*. 1998.

- [78] P-A Amaudruz et al. “In-situ characterization of the Hamamatsu R5912-HQE photomultiplier tubes used in the DEAP-3600 experiment”. In: *Nuclear Instruments and Methods in Physics Research Section A: Accelerators, Spectrometers, Detectors and Associated Equipment* 922 (2019), pp. 373–384.
- [79] A. Erlandson & S. Westerdale. *Cosmogenic Backgrounds for the One Year Open Data Set Paper Rev 0*. URL: https://www.snolab.ca/deap/private/TWiki/pub/Main/DeapStr2018x021/Cosmogenics_STR_Rev1.pdf.
- [80] Angel Morales, Julio Morales, and JA Villar. *TAUP 91: Proceedings of the Second International Workshop on Theoretical and Phenomenological Aspects of Underground Physics*. Elsevier, 2016.
- [81] Thomas Lindner. “DEAP-3600 Data Acquisition System”. In: *Journal of Physics: Conference Series*. Vol. 664. 8. IOP Publishing. 2015, p. 082026.
- [82] S Ritt, P Amaudruz, and K Olchanski. “MIDAS documentation”. In: URL <http://ladd00.triumf.ca/~daqweb/doc/midas/html> (1993).
- [83] Rene Brun and Fons Rademakers. “ROOT—an object oriented data analysis framework”. In: *Nuclear Instruments and Methods in Physics Research Section A: Accelerators, Spectrometers, Detectors and Associated Equipment* 389.1-2 (1997), pp. 81–86.
- [84] T Caldwell. “Simulation of noble liquid detectors using rat”. In: *AARM Meeting at Fermilab*. 2014.
- [85] Sea Agostinelli et al. “GEANT4—a simulation toolkit”. In: *Nuclear instruments and methods in physics research section A: Accelerators, Spectrometers, Detectors and Associated Equipment* 506.3 (2003), pp. 250–303.
- [86] D-M Mei et al. “A model of nuclear recoil scintillation efficiency in noble liquids”. In: *Astroparticle Physics* 30.1 (2008), pp. 12–17.

- [87] WB Wilson et al. “Sources: A code for calculating (α , n), spontaneous fission, and delayed neutron sources and spectra”. In: *Progress in Nuclear Energy* 51.4-5 (2009), pp. 608–613.
- [88] S Westerdale and Peter Daniel Meyers. “Radiogenic neutron yield calculations for low-background experiments”. In: *Nuclear Instruments and Methods in Physics Research Section A: Accelerators, Spectrometers, Detectors and Associated Equipment* 875 (2017), pp. 57–64.
- [89] WH Lippincott et al. “Scintillation time dependence and pulse shape discrimination in liquid argon”. In: *Physical Review C* 78.3 (2008), p. 035801.
- [90] Tina Pollmann, Mark Boulay, and Marcin Kuźniak. “Scintillation of thin tetraphenyl butadiene films under alpha particle excitation”. In: *Nuclear Instruments and Methods in Physics Research Section A: Accelerators, Spectrometers, Detectors and Associated Equipment* 635.1 (2011), pp. 127–130.
- [91] P-A Amaudruz et al. “First results from the DEAP-3600 dark matter search with argon at SNOLAB”. In: *Physical Review Letters* 121.7 (2018), p. 071801.
- [92] M Akashi-Ronquest et al. “Improving photoelectron counting and particle identification in scintillation detectors with Bayesian techniques”. In: *Astroparticle Physics* 65 (2015), pp. 40–54.
- [93] A Butcher et al. “A method for characterizing after-pulsing and dark noise of PMTs and SiPMs”. In: *Nuclear Instruments and Methods in Physics Research Section A: Accelerators, Spectrometers, Detectors and Associated Equipment* 875 (2017), pp. 87–91.
- [94] M Burghart. “Background suppression through pulse shape analysis in the DEAP-3600 dark matter detector”. PhD thesis. Master’s thesis, Technical University of Munich, 2018.

- [95] P Adhikari et al. “The liquid-argon scintillation pulseshape in DEAP-3600”. In: *The European Physical Journal. C, Particles and Fields*. 80.4 (2020).
- [96] R Saldanha et al. “Cosmogenic production of ^{39}Ar and ^{37}Ar in argon”. In: *Physical Review C* 100.2 (2019), p. 024608.
- [97] AC Hayes et al. “Systematic uncertainties in the analysis of the reactor neutrino anomaly”. In: *Physical Review Letters* 112.20 (2014), p. 202501.
- [98] Leendert Hayen et al. “First-forbidden transitions in the reactor anomaly”. In: *Physical Review C* 100.5 (2019), p. 054323.
- [99] Patrick Huber. “Determination of antineutrino spectra from nuclear reactors”. In: *Physical Review C* 84.2 (2011), p. 024617.
- [100] Xavier Mougeot. “BetaShape: A new code for improved analytical calculations of beta spectra”. In: *EPJ Web of Conferences*. Vol. 146. EDP Sciences. 2017, p. 12015.
- [101] Joel Kostensalo, Jouni Suhonen, and Kai Zuber. “Spectral shapes of forbidden argon β decays as background component for rare-event searches”. In: *Journal of Physics G: Nuclear and Particle Physics* 45.2 (2017), p. 025202.
- [102] Gregory Choppin, Jan-Olov Liljenzin, and Jan Rydberg. *Radiochemistry and nuclear chemistry*. Butterworth-Heinemann, 2002.
- [103] H Daniel et al. “Shapes of Allowed and Unique First-Forbidden β -Ray Spectra: In 114, K 42, Rb 86, Sr 90, and Y 90”. In: *Physical Review* 136.5B (1964), B1240.
- [104] R Ajaj et al. “Electromagnetic Backgrounds and Potassium-42 Activity in the DEAP-3600 Dark Matter Detector”. In: *Physical Review D* 100.7 (2019), p. 072009.

- [105] Allen Caldwell, Daniel Kollár, and Kevin Kröninger. “BAT—The Bayesian analysis toolkit”. In: *Computer Physics Communications* 180.11 (2009), pp. 2197–2209.
- [106] Jool van Ham, LJHM Janssen, and Rob J Swart. *Non-CO2 Greenhouse Gases: Why and How to Control?: Proceedings of an International Symposium, Maastricht, The Netherlands, 13–15 December 1993*. Springer Science & Business Media, 2012.
- [107] Paolo Agnes et al. “Results from the first use of low radioactivity argon in a dark matter search”. In: *Physical Review D* 93.8 (2016), p. 081101.
- [108] Y Hui et al. “Measurement of Mine Dust Deposited on Sanded Acrylic Surface Under Bonding Conditions at the 4600 Laboratory”. In: *SNO-STR-92-26* (1992).
- [109] Matthew Gordon Dunford. “A Search for the Neutrinoless Double Electron Capture of ^{36}Ar and a Measurement of the Specific Activity of ^{39}Ar in Atmospheric Argon with the DEAP-3600 Detector”. In: (2018).